

國立交通大學

電子工程學系電子研究所

博士論文

通信接收機之數位訊號處理演算法：

同步，等化和通道估計

Digital Signal Processing Algorithms for
Communication Receivers:
Synchronization, Equalization
and Channel Estimation

研究生：洪崑健

指導教授：林大衛

中華民國九十七年十月

通信接收機之數位訊號處理演算法：同步，等化和通道估計

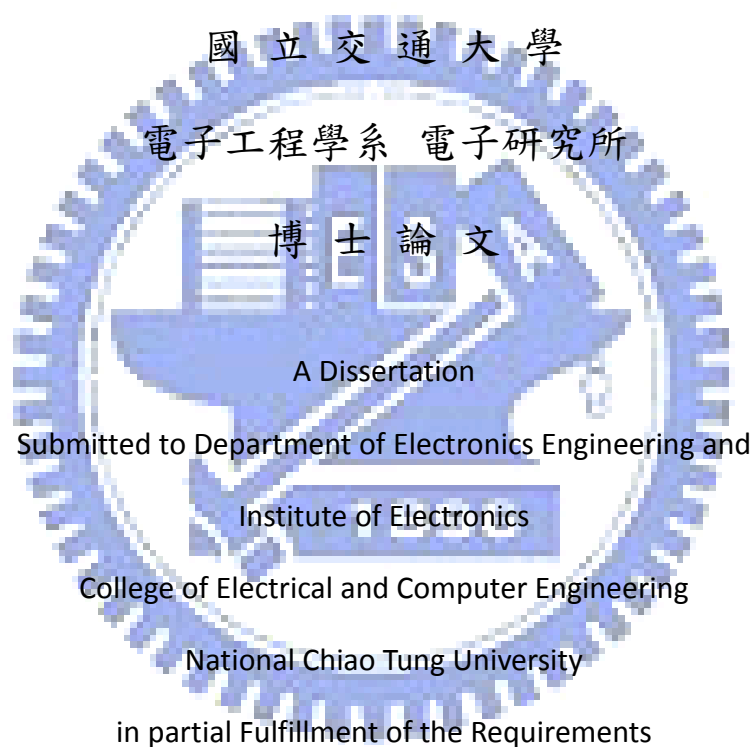
Digital Signal Processing Algorithms for Communication Receivers:
Synchronization, Equalization and Channel Estimation

研究生：洪崑健

Student : Kun-Chien Hung

指導教授：林大衛

Advisor : David W. Lin



for the Degree of

Doctor of Philosophy

in

Electronics Engineering

October 2008

Hsinchu, Taiwan, Republic of China

中華民國九十七年十月

通信接收機之數位訊號處理演算法：同步，等化和通道估計

研究生：洪崑健

指導教授：林大衛博士

國立交通大學
電子工程學系 電子研究所

摘要

數位通訊接收機設計，可分為訊號處理單元與資料處理單元。其中訊號處理單元用以解決訊號同步、通道等化與通道估計等問題。本論文以接收機之數位處理演算法設計為主題，探討各種通訊系統之同步、等化與通道估計議題。本論文根據應用之系統，分為三個部份。第一部份為有線單載波之接收機設計；第二部份為無線多載波系統之接收機設計；第三部份為寬頻多進多出系統之傳送與接收設計。

第一部份，單載波接收機設計議題，我們探討載波頻率回復與盲目決策回復等化器等議題。就載波回復機制問題，我們探討兩種技術：頻率估計與載波回復迴路。針對頻率估計議題，我們研究延滯交互相關之頻率估計技術。從中探討費氏(Fitz' s)演算法之效能，進而推演出一套低複雜度高精準度之多解析演算法並將此演算法運用於 QAM 系統。針對載波回復迴路設計，我們根據星圖降階(reduced constellation)的概念提出一系列之盲目相位偵測器以增加頻率搜尋範圍。此外考量收斂速度與穩定追蹤，我們進而推演出一套結合星圖降階與決策導向(decision-directed)的混合相位偵測器與迴路濾波器頻寬動態控制機制。就盲目決策回復等化器設計議題，我們探討盲目適應性演算法之加速，並且提出一套運用於盲目等化器之可變步階係數(Variable stepsize)演算法；此外，我們提出適應性演算法之軟式切換概念，並且提出一套結合盲目與決策導向之混合

式適應性演算法以加速適應性訊號處理演算法之模式切換。最後，我們探討幾種結合載波回復與決策回復等化器設計之運作策略。

第二部份，多載波接收機設計議題，我們探討通道估計與 WiMAX 系統中的細胞偵測既整數載波漂移估計等議題。首先，針對同步議題之細胞偵測既整數載波漂移估計，我們根據理論推導出最佳偵測演算法。針對最佳演算法化簡，推得頻域濾波概念，並且根據該概念推出幾種簡化之演算法。就通道估計議題，我們提出兩種類型的通道估計演算法。首先，我們探討多項式內插通道估計演算法的估計誤差之最佳化，提出濾波器窗口漂移(window shift)概念，在給定內插階數的情況下，推得最佳漂移量的理論值與其值估計方法。另一方面，我們採取近似最小誤差估計作為通道估計演算法。在這議題中，為得到在頻域的近似通道交互相關函數，我們推得通道的“延滯方均值”與“延滯均值”簡易估計演算法。最後，我們將其估計法應用於梳型 (comb-type) OFDM 與 WiMAX 等系統之通道估計。

第三部份，寬頻多進多出(Wide-band MIMO)傳送接收機設計議題，我們討論最佳傳送器設計以及其接收機等化與通道估計演算法。針對錯誤更正碼保護之 MIMO OFDM 傳輸，加入一空間-頻率轉換(Space-frequency transform)，用以最佳化其分集增益(diversity gain)與編碼增益(coding gain)。該空頻轉換式採取兩階段運算程序：正交轉換(orthogonal transform)、空頻錯置(space-time interleaving)。在接收端，針對通道等化與解調設計，採取渦輪決策回復等化器作為遞迴解碼程序。在演算法實現，使用頻域等化器降低接收機複雜度，並且提出可分離之空頻錯置設計，如此可將空頻錯置與渦輪決策迴路分離。我們也提出結合遞迴通道估計與資料偵測演算法以降低嚮導符碼的使用。

Digital Signal Processing Algorithms for Communication Receivers: Synchronization, Equalization and Channel Estimation

Student: Kun-Chien Hung

Advisor: Dr. David-W. Lin

Department of Electronics Engineering
& Institute of Electronics
National Chiao Tung University

Abstract

The communication receiver can be divided into the signal processing unit and the data processing unit. The signal processing unit is mainly used to solve problems of the signal synchronization, the channel equalization and the channel estimation. The topic of this thesis is design of the signal processing algorithms and discusses various issues in synchronization, equalization and channel estimations. According to the application of the systems, this work is divided into three parts. Part I is the receiver design in wired single carrier (SC) system; Part II is the receiver design of multi-carrier orthogonal frequency-division multiplexing (OFDM) systems over a wireless channel; Part III is the transceiver design of the wide-band MIMO systems.

In Part I, the topics of the receiver design in SC systems, we address the carrier recovery and the blind decision-feedback equalization (DFE). In carrier recovery issue, we discuss two techniques: the carrier frequency estimation and the carrier recovery loop. For the carrier frequency estimation, we study the frequency estimator using the delay correlation, derive the performance of the Fitz's algorithm, propose a low-complexity and high-accuracy multi-resolution algorithm, and then apply the proposed algorithm for the frequency estimation in QAM system. For the carrier recovery loop, we propose a series of the blind phase detections (PDs) according to the reduced-constellation concept, which can enhance the acquisition range of the carrier frequency offset. In addition, when considering the acquisition speed and the tracking stability, we furthermore derive a hybrid PD, which combines the decision-directed PD and the reduced-constellation PD, and the mechanism of the dynamic control of the loop bandwidth. In the design topic of blind DFE, we focus on the improvement of the convergence speed of the blind adaptive algorithm and

propose a variable stepsize (VSS) algorithm, which is applicable to blind algorithms. In addition, we suggest the soft-switching concept of the adaptive mode and present a hybrid adaptive algorithm, which combines the blind algorithm and the DD-LMS algorithm, to speed up the operation mode switch of the adaptive algorithm. At final of this part, we discuss several operation strategies of the joint carrier recovery and the DFE.

In Part II, the topics of the receiver design in multi-carrier systems, we discuss the issues of the channel estimation and the joint estimation of the Cell-ID and integral CFO in WiMAX system. First, for the synchronization issue in joint estimation of the cell-ID and integral CFO, we derive an optimal detection algorithm according to theoretical derivation. Moreover, from the simplification of the optimal detection algorithm, we suggest the concept of the frequency domain filtering and propose several simple detection algorithms according to the concept. In the topic of the channel estimation, we propose two kinds of the channel estimation algorithms. First, we study the optimization of the estimate mean-square error of the polynomial interpolation. We introduce a window shift concept, derive the optimal window shift, and propose the estimation method of the value under a given interpolation order. Besides, we apply the approximate minimal mean-square error (MMSE) estimator to the channel estimation. In this topic, in order to derive the approximate cross-correlation function in frequency domain, we propose the simple estimation of the root-mean-square delay spread and the mean delay of the channel. We apply the estimators in the channel estimation of the comb-type OFDM and WiMAX systems.

In part III, the topic of the transceiver design in wide-band MIMO systems, we address the design of the optimal transmitter and the corresponding receiver. For the coded MIMO OFDM transmission, we insert a space-frequency transform (SFT) to maximize the diversity gain and the coding gain. The transform is realized in a two-step process: the orthogonal transform and then the space-frequency interleaving (SFI). At the receiver, for the design of the channel equalization and demodulation, we adopt the turbo-DFE as the iterative decoding process. In the algorithm realization, we use the frequency domain equalization to reduce the receiver implementation cost and propose the separable SFI design. By this way, the SFI can be moved outside the turbo-DFE loop. In addition, we propose the algorithm of joint channel estimation and the data detection to reduce the utilization of the pilot symbols.

致 謝

這篇論文的完成，必須感謝各方的支持。首先，感謝林大衛教授的諄諄教誨，從專題生到博士畢業生，這九年的學習生涯中，老師扮演著學海中領航的明燈。從指導中感受到老師對於理論的執著與嚴謹的態度。九年是一段漫長的時間，感謝老師的付出，在此獻上最誠摯的大感謝。感謝桑梓賢老師一同參與研究討論，並予以指導。感謝家人的支持，讓我在學習的過程中，於經濟上、生活上不曾感受到困頓匱乏。感謝國科會等機構的研究計畫經費支持。感謝學習後半段加入的阿驢兒，成為我挫折時最好的寄託與失落時吐苦水的好對象。感謝實驗室學長學弟們在實驗室管理上得協助、在學術議題上的討論與心得分享。特別感謝林大師學弟，總是在深夜陪我慢跑。



Contents

1	Thesis Introduction	1
1.1	Communication Systems	1
1.2	Issues of Receiver Design	2
1.3	Design Target of Receiver Algorithms	2
1.3.1	Methods to Achieve Design Target	3
1.4	Structure of Receiver	3
1.4.1	Carrier Frequency Estimation	4
1.4.2	Data Detection	5
1.4.3	Channel Estimation	6
1.5	Thesis Organization And Studied Algorithms	7
I	Receiver Design in Single Carrier System over Cable Channels	9
2	Carrier Synchronization	12
2.1	Open-loop Frequency Estimator	13
2.1.1	Spectrum Analysis using FFT	13
2.1.2	Fitz's Algorithm	14
2.1.3	Performance Analysis of the Fitz's Algorithm	15
2.1.4	Multi-resolution Algorithm and Modified Fitz's Estimator	18
2.1.5	Optimization of Multi-resolution Algorithm	19
2.1.6	Fourth Power Frequency Estimator in QAM System	24
2.2	Carrier Recovery Loop	29
2.2.1	Carrier Recovery Loop	29
2.2.2	Data Aided/Decision Directed Phase Detector	30
2.2.3	Reduced-Constellation Phase Detector	30
2.2.4	Characterization of Reduced-Constellation Phase Detectors	32
2.2.5	Hybrid PD	37
2.2.6	Dynamic Loop Bandwidth Control	39
2.3	Conclusions	44
3	Blind Adaptive Decision Feedback Equalization	45
3.1	Optimal Coefficient and LMS Algorithm	46
3.2	Blind Adaptive Algorithms	47
3.2.1	Constant Modulus Algorithm	47
3.2.2	Multi-Modulus Algorithm	47
3.2.3	Steady-state MSE Caused by Blind Algorithm	48
3.3	Variable Stepsize Algorithm and Hybrid Algorithm	49
3.3.1	MSE Measurement: Boundary Mean-Square Error	51
3.3.2	Variable Stepsize Algorithm	52

3.3.3	Hybrid Algorithm: Combination of Blind and DD-LMS	54
3.3.4	Simulation Studies	55
3.4	Conclusions	58
4	Jointly Operation of Carrier Synchronization and Blind Adaptive DFE	59
4.1	Conventional Procedure	59
4.1.1	Multi-stage Procedure	59
4.1.2	Multi-module Co-training	60
4.2	Approach based on Phase Irrelevant DFE	60
4.2.1	Phase Irrelevant DFE (π DFE)	61
4.2.2	Startup Procedure Using π DFE	61
4.2.3	Radius BMSE for VSS Algorithm in π DFE	62
4.2.4	Simulation Studies	62
4.3	Conclusions	63
II	Receiver Design in OFDM/OMDMA System over Wireless Channels	66
5	Introduction to Receiver Design in WiMAX System	69
5.1	Frame Structure and Types of Subchannel Organization	69
5.1.1	Subchannel Organization in PUSC	70
5.2	Main Signal Processing Functions in OFDMA Receiver	71
6	Synchronization in WiMAX System	73
6.1	Initial Synchronization	73
6.1.1	Pre-FFT Synchronization Using CP Correlation	74
6.2	Joint Operation of Preamble Search and Integral CFO Estimate	76
6.2.1	Maximum Likelihood Symbol Detection	76
6.2.2	Joint Preamble Search and Integer CFO Estimation	79
6.3	Performance Studies of Joint Detection Schemes	82
6.3.1	Mathematical Analysis	83
6.3.2	Numerical Studies and Comparisons	87
6.4	Conclusions	89
7	Channel Estimations in Pilot-Aided Multi-Carrier System	91
7.1	MMSE Optimization of Polynomially Interpolative Channel Estimate	92
7.1.1	Introduction	92
7.1.2	MMSE Window Shifting	94
7.1.3	Performance With Comb-Type Pilots	99
7.1.4	Application to WiMAX Downlink	105
7.2	Approximate LMMSE CE with Estimations of Mean Delay and RMS Delay Spread	112
7.2.1	Introduction	112
7.2.2	LMMSE Channel Estimation with Approximate Channel Correlation	114
7.2.3	Simple Estimation Scheme of RMS Delay Spread and Mean Delay	115
7.2.4	Numerical Evaluation and Simulation Study	120
7.2.5	Appilcation in WiMAX Channel Estimation	123
7.3	Conclusions	125

III Transmitter Design over Wide-band MIMO and Its Block Iterative Receiver	129
8 Space Frequency Transformed MIMO OFDM System	131
8.1 System Model	131
8.1.1 Transmission System Structure	131
8.1.2 Channel Model	131
8.2 Condition for Maximum Diversity Gain	133
8.2.1 PEP of Coded and Transformed MIMO OFDM under Multipath Rayleigh Fading	133
8.2.2 Principle of Design for Maximum Diversity Gain	134
8.2.3 Performance of Coded MIMO OFDM Without Transform	135
8.3 Principles of Practical Transform Design	135
9 Receiver Design In Transformed MIMO OFDM System	137
9.1 Block Turbo DFE	137
9.1.1 Block Turbo DFE as Iterative Solution to Constrained Least-Square Problem	137
9.1.2 MMSE Shaping Filtering	138
9.1.3 Employing Fixed Shaping Filter for Reduced Complexity	139
9.1.4 Benefit of Whitening Transform to Turbo DFE Performance	139
9.2 Design for Receiver-Complexity Reduction	139
9.2.1 Turbo DFE in Frequency Domain	140
9.2.2 The Equalizer-Decoder Loop	140
9.2.3 Design of Space-Frequency Interleaving	141
9.2.4 Computational Complexity	142
9.3 Simulation Results	142
9.3.1 Simulation Case 1: A Difficult Channel	143
9.3.2 Simulation Case 2: The ETSI Vehicular A Channel	143
9.4 Joint Channel Estimation and Data Detection	145
9.4.1 Frame Structure and Initial Channel Estimation	145
9.4.2 Jointly Iterative Channel Estimation and Data Detection	146
9.4.3 Simulation Study	147
9.5 Conclusions	148
10 Thesis Conclusions and Future Topics	151
10.1 Future Research Topics	151

List of Figures

1.1	Comparison of the structures of open-loop estimator and closed-loop estimator.	4
1.2	Prototypical transmission system block diagram.	10
2.1	The comparisons of $A(K)$ and the CRB constant $\frac{6}{T(T^2-1)} = 4.8 \times 10^{-8}$ when $T = 500$	17
2.2	MSE of angle frequency $\omega \triangleq 2\pi f/F_s$ for the Fitz's algorithm with $T = 60$ and $K \in [5, 10, 20]$	18
2.3	The simulated and analytic variance of the unwrap error σ_ξ^2 for $T = 100$ and different r_l	22
2.4	The simulated and analytic variance of the unwrap error σ_ξ^2 for $T = 100$ and constant ratio $r_l = 3$	23
2.5	The simulated and analytic probabilities of the unwrapping error.	24
2.6	Performance studies in multi-resolution algorithm.	25
2.7	The analytic probabilities of the unwrapping error for multi-resolution approach.	25
2.8	Structure of the fourth power frequency estimator using correlations.	26
2.9	SNR of $x^4(t)$ corresponding to input SNR in dB.	27
2.10	Simulated unwrapping error probability versus T in X^4 SFE.	28
2.11	Simulated and analytical MSE of the frequency estimator versus T	28
2.12	Typical structure of carrier recovery loop in the receiver design.	29
2.13	Illustration of signal distributions and various quantities used in the analysis of PD.	33
2.14	S curves associated with different PDs, both theoretical (approximate) and actual (in noise). (a) PD 0. (b) PD 1.	34
2.15	S curves associated with different PDs, both theoretical (approximate) and actual (in noise). (a) PD 2. (b) PD 3.	35
2.16	Steady-state variances of DDPD and RCPD.	36
2.17	S-curves of DDPD and RCPD.	37
2.18	S-curves of DDPD, RCPD, and the HPD.	38
2.19	Steady-state variances of DDPD, RCPD and the HPD.	38
2.20	Structure of the proposed dynamic loop bandwidth control.	39
2.21	Selection of the threshold (T) of proposed lock detector in 64QAM system with 18dB SNR. (a) Mean behavior of the lock value versus θ . (b) Variance of the lock value when $\theta = 0$ versus T . (c) Useful percentages of the samples versus T	40
2.22	Simulated results of Case 1, the CRL using RCPD without dynamic loop bandwidth control. At top: estimated frequency normalized to sampling frequency. At bottom: lock indication value.	42
2.23	Simulated results of Case 2, the CRL using HPD without dynamic loop bandwidth control. At top: estimated frequency normalized to sampling frequency. At bottom: lock indication value.	42

2.24	Simulated results of Case 3, the CRL using RCPD with dynamic loop bandwidth control. At top: estimated frequency normalized to sampling frequency. At bottom: lock indication value.	43
2.25	Simulated results of Case 4, the CRL using HPD with dynamic loop bandwidth control. At top: estimated frequency normalized to sampling frequency. At bottom: lock indication value.	43
3.1	The structure of the decision feedback equalizer that is composed by a feed forward filter, a feedback filter, a decision circuit and a filter coefficient adapter. . .	45
3.2	The simulated and analytical steady-state MSEs of the DFE with MMA versus different stepsize μ	50
3.3	Motivation and principle of boundary MSE estimation, illustrated for the case of 4-PAM (applicable also to 16-QAM). The constellation points are at ± 1 and ± 3 . Dashed lines illustrate PDFs of equalizer filter output $y(n)$ corresponding to different values of a_k ; solid line their sum.	52
3.4	Simulated and analytic ratios of MSE to BMSE for QPSK, 16QAM, 64QAM, 256QAM, and 1024QAM.	53
3.5	Comparisons of the proposed blind adaptive algorithms which include the pure blind, the VSS MMA, the MS-VSS MMA, the HVSS MMA and the HVSS-SGA MMA.	56
3.6	Output SNR of H-VSS CMA(*), CC-CMA(*), M-CMA(Δ) and DDCF M-CMA(∇) under 256-QAM in the SPIB chan10.	57
3.7	Output SNR of H-VSS MMA(*), CC-MMA(*), M-MMA(Δ) and DDCF M-MMA(∇) under 256-QAM in the SPIB chan10.	57
4.1	The structure of the joint CRL and DFE, which can be classified as left part:the post-FFF CRL design and right part: the pre-FFF CRL design	59
4.2	Top: (R)BMSE estimation trajectory; bottom: μ_b and μ_d normalized to $\mu_{b,max}$ and $\mu_{d,max}$ correspondingly	63
4.3	Estimation of the CFO.	64
4.4	Snapshots of the constellations, left-top: DFE inputs; right-top: DFE outputs at first stage; left-bottom: DFE outputs at 2nd stage; right-bottom: DFE outputs at final stage.	64
5.1	OFDMA TDD frame example, showing mandatory zone only [48, Fig. 218]. . . .	70
5.2	PUSC DL cluster structure.	71
5.3	PUSC UL tile structure.	71
5.4	Typical OFDMA baseband receiver structure.	72
6.1	Two stage synchronization structure includes pre-FFT synchronization to acquire the fractional CFO and symbol time and post-FFT synchronization to estimate the integral CFO and the preamble index.	74
6.2	Pre-FFT synchronization use blind CP correlation to estimate CFO and symbol time.	75
6.3	Two-stage Implementation of the post-FFT synchronization comprises the coarse integer CFO estimate and the fine joint detection.	79
6.4	Performance comparison of proposed algorithms over AWGN channel.	88
6.5	Performance comparison of proposed algorithms over Rayleigh fading channel. .	89
6.6	Simulation results over vehicular A channel.	90
7.1	Comparison of different ways of interpolation in terms of the equivalent time-windowing effects.	93

7.2	Histogram of estimated window shifts for different orders of polynomial interpolations over SUI-4 at 30 dB SNR.	101
7.3	Histogram of estimated window shifts for different orders of polynomial interpolations over SUI-5 at 30 dB SNR.	101
7.4	Normalized MSE (NMSE) of different channel estimation methods under the SUI-4 PDP, where “PS” stands for “phase-shifted.”	102
7.5	NMSE of different channel estimation methods under the SUI-5 PDP, where “PS” stands for “phase-shifted.”	102
7.6	MSE performance in different update periods of window shift under different channel models and motion speed.	104
7.7	Cluster structure in Mobile WiMAX downlink and corresponding channel estimation method.	105
7.8	CE performance in WiMAX DL transmission at 100 km/h mobile speed with different orders of interpolation.	109
7.9	Comparison of adaptive interpolation with fixed interpolation at 100 km/hr mobile speed.	111
7.10	Mean of estimation errors in delay estimation. Top: Probability of mean in $\Delta\tau_\mu$; bottom: probability of mean in $\Delta\tau_{\text{rms}}^2$	121
7.11	Precision of theory in predicting noise effects in delay estimation. Left: standard deviation in $\Delta\tau_\mu$; right: standard deviation in $\Delta\tau_{\text{rms}}^2$	121
7.12	Normalized MSE in channel estimation for multi-carrier system with comb-type pilot assignment.	122
7.13	Simulation studies of the periodic update scheme for multi-carrier with comb-type pilots at 100 KM/Hr mobility speed.	124
7.14	Simulation studies of the CE schemes for WiMAX DL path at 100 Km/Hr mobility speed.	126
7.15	Simulation studies of the CE schemes for WiMAX UL in 100 Km/Hr mobility speed.	127
8.1	Structure of the MIMO OFDM system considered.	131
8.2	Proposed transform design and associated receiver structure.	136
9.1	The equalizer-decoder loop.	141
9.2	The illustration of separable space-frequency interleaving.	141
9.3	Simulation case 1: BER performance of different systems under a difficult channel.	143
9.4	Simulation case 1: BLER performance of different systems under a difficult channel.	144
9.5	Simulation case 2: BER performance of different systems under an ETSI Vehicular A-based channel condition.	144
9.6	Simulation case 2: BLER performance of different systems under an ETSI Vehicular A-based channel condition.	145
9.7	The pilot-data separated frame structure considered.	146
9.8	Block (symbol) error rates of different transmission schemes over block time-varying channel.	148
9.9	Bit error rates of different transmission schemes over block time-varying channel.	149

List of Tables

2.1 Some phase detector functions 31

10.1 Proposed algorithms for the corresponding issues 153



Chapter 1

Thesis Introduction

This thesis studies the digital signal process algorithms for the communication system designs and focuses on the inner transceiver design, which includes the synchronization, the equalization, the channel estimation, and the space-time transceiver designs. The studied systems cover the single carrier cable system, the multi-carrier wireless system and the wide-band MIMO system. Although the topics are multifarious, we still present the studied algorithms using several viewpoints including the design issues, the design targets, the methods, and the receiver structures. The design issues cover the synchronization issues and the channel effects. The design targets include the receiver performance, the latency, the stability, the cost, and the joint consideration of these factors. We also introduce the problem-solving methods to achieve the targets. The open-loop and closed-loop structures are presented with the examples in carrier recovery, data detection, and channel estimation.

1.1 Communication Systems

Communication system requires the inner receiver to compensate the mismatch between transmitter and receiver and to eliminate the channel interference. The receiver design is the successive signal processes mainly including the signal analyses and signal reconstructions. This thesis focuses on these signal processes in communication systems.

Three communication techniques are studied in thesis including the single carrier (SC) transmission, the multi-carrier or the orthogonal frequency division multiplex (OFDM) transmission, and the wide-band multiple-input-multiple-output (WB-MIMO) transmission. The SC transmission advantages in the low peak-to-average power ratio (PAPR) and the low cost transmitter requirement. However, it takes the great price in receiver design over multi-path environment. The OFDM system can provide flexible multiplexing and has lower cost receiver design over multi-path environment than SC system. However, it requires better RF properties, such as better linearity of power amplify, better phase noise property. In advanced communication, multi-antenna transceiver provides larger capacity and/or better diversity with spatial multiplexing schemes or space-time code.

Several real communication systems are given as the examples for the receiver designs. In SC communication, we study the receiver design in quadrature amplitude modulation. For examples, this modulation scheme is adopted in DVB-C and J. 83B. In OFDM communication, the pilot-aided scheme is most popular currently due to the low-cost implementation of the channel estimation in receiver. In this scheme, we take 802.16e mobile WiMAX as the example. In WB MIMO, we consider the joint design of the transmitter and the receiver to maximize the diversities under given channel codes.

1.2 Issues of Receiver Design

In the end-to-end communication, we need to consider three major issues, which can be classified as the synchronization, the channel compensation and the radio-frequency (RF) calibrations. The synchronization deals with the mismatch between the transmitter(Tx) and the receiver (Rx) and estimate unknown Tx parameter at Rx. The channel compensation considers the removal and elimination of the channel distortion. The channel compensation issues include channel equalization and the channel estimation. The RF calibrations compensate the RF distortions in digital domain. The RF calibrations are the practical issues in realization of the communication receiver; however, this study mainly discusses the first two issues only.

The Tx-Rx mismatch problem happens mainly due to different oscillators at Tx and Rx, which yields the sampling mismatch, the timing mismatch and the carrier mismatch. In addition to oscillator issue, the mobility of Tx and Rx also introduces the frequency offset due to Doppler effect. The distance uncertainty yields the propagation and introduces the symbol time uncertainty.

The unknown parameter estimation is the special function requirement at the receiver. For example in 802.16e mobile WiMAX [48, 98], the mobile station(MS) may need to estimate the cyclic-prefix ration, the occupied bandwidth, and the cell identification (ID-Cell) of the serving base station(BS) before entering the system and sending register message.

The data detection process mainly takes care of the channel distortion problems including the multipath propagation, the time-varying channel fading, the interference and the additive white noise. It mainly includes the equalizer, the channel estimator, and the forward-error-correct(FEC) decoder. The equalizer is used to compensate the multi-path propagation effect; whereas the channel estimator is used to get the channel state information for the equalizer. The FEC code is used to protect the information bits in the AWGN and interference environments.

Besides the synchronization and the channel compensation, the radio-frequency (RF) imperfect effects are also the receiver design issue, which effects includes the IQ imbalance, the LO leakage, and the nonlinearity effects. However, the calibration algorithms are not included in this thesis.

The thesis discusses both the time-division multiplexing SC and OFDM since the time-frequency duality yields similar properties in both system. Thus, the same signal processing concept can be used to deal with different issues in different domains. For example, the equalizer originally is used in SC system to eliminate the ISI issue over multipath channel; this technique now is applied in OFDM system to combat the ICI issue due to frequency offset and Doppler effect. As another example, the spectrum analysis concept of the temporal signal can be used to estimate the delay paths of the channel in OFDM system. Besides, the delay correlation concept is used to estimate both the frequency offset and time shift in our studies.

1.3 Design Target of Receiver Algorithms

The algorithm design should consider the optimization objectives. These factors: the accuracy, the latency, the robustness and the cost are typically considered in the receiver design targets. The accuracy is the Rx performance measure. The commonly used accuracy indications include the error rate (such as the bit error rate and symbol error rate), the mean-square error (MSE), and the signal to noise/interference ratio (SNR/SIR). The latency is the wait time from the start to the steady state. In the adaptive process, the convergence time can be viewed as the latency of the process. Thus, the optimization of the latency in adaptive process is to improve the convergence speed. The robustness is the stability of the design in different environment or in the track of the process, that the target performance can be achieved. In fact, it is hard to quantify the robustness factor, but can be evaluated via the simulation or the test over different

conditions. The cost is the required operations or the hardwares to realize the design. For a signal processor, the requirements of the operations can be the indication of the cost; whereas, for the hardware design, the gate count is typically used as the indication. In addition, the storage requirement is another cost factor.

In practice, these factors may have collisions. We may consider the selection of the algorithm to meet the target consideration. For example, in the adaptive filter algorithms, the recursive least-square (RLS) algorithm can provide fast convergence but needs large computation cost; whereas, the least-mean-square (LMS) algorithm requires cost much fewer than the RLS but it also has slower convergence speed. Thus, one issue in selection of the adaptive algorithm is the trade-off between the convergence and the cost. The choice of the stepsize parameter is another typical constrain in the selection between the convergence speed and the steady-state performance. When the large stepsize is used, the algorithm has fast convergence but poor steady-state performance; in contrast, small stepsize yields better performance but poor convergence.

The optimization target sometimes is the joint cost function or the constrained objective function. We may consider reducing the implementation cost such that the performance degradation is acceptable, or we try to increase the convergence speed of the adaptive filter under the condition of the same final steady-state performance and limited complexity increase. Another example considers the algorithm design to obtain both the stability and the convergence speed with the reasonable cost.

1.3.1 Methods to Achieve Design Target

The design process to achieve the design target is somehow the modifications of the existing methods or the simplifications of the optimal algorithms. In the summary of the thesis, we adopt the methods to modify the existing algorithms to achieve the design target, which are given as follows:

1. dynamic controlled parameters, that the parameters are changed according to the status of the estimator;
2. functional approximation, that the reasonable and simple function is used to approximate the complicated or poor-formulated functions;
3. reduced solution space, that the solution space is constrained in the finite or quantized elements to simplify the solving process of the optimization problem;
4. multistage increasing accuracy, that, for the convex problem, the solution accuracy is increased with stage-by-stage reducing the search region and increasing the resolution;
5. iterative process, that the optimization is formulated in a recursion process to reduce the implementation complexity;
6. hybrid function, that the function mixed with several functions/methods is used to take the advantages of those functions/methods in different purposes.

1.4 Structure of Receiver

The structure of the receiver design can be classified into two types: the open-loop structure and the closed-loop structure. For example in parameter estimator, the structures are illustrated in Fig. 1.1. In the left part, the open-loop estimator uses averaging filter to smooth the sampled observations and feeds the produced material to the parameter estimator to calculate the value in one-shot process. Whereas, the closed-loop estimator uses the closed-loop adaptation that

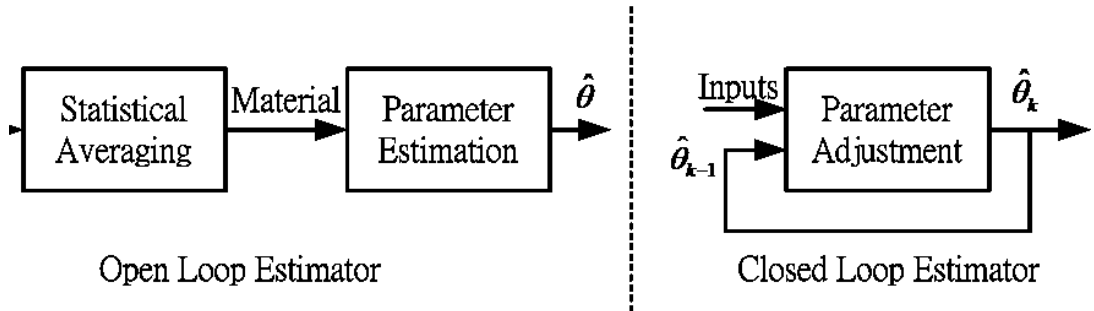


Figure 1.1: Comparison of the structures of open-loop estimator and closed-loop estimator.

iteratively adjusts the estimated parameter according to the difference of the reconstructed result(s) and the new income(s). The use of the structures depends on the property of the estimation/detection target and the realization cost.

We consider a simple example of the estimate of the sample mean to explain the difference between the open-loop estimator and the closed-loop estimator. Let x_0, x_1, \dots, x_{N-1} be the input samples. We want to calculate the mean value of these samples. From the open-loop structure, we have

$$\bar{X} = \frac{1}{N} \sum_{n=0}^{N-1} x_n. \quad (1.1)$$

If the closed-loop structure is considered, we iteratively update the estimation via

$$\bar{X}_{n+1} = \bar{X}_n + \mu(x_n - \bar{X}_n) = (1 - \mu)\bar{X}_n + \mu x_n. \quad (1.2)$$

An effective factor of the closed-loop estimator is the selection of the stepsize μ . The selection of the stepsize depends on two factors: the convergence time constant and the steady-state accuracy. Smaller one provides smaller estimation mismatch but requires longer time to converge. To achieve the same accuracy as the open-loop structure, the stepsize should be set to $\mu = \frac{2}{N+1}$. Another factor affects the convergence property is the initial condition. Good initial points yield good convergence properties as well as the final estimate results. Need to notice that the closed-loop estimator may not guarantee the optimal estimate results with the arbitrary initial conditions.

We give the examples of the estimator/detector structures for the carrier frequency estimation, the data detection and the channel estimation as follows.

1.4.1 Carrier Frequency Estimation

Consider the problem in carrier frequency estimation that we find out the ω from the observed signal samples, which are given by

$$r(n) = e^{j\omega n + j\theta} + w(n) \quad (1.3)$$

for $n = 0 \cdots N - 1$, where θ is the phase offset and $w(n)$ is the Gaussian noise. The maximally likely solution of the ω satisfies that

$$\hat{\omega} = \arg \min_{\omega} \sum_{n=0}^{N-1} \left| r(n) - e^{j\omega n + j\theta} \right|^2. \quad (1.4)$$

In the open-loop structure, we may directly calculate the matrices of the quantized solution candidates as

$$J(\omega) = \left| \sum_{n=0}^{N-1} r(n) e^{-j\omega n} \right|^2, \quad (1.5)$$

and find out the ω which has the maximal $J(\omega)$. The metric calculations corresponding to the ω can be accomplished via the spectrum analysis with Fourier transform [68, Sec. 8.2.1].

In the closed-loop structure, we adopt the carrier recovery loop to estimate both the phase and the frequency offsets. One feasible recursions of the carrier recovery loop are given by

$$\hat{\omega}(n+1) = \hat{\omega}(n) + K_I \phi(n); \quad (1.6)$$

$$\hat{\theta}(n+1) = \hat{\theta}(n) + K_P \phi(n) \quad (1.7)$$

where $\phi(n) = \angle r(n) - \left(\hat{\omega}(n)n + \hat{\theta}(n) \right)_{2\pi}$ is the phase error function in the recursion and $(\cdot)_{2\pi}$ denotes the module operation with respect to a 2π interval. With suitable selection of K_I , K_P and the initial condition, the recursion of $\hat{\omega}(n)$ would achieve the ML result.

1.4.2 Data Detection

Consider the data detection of the binary shift-keying modulation over the two-path channel with path gains $= [1 \ h_1]$. Let $[x(0) \ x(1) \ \cdots \ x(N-1)]$ be the transmitted sequence, where $x(n) \in \{1, -1\}$. The received signal can be represented by

$$r(n) = x(n) + h_1 x(n-1) + w(n) \quad (1.8)$$

for $n > 1$ and $r(0) = x(0) + w(0)$.

We can adopt the maximal likelihood sequence estimation (MLSE) by finding out the sequence which minimizes the metric:

$$J(\hat{x}(0) \cdots \hat{x}(N-1)) = |r(0) - \hat{x}(0)|^2 + \sum_{n=1}^{N-1} |r(n) - \hat{x}(n) - h_1 \hat{x}(n-1)|^2. \quad (1.9)$$

One structuralized search scheme of the MLSE is the Viterbi detector/decoder, which is widely adopted in the decoder of the convolutional code (CC).

Beside the MLSE approach, another feasible way is the linear equalizer. In matrix view, the received vector is presented by

$$\underline{r} = \mathbf{H}\underline{x} + \underline{w} \quad (1.10)$$

where

$$\mathbf{H} = \begin{bmatrix} 1 & 0 & \cdots & 0 \\ h_1 & 1 & \cdots & 0 \\ 0 & h_1 & \cdots & 0 \\ \vdots & \ddots & \ddots & \vdots \\ 0 & \cdots & h_1 & 1 \end{bmatrix} \quad (1.11)$$

is the toeplitz channel matrix. Assume \mathbf{W} be the equalization matrix, the equalized output is given by

$$\tilde{\underline{x}} = \mathbf{W}\underline{r} \quad (1.12)$$

and the detected data is obtained by performing the decision:

$$\hat{x}(n) = \text{sgn}(\tilde{x}(n)). \quad (1.13)$$

According to the minimal mean-square error criterion, the equalization matrix has the formulation:

$$\mathbf{W} = (\mathbf{H}^H \mathbf{H} + \sigma_n^2 \mathbf{I})^{-1} \mathbf{H}^H \quad (1.14)$$

where σ_n^2 is the noise variance. Both the MLSE and the linear equalizer obviously have the open-loop structures.

For complexity reason, we may adopt the interference cancellation (IC) to remove the inter-symbol interference (ISI) caused by the second path of the channel. One of the IC successively deletes the ISI terms generated by the prior tentative decided symbols. This kind IC is called as the successive IC (SIC), or the decision-feedback equalization in single carrier system. The recursion of the SIC/DFE is given by

$$\hat{x}(n) = \text{sgn}(r(n) - h_1 \hat{x}(n-1)) \quad (1.15)$$

where $\text{sgn}(\cdot)$ is the sign operation or the decision in general, and $\hat{x}(n)$ is the detection of $x(n)$. The DFE would cause the error propagation effect when the prior tentative decision is wrong. Thus, this is a sub-optimal detection scheme.

In addition to SIC, another IC scheme treats the sequence detection as the signal restoration problem and adopts the iterative process to recovery the sequence. This kind IC is named as the parallel IC (PIC) since it operates in a parallel manner. One familiar PIC is the (constrained) gradient descent algorithm [24] as well as the projected Landweber iteration [82]. Let $\hat{\mathbf{x}}_{k-1}$ be $k-1$ st tentatively detected vector. The constrained gradient descent algorithm in k th iteration is given by

$$\hat{\mathbf{x}}_k = \text{sgn}(\hat{\mathbf{x}}_{k-1} + \mu \mathbf{H}^H (r - \mathbf{H} \hat{\mathbf{x}}_{k-1})) \quad (1.16)$$

$$= \text{sgn}(\mathbf{F} r + \mathbf{B} \hat{\mathbf{x}}_{k-1}) \quad (1.17)$$

where $\mathbf{F} = \mu \mathbf{H}^H$, $\mathbf{B} = \mathbf{I} - \mu \mathbf{H}^H \mathbf{H}$ and μ is the stepsize of the recursion, which should satisfy the non-expansive (NE) property [24]. This recursion does still not guarantee the optimal solution since the solution constrain (or the sign operation) does not satisfy the convex property. This kind PIC is also named as the iterative block decision feedback equalization (IBDFE) [13] in the viewpoint of the channel equalizer. Moreover, if the tentative detections are regenerated by the forward error correcting (FEC) decoder, this kind PIC is specially called the turbo DFE (TDFE), which is a simple version of the turbo equalization [56]. Both the SIC and PIC have the closed-loop structures.

1.4.3 Channel Estimation

Consider the coefficient estimation in the single path channel. Let $\underline{x} = [x(0) x(1) \cdots x(N-1)]^T$ be the transmitted pilot signal, which is known at the receiver. Let α be the channel gain to be identified. The received signal vector can be expressed as

$$\underline{r} = \underline{x} \alpha + \underline{w} \quad (1.18)$$

where \underline{w} is the noise vector. If the noise has Gaussian distribution, the maximal likelihood estimation of the channel gain is to determine the $\hat{\alpha}$ such that $\|\underline{r} - \underline{x} \hat{\alpha}\|^2$ is minimal. The well-known least square (LS) solution of the estimation is given by

$$\hat{\alpha} = (\underline{x}^H \underline{x})^{-1} \underline{x}^H \underline{r}. \quad (1.19)$$

The LS estimation in this case has the open-loop structure, which collects all the received samples and performs one-shot process to determine the channel coefficient.

Besides the LS estimation, we can adopt the adaptive least-mean square algorithm to train the channel coefficient. The cost function of the LMS adaptor in this case is $J = E|r(n) - x(n)\alpha|^2$. By taking gradient of J with respect to α and replacing α as $\hat{\alpha}_n$, which is the tentative solution at n th iteration, we have the recursion of the LMS estimator as

$$\hat{\alpha}_{n+1} = \hat{\alpha}_n + \mu (r(n) - \alpha x(n)) x(n)^* \quad (1.20)$$

where μ is the stepsize in the recursion. Obviously, the LMS for the channel estimation is a kind of the closed-loop structure in this case.

1.5 Thesis Organization And Studied Algorithms

The thesis is divided into three parts. Part I presents the receiver design in SC system over fixed multipath channel. The carrier synchronization, the channel equalization, and the joint process of these two functions are studied in this chapter. Part II considers the receiving algorithms in wireless OFDM system. In this part, we mainly study the Cell-ID detection problem in WiMAX system and the channel estimation issue. Part III discusses the transmitter and receiver designs over wide-band MIMO.

Part I contains Chapter 2–4. Chapter 2 studies the carrier synchronization in SC system¹. Two algorithms with different structure are proposed in this chapter. The first algorithm operated in open-loop structure is an extreme low complexity algorithm for the single frequency estimation. We also address its application in frequency offset estimation in QAM system. The second algorithm is the closed-loop carrier recovery loop. We suggest a class of the blind phase detection and the hybrid operation of the blind and decision-directed phase detection. Besides, we also propose a dynamic loop bandwidth control algorithm to provide both the fast convergence and good tracking stability. The design target of the first algorithm is to reduce the implementation cost. The applied design method is the “multistage increasing accuracy”. The second algorithm is to provide fast convergence and robust tracking. Besides, we also consider enlarging the estimate range of the frequency offset. The used design method is including “dynamic controlled parameters”, “functional approximation”, “iterative process”, and “hybrid function”.

Chapter 3 studies the blind channel equalization in SC system². Two algorithms are proposed in this chapter. The first one establishes the variable stepsize concept in the blind adaptive algorithm to enhance the convergence speed of the blind equalizer. In the second algorithm, we consider the soft-switching mechanism from the blind to decision-directed LMS tracking. We propose the hybrid operation concept in this algorithm. Both algorithms operate in close-loop structure and provide the fast convergence and stability in tracking operation. The used design methods comprise “dynamic controlled parameters”, “multistage increasing accuracy”, “iterative process”, and “hybrid function”.

Chapter 4 studies the joint startup process of the carrier synchronization and the blind channel equalization. We present a new operation process using the proposed blind phase irrelevant decision-feed equalizer (π DFE), which can provide convergence of the blind equalizer under received signal with frequency offset. The variable stepsize concept is also applied in the π DFE algorithm. The design target and the design methods are similar to previous two chapters. Both the open-loop and close-loop structures are used in this chapter.

¹The corresponding publication is the reference [35]

²The corresponding publications are the references [34, 36].

Part II includes Chapter 5–7. Chapter 5 is an introduction to WiMAX receiver design. Chapter 6 studies the synchronization in mobile WiMAX system³. The main issue in this chapter is the IDCell identification problem. According to the theoretical derivation, we propose the frequency domain filtering concept and develop several simplified algorithms in the issue. The performance analysis is also addressed. The design target in this chapter is to reduce the complexity under acceptable performance. The design methods is mainly the “functional approximation”. The proposed detector works in open-loop structure.

Chapter 7 studies the channel estimation problem in comb-type OFDM and mobile WiMAX systems⁴. We propose two pilot-aided channel estimation algorithms. These two algorithms both use the interpolation to estimate the missing channel response. The first algorithm improves the polynomial interpolative channel estimation algorithm by introducing the time-domain window-shift concept. We derive the optimal window shifts under arbitrary interpolation orders and propose the corresponding estimation scheme. The second algorithm considers the realization of the Wiener interpolation. Instead of the estimation of the channel correlation, we use the model-based approximation of the correlation. To generate the correlation approximation, we propose a simple estimation scheme of the channel mean delay and the delay spread. The design target of the first algorithm is the performance improvement with some computation increase, and the used methods are including “functional approximation” and “reduced solution space”. The first algorithm operates in open-loop structure. For the second algorithm, the goal is to reduce the realization complexity. We adopt the same methods and structure as fist algorithm.

Part III includes Chapter 8–9. Chapter 8 presents the optimal transmission process for FEC coded system over the correlated WB-MIMO⁵. We derive the condition of the transform design to optimize the diversity gain in the coded system and then propose a simple near-optimal space-frequency transformation to achieve the condition. Then, in Chapter 9, we study the receiver design⁶. We adopt the block turbo DFE to detect the transmitted information. To improve the convergence and to reduce the cost, we propose a shaped turbo DFE and its simplification using fixed shaping filter to reduce the implementation cost. Then, we consider the joint problem of the channel estimation and the data detection and propose the joint iterative algorithm. The design of the receiver is targeted at the low complexity and good convergence property. The used methods includes “iterative process”, “functional approximation”, and “dynamic controlled parameters”.

³The corresponding publication is the reference [37].

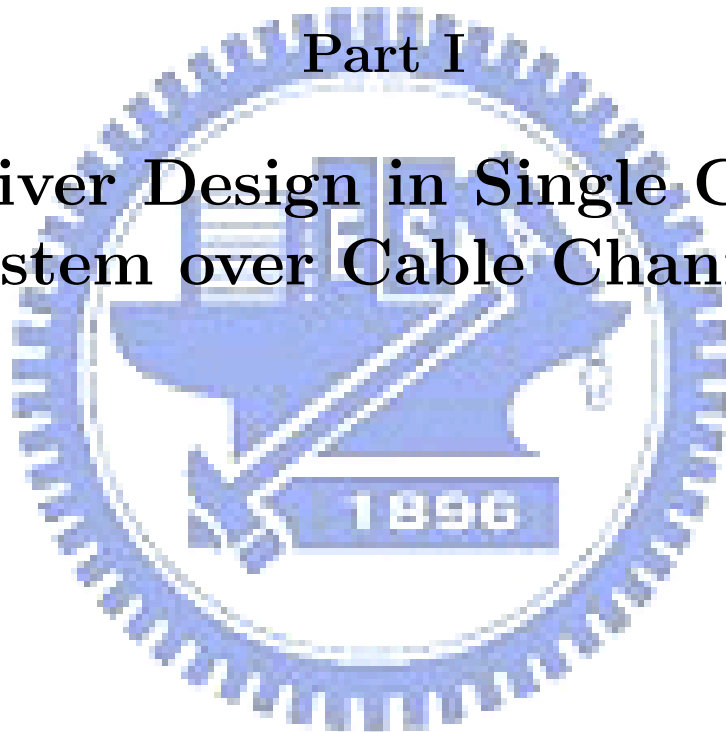
⁴The corresponding publications are the references [41, 42, 43, 44, 45].

⁵The corresponding publication is the reference [38].

⁶The corresponding publications are the references [38, 39, 40].

Part I

Receiver Design in Single Carrier System over Cable Channels



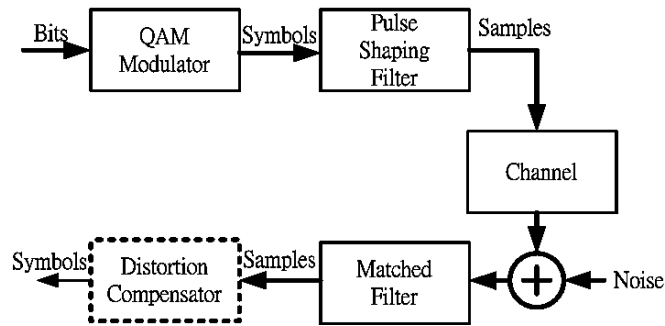


Figure 1.2: Prototypical transmission system block diagram.

The single carrier modulation scheme is widely adopted in recent communication system, such as the DVB-C and the J-83B for cable TV broadcasting, ATSC for wireless TV broadcasting, GSM for cellular mobile communication. This modulation scheme is not a fresh one since it has been studied over 4 decades. There are mass literatures and technical contributions for the scheme; however, we still present several techniques to accelerate the convergence of the receiver and to provide more accuracy of the synchronizer.

The quadrature amplitude modulation (QAM) is one of the popular modulation in the single carrier system. For example, the DVB-C adopts 16-QAM, 32-QAM, 64-QAM, 128-QAM and 256-QAM according to data rate of the TV program and the channel bandwidth. The 16-QAM, 64-QAM and 256-QAM are square QAMs, but 32-QAM and 128-QAM are cross QAMs which have square constellation but lack the corner. The shortage of the corner in cross QAM makes the poor performance with larger acquisition time in synchronization, especially for the carrier frequency synchronization. In this part, we mainly consider the receiving techniques for the square QAM format, but the presented techniques still can be applied to the cross QAM with longer training period.

A typical transmission system structure is shown in Fig. 1.2. We consider the equivalent low-pass discrete model of the transceiver system. Thus, we omit the digital-to-analog converter (DAC) and analog-to-digital converter (ADC) modules. At transmitter, the information bits, which may be protected by the forward error correcting (FEC) code, are mapped into the QAM symbol constellation by the modulator and then the modulated sources is fed into the pulse-shaping filter (PSF). After the PSF, the samples are corrupted due to the multipath channel and perturbed by additive white Gaussian noise (AWGN). At receiver, the sampled signal first is filtered by the matched filter and then passes into the distortion compensator and the signal detection module. The distortion compensator, what we consider, contains the functionality of the synchronization and the channel equalization. The part focuses on the design of the distortion compensator and especially the carrier frequency synchronization and the channel equalization.

This part addresses the carrier synchronization issues and the blind equalization; to enhance, we focus on the high-order QAM environment. In high-order QAM system, the decision-aided/decision-directed (DD) carrier recovery loop (CRL) can not provide high acquisition range of the frequency offset since the high SNR requirement is required for the CRL to achieve better acquisition capability and this is not the case when the blind adaptive equalizer is used in initial training. Therefore, we consider two approaches to enlarge the acquisition range. First, we use the open-loop frequency estimator to estimate frequency offset at first stage. We first study the Fitz's algorithm [23] to provide high accuracy estimator and analyze its performance. However,

the Fitz's algorithm has two drawback. First, it exists the wrap effect in the angle of high-order correlation; second, it requires heavy complexity in the estimation of the delay correlations. For this, we propose a low complexity and high accuracy frequency estimation using high order delay correlation. Key issue in the proposed frequency estimation is also the unwrap process. According to the unwrap algorithm suggested in [22], we propose a multi-stage unwrap process to reduce the probability of unwrap error. To resolve the frequency in QAM system, we integrate the times four process [96, 10] with the proposed frequency estimator to provide high accuracy and low complexity frequency estimator in high order QAM system.

Then, the CRL circuit is studied. Similarly, to enlarge acquisition range in high-order QAM, we suggest a series of the reduced-constellation phase detectors (RCPD). But, this RCPD type has poor locking capability due to its large phase noise in tracking operation. Thus, we furthermore propose a hybrid phase detector, which is a combination the DDPD and the RCPD, to provide both advantages of the DDPD in good tracking capability and the RCPD in wide acquisition capability. In addition, we propose a dynamic loop bandwidth control mechanism to adjust the loop bandwidth according to the lock indicator [58]. However, the lock indicator has poor resolution in high-order QAM; thus, we furthermore suggest a modification of the lock indicator for high-order QAM.

The blind adaptive algorithm [49, 104] is used for initial training of the decision-feedback equalizer in the low-order QAM system. However, its convergence behavior is poor when the high-order QAM system is considered. To speedup the convergence, we consider the variable stepsize (VSS) approach. The VSS algorithm requires two factors: the convergence indicator and the stepsize control function. For the convergence indication, we propose a low complexity and high accuracy boundary mean-square error estimator to estimate the decision-point MSE directly and use this value as the convergence indicator. Then, the stepsize control function, we propose two types including the multistage gear function and the proportional function. The proposed algorithm can provide speedy convergence of the blind DFE in high-order QAM. Beside the improvement of the blind adaptive algorithm, we consider the operation mode switch for the blind acquisition to the decision-direct LMS tracking. The dual mode or soft-switching concept is considered in [65, 30, 12]. We follow the VSS approach and propose a hybrid algorithm to provide the soft-switching functionality, which directly combines two error functions of the adaptive algorithms. The proportional stepsize function is also used in blind part; whereas, two stepsize functions are proposed for the DD part. The proposed hybrid algorithm provide fast and stable convergence in high-order QAM system.

Final chapter in this part discusses the joint startup process of the CRL and the blind DFE. We suggest three approaches. First one is the conventional multi-stage separate training procedure; the second one is the jointly mixed training procedure. The first stage requires an additional training period in blind linear equalization using CMA for purpose of the estimation of frequency offset and CRL; whereas, the second approach do not guarantee perfectly convergence in the co-training of the DFE and the CRL especially when the CFO is large. Thus, we furthermore suggest a phase-irrelevant DFE(π -DFE) structure and a jointly startup procedure based on the π -DFE. The proposed algorithms are all used in this process including the frequency estimator, the CRL with dynamic bandwidth control and hybrid VSS algorithm.

Chapter 2

Carrier Synchronization

The communication receiver contains the synchronization circuits. The tasks of the synchronizer is to deal with the timing mismatch and the carrier mismatch. In this chapter, we discuss the carrier synchronization design. There are two factors in the carrier mismatches including the carrier frequency offset and the carrier phase offset. In mathematic, the received signal in equivalent model can be formulated as

$$r(t) = s(t)e^{j(2\pi\Delta f t + \theta)} \quad (2.1)$$

where Δf is the frequency offset and θ is the phase offset. The carrier synchronization is to compensate the factor Δf and θ .

Two approaches are typically used in the carrier synchronization. One is the open-loop estimation and then compensation; the other is the direct closed-loop recovery of the signal. The advantage of the open-loop estimation and compensation is the large estimation range of the offsets; whereas, the closed-loop recovery can track the time-variation of the offset and finely adjust the mismatch. Both types are used according to the modulated signal property. For example, In OFDM system, the carrier frequency estimator using the correlation of the cyclic-prefix is a typical approach of open-loop estimation and compensation. In single carrier (SC) system, the closed-looped carrier recovery loop (CRL) is typically used. Besides, the two approaches may be used jointly in a two-stage manner. For instance, at first stage, the open-loop estimation is used to acquire the mismatch since it has large estimation range; next, the closed-loop recovery is used to provide more accuracy estimation and tracking capability.

In this chapter, we consider both approaches of the carrier synchronization in the QAM system. In the first half part, we present the design of the frequency estimator and the application in the QAM signaling. We introduce the Fitz's algorithm [23] and extend to a multi-resolution algorithm. According to observation and theoretical derivation, we can estimate the frequency using high-order correlation to improve the accuracy. However, the estimator using high-order correlation would face the angle wrap effect; thus, the unwrap process is necessary. But, high-order unwrap process would make error easily and yield great estimate mismatch. For this issue, we propose the multiple stage multi-resolution algorithm to reduce the probability of unwrap error. Then, we apply the proposed algorithm in the QAM system.

Next, we present the design of the closed-loop carrier recovery. By introducing new class of the blind phase detector (PD) based on reduced-constellation concept, we widen the acquisition capability of the closed-loop estimator. In addition, we proposed the hybrid PD, which combines the decision-directed PD(DDPD) and reduced constellation PD(RCPD), and the dynamic loop bandwidth control to provide advantage of both the fast acquisition and stable tracking capability.

2.1 Open-loop Frequency Estimator

The open-loop frequency estimator is studied in past four decades [22, 23, 51, 79, 85, 93]. The approaches typically can be classified as the frequency analysis [79, 85] and the cross-correlation based estimation [93, 51, 23, 22]. The advantage of the spectrum analysis is its accuracy; however, the accuracy is gained in the price of the complexity of the discrete Fourier transform, even if the fast Fourier transform (FFT) is used. The cross-correlation estimator has lower complexity, but also poor accuracy. To improve the accuracy and widen the estimation range, additional signal process schemes are required to reduce the noise effect [68, 51, 23].

In this section, we first give a brief introduction of the FFT based frequency analysis approach. Then, we mainly focus on the low-complexity close-correlation approach. We start from the Fitz's algorithm [23], which is a modification of Kay's estimator [51]. From the survey of papers, as far as we know, it is lack of the performance analysis in the Fitz's algorithm in terms of the amounts of used correlation items. Therefore, we give the theoretical analysis of the estimator.

According to the analysis, we observe the property of the frequency accuracy of the correlation items, and propose the multiple resolution algorithm to exact the frequency via fewer correlation items. We also give the performance analysis of the proposed algorithm. And then, we adopt the multiple resolution approach to estimate the frequency offset component in the QAM system with the operation of times-four [10, 11, 15, 16, 71, 96].

2.1.1 Spectrum Analysis using FFT

We first give the mathematical modeling of the single frequency waveform. It can expressed as

$$x(t) = Ae^{j(2\pi\frac{f}{F_s}t+\theta)} + n(t) \quad (2.2)$$

where F_s is the sampling frequency, θ is an unknown phase offset and $n(t)$ is the additive noise.

Based on the maximal likelihood (ML) criterion [85], the optimal frequency is derived via

$$\hat{f} = \arg \max_f \left| \sum_{t=0}^{T-1} x(t)e^{j(-2\pi\frac{f}{F_s}t)} \right|^2. \quad (2.3)$$

The ML estimation can be derived via the spectrum analysis process; therefore, the FFT can be used to the single frequency estimation in low cost manner as follows [68, 85]:

1. if $T > K$, the FFT size, divide the observed signals into several segments with length = K ; else, pad zeros after observed signal to the length of K ;
2. perform the FFT of the segments and calculate its power spectrum;
3. sum up these power spectrum of each segments if number of the segments is great than one and find out the frequency of peak power location denoted as \hat{k} ;
4. translate \hat{k} into \hat{f} via $\hat{f} = \frac{\hat{k}}{K}F_s$.

The accuracy of the estimator is bounded by the size of FFT or the CRB if resolution of FFT is larger than the bound. Therefore, in order to provide higher accuracy of the estimator, the larger size FFT is required; however, it also costs great implementation complexity. The art of single frequency estimator is using less cost to achieve the CRB, and this is the goal what we present in next subsections.

2.1.2 Fitz's Algorithm

The frequency information f can be acquired from the correlation $x(t)$ and its delayed version $x(t-1)$ as given by

$$R_x(1) = \frac{1}{T-1} \sum_{t=1}^{T-1} x(t)x^*(t-1) = A^2 e^{j2\pi \frac{f}{F_s}} + \eta_1 \quad (2.4)$$

and

$$\hat{f} = \frac{F_s \angle \{R_x(1)\}}{2\pi} \quad (2.5)$$

where η_1 is the noise caused from AWGN. The implementation of the correlation method is much less than the FFT based spectrum analysis; however, its accuracy is also severely poor than spectrum analysis approach.

For this, Fitz [23] suggests using multiple correlations to improve the accuracy. With the k -th delay correlation estimated by

$$R_x(k) = \frac{1}{T-k} \sum_{t=k}^{T-1} x(t)x^*(t-k) = A^2 e^{j2\pi \frac{kf}{F_s}} + \eta_k, \quad (2.6)$$

the truncated version of Fitz's frequency estimator is given by

$$\hat{f} = \frac{F_s}{2\pi} \sum_{k=1}^K C(K, k) \angle R_x(k), \quad (2.7)$$

in which $C(K, k) = \frac{k}{\sum_{k=1}^K k^2}$. The estimation range is bounded in $[-\frac{F_s}{4\pi K}, \frac{F_s}{4\pi K}]$ if we do not consider the unwrap process. Thus, to improve the estimation range, the unwrap is needed.

Now, we explain the optimal coefficients of the Fitz's algorithm. The angle of the correlation is given by

$$\Omega_k = \angle R_x(k) = 2\pi \frac{k}{F_s} f + \epsilon_k \quad (2.8)$$

where ϵ_k is the phase noise introduced by η_k . Assume that the angle is perfectly unwrapped. In the matrix form representation, the frequency estimation problem is presented by

$$\underline{\Omega} = \frac{2\pi}{F_s} V f + \underline{\epsilon} \quad (2.9)$$

where

$$\begin{aligned} \underline{\Omega} &= [\Omega_1 \cdots \Omega_K]^T; \\ V &= [1 \cdots K]^T; \\ \underline{\epsilon} &= [\epsilon_1 \cdots \epsilon_K]^T. \end{aligned}$$

Based on the least square solution, we have that

$$\hat{f} = \frac{F_s}{2\pi} (V^T V)^{-1} V^T \underline{\Omega} = \frac{F_s}{2\pi} \frac{V^T \underline{\Omega}}{\sum_{k=1}^K k^2} \quad (2.10)$$

and that yields the Fitz's algorithm in (2.7).

2.1.3 Performance Analysis of the Fitz's Algorithm

According to [85], the Cramer Rao bound of the estimation is given by

$$\text{Var}(\hat{f}) \leq \frac{6F_s^2\rho}{(2\pi)^2T(T^2-1)} \quad (2.11)$$

where $\rho = \frac{\sigma^2}{A^2}$ is the reciprocal of single to noise ratio (SNR), T is the sample length and F_s is the sampling frequency. We try to evaluate the Fitz's algorithm in which condition to achieve CRB.

Property of Phase Noise of the Correlation Estimation

we first consider the phase noise ϵ_k of the estimation of k -th correlation. For simplification, we assume $A = 1$ and the actual $f = 0$; but, the derivation result still holds in the general case. Now, we have the signal model: $x(t) = 1 + n(t)$. The estimation of k th correlation can be expressed as

$$R_x(k) = 1 + \frac{1}{T-k} \sum_{t=k}^{T-1} (n(t) + n^*(t-k) + n(t)n^*(t-k)) = 1 + V(k). \quad (2.12)$$

According to [93], if $V(k)$ is small enough, we have the approximation:

$$R_x(k) = e^{j \tan^{-1}(\frac{V_i(k)}{1+V_r(k)})} \approx e^{jV_i(k)}, \quad (2.13)$$

in which $V_i(k)$ is the imaginary part of $V(k)$. Therefore, we have that $\epsilon_k = V_i(k)$.

There are two cases in the derivation of variance of $V_i(k)$. When $k > \frac{T}{2}$, there are no overlapped terms of $n(t)$ and $n^*(t-k)$. Thus, we have

$$V(k) = V_1(k) + V_2(k) + V_3(k), \quad (2.14)$$

with

$$\begin{aligned} V_1(k) &= \frac{1}{T-k} \sum_{t=0}^{T-k-1} n^*(t), \\ V_2(k) &= \frac{1}{T-k} \sum_{t=k}^{T-1} n(t) \\ \text{and } V_3(k) &= \frac{1}{T-k} \sum_{t=k}^{T-1} n(t)n^*(t-k). \end{aligned}$$

Based on LLN, we have that $V_1(k)$, $V_2(k)$ and $V_3(k)$ are all zero-mean complex Gaussian random variables, and the variances correspondingly $\sigma_{V_1}^2(k) = \sigma_{V_2}^2(k) = \frac{1}{T-k}\rho$, $\sigma_{V_3}^2(k) = \frac{1}{T-k}\rho^2$. Thus, the variance of ϵ_k is given by

$$\sigma_{\epsilon}^2(k) = \frac{1}{2} (\sigma_{V_1}^2(k) + \sigma_{V_2}^2(k) + \sigma_{V_3}^2(k)) = \frac{(\rho + \rho^2/2)}{T-k} \approx \frac{\rho}{T-k} \quad (2.15)$$

where the approximation holds if ρ is small enough.

Now, if $k < \frac{T}{2}$, there are overlapped noise terms in (2.12). We have that

$$V(k) = V_0(k) + V_1(k) + V_2(k) + V_3(k), \quad (2.16)$$

in which

$$\begin{aligned}
V_0(k) &= \frac{1}{T-k} \sum_{t=k}^{T-k-1} (n(t) + n^*(t)), \\
V_1(k) &= \frac{1}{T-k} \sum_{t=0}^{k-1} n^*(t), V_2(k) = \frac{1}{T-k} \sum_{t=T-k}^{T-1} n(t) \\
\text{and } V_3(k) &= \frac{1}{T-k} \sum_{t=k}^{T-1} n(t)n^*(t-k).
\end{aligned}$$

Similarly, $V_1(k), V_2(k)$ and $V_3(k)$ are also complex Gaussian random variable and $V_0(k)$ is real Gaussian. The variances are given by $\sigma_{V_0}^2(k) = \frac{2(T-2k)}{(T-k)^2} \rho$, $\sigma_{V_1}^2(k) = \sigma_{V_2}^2(k) = \frac{k}{(T-k)^2} \rho$ and $\sigma_{V_3}^2(k) = \frac{1}{T-k} \rho^2$ correspondingly. Then, we have the variance

$$\sigma_{\epsilon}^2(k) = \frac{k\rho}{(T-k)^2} + \frac{\rho^2}{2(T-k)}. \quad (2.17)$$

Performance of Fitz's Algorithm

Then, we analyze the Fitz's algorithm. We just consider the case when $K \leq \frac{T}{2}$, since its performance can converge to CRB with K less than $T/2$ [23] and the comparative study later shows this result.

Since $K \leq \frac{T}{2}$, the phase noise is given by

$$\epsilon = \frac{\sum_{k=1}^K k\epsilon_k}{\sum_{k=1}^K k^2} \approx \frac{\sum_{k=1}^K k\Im(V_1(k) + V_2(k) + V_3(k))}{\sum_{k=1}^K k^2} = \frac{\Im\{V_1 + V_2 + V_3\}}{\sum_{k=1}^K k^2} \quad (2.18)$$

where $V_1 = \sum_{k=1}^K kV_1(k), V_2 = \sum_{k=1}^K kV_2(k)$ and $V_3 = \sum_{k=1}^K kV_3(k)$. Moreover, we have that

$$\begin{aligned}
V_1 &= \sum_{k=1}^K \sum_{t=0}^{k-1} \left(\frac{k}{T-k} n^*(t) \right) = \sum_{t=0}^{K-1} M(K, t+1) n^*(t) \\
V_2 &= \sum_{k=1}^K \sum_{t=0}^{k-1} \left(\frac{k}{T-k} n(t+T-k) \right) = \sum_{t=0}^{K-1} M(K, t+1) n(t+T-K)
\end{aligned}$$

where

$$M(K, t) = \sum_{k=t}^K \frac{k}{T-k}. \quad (2.19)$$

Thus, we can get that

$$\sigma_{V_1}^2 = \sigma_{V_2}^2 = \rho \sum_{k=1}^K M^2(K, k), \quad (2.20)$$

$$\sigma_{V_3}^2 = \rho^2 \sum_{k=1}^K \frac{k^2}{T-k}, \quad (2.21)$$

and the variance of ϵ is obtained by

$$\sigma_{\epsilon}^2(K) = A(K)\rho + B(K)\rho^2 \quad (2.22)$$

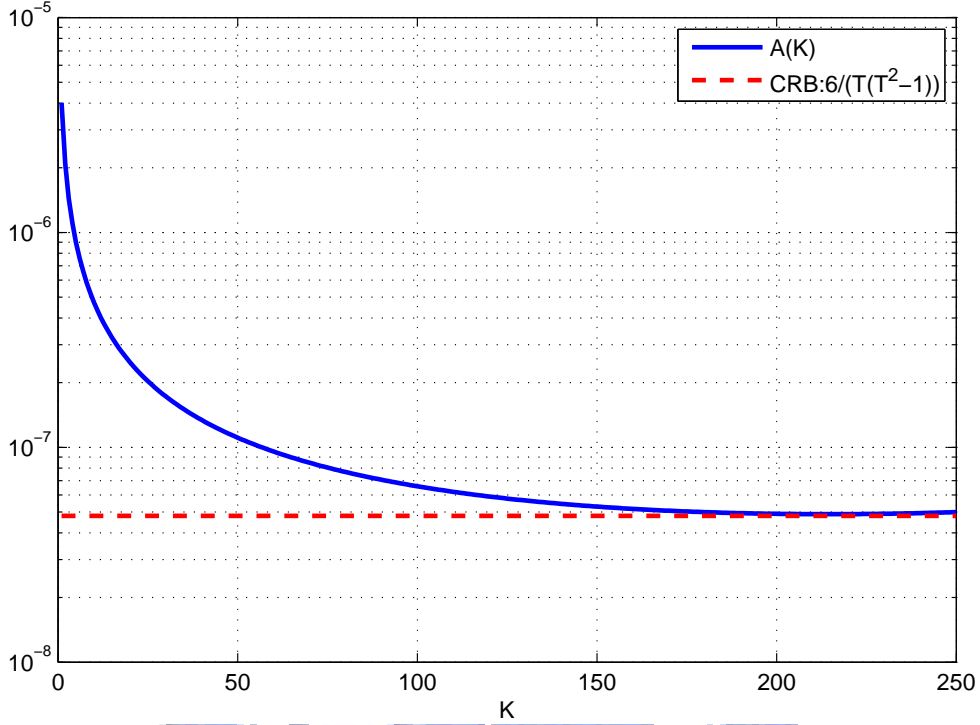


Figure 2.1: The comparisons of $A(K)$ and the CRB constant $\frac{6}{T(T^2-1)} = 4.8 \times 10^{-8}$ when $T = 500$.

where

$$A(K) = \frac{\sum_{k=1}^K M^2(K, k)}{\left(\sum_{k=1}^K k^2\right)^2} \quad (2.23)$$

and

$$B(K) = \frac{\sum_{k=1}^K \frac{k^2}{T-k}}{2 \left(\sum_{k=1}^K k^2\right)^2}. \quad (2.24)$$

Thus, we have

$$\sigma_f^2(K) = E|f - \hat{f}|^2 = \frac{F_s^2}{4\pi^2} (A(K)\rho + B(K)\rho^2) \quad (2.25)$$

When ρ is small, $A(K)$ dominates the variance of estimation error. Thus, we compare $A(K)$ with the CRB constant $\frac{6}{T(T^2-1)}$ when $T = 500$. Fig.2.1 illustrates the results. As shown, $A(K)$ decays with the increase of K . It shows the convergence of $A(K)$ is slow when K is large and $A(K)$ approaches the CRB constant at $K = 170$ which is near $\frac{T}{3}$. As shown, the performance of Fitz's algorithm is built on the price of the number of the correlators.

Fig.2.2 shows the simulation studies of the Fitz's algorithm. The simulation parameters are setting as $T = 60$, $K \in [5, 10, 20]$ and $\frac{f}{F_s} = 0.2$. As illustrated, the analytical results almost perfectly match the simulated ones when the SNR is larger than 0 dB. The figure also illustrates the Fitz's algorithm can approach the CRB if K is large enough such as the results in the case of $K = 20 = \frac{T}{3}$. The great drift of the simulated result at extreme low SNR is due to the error caused by the unwrapping process, which we assume perfect.

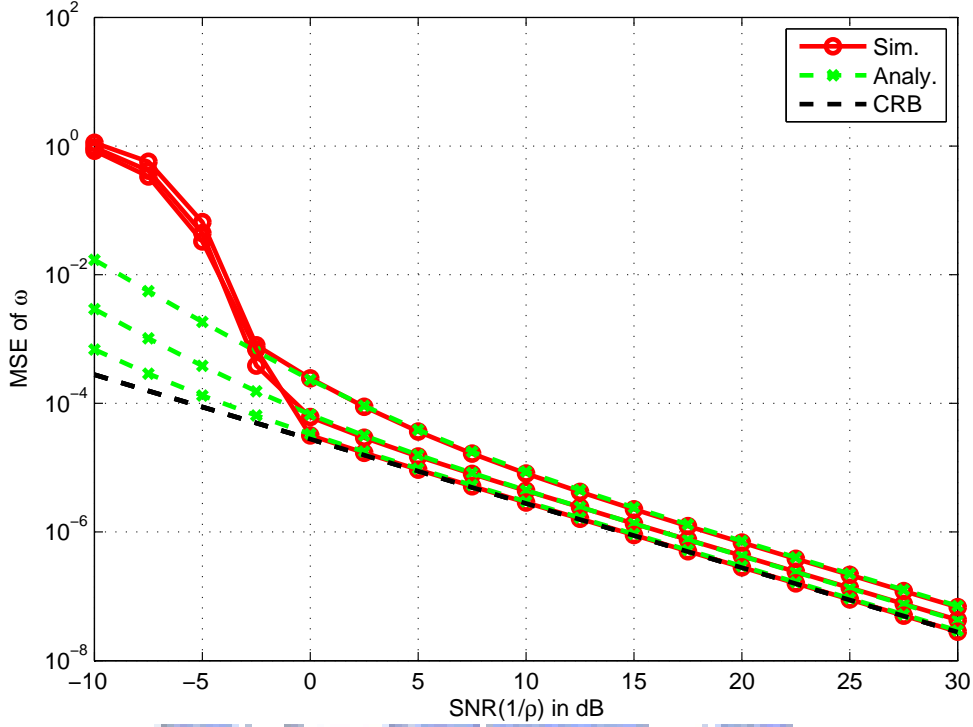


Figure 2.2: MSE of angle frequency $\omega \triangleq 2\pi f/F_s$ for the Fitz's algorithm with $T = 60$ and $K \in [5, 10, 20]$.

2.1.4 Multi-resolution Algorithm and Modified Fitz's Estimator

In absence of the wrap effect of the angle, we can use k -th delayed correlation to estimate the frequency by

$$\hat{f}_k = \frac{F_s}{2\pi k} \Omega_k = f \mp \frac{F_s \epsilon_k}{2\pi k}. \quad (2.26)$$

According to the phase noise analysis in previous section, the estimation variance is

$$\sigma_f^2 = E \left| f - \hat{f}_k \right|^2 = \frac{F_s^2 \sigma_\epsilon^2(k)}{(2\pi)^2 k^2}. \quad (2.27)$$

If $k \leq \frac{T}{2}$, we have

$$\sigma_f^2 = \frac{F_s^2 \rho}{(2\pi)^2 k(T-k)^2}; \quad (2.28)$$

else

$$\sigma_f^2 = \frac{F_s^2 \rho}{(2\pi)^2 k^2(T-k)}. \quad (2.29)$$

The accuracy of estimator using k th order correlation is increasing with the increment of k . Thus, we can use high order correlation to estimate the frequency. However, if the frequency offset is greater than F_s/k , the ambiguity occurs due to the angle wrap of the correlation.

To prevent the ambiguity and enlarge the acquisition range, we can use the multi-stage and multi-resolution approach. At first stage, the first correlation is used to maintain the estimation range. Then, the higher order correlation in stage-by-stage is used to diminish the uncertainty and keep the correct region of the frequency. Let $k(l)$ be the order of the used correlation at l th stage and $\Omega_{k(l)}$ be the angle after unwrapping operation. The estimated frequency at l th stage is given by

$$\hat{f}_l = \frac{F_s \Omega_{k(l)}}{2\pi k(l)}. \quad (2.30)$$

The key operation of the multi-resolution approach is the “unwrapping” operation that locates the correct estimating interval at the current stage. Let $\tilde{\Omega}_{k(l)} = \angle R_x(k(l))$ be the angle of $R_x(k(l))$ before unwrap. According to [22], the angle after unwrap at l stage is given by

$$\Omega_{k(l)} = \tilde{\Omega}_{k(l)} + Q_z \left(k(l)\Omega_1^{(l-1)} - \tilde{\Omega}_{k(l)} \right) \quad (2.31)$$

$$= \tilde{\Omega}_{k(l)} + Q_z \left(\frac{k(l)}{k(l-1)}\Omega_{k(l-1)} - \tilde{\Omega}_{k(l)} \right), \quad (2.32)$$

where $Q_z(x) = 2\pi \lfloor \frac{x}{2\pi} + 0.5 \rfloor$ is the rounded quantization of x with quantization step-size = 2π and $\Omega_1^{(l-1)} = \frac{2\pi}{F_s} \hat{f}_{l-1} = \frac{\Omega_{k(l-1)}}{k(l-1)}$.

Besides the multi-resolution approach, the similar concept can directly be applied to the Fitz’s algorithm since $\omega_{k(l)}$ s for all l are available at the l -th stage. If there are total L stages, the modified Fitz’s algorithm is derived by substituted $k(l)$ for k of the entries in V ; then, we have

$$\hat{f} = \frac{F_s}{2\pi} \frac{\sum_{l=1}^L k(l)\Omega_{k(l)}}{\sum_{l=1}^L k(l)^2}. \quad (2.33)$$

2.1.5 Optimization of Multi-resolution Algorithm

Two issues should be considered in the realization of the proposed algorithms. First, the used orders of the correlations affect both the complexity and the accuracy. Secondly, the ratio of the orders of the correlations between two stages will constrain the correctness of the unwrap process. The proposed design flow first selects the last stage correlation order, which would optimize the estimation accuracy. Then, we decide the numbers of the stages and the ratios of the orders between any two successive stages. Therefore, there are two questions for the design flow. First is what the optimal correlation order is; the second is the selection of the best ratio that minimizes the unwrap error.

Selection of Optimal Correlation Order

To answer first question, we consider the performance of the estimator using k -th correlation. It has two cases: $k < T/2$ and $K > T/2$.

If $k < T/2$, from (2.28), we have the cost function

$$J(k) = \frac{F_s^2}{(2\pi)^2} \left(\frac{\rho}{k(T-k)^2} + \frac{\rho^2}{2k^2(T-k)} \right) \quad (2.34)$$

From $\partial_k J(k) = 0$, we get that the optimal k should satisfy

$$3\left(1 - \frac{\rho}{2}\right)k^2 - \left(1 - \frac{5\rho}{2}\right)kT - \rho T^2 = 0. \quad (2.35)$$

The solutions are given by

$$k^o = \frac{T}{6} \frac{2 - 5\rho \pm \sqrt{4 + 28\rho + \rho^2}}{2 - \rho}. \quad (2.36)$$

If ρ is small, we can get the approximate optimal value of k as

$$k_1^o \approx \frac{T}{3}, \quad (2.37)$$

and the optimal MSE is given by

$$J_1^o = \frac{F_s^2}{(2\pi)^2} \left(\frac{27(\rho + \rho^2)}{4T^3} \right) \approx \frac{6.75F_s^2\rho}{(2\pi)^2T^3} \quad (2.38)$$

which is roughly 12.5% larger than the CRB.

If $K > \frac{T}{2}$, similar derivation gives the results that

$$k_2^o \approx \frac{2T}{3} \quad (2.39)$$

and

$$J_2^o = \frac{F_s^2}{(2\pi)^2} \left(\frac{6.75(\rho + \rho^2/2)}{T^3} \right) \approx \frac{6.75F_s^2\rho}{(2\pi)^2T^3} \quad (2.40)$$

which is less than the J_1^o .

Therefore, $k(L) = \frac{L}{3}$ or $\frac{2L}{3}$ at final stage is recommend. The choice of $\frac{L}{3}$ or $\frac{2L}{3}$ is the trade-off between the operations of the correlator and the length of the buffer size. When $\frac{T}{3}$ is used, it requires $\frac{2T}{3}$ operations of correlator and $\frac{T}{3}$ buffer sizes; on contrast, if $k(L) = \frac{T}{3}$, it only requires $\frac{T}{3}$ operations of correlator but $\frac{2T}{3}$ buffer sizes.

Selection of Ratio of Orders between Two Stages

The selection of the ratio of orders between two stages depends on the correctness of unwrapping operation. Let $\tilde{\Omega}_k^o(l) = \tilde{\Omega}_k(l) - \epsilon_{k(l)}$ and $\Omega_k^o(l-1) = \Omega_k(l-1) - \epsilon_{k(l-1)}$ be the true values of $\tilde{\Omega}_k(l)$ and $\Omega_k(l-1)$. We have that

$$r_l \Omega_k^o(l-1) - \tilde{\Omega}_k^o(l) = 2\pi M \quad (2.41)$$

where $r_l = k(l)/k(l-1)$, M is an integer and $2\pi M$ is the correct region of $\Omega_k^o(l)$.

Substituting $\tilde{\Omega}_k(l) = \tilde{\Omega}_k^o(l) + \epsilon_{k(l)}$ and $\Omega_k(l-1) = \Omega_k^o(l-1) + \epsilon_{k(l-1)}$ into (2.31), we can get that

$$\begin{aligned} \Omega_k(l) &= \tilde{\Omega}_k(l) + Q_z \left(r_l \Omega_k^o(l-1) - \tilde{\Omega}_k^o(l) + r_l \epsilon_{k(l-1)} - \epsilon_{k(l)} \right) \\ &= \tilde{\Omega}_k(l) + 2\pi M + Q_z \left(r_l \epsilon_{k(l-1)} - \epsilon_{k(l)} \right). \end{aligned} \quad (2.42)$$

Let $\xi(l) \triangleq r_l \epsilon_{k(l-1)} - \epsilon_{k(l)}$. The unwrapping error occurs if $Q_z(\xi(l)) \neq 0$ or equivalently $|\xi(l)| > \pi$. If $\xi(l)$ has a Gaussian distribution, which condition holds when the noise is Gaussian and T is large, the probability of the incorrect unwrapping at l th stage is given by

$$P_e(l) = 2 \int_{\pi}^{\infty} \frac{1}{2\pi\sigma_{\xi}^2(l)} e^{-\frac{t^2}{2\sigma_{\xi}^2(l)}} dt = 2\Phi \left(\frac{\pi}{\sigma_{\xi}(l)} \right) \quad (2.43)$$

where $\Phi(z)$ is the Q function of Gaussian distribution and $\sigma_{\xi}^2(l)$ is the variance of $\xi(l)$. The full error probability is given by

$$P_e = \sum_{t=2}^L \left(P_e(t) \prod_{l=1}^{t-1} (1 - P_e(l)) \right) \approx \sum_{l=2}^L P_e(l). \quad (2.44)$$

Moreover, we have $P_e(1) = 0$ since the first order delayed correlation is used at first stage.

There are some comments on the derivation. First, the incorrect unwrap occurs if one error at any stage happens at least, so the overall error probability is approximately the summation of the error probabilities at each stage. Besides, The Q function is dramatic increasing with its argument; therefore, the error probability is minimized by the selecting those r_l s that have balanced $\sigma_{\xi}^2(l)$ s. Therefore, a sub-optimal heuristic choice is considered to use ‘‘near-constant’’ ratios.

To give more insights of the unwrap error probability, we need to analyze the variance of $\xi(l)$. When $k(l) < \frac{T}{2}$, we have

$$\begin{aligned}\xi(l) &= r_l \epsilon_{k(l-1)} - \epsilon_{k(l)} \\ &= r_l \mathfrak{S} \{V_1(k(l-1)) + V_2(k(l-1)) + V_3(k(l-1))\} \\ &\quad - \mathfrak{S} \{V_1(k(l)) + V_2(k(l)) + V_3(k(l))\},\end{aligned}\tag{2.45}$$

and

$$\begin{aligned}r_l V_1(k(l-1)) - V_1(k(l)) &= \left(\frac{r_l}{T - k(l-1)} - \frac{1}{T - k(l)} \right) \sum_{t=0}^{k(l-1)-1} n^*(t) \\ &\quad - \frac{1}{T - k(l)} \sum_{t=k(l-1)}^{k(l)-1} n^*(t);\end{aligned}\tag{2.46}$$

$$\begin{aligned}r_l V_2(k(l-1)) - V_2(k(l)) &= \left(\frac{r_l}{T - k(l-1)} - \frac{1}{T - k(l)} \right) \sum_{t=T-k(l-1)}^{T-k(l)-1} n(t) \\ &\quad - \frac{1}{T - k(l)} \sum_{t=T-k(l)}^{T-1} n(t);\end{aligned}\tag{2.47}$$

$$\begin{aligned}r_l V_3(k(l-1)) - V_3(k(l)) &= \frac{r_l}{T - k(l-1)} \sum_{t=k(l-1)}^{T-1} n(t) n^*(t - k(l-1)) \\ &\quad - \frac{r_l}{T - k(l)} \sum_{t=k(l)}^{T-1} n(t) n^*(t - k(l)).\end{aligned}\tag{2.48}$$

Therefore, the variance of $\xi(l)$ is given by

$$\sigma_{\xi}^2(l) = C(l)\rho + D(l)\rho^2\tag{2.49}$$

where

$$C(l) = \left(k(l-1) \left(\frac{r_l}{T - k(l-1)} - \frac{1}{T - k(l)} \right)^2 + \frac{k(l)}{(T - k(l))^2} \right)\tag{2.50}$$

and

$$D(l) = \left(\frac{r_l^2}{T - k(l-1)} + \frac{1}{T - k(l)} \right) / 2.\tag{2.51}$$

Then, when $k(l) > \frac{T}{2}$ and $k(l-1) < \frac{T}{2}$, similar derivation yields the same formulation of $\sigma_{\xi}^2(l)$ in (2.49), but its coefficient $C(l)$ is different. There are two cases in this condition. When $T \leq k(l-1) + k(l)$, we have

$$C(l) = k(l-1) \left(\frac{r_l}{T - k(l-1)} - \frac{1}{T - k(l)} \right)^2 + \frac{T - k(l) - k(l-1)}{(T - k(l))^2};\tag{2.52}$$

otherwise,

$$C(l) = (T - k(l)) \left(\frac{r_l}{T - k(l-1)} - \frac{1}{T - k(l)} \right)^2 + \frac{r_l^2 (k(l) + k(l-1) - T)}{(T - k(l-1))^2}.\tag{2.53}$$

Finally, when $k(l) > k(l-1) > \frac{T}{2}$, we have

$$C(l) = (T - k(l)) \left(\frac{r_l}{T - k(l-1)} - \frac{1}{T - k(l)} \right)^2 + \frac{r_l^2 (k(l) + k(l-1) - T)}{(T - k(l-1))^2}.\tag{2.54}$$

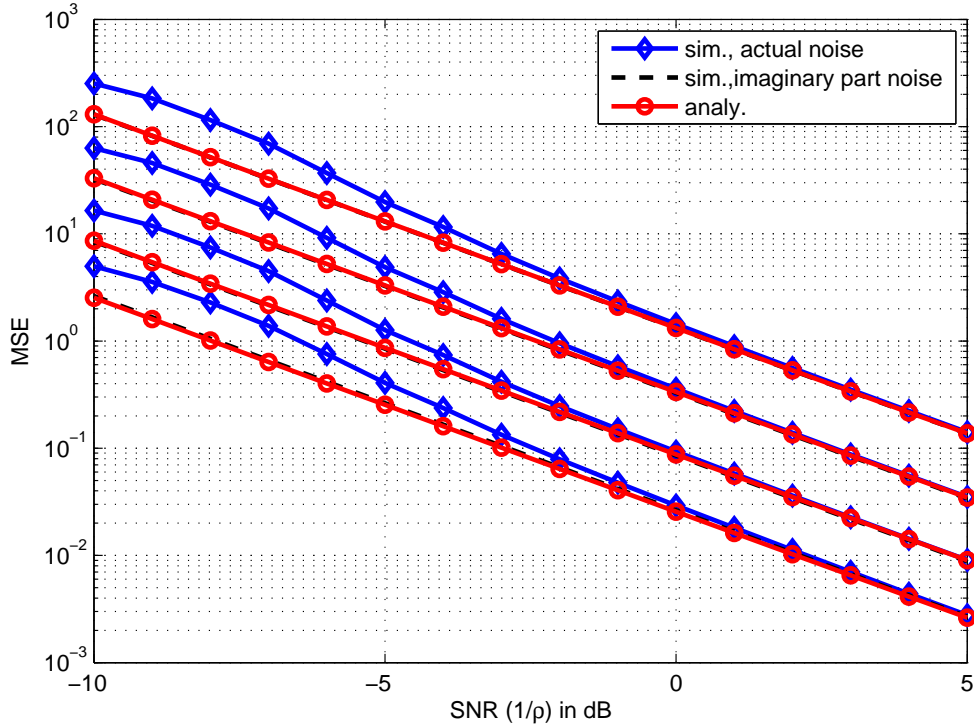


Figure 2.3: The simulated and analytic variance of the unwrap error σ_{ξ}^2 for $T = 100$ and different r_l .

If the SNR ρ is high, we can omit the ρ^2 in (2.49); thus, ratio setup mainly depends on the $C(l)$. The minimization of $C(l)$ yields minimization of $\sigma_{\xi}^2(l)$ as well as $P_e(l)$. But, when ρ is low, such as $\rho > 1$, the parameter $D(l)$ becomes the dominated term and the ratio setup in this situation mostly relies on $D(l)$ rather than $C(l)$.

Verification of Unwrap Error Probability

We first compare the analytical derivation and the simulated result of σ_{ξ}^2 . We fix the first stage as $k(1) = 1$, and test different second stage order as follows $k(2) = 2, 4, 8$ and 16 for $T = 100$. The variance of imagine part of $rR_x(1) - R_x(k(2))$, denoted as σ_{ξ}^2 , is also provided in this study when $f = 0$. Fig.2.3 illustrates the comparisons. We can find that the σ_{ξ}^2 perfectly matches the analytical results in any cases of any SNRs, which demonstrates the correctness of the analysis. However, the actual σ_{ξ}^2 approaches the analytical results only if the SNR is high. This is because of the mismatch of the linear approximation of the phase noise in the analysis.

Next, consider the scenario of the constant ratio settings. We use the pairs of different stage orders as follows: $(k(1), k(2)) = (1, 3), (k(1), k(2)) = (3, 9)$ and $(k(1), k(2)) = (9, 27)$, but constant ratio $r = 3$ with $T = 100$. As illustrated in Fig.2.4, the difference of the variances σ_{ξ}^2 with different simulation settings are not significant. Thus, the heuristic near constant ratio assignment is reasonable in the system design.

We now consider a study of two stages approach to verify the derivation of the error probability. The parameters are given as follows: $T \in [100 \ 200 \ 400]$, $k(1) = 1$, $k(2) = 66$. The frequency used in the testing is $f = 0.2F_s$. From numerical calculation, the ratio $r_2 = 66$ and the variance of $\xi(2)$ is $\sigma_{\xi}^2(2) = 0.4346\rho + 22.0147\rho^2$ for $T = 100$, $\sigma_{\xi}^2(2) = 0.1088\rho + 10.9485\rho^2$ for $T = 200$ and $\sigma_{\xi}^2(2) = 0.027\rho + 5.4601\rho^2$ for $T = 400$. Fig.2.5 illustrates the comparisons of the error probabilities of the setups. As shown, the analytic results almost perfectly match the simulated ones.

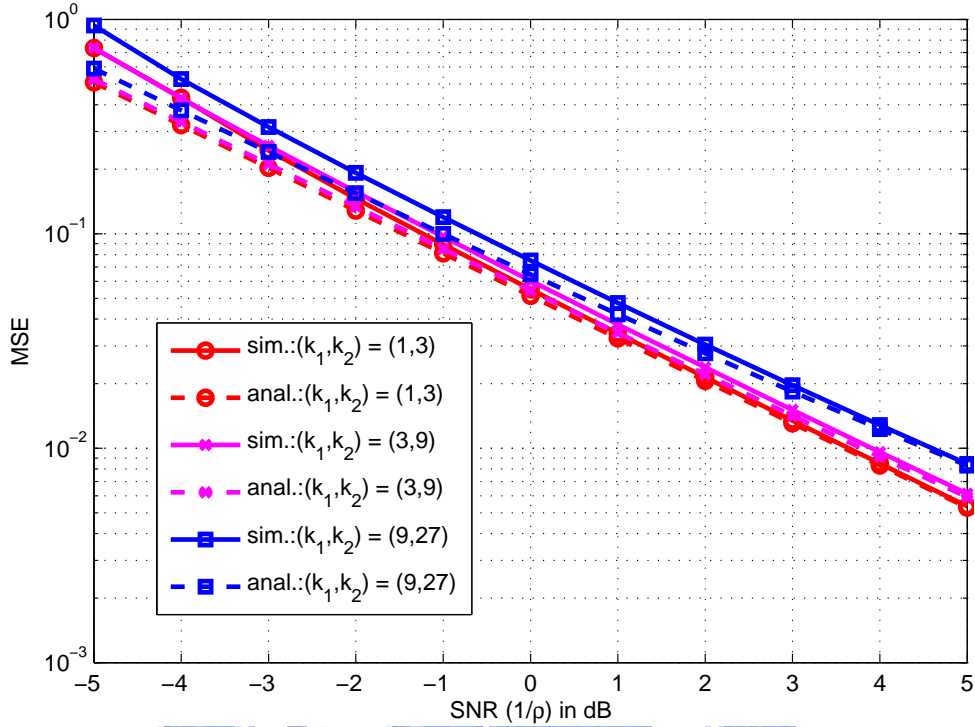


Figure 2.4: The simulated and analytic variance of the unwrap error σ_{ξ}^2 for $T = 100$ and constant ratio $r_l = 3$.

The choice of total stages relies on the length of observations and longer one requires more stages. Fortunately, the number of stages has a log relationship with the total length in the near constant ratio scheme. The stage ratio depends on both the length of observation and the target operation environment. For example, as the cases given above, the stage ratios of the cases all are 66. If $P_e = 10^{-4}$ is the near error-free condition, the threshold is roughly 8 dB for $T = 100$, 6.5 dB for $T = 200$ and less than 5 dB for $T = 400$.

Design Example and Performance Study

Now, we present a design example of the parameter setup when $T = 200$. First of all, we set final stage order as $k = \lceil \frac{2T}{3} \rceil = 134$. Then, we consider the designs using 3 stages, 4 stages and 5 stages. The constant ratio is equal to $r_l = \sqrt{134} = 11.52$ for $L = 3$, $r_l = 134^{1/3} = 5.12$ for $L = 4$, and $r_l = 134^{1/4} = 3.402$ for $L = 5$. After theoretical error probability test, we set $k = [1 \ 12 \ 134]$ for $L = 3$, $k = [1 \ 5 \ 27 \ 134]$ for $L = 4$ and $k = [1 \ 4 \ 13 \ 40 \ 134]$ for $L = 5$, which are the optimal settings of each design. The required complexity in the estimation of the correlations, which is the major cost of the correlation-based estimators, is given

$$N = \sum_{l=1}^L (T - k(l)) = LT - \sum_{l=1}^L k(l). \quad (2.55)$$

Therefore, the complexities of the setups are given as follows: 453 for $L = 3$, 633 for $L = 4$, and 808 for $L = 5$.

Fig.2.6 shows the simulated and the theoretical results. As shown, all of the settings can approach the bound at the SNR higher than 0 dB. The threshold in 3 stage approach is -1 dB, in 4 stage approach is -4 dB and in 5 stage approach is -5 dB, which are related to the unwrap error probability. As shown in Fig.2.7, the analytical error probabilities versus different settings demonstrate the thresholds of the SNR. For example, in 5 stages approach, the error probability

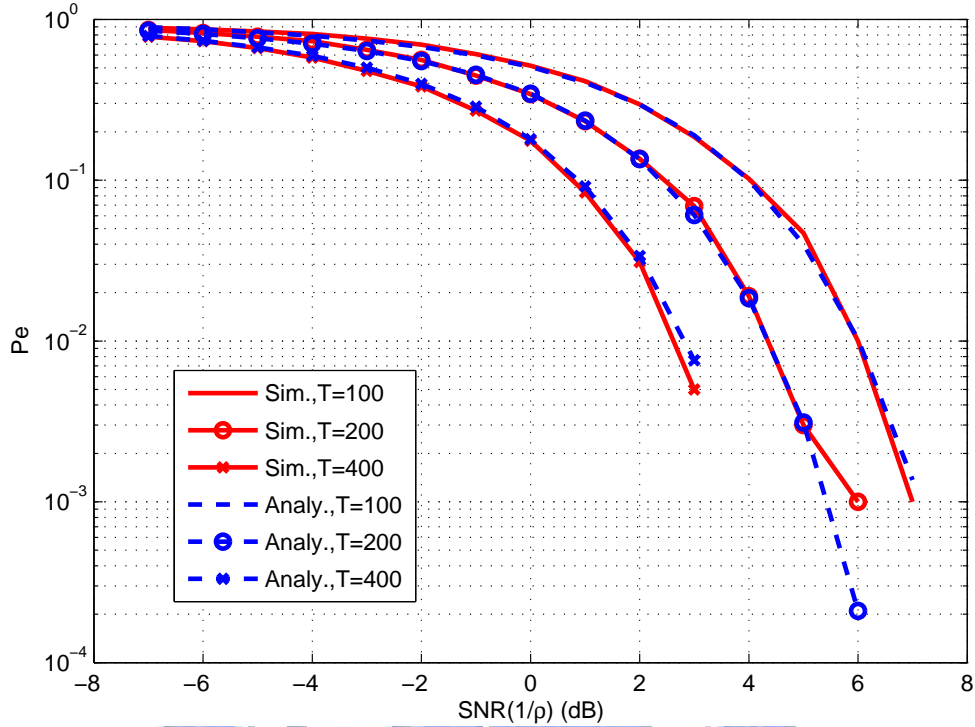


Figure 2.5: The simulated and analytic probabilities of the unwrapping error.

is less than 10^{-4} when SNR is larger than -5.5 dB which is close to the SNR threshold in 5 stages approach. The same result holds on the thresholds and the analytical unwrap error probabilities for 3 stages approach and 4 stages approach.

2.1.6 Fourth Power Frequency Estimator in QAM System

Now, we present the CFO estimation in QAM systems. Since the expectation value of the QAM signals is 0, we can not directly apply the correlation-based estimator in QAM system. There are literatures addressed this issues. Moeneclaey and de Jonghe [71] show that the fourth-power estimator can provide an approximate ML phase estimator for any arbitrary two-dimensional rotationally symmetric constellations, such as the QAM system. Cartwright [10, 11] also present the phase estimators based on the similar concept. Ciblat *et al.* [15] study the blind phase and carrier frequency offset estimate using the fourth power estimator in the QAM system through frequency selective channel. Wang *et al.* [96] give the optimal nonlinear transform of the received signal for the purpose of the phase and frequency estimation based on the fourth power estimator. The performance of the blind nonlinear least square approach of the frequency estimator is studied in the literature [16]. However, the analysis is aimed at the FFT based approach.

In this section, we present the frequency estimation for QAM system over AWGN channel based on the fourth power estimator and the multi-resolution algorithm. We first introduce the system structure of fourth power single frequency estimator (X^4 -SFE). Then, we give an design example and its performance study after the analysis of the variance of $x(t)^4$.

Structure of Fourth Power Single Frequency Estimator (X^4 -SFE)

Consider the received single model

$$x(t) = s(t)e^{j(2\pi\frac{f}{F_s}t+\theta)} + w(t), \quad (2.56)$$

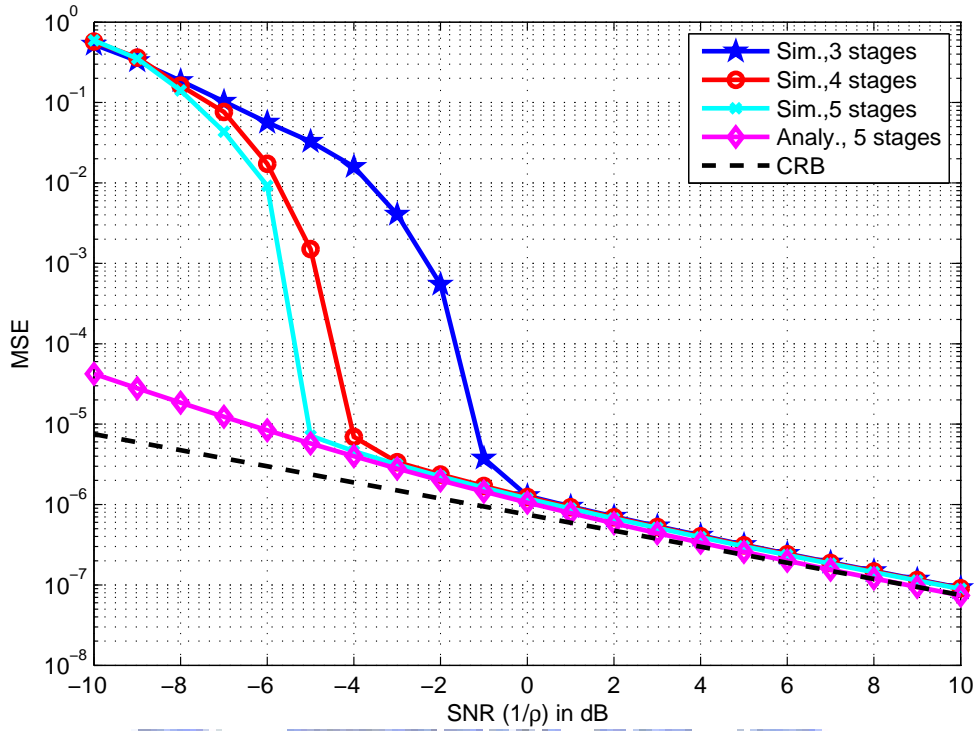


Figure 2.6: Performance studies in multi-resolution algorithm.

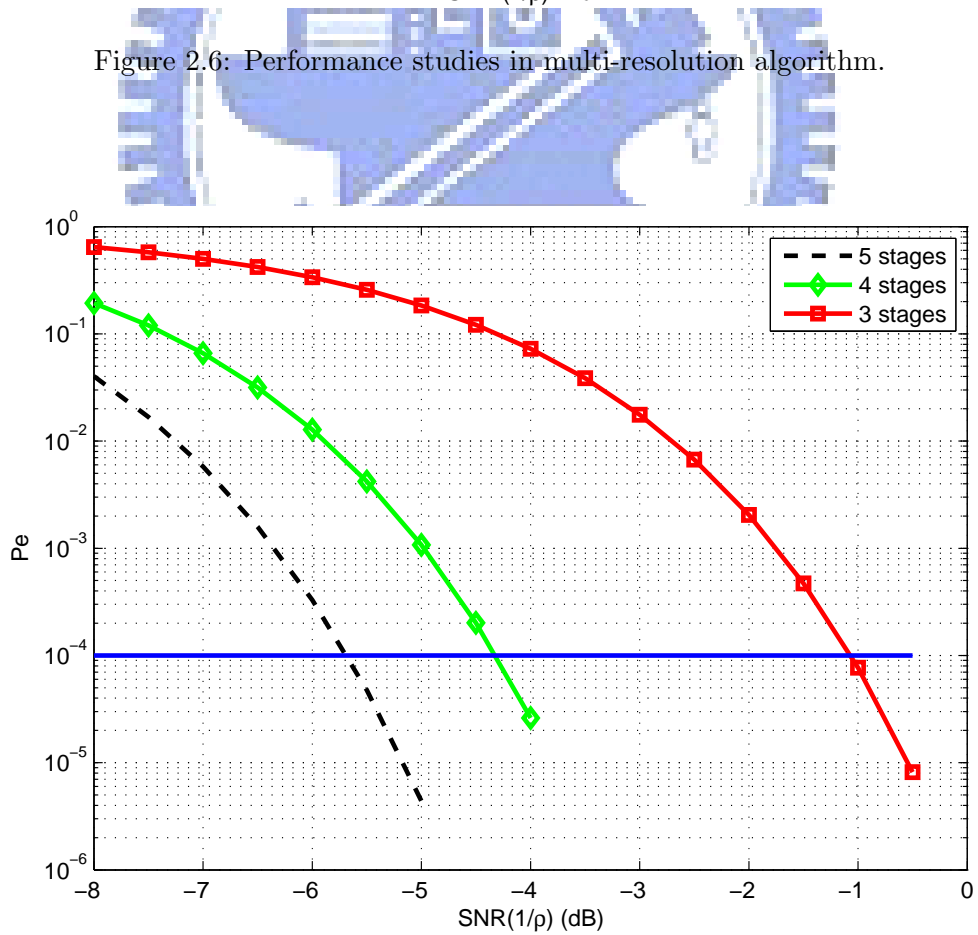


Figure 2.7: The analytic probabilities of the unwrapping error for multi-resolution approach.

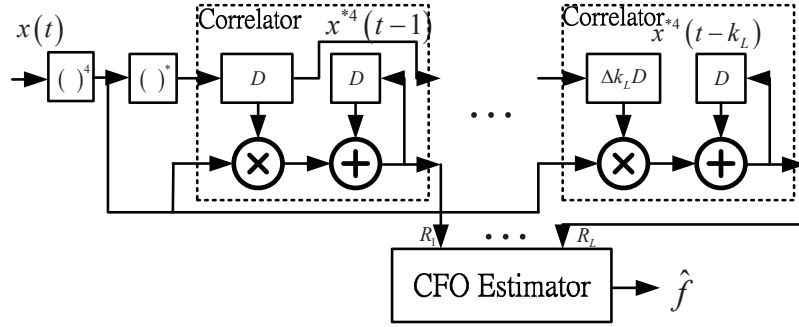


Figure 2.8: Structure of the fourth power frequency estimator using correlations.

where $s(t) \in \mathcal{C}$ and \mathcal{C} is the constellation of the QAM signaling. The expectation value of the correlation of the received signal is given by

$$E[x(t)x^*(t-k)] = E[s(t)s^*(t-1)]e^{j(2\pi\frac{f}{F_s})}. \quad (2.57)$$

Since $E[s(t)s^*(t-1)] = E[\mathcal{C}]^2 = 0$ for the IID assumption of $s(t)$, the correlation can not resolve the frequency offset.

We consider the fourth power of the received signal; the correlation of fourth power of the signal is given by

$$E[x(t)^4(x^4(t-1))^*] = E[\mathcal{C}^4]^2 e^{j(2\pi\frac{4f}{F_s})}, \quad (2.58)$$

which holds f information since $E[\mathcal{C}^4] \neq 0$. Furthermore, because $4\angle x(t)$ appears in the $x(t)^4$ naturally, the acquisition range is limited in $[-\frac{F_s}{8}, \frac{F_s}{8}]$, but the accuracy is improved 4 times better than conventional single frequency estimator.

According to this property, Fig.2.8 shows the proposed structure of the carrier frequency estimation using the fourth power of the received signal. The received signal $x(t)$ first is fed into fourth power function to obtain $x^4(t)$. Then, $x^4(t)$ signal passes to the bank of the correlators to get the correlation R_l . The frequency estimator collects those correlations and performs the frequency estimation algorithm. Both the multi-resolution algorithm or the modified Fitz's algorithm is the possible candidate in our approach.

Analysis of the Variance of $x^4(t)$

From the literature note [16], the signal $x^4(t)$ can be decomposed as

$$x^4(t) = S e^{j(2\pi\frac{4ft}{F_s} + 4\theta)} + e(t) \quad (2.59)$$

with $S = E[s(t)^4]$ and $e(t)$ is a zero-mean white noise but not a complex Gaussian random variable. The variance of $e(t)$ is derived in the literature [16] as given by

$$\sigma_e^2 = S_8 + 16S_6N_2 + 36S_4N_4 + 16S_2N_6 + N_8 - S^2 \quad (2.60)$$

where $S_m = E|s(t)|^m$ and $N_m = E|n(t)|^m$, and the SNR inverse of $x^4(t)$ here is given by

$$\rho = \frac{\sigma_e^2}{S^2}. \quad (2.61)$$

Further derivations gives that

$$N_2 = \frac{\sigma_n^2}{2}, \quad N_4 = 2\sigma_n^4, \quad N_6 = 6\sigma_n^6, \quad \text{and} \quad N_8 = 24\sigma_n^8,$$

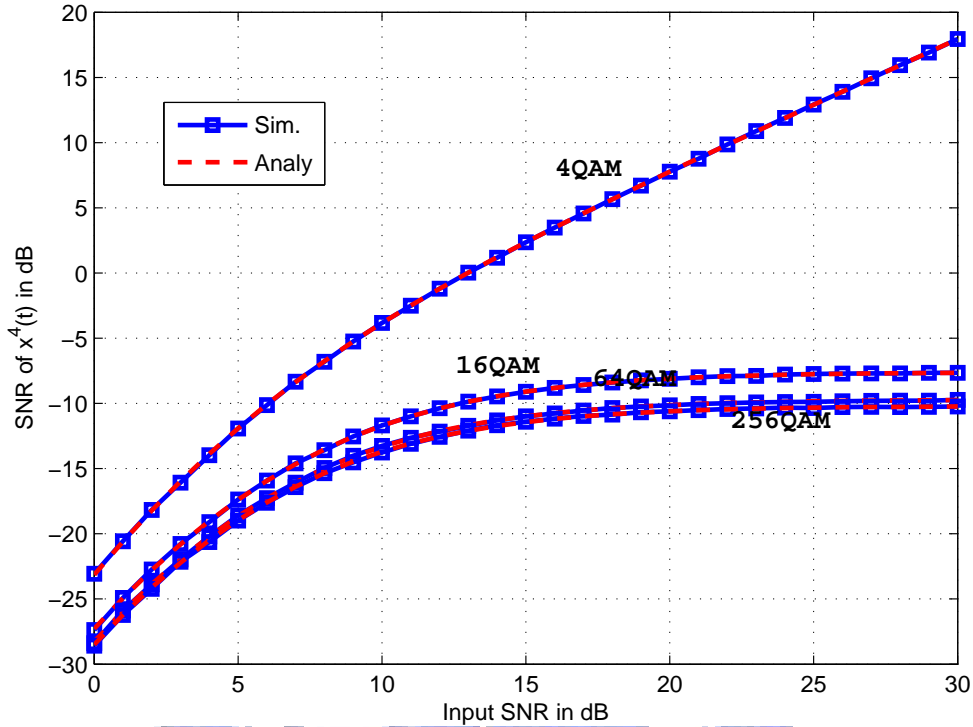


Figure 2.9: SNR of $x^4(t)$ corresponding to input SNR in dB.

in which σ_n^2 is the variance of AWGN.

Fig.2.9 illustrates the SNR $\frac{S^2}{\sigma_e^2}$ of $x^4(t)$ relative to the input SNR $\frac{S_2}{\sigma_n^2}$ for 4QAM, 16QAM, 64QAM and 256QAM systems. As shown in the figure, the SNR of $x^4(t)$ exists error floor for 16QAM, 64QAM and 256QAM system which is introduced by $s^4(t)$ itself, but this does not happens in QPSK system since it has constant modulus constellation. The saturated SNRs are -7.59, -9.72 and -10.21 dB for 16QAM, 64QAM and 256QAM correspondingly, and the input SNR achieving the saturation is roughly 20 dB of all.

Design Example of X^4 -SFE Using Multi-resolution Algorithm

Now, we give a design example of the CFO estimator using multi-resolution algorithm in QAM system. The operation setting is the 256QAM system over 15 dB AWGN channel, which is equivalent to theoretical $\rho = 13.3$ from (2.61). There are four correlators with $k(l) = [1 \ 3 \ 9 \ 30]$ in the estimator. We try the different lengths of the total observed samples and compare the MSE of estimated frequency with the analytical result in (2.28) and the unwrapping error probability.

Fig.2.10 shows the error probability of the unwrapping process. It shows the error probability has a constant slope in log domain, which is not the property of the Q function. It is reasonable because the estimation error is not Gaussian random variable. After $T > 4000$, the errors do not occur anymore in our simulated runs. Fig.2.11 illustrates the MSE of the frequency estimator versus T in the condition of correct unwrap process. As shown, the simulated results match the analytical ones and the curves also present near constant slopes in log domain after $T > 4000$, and it appears that increase of T linearly improves the accuracy if the order of the final stage is fixed. However, to avoid the unwrapping error, the $T > 4000$ is suggested in this case.

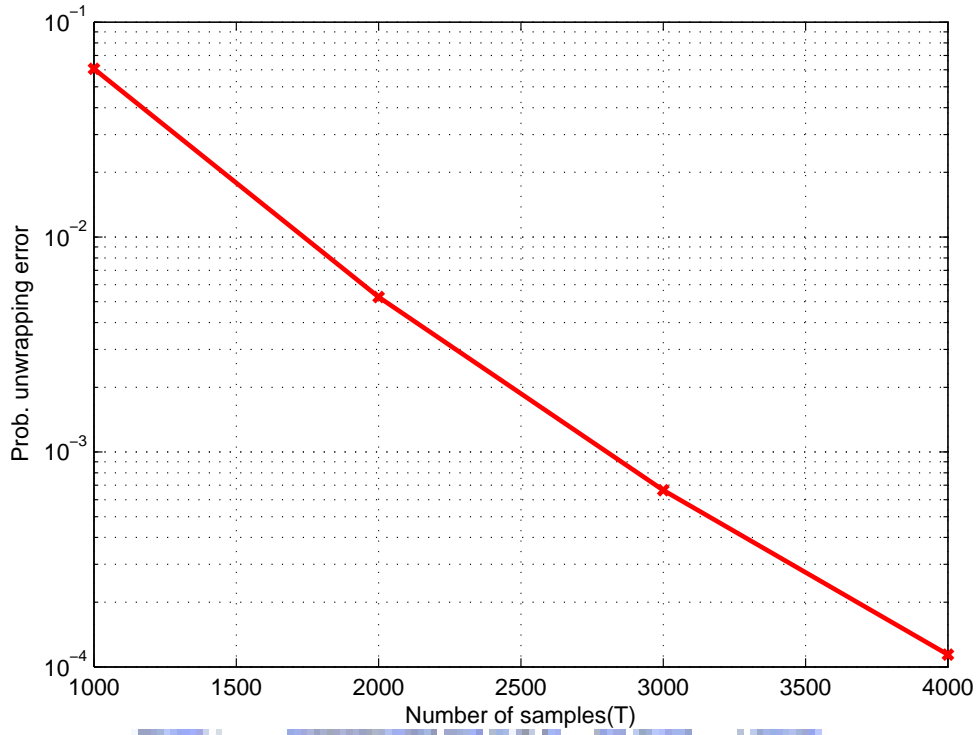


Figure 2.10: Simulated unwrapping error probability versus T in X^4 SFE.

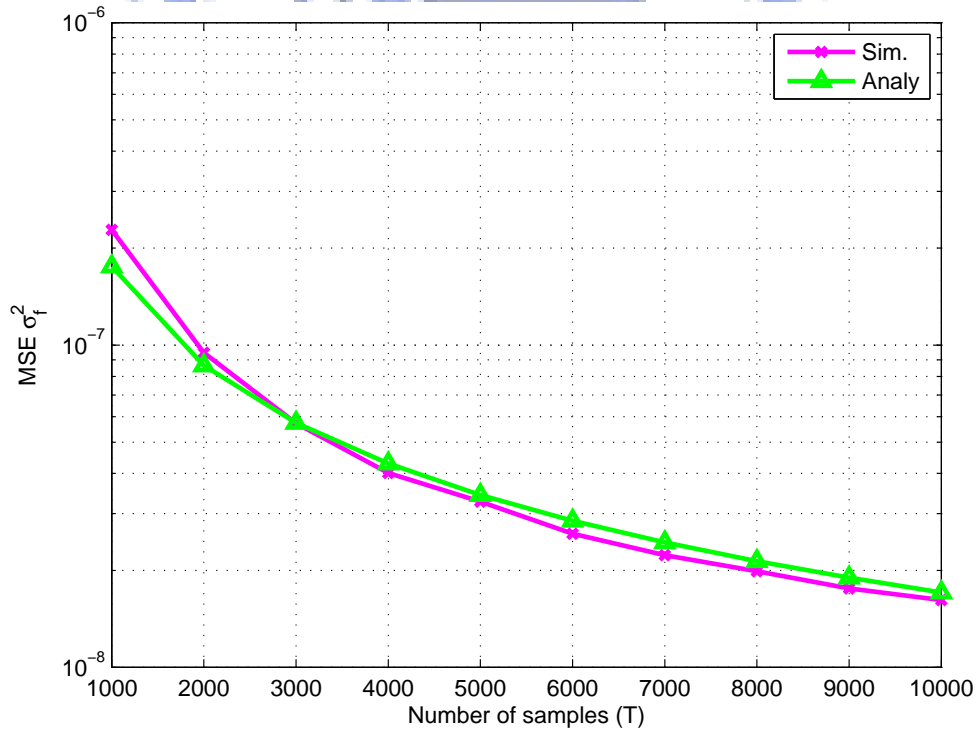


Figure 2.11: Simulated and analytical MSE of the frequency estimator versus T .

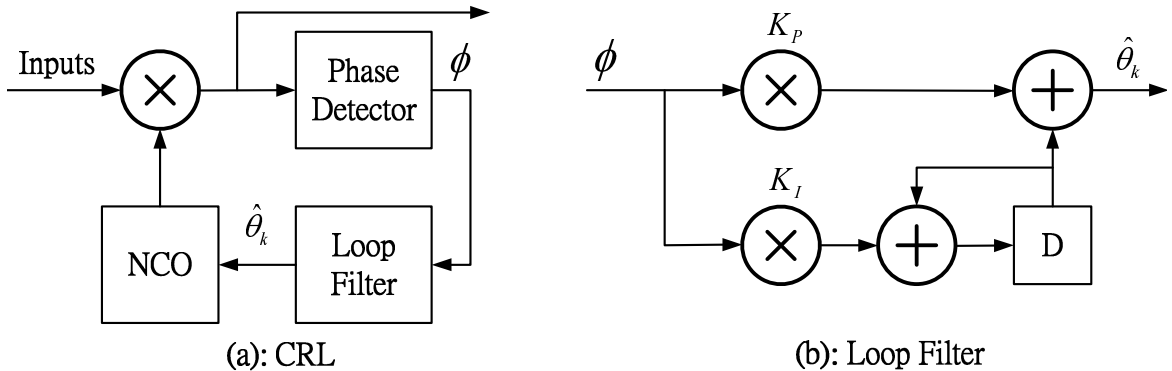


Figure 2.12: Typical structure of carrier recovery loop in the receiver design.

2.2 Carrier Recovery Loop

The closed-loop carrier recovery loop not only estimates the carrier frequency offset but also tracks and compensates the carrier phase rotation. It is typically adopted in the digital receiver hardware due to its low implementation cost. This section presents the carrier recovery loop design for the QAM system. The main focused topics are the phase detector in the recovery loop, which acquires the phase offset between the observed and the synthesis reference, and the advanced loop bandwidth control, which adjusts the loop bandwidth according to current status of the CRL.

2.2.1 Carrier Recovery Loop

As shown in Fig.2.12(a), the carrier recovery loop (CRL) is an closed-loop parameter estimator. It typical includes the components: the phase detector (PD), the loop filter (LF), the numerical control oscillator (NCO) and the compensator-the complex multiplier.

The output of the CRL is the frequency and phase compensated signal, which is what we want. The purpose of the PD is to acquire the phase difference information between the input and compensated signal and it is the reference of the phase adjustment mechanism. The LF is to reduce the noise of the detected phase information from the PD. The NCO is a lookup table that maps the estimated phase into actual sinusoidal waveform. In addition, the multiplier is used to compensate the estimated phase and frequency offset.

As shown in Fig.2.12(b), the two-branched Π structure is used typically in the LF design. The coefficients in the integral part K_I and the fractional part K_P are given by [6]

$$K_P = 2 \left(1 - e^{-\zeta\omega} \cos(\omega\sqrt{1-\zeta^2}) \right), \quad (2.62)$$

$$K_I = e^{-2\zeta\omega} - 1 + K_P, \quad (2.63)$$

which are parameterized by the damping factor ζ and the normalized nature frequency ω . Typically, the filter behavior is controlled by the loop bandwidth ω only, and the damping factor ζ is set to $\frac{1}{\sqrt{2}} \approx 0.71$ for the stabilization. Furthermore, to simplify the hardware design, the loop coefficients typically is quantized into 2's power.

The PD is the key design in the CRL. We consider two type PDs in this section. If the training signals are available or the good tentative detected data in high decision-point SNR, the data aided PD (DAPD) or the decision-directed PD (DDPD) is considered to provide high accuracy of the phase information. However, when the reference constellation points are not available in low SNR environment or the tentative decision is not reliable, we consider the blind PD and propose a set of reduced constellation based PD (RCPD) to provide large acquisition range at low SNR.

2.2.2 Data Aided/Decision Directed Phase Detector

When the training data is available or the good tentative detected data in high decision-point SNR, the optimal estimate of the phase error is given by

$$\phi(y) = \angle\{a^*y\} \quad (2.64)$$

where a is the actual or the decided reference constellation point and y is the compensated signal. However, this PD needs the cost on angle finding. If the angle is not large, the alternative estimate can be approximated by

$$\phi_D(y) \approx \frac{\Im\{(a-y)^*a\}}{|a|^2} = \frac{y_i a_r - y_r a_i}{|a|^2} \quad (2.65)$$

where y_r and y_i are the real and imagine parts of x , and so are a_r and a_i . To simplify, we can use $E|a|^2$ replacing $|a|^2$; thus we get

$$\phi_D(y) = y_i a_r - y_r a_i. \quad (2.66)$$

In absence of noise, assume $y = ae^{j\theta}$ with small residual angle rotation θ . From (2.65) we can derive that

$$\phi_D(y) = \Im\{1 - e^{j\theta}\} \approx \theta. \quad (2.67)$$

Therefore, the detector presents the phase information.

When the tentative decision of y is used as the reference, the DAPD becomes the decision-directed PD (DDPD). But, when the noise term or the phase offset is large, the decision error occurs. This would limit the acquisition capability of the CRL.

2.2.3 Reduced-Constellation Phase Detector

Basic RCPD

In low SNR, we consider a reduced-constellation alternative. Specifically, since the decision-point SNR is low, the value of \hat{a} cannot be trusted, but its sign may still be reliable. Hence, we may consider using $\text{sgn}(\hat{a}_r)$ and $\text{sgn}(\hat{a}_i)$ in place of \hat{a}_r and \hat{a}_i in (2.66). Since $\text{sgn}(\hat{a}_r) = \text{sgn}(y_r)$ and $\text{sgn}(\hat{a}_i) = \text{sgn}(y_i)$, we then have the PD as

$$\phi(y) = y_i \cdot \text{sgn}(y_r) - y_r \cdot \text{sgn}(y_i). \quad (2.68)$$

A similar technique has been proposed in the literature [14].

For convenience in comparing different PDs, we (approximately) normalize their detection gains; that is, we normalize the slopes of their S curves at zero phase error. For this we first obtain the expected value of the PD output when θ is small. Because the QAM constellation has $\pi/2$ symmetry, we only need to analyze the case when y is in the first quadrant.

In this case, the output y can be described as

$$y_r = a_r \cos \theta - a_i \sin \theta + n_r; \quad (2.69)$$

$$y_i = a_r \sin \theta + a_i \cos \theta + n_i. \quad (2.70)$$

Table 2.1: Some phase detector functions

	Weighting Function	PD Function
0	$w_0(y) = 1$	$\phi_0(y) = \frac{1}{2E\{a_r\}}\phi(y)$
1	$w_1(y) = y $	$\phi_1(y) = \frac{ y }{2E\{ a_r\}}\phi(y)$
2	$w_2(y) = y ^2$	$\phi_2(y) = \frac{ y ^2}{2E\{ a_r\}}\phi(y)$
3	$w_3(y) = y_r + y_i $	$\phi_3(y) = \frac{ y_r + y_i }{2E\{ a_r\}}\phi(y)$

Then, we have

$$\begin{aligned}
 E\{\phi(y)|\theta\} &= E\{y_i - y_r|\theta\} \\
 &= E\{a_i + a_r\}\sin\theta + E\{a_r - a_i\}\cos\theta + E\{\eta_i - \eta_r\} \\
 &\approx 2E\{a_r\}\theta,
 \end{aligned} \tag{2.71}$$

where $n_r = \Re\{n\}$ and $n_i = \Im\{n\}$ with n being the additive noise, and we have omitted the time indices for notational simplicity. Hence the basic RCPD, after normalization, is given by

$$\phi_0(y) \triangleq \frac{\phi(y)}{2E\{a_r\}}. \tag{2.72}$$

Weighted RCPD

Note that all input samples do not have the same reliability for phase error estimate. Better PD performance may result if we emphasize the samples that are more reliable. Hence we consider modifying the (unnormalized) PD to

$$\phi_g(y) = w(y) \cdot \phi(y), \tag{2.73}$$

where $\phi(y)$ is as given in (2.68) and $w(y)$ is a weighting function that emphasizes the more reliable samples. Intuitively, the weighting function should be symmetric about the $\pm 45^\circ$ lines in the 2-D space to effect unbiased estimation.

To obtain the proper normalization factor under a given $w(y)$, we again derive $E\{\phi_g(y)|\theta\}$ for small θ . Again, by symmetry, we only need to analyze the case when $y(n)$ is in the first quadrant, which gives

$$\begin{aligned}
 E\{\phi_g(y)|\theta\} &= E\{w(y) \cdot (a_r + a_i)\}\sin\theta \\
 &\quad + E\{w(y) \cdot (a_i - a_r)\}\cos\theta
 \end{aligned} \tag{2.74}$$

By symmetry of the weighting function to the $\pm 45^\circ$ lines, i.e., $w(y_r + jy_i) = w(y_i + jy_r)$, we have $E\{w(y)a_r\} = E\{w(y)a_i\}$. Hence

$$E\{\phi_g(y)|\theta\} = 2E\{w(y)a_r\}\sin\theta \approx 2E\{w(a)a_r\}\sin\theta, \tag{2.75}$$

where the second equality has been obtained through first-order approximation of the weighting function. Therefore, to get unity PD gain, the normalization factor is given by

$$k = 2E\{w(a) \cdot a_r\}. \tag{2.76}$$

Some easily conceivable weighting functions and the corresponding weighted PDs are listed in Table 2.1. All three weighting functions w_1 , w_2 , and w_3 emphasize larger signal values, which should give more reliable phase error estimates. Incidentally, the PD proposed by Kim and Choi [54] can be viewed as a weighted reduced-constellation PD with the weighting function being $w(y) = u(|y| - \tau)/|y|^2$, where $u(x)$ is the unit step function and τ is a pre-calculated threshold. (That is, only the corner samples are considered trustworthy and used in phase error estimates.) We omit further discussion of this PD.

2.2.4 Characterization of Reduced-Constellation Phase Detectors

In this section, we derive and verify the S curves of the proposed PDs under QAM. They give indications to the acquisition capability of the CRL.

PDs with Rotation-Invariant Weighting Functions

The weighting functions of PDs 0, 1, and 2 are rotation-invariant. We only need to consider symbols in the first quadrant. For a large QAM constellation, we may assume that, in absence of phase error and the decision-point signal samples are approximately uniformly distributed over a square area of dimension $2A \times 2A$ where $A = E[a_r] = E[a_i]$. For convenience, let z be the phase-correct version of y ; that is,

$$y_r = z_r \cos \theta - z_i \sin \theta, \quad y_i = z_r \sin \theta + z_i \cos \theta. \quad (2.77)$$

Then for the rotation-invariant weighting functions, $w(y) = w(z)$. In addition, we have the PD normalization factor

$$k \approx 2E\{w(z) \cdot z_r\} \triangleq 2A_w. \quad (2.78)$$

Consider the case where $0 < \theta < \pi/4$. The situation with negative θ is complementary. For y located in the first quadrant, the PD output is given by

$$\begin{aligned} \phi_c(y) &\triangleq \frac{w(y)}{2A_w} \cdot (y_i - y_r) \\ &= \frac{w(z)}{2A_w} \cdot [(z_r + z_i) \sin \theta + (z_i - z_r) \cos \theta]. \end{aligned} \quad (2.79)$$

In contrast, for y located in the second quadrant, the sign of y_r becomes negative and the PD output becomes

$$\phi_e(y) \triangleq \frac{w(x)}{2A_w} \cdot [(z_i - z_r) \sin \theta - (z_r + z_r) \cos \theta]. \quad (2.80)$$

Define

$$X_{rc} = E[w(z) \cdot z_r | y \in \text{first quadrant}], \quad (2.81)$$

$$X_{re} = E[w(z) \cdot z_r | y \in \text{second quadrant}], \quad (2.82)$$

$$X_{ic} = E[w(z) \cdot z_i | y \in \text{first quadrant}], \quad (2.83)$$

$$X_{ie} = E[w(z) \cdot z_i | y \in \text{second quadrant}]. \quad (2.84)$$

Figure 2.13 illustrates the meaning of these quantities, which shows that (X_{rc}, X_{ic}) is the weighted center of mass of the signal samples that are located in the correct quadrant and (X_{re}, X_{ie}) is that located not in the correct quadrant. The S curve is then

$$\begin{aligned} S(\theta) &= E\{\phi(y) | \theta\} = E\{\phi_c(y) | \theta\} P_c + E\{\phi_e(y) | \theta\} P_e \\ &= \frac{\sin \theta}{2A_w} (X_{rc} P_c + X_{ic} P_c + X_{ie} P_e - X_{re} P_e) \\ &\quad + \frac{\cos \theta}{2A_w} (X_{ic} P_c - X_{ie} P_e - X_{rc} P_c - X_{re} P_e), \end{aligned} \quad (2.85)$$

where P_c and P_e are the probabilities of the correct and the incorrect cases, respectively. Since the weighted center of mass of the decision input constellation in the first quadrant in absence of phase error is (A_w, A_w) , it is easily shown that

$$A_w = X_{rc} P_c + X_{re} P_e = X_{ic} P_c + X_{ie} P_e. \quad (2.86)$$

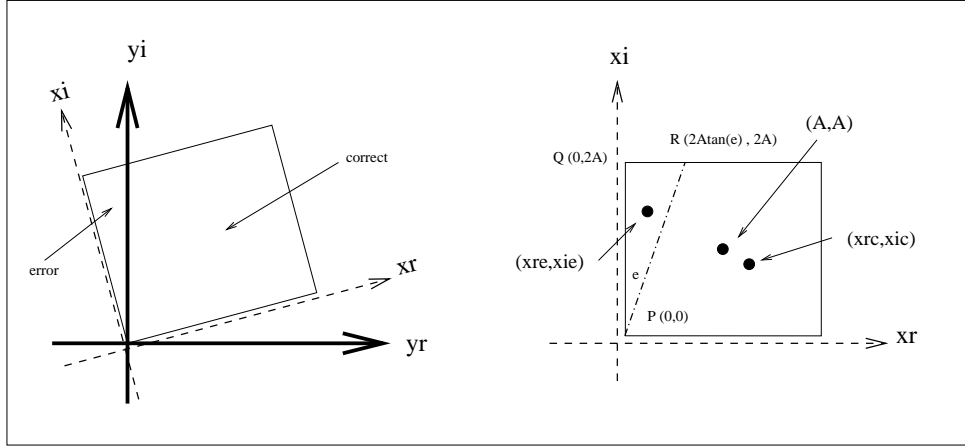


Figure 2.13: Illustration of signal distributions and various quantities used in the analysis of PD.

Substituting it into (2.85) yields the S curve as

$$S(\theta) = \sin \theta - \frac{X_{re} P_e}{A_w} \sin \theta - \frac{X_{ie} P_e}{A_w} \cos \theta. \quad (2.87)$$

Specializing it to PDs 0, 1, and 2, we get their S curves as

$$S_0(\theta) = \frac{1}{3} \sin \theta (1 - \tan^2 \theta), \quad (2.88)$$

$$S_1(\theta) = \sin \theta (1 - 0.23 (\sec^3 \theta - 1)) - 0.34 \cos \theta (\sinh^{-1}(\tan \theta) + \tan \theta \cdot \sec \theta), \quad (2.89)$$

$$S_2(\theta) = \sin \theta \cdot \left(1 - \frac{3}{25} (\sec^4 \theta - 1) \right) - \frac{4}{25} \sec^2 \theta (3 \sin \theta + \sin 3\theta), \quad (2.90)$$

respectively, where the phase error satisfies $-\pi/4 \leq \theta \leq \pi/4$.

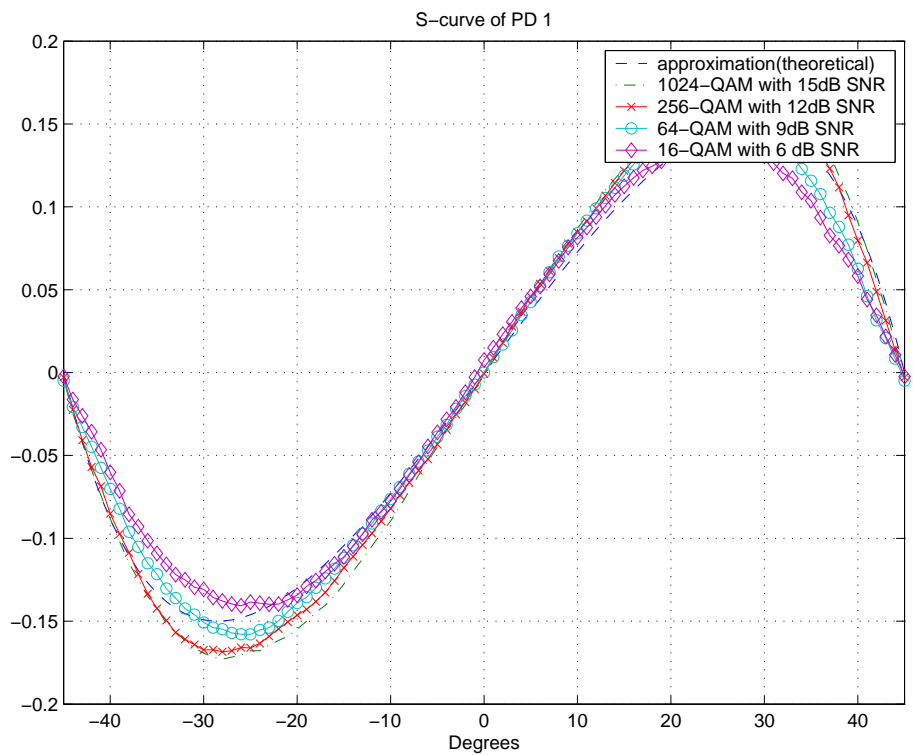
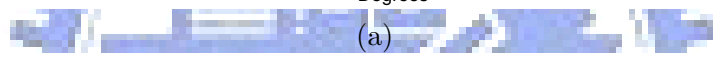
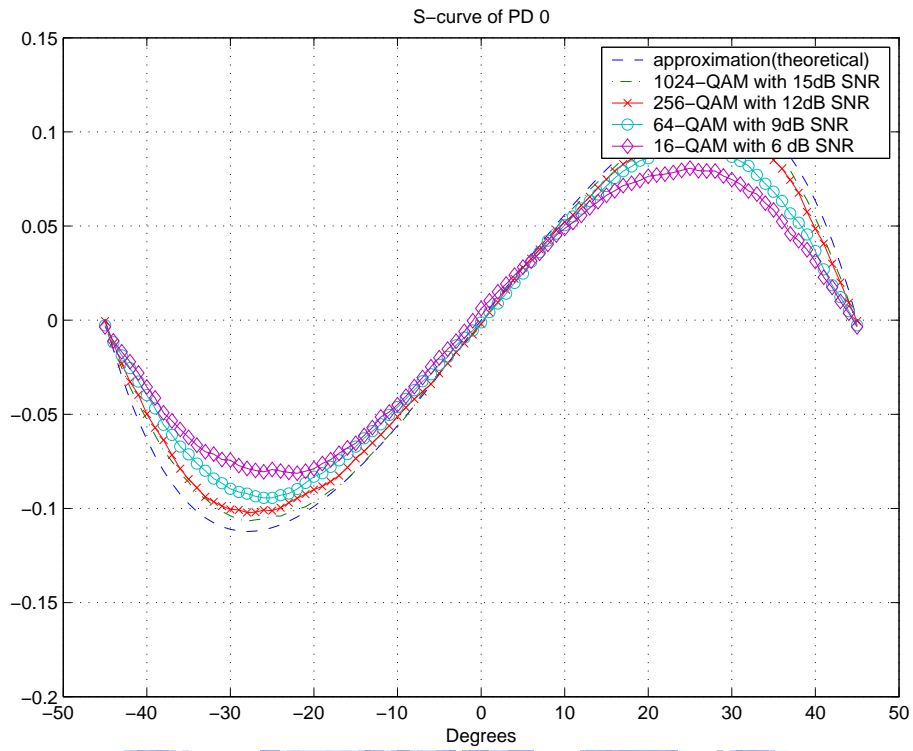
PD with Rotation-Variant Weighting Function

The weighting function associated with PD 3 is rotation-variant. Nevertheless, a similar approach as the above can be used to obtain the corresponding S curve. The result is

$$S_3(y) = \frac{3}{7} \sin 2\theta \cdot (1 - \tan^2 \theta) + \frac{1}{7} \cos 2\theta \cdot (\tan^3 \theta - 3 \tan \theta). \quad (2.91)$$

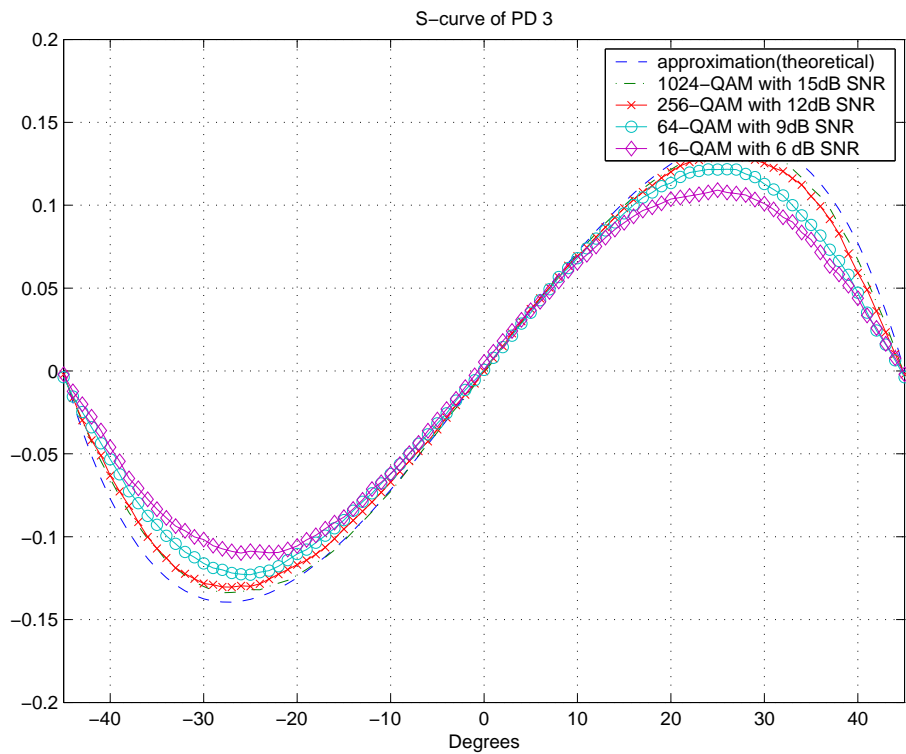
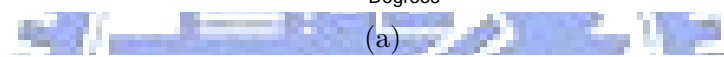
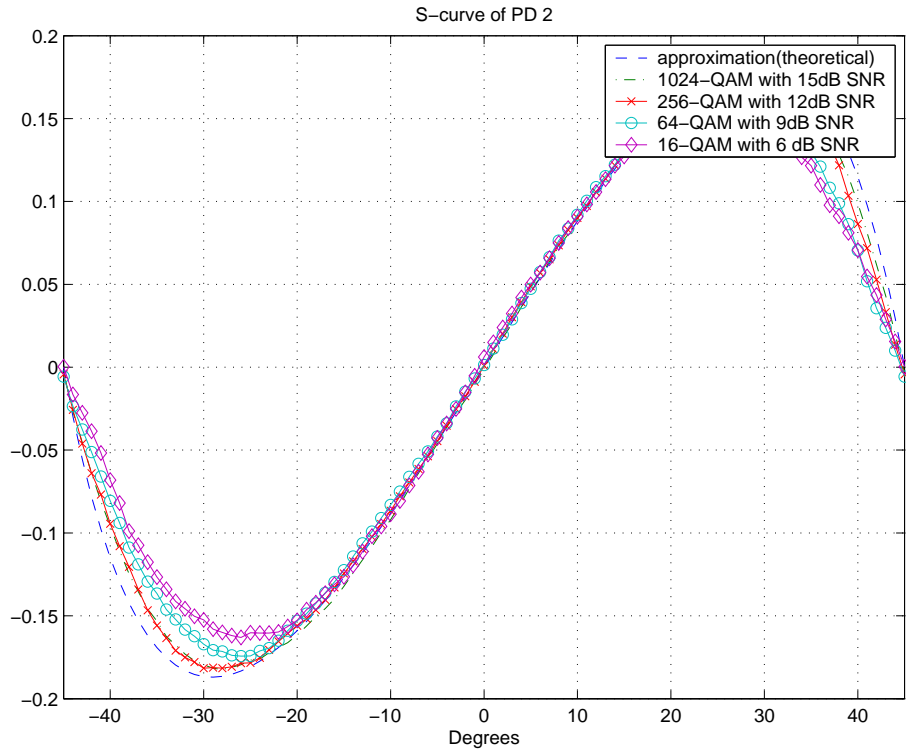
Numerical Results

Figures 2.14 and 2.15 show the approximate S curves derived above and the actual ones in (large) additive noise. As expected, they match better with increase in modulation order. For 1024-QAM, PD 2's curve peaks at a somewhat bigger value of phase error. This indicates that PD 2 may have a larger lock range in frequency errors than the other PDs. Simulation results confirm this conjecture.



(b)

Figure 2.14: S curves associated with different PDs, both theoretical (approximate) and actual (in noise). (a) PD 0. (b) PD 1.



(b)

Figure 2.15: S curves associated with different PDs, both theoretical (approximate) and actual (in noise). (a) PD 2. (b) PD 3.

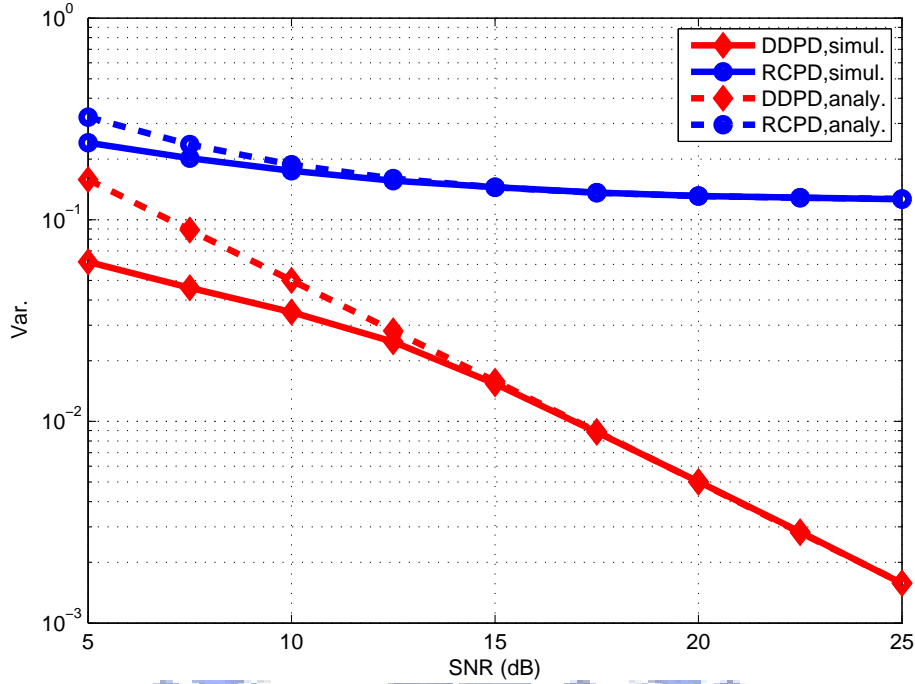


Figure 2.16: Steady-state variances of DDPD and RCPD.

Comparison of DDPD and RCPD

Now, consider the variance of the output noise of the DDPD and the basic RCPD when $\theta = 0$. When ρ is large (such as larger than -5dB SNR) for high order QAM, it is hard to analyze the variance of $\phi_D(y)$ and $\phi_0(y)$ since a great quantity of the decision errors and sign errors happen. However, since we concern the reasonable QAM operation SNR region, we consider that ρ is not large.

First, Consider DDPD. Assume decision be correct. Since $E\{\phi_D(y)\} = 0$ when $\theta = 0$, the output variance is given by

$$\sigma_{\phi_D}^2(\theta)|_{\theta=0} = E(\phi_D^2(y)) = 2E(a_i^2) \cdot E(n_i^2) = E(a_i^2) \rho. \quad (2.92)$$

Next, consider the RCPD. Assume the sign value be correct. Since $E(\phi_0(y)) = 0$ when $\theta = 0$, we have that

$$\sigma_{\phi_0}^2(\theta)|_{\theta=0} = E(\phi_0^2(y)) = \frac{(2E(a_i^2) - 2E(|a_i|)^2 + \rho)}{4E(|a_r|)^2}. \quad (2.93)$$

Fig.2.16 shows the simulated and analytical comparisons. Several observations are given as follows. First, the analytical results fit in with simulated ones only at high SNR as what we claim previous. Then, fortunately, the simulation results are better than the analytical predictions at low SNR. Finally, maybe the most important one is that the RCPD faces saturated noise variance introduced by the QAM constellation itself, but noise variance of DDPD performs a linear decrease with the increase of SNR. Now, we adjust the detection gain of the DDPD to match the same output noise variance with the RCPD, when $\theta = 0$ in a 64QAM system over 15dB SNR AWGN channel. Fig.2.17 illustrates the simulated S-curve of the DDPD and basic RCPD based on this setting, and it demonstrates the better acquisition ability of RCPD.

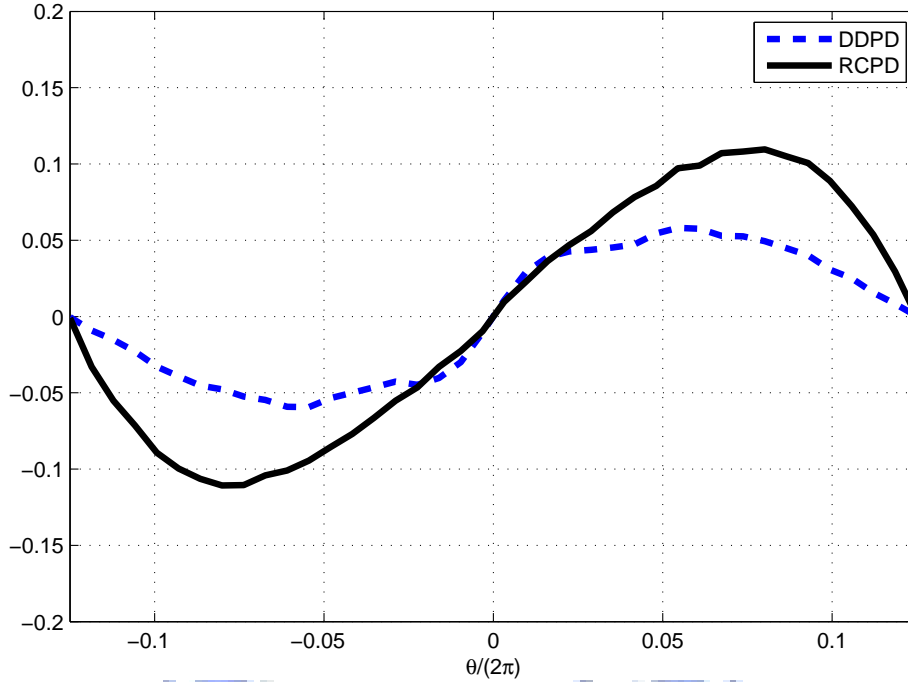


Figure 2.17: S-curves of DDPD and RCPD.

2.2.5 Hybrid PD

Now, we present a technique combines the advantages of DDPD and RCPD. The hybrid PD (HPD) is formulated by

$$\phi_H(y) = f(\phi_{RC}(y), \phi_D(y)) \quad (2.94)$$

where ϕ_{RC} is one of any kind RCPD and ϕ_D is the DDPD. This combination of the RCPD and DDPD tents to obtain both advantages of the RCPD in large acquisition range and fast convergence, and the DDPD in good lock capability.

Consider a combined cost function as given by

$$\phi_H(y) = U(|y| - T)\phi_{RC}(y) + U(T - |y|)\phi_D(y) \quad (2.95)$$

where $U(t)$ is an unit-step function and T is the threshold to determine which mode is used. According to this cost function, when $|y| \geq T$ the RCPD is used; otherwise, the DDPD is used. This setting is reasonable since larger $|y|$ provides more reliability of phase information for RCPD. Thus, the outer constellation points are used to provide acquisition range, and the inner ones are used to maintain tracking stability.

Now, we give an example of the hybrid PD design in the 64QAM system. According to try-and-error selection of threshold value, Fig. 2.18 shows the S-curves of DDPD, the basic RCPD and the HPD with $T = 1.2$ at 15dB SNR. The curves of RCPD and HPD are almost overlapped and the peak values are better than of DDPD. However, as shown in Fig. 2.19, the variance of the HPD is smaller than that of the RCPD but larger than that of the DDPD.

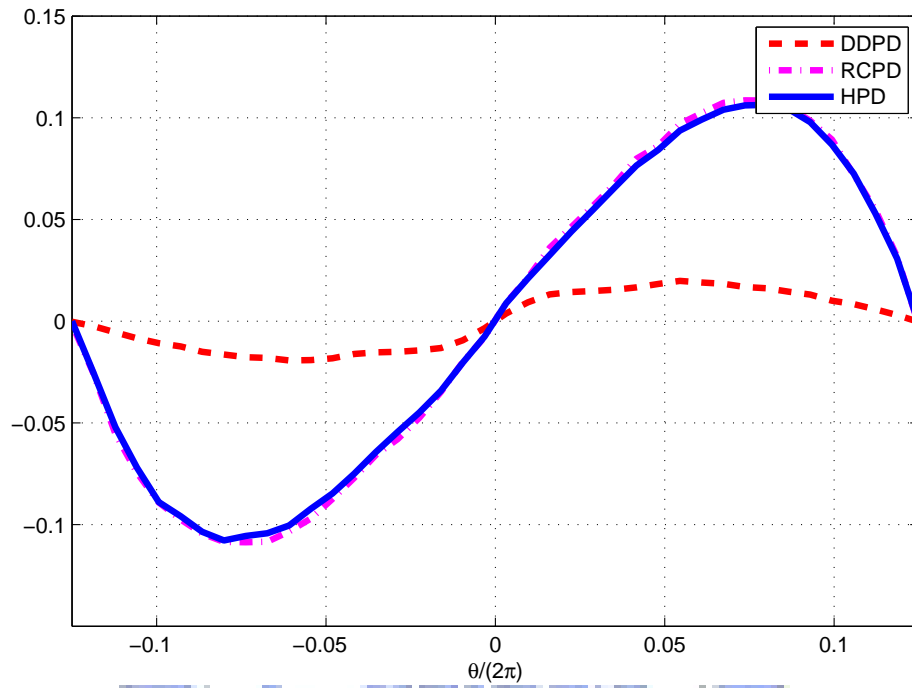


Figure 2.18: S-curves of DDPD, RCPD, and the HPD.

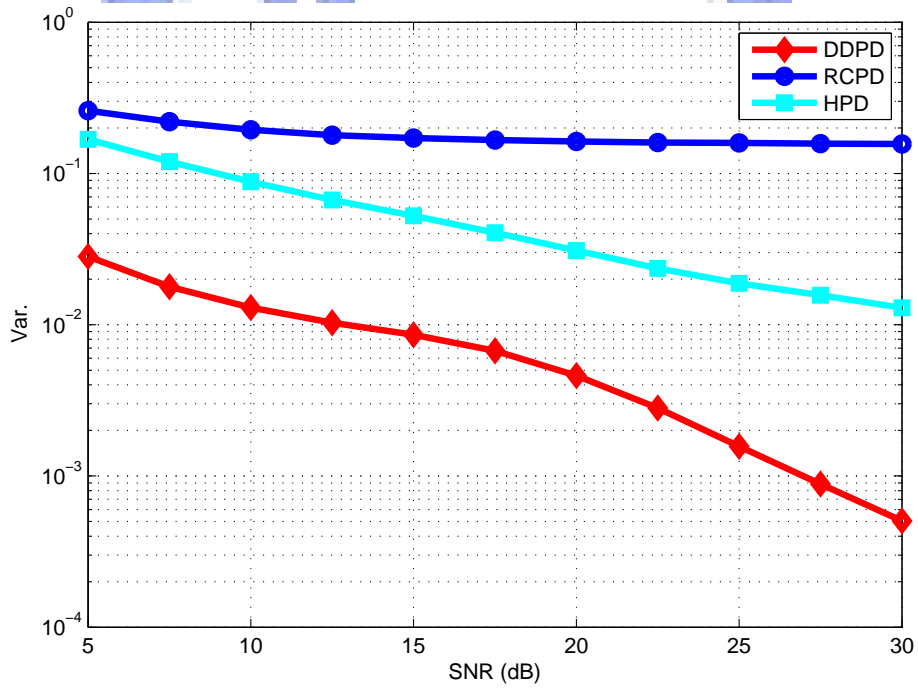


Figure 2.19: Steady-state variances of DDPD, RCPD and the HPD.

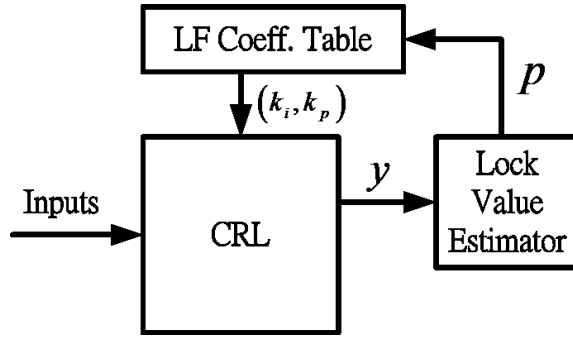


Figure 2.20: Structure of the proposed dynamic loop bandwidth control.

2.2.6 Dynamic Loop Bandwidth Control

Beside the phase detector design, the approach using dynamic loop bandwidth control is another feasible way [52] to provide large acquisition range and good tracking stability. Fig.2.20 illustrates the structure of the proposed dynamic loop bandwidth control. Unlike the scheme proposed by Ke *et al.* [52], the proposed scheme comprises a lock indicator and a lookup table of the LF parameters. In mathematical, the loop parameters $k_i = f_i(p)$ and $k_p = f_p(p)$ are both function of the lock value p .

Lock Indication

The lock detector is an indicator of the locking quality and used to monitor and control the synchronizer and equalizer. Lee *et al.* [58] propose a simplification of the detector in [69] for QPSK constellation, and it is give by

$$p = E \left\{ (\sqrt{2} + 1)y_{\min} - y_{\max} \right\}, \quad (2.96)$$

where $y_{\max} = \max \{|y_r|, |y_i|\}$ and $y_{\min} = \min \{|y_r|, |y_i|\}$. However, this indicator can not provide precise accuracy for high-order QAMs.

Based on the concept that y with larger $|y|$ provides better reliability of the angle information, we modify the lock indicator(2.96) by a conditional expectation as

$$p = E \left\{ (\sqrt{2} + 1)y_{\min} - y_{\max} \mid |y| > T_p \right\}. \quad (2.97)$$

We only count the lock indication value when $|y|$ is larger than a predefined threshold T_p .

The selection of T_p depends on the conditions including the mean behavior of p , its variance and the percentages of the useful samples. Figs.2.21 shows the experimental results of the different thresholds. We try the thresholds from 0 to 1.4 with 0.1 step-size. Part(a) demonstrates the mean curve of the lock value. As shown, the larger thresholds yield larger peak values. Part(b) is the variance of the lock value when $\theta = 0$, which presents the reliability of the estimated lock value. Part(c) is the used percentages of the total samples; straightforwardly, the lock indicator with larger threshold can use fewer samples and the part(c) results supports this inference.

To choice the threshold, we should take into consideration of the decision among the peak value, the variance and useful samples. In this case, $T_p = 1.3$ is a considerable selection because of its large peak value, small variance and acceptable sample utility.

Dynamic Loop Bandwidth Control

The proposed dynamic loop bandwidth control is achieved via the changes of the (k_i, k_p) according to the lock value p . We consider a simple multi-step function to implement this function set.

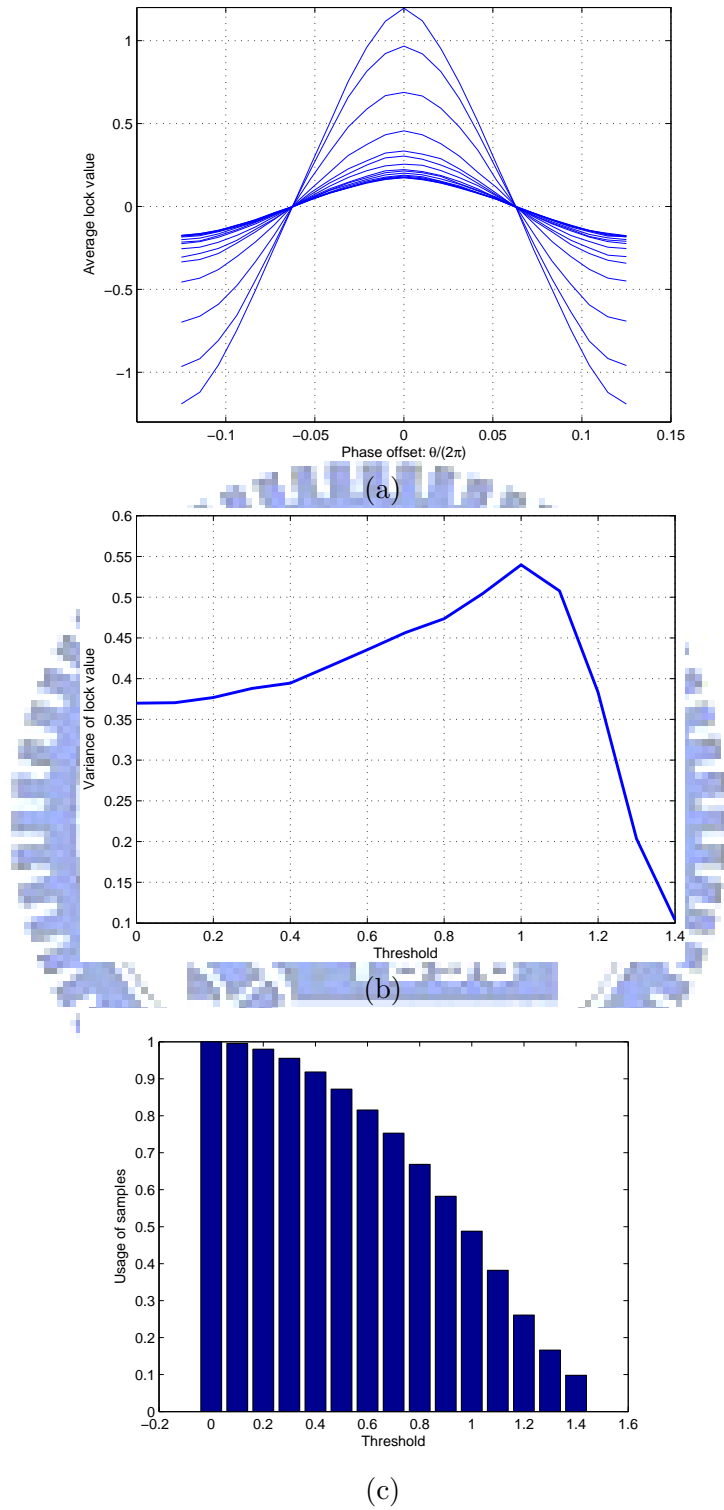


Figure 2.21: Selection of the threshold (T) of proposed lock detector in 64QAM system with 18dB SNR. (a) Mean behavior of the lock value versus θ . (b) Variance of the lock value when $\theta = 0$ versus T . (c) Useful percentages of the samples versus T .

Let L be the total stages of the multi-step function. The control maintains L step thresholds P and L sets of (k_i, k_p) . When p value locates at the region $P(l) = < p < P(l+1)$, l -th parameter pair: $(k_i, k_p)_l$ is the output. To design the coefficient pairs, we fix the damping ratio to 0.707, and decide nature frequency $\omega(l)$ in each stage.

Now, we give a design example in the 64QAM system. The function with four steps is used. For convenience, we assume $P(1) = -\infty$; thus, the step thresholds are $P = [-\infty \ 0.25 \ 0.5 \ 0.7]$ and the nature frequency are $\omega = [0.05 \ 0.01 \ 0.003 \ 0.001]$ which yield $k_p = [0.0707 \ 0.0141 \ 0.0042 \ 0.0014]$ and $k_i = [2.41 \ 0.0993 \ 0.009 \ 0.001] \times 10^{-3}$ accordingly. The threshold of lock indication value estimator is 1.3. We use the exponential average filter with 0.99 forgetting factor to smooth the estimation of p .

We now present the simulation studies for the proposed algorithms. The experimental settings are given by: SNR = 15 dB, 64QAM system, $f = 0.11$ normalized to sampling rate. We test four cases as follows:

- case 1, the CRL using RCPD without dynamic loop bandwidth control;
- case 2, the CRL using HPD without dynamic loop bandwidth control;
- case 3, the CRL using RCPD with dynamic loop bandwidth control;
- case 4, the CRL using HPD with dynamic loop bandwidth control.

Figs. 2.22, 2.23, 2.24 and 2.25 illustrate the simulation results of the case 1 to case 4 sequentially. First, when comparing the steady-state performances of all, the steady-state MSE of the frequency estimations are given by $\sigma_f^2 = 6.52 \times 10^{-4}$ for case 1, $\sigma_f^2 = 1.52 \times 10^{-5}$ for case 2, $\sigma_f^2 = 5.06 \times 10^{-11}$ for case 3, and $\sigma_f^2 = 6.55 \times 10^{-12}$ for case 4.

It shows the case 4 is superior than others. Considering the comparison of the HPD and RCPD, the tracking stability of HPD is much better than the RCPD as compared in case 1 and case 2, and the HPD can provide much faster stabilized transition from initial step to final step as compared in case 3 and case 4. Considering the ability of the dynamic loop bandwidth control, no matter case 3 or case 4, the CRL with dynamic loop bandwidth control has more better stability than that without dynamic loop bandwidth control in case 1 and case 2, which is demonstrated in the trajectory of the frequency estimation and its steady-state MSE. Thus, we get a brief conclusion: the CRL using HPD with dynamic loop bandwidth control provides the superiority in both acquisition ability and tracking stability.

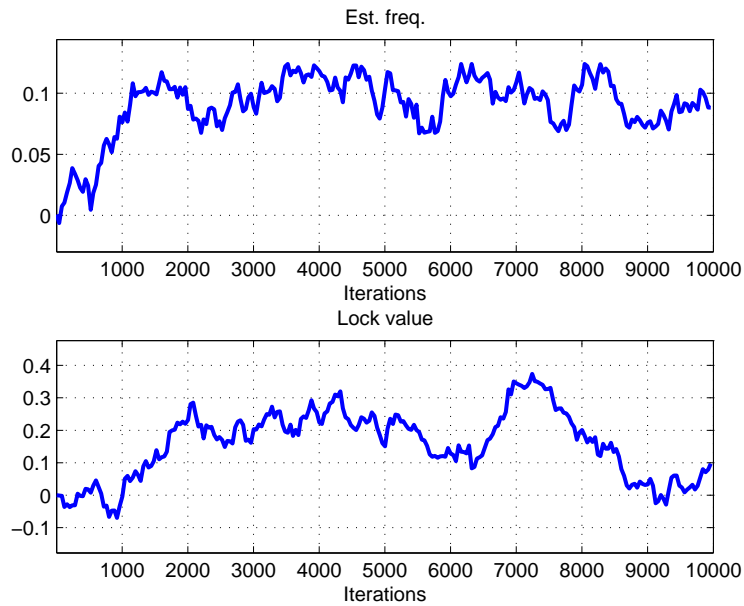


Figure 2.22: Simulated results of Case 1, the CRL using RCPD without dynamic loop bandwidth control. At top: estimated frequency normalized to sampling frequency. At bottom: lock indication value.

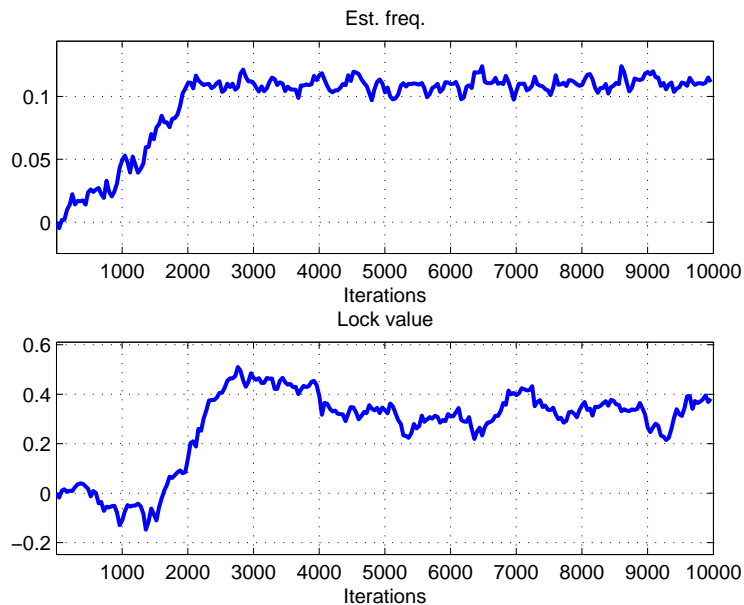
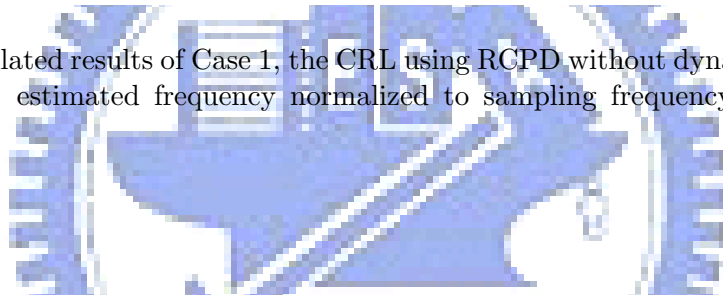


Figure 2.23: Simulated results of Case 2, the CRL using HPD without dynamic loop bandwidth control. At top: estimated frequency normalized to sampling frequency. At bottom: lock indication value.

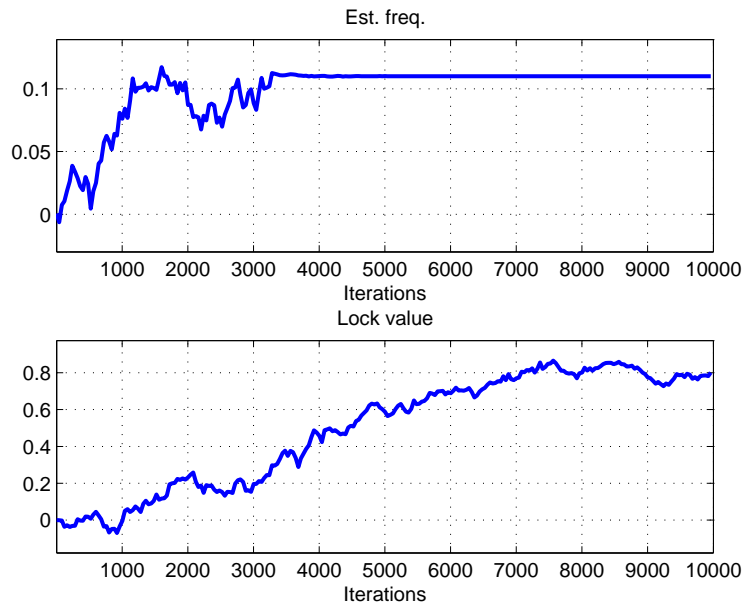


Figure 2.24: Simulated results of Case 3, the CRL using RCPD with dynamic loop bandwidth control. At top: estimated frequency normalized to sampling frequency. At bottom: lock indication value.

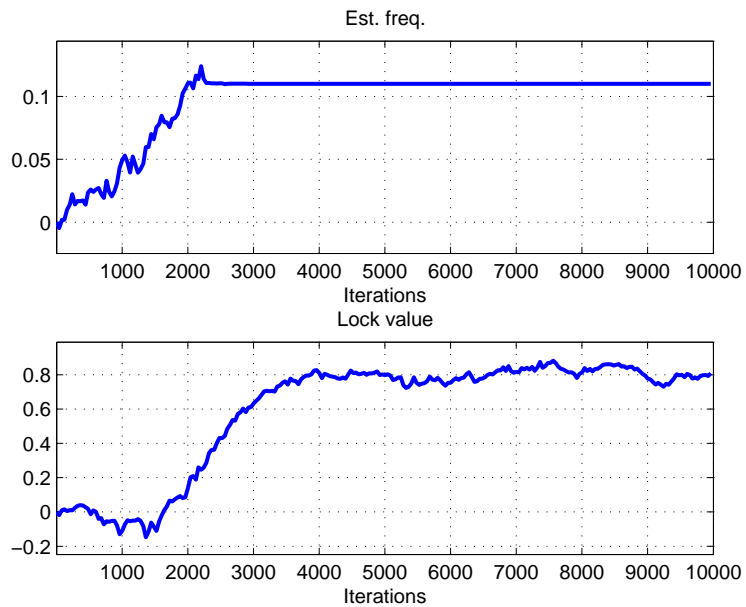
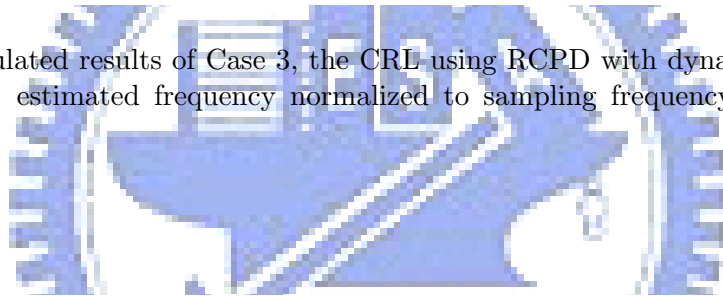


Figure 2.25: Simulated results of Case 4, the CRL using HPD with dynamic loop bandwidth control. At top: estimated frequency normalized to sampling frequency. At bottom: lock indication value.

2.3 Conclusions

This chapter introduced the carrier frequency and phase synchronization. We consider both the open-loop and the closed-loop structures. In the open-loop structure, we study the Fitz's algorithm for the signal frequency estimation and then propose a multi-resolution algorithm and the modified Fitz's algorithm according the analysis of the Fitz's algorithm. Analytical and simulated results illustrate the proposed algorithms can reach near CRB in a low cost manner. The X^4 SFE is also studied to solve the frequency estimation in QAM system.

In the other part of this chapter, we study the closed-loop synchronize. The main topic in this section focuses on the design of blind PDs and the dynamic loop bandwidth control scheme. We first propose a set of the PD based on the reduced constellation concept; then, a hybrid combination of the RCPD and the DDPD is used to provide both the better acquisition ability and the tracking stability. Besides, the dynamic loop bandwidth control is also presented using the lock indication triggered manner. Final simulations demonstrate that the CRL using HPD and the dynamic loop bandwidth control provide superior capability in both the acquisition ability and tracking stability.



Chapter 3

Blind Adaptive Decision Feedback Equalization

The equalizer is used to combat the inter-symbol-interference (ISI) channel distortion. There are many equalization structures, such as the linear equalization, the maximal likelihood sequence estimation, the turbo-equalization. However, the implementation cost and the performance have made the decision feedback equalizer the most commonly used structure for the application over static channel environment.

A typical equalizer contains two properties: the structure and the coefficients. In the example of the DFE, its structure includes a feed forward filter (FFF), a feedback filter (FBF) and a decision circuit, as illustrated in Fig. 3.1. The FFF is to shorten the channel response and the FBF is to remove the residual ISI term. The responses of the filters are the filter coefficients which are determined by the channel responses. As shown in Fig. 3.1, the coefficients are generated by the coefficient adapter. The realization of the coefficient adaptor depends on the available materials and the implementation costs.

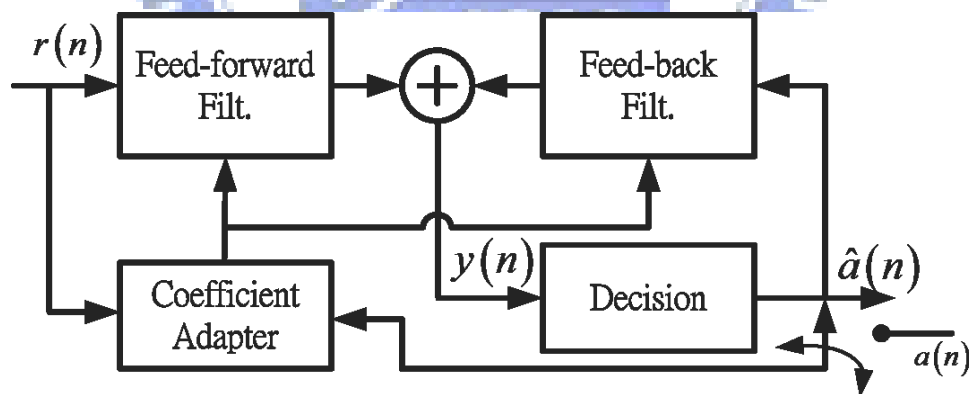


Figure 3.1: The structure of the decision feedback equalizer that is composed by a feed forward filter, a feedback filter, a decision circuit and a filter coefficient adapter.

This chapter mainly focuses on the coefficient adaptation. We adopt the blind adaptive filter [29] to realize the adaptor. The key issue in blind adaptive process is tradeoff between the steady-state and training speed. We suggest the variable stepsize (VSS) algorithm to compromise this tradeoff. After the blind start operation, the DFE is worked in the tracking mode to provide small mean-square error when the tentative decisions are near error-free.

Switch time of the operation mode is another critical issue in adaptor design. For this, we introduce a soft-switching concept that the operation mode smoothly transfers from blind acquisition to decision-directed tracking. To achieve this soft-switching, we suggest the hybrid

blind algorithm that combines directly the decision-directed least-mean square algorithm [29] and the blind VSS adaptive algorithm.

3.1 Optimal Coefficient and LMS Algorithm

Before the description of the blind mode operation of the DFE, we first consider the minimal mean-square error (MMSE) coefficients of the equalizer. We first consider the coefficient adaptor in linear equalizer and extend to the adaptor of the DFE.

Let \mathbf{H} be the Toeplitz matrix of the “composite” channel (which includes the responses of the transmitting filter, the channel and the receiving filter), a_k be the k -th input signal, and r_k be the k -th output sample of the channel. The received signal r_k can be expressed as

$$\underline{r}_k = \mathbf{H}\underline{a}_k + \underline{n}_k \quad (3.1)$$

where $\underline{r}_k = [r_k \ r_{k-1} \ \cdots \ r_{k-L+1}]^T$ is received vector, $\underline{a}_k = [a_k \ a_{k-1} \ \cdots \ a_{k-M+1}]^T$ is the transmitted vector, and \underline{n}_k is AWGN vector.

Now, consider the equalizer operation. If \underline{w} is the $L \times 1$ coefficient vector of the equalizer and \underline{x} is the input vector of the equalizer, we have that

$$y_k = \langle \underline{w}, \underline{x}_k \rangle = \sum_{l=0}^{L-1} w(k-l)x_{k-l}. \quad (3.2)$$

If the linear equalization structure is used, we have that $\underline{x}_k = \underline{r}_k$. The target of the channel equalization is to inverse the channel effect. In MMSE manner, we want to minimize the cost function that

$$J = E |y_k - a_{k+d}|^2, \quad (3.3)$$

in which d is the process delay of the equalizer. If the channel response and the noise variance are available, from the Wiener filter, the coefficients of linear MMSE equalizer are given by [29]

$$\underline{w} = (\mathbf{H}^H \mathbf{H} + \sigma_n^2 \mathbf{I})^{-1} \underline{h}_d \quad (3.4)$$

where \underline{h}_d is the Hermitian of the d -th row of \mathbf{H} .

In practice, we can estimate the channel response and the noise variance for the coefficient calculation. Alternatively, if considering low-cost implementation, we can adopt the adaptive signal process to realize the coefficient adaptor. When the training data or the correctly tentative decisions exist, the least-mean-square (LMS) algorithm [29] is feasible and widely adopted one to train the coefficients, which adaptation is given by

$$\underline{w}_{k+1} = \underline{w}_k - \mu e_k \underline{x}_k^* \quad (3.5)$$

where μ is the stepsize, and

$$e_k = a_k - y_k \quad (3.6)$$

is the error function. In steady-state of the LMS adaptor, the performance of the LMS adaptor approaches the MMSE equalizer when eliminating the excess error due to the LMS adaptation algorithm or when the stepsize is small enough [29].

When the DFE structure is considered, we can let

$$\underline{w}_k = \begin{bmatrix} \underline{f}_k^T & \underline{b}_k^T \end{bmatrix}^T, \quad \underline{x}_k = \begin{bmatrix} \underline{r}_k^T & \hat{\underline{a}}_{k-1}^T \end{bmatrix}^T \quad (3.7)$$

where \underline{f} and \underline{b} are the coefficient of the FFF and FBF relatively, and \hat{a} is the tentative decision. Thus, the above LMS algorithm can be directly applied in the DFE coefficient adaptor.

3.2 Blind Adaptive Algorithms

If there are lack of the training sequence, we can adopt the blind adaptive algorithm in the initial training of the equalizer. Recently, the most popular blind adaptive algorithms are the stochastic gradient descent type, such as the constant modulus algorithm (CMA) [49] and the multi-modulus algorithm (MMA) [104]. Both the CMA and MMA can be realized in the gradient descent recursion as

$$\begin{aligned}\underline{w}_{k+1} &= \underline{w}_k - \mu \nabla_w \Psi(y_k) \\ &= \underline{w}_k - \mu \psi(y_k) \underline{x}_k^*\end{aligned}\quad (3.8)$$

where $\Psi(y_k)$ is the cost function and the $\psi(y_k)$ is the relative error function.

3.2.1 Constant Modulus Algorithm

Omit the time index k , the CMA attempts to minimize the distance of the radius of the equalizer outputs and a constant parameter, which cost function is given by [89, 104]

$$\Psi_c(y) = E \left[(|y|^2 - R_c)^2 \right] \quad (3.9)$$

with

$$R_c = \frac{E |a|^4}{E |a|^2}. \quad (3.10)$$

Taking the gradient of $\Psi_c(y)$ with respect to y , we can derive that

$$\psi_c(y) = y (|y|^2 - R_c). \quad (3.11)$$

When the kurtosis of the complex signal is non negative and the channel is perfectly equalized, the cost function of the CMA can reach minimal value [89].

3.2.2 Multi-Modulus Algorithm

The MMA [104] seeks to minimize a cost function given by

$$\Psi_m(y) = E[(y_r^L - R_m^L)^2 + (y_i^L - R_m^L)^2] \quad (3.12)$$

with

$$R_m^L = \frac{E (a_r^{2L})}{E (|a_r|^L)} = \frac{E (a_i^{2L})}{E (|a_i|^L)}, \quad (3.13)$$

where y_r and y_i are the real and imaginary parts of y respectively, a_r and a_i are the real part and the imaginary part of a , L is a positive integer, and R_m is the constant value of the algorithm. In practice, $L = 2$ is a good choice to compromise between implementation complexity and performance [104]. Letting $L = 2$ and taking the gradient of $\Psi(y)$ with respect to y yield

$$\psi_m(y) = y_r (y_r^2 - R_m^2) + j y_i (y_i^2 - R_m^2). \quad (3.14)$$

As shown in [104], the optimal cost function exists only if the residual ISI terms of the combined channel are zero, i.e. the case of ISI-free channel.

Automatic Phase Recovery Property of MMA

We introduce an interest property of the MMA. Unlike the requirement of the phase recovery circuit in the CMA, it can provide the “automatic phase recovery” if there is no frequency offset. The same result is presented in the paper [106]. However, we give a short and simple proof of this property in this subsection.

To prove this property, we need to prove that the optimal cost function of the MMA happens only if the phase rotation θ is $\frac{N\pi}{2}$ for integer N . First, assume $y = ae^{j\theta}$ is the rotated version of a . Expanding the cost function of the MMA, we have that

$$\Psi_M(y) = -2E[y_r^2 y_i^2] + E|y|^4 - 2R_m^2 E|y|^2 + 2R_m^2. \quad (3.15)$$

Since $|y|^2$ is independent with θ , the cost function is minimal if

$$\Psi'(\theta) = E[y_r^2 y_i^2] \quad (3.16)$$

is maximal. Now, expressing $y_r^2 y_i^2$ in terms of a and θ , we have that

$$\begin{aligned} y_r^2 y_i^2 &= \left(\frac{-j}{4} (ae^{j\theta} + a^* e^{-j\theta})(ae^{j\theta} - a^* e^{-j\theta}) \right)^2 \\ &= -\frac{1}{16} \left(a^2 e^{j2\theta} - (a^2)^* e^{-j2\theta} \right)^2 = \frac{1}{8} \left(|a|^4 - \Re\{a^4 e^{j4\theta}\} \right). \end{aligned} \quad (3.17)$$

Therefore, the modified cost function is given by

$$\Psi'(\theta) = \frac{E|a|^4}{8} - \frac{E[a^4]}{8} \Re\{e^{j4\theta}\} \quad (3.18)$$

Since $E[a^4]$ is a real negative value for all QAMs, we have the maximal value of $\Psi'(\theta)$ and minimum of the MMA cost function if $4\theta = 2N\pi$, or equivalently $\theta = \frac{N\pi}{2}$.

3.2.3 Steady-state MSE Caused by Blind Algorithm

This subsection analyzes the steady-state mean-square error of the blind algorithm. In the following derivation, we consider the case in absence of the AWGN, and also assume that the correct decisions always happen.

Let \underline{w}_{opt} be the optimal filter coefficient vector and $\tilde{\underline{w}}_k = \underline{w}_{opt} - \underline{w}_k$. A priori and the a posteriori estimation errors are given by, respectively,

$$e_a(k) = \underline{x}_k \tilde{\underline{w}}_{k-1}, \quad (3.19)$$

$$e_p(k) = \underline{x}_k \tilde{\underline{w}}_k = e_a(k) - \mu \|\underline{x}_k\|^2 \psi(y_k). \quad (3.20)$$

In the steady state when $E\{\tilde{\underline{w}}_k\} = E\{\tilde{\underline{w}}_{k-1}\}$, the mean-squares of the estimation errors are related by [67]

$$E \left\{ \frac{|e_a(k)|^2}{\|\underline{x}_k\|^2} \right\} = E \left\{ \frac{|e_a(k) - \mu \|\underline{x}_k\|^2 \psi(y_k)|^2}{\|\underline{x}_k\|^2} \right\}, \quad (3.21)$$

which can be simplified to

$$E\{\Re[e_a(k)\psi(y_k)]\} = \frac{\mu}{2} E\{\|\underline{x}_k\|^2 |\psi(y_k)|^2\}. \quad (3.22)$$

Assume that the residual errors are small when the equalizer is converged. Then first-order approximation as in [60] gives

$$\psi(y_k) \approx \psi(a_k) + \psi'(a_k) e_a(k), \quad (3.23)$$

(Without loss of generality, the transmission and filtering delays are disregarded.) Substituting (3.23) into (3.22) and assuming independence among $\psi(a_k)$, $e_a(k)$, and $\|\underline{x}_k\|^2$ as in [67], we obtain the MSE as

$$E\{|e_a|^2\} = \frac{\mu E(\|\underline{x}\|^2) \cdot E(|\psi(a)|^2)}{2 E\{\Re[\psi'(a)]\}}. \quad (3.24)$$

We first consider the case of LE. Since $E(\|\underline{x}\|^2) = L \sigma_a^2 \sigma_h^2$ where $\sigma_a^2 = E\{|a|^2\}$ is the QAM symbol energy and $\sigma_h^2 = \|h_1\|^2$ is the channel energy and h_1 is the first column of \mathbf{H} , we have

$$E\{|e_a|^2\} = \frac{\mu E(|\psi(a)|^2)}{2 E\{\Re[\psi'(a)]\}} \cdot \sigma_a^2 \sigma_h^2 L. \quad (3.25)$$

We turn to the case of DFE. Substituting $\underline{x} = [\underline{r}^T \hat{\underline{a}}^T]^T$ and $\underline{w} = [\underline{f}^T \underline{b}^T]^T$ into (3.24), we have

$$E\{|e_a|^2\} = \frac{\mu E\{|\psi(a)|^2\}}{2 E\{\Re[\psi'(a)]\}} \cdot \sigma_a^2 (\sigma_h^2 L_f + L_b) \quad (3.26)$$

where L_f is the number of the FFF coefficients and L_b is the number of the FBF coefficients.

Considering the $\psi'(y)$ of the CMA and MMA, simple derivations give that

$$\psi'(y) = 2|y|^2 - R_c \quad (3.27)$$

for the CMA case, and

$$\psi'(y) = \frac{3}{2}|y|^2 - R_m \quad (3.28)$$

for the MMA case. Substituting (3.27) and (3.28) into (3.26), we have the steady-state MSE performances of the DFE with CMA and MMA correspondingly.

Simulation Comparison

The simulation settings are given by: channel response $h_1 = [1 \ 0 \ 0 \ 0 \ 0.5e^{j\pi/3}]$, 16-QAM, $L_f = L_b = 20$, no additive noise. We test two configurations of the DFE. One uses the realistic decisions as the inputs of the FBF; the other case uses the true data as the inputs. Fig. 3.2 shows the comparison of the simulation and analysis of MMA adaptation. In Fig. 3.2, the results of realistic DFE are close to the DFE with perfect FB when stepsize is large, but has gap when stepsize is small enough. Besides, the simulated results in perfect feedback condition agrees the analytical ones when stepsize is small.

3.3 Variable Stepsize Algorithm and Hybrid Algorithm

A well-known design issue of stochastic-gradient type of adaptive algorithms is the choice of the adaptation step size, which has to strike a balance between convergence speed and steady-state MSE. In QAM-based transmission, this issue is more acute for higher-order modulations than for lower-order ones, because the former require higher SNR values to attain a given error performance than the latter and thus the convergence speed has to be sacrificed more. A way to alleviate this problem is to employ a variable stepsize (VSS) [55], [95]. For automatic adjustment of the stepsize, we need a metric that indicate the convergence property. For example, Ueng and Su [95] suggest using the residual ISI or the MSE as the metric.

Herein lies another problem that is more serious for blind equalization under higher-order QAMs than under lower-order ones. That is, the equalizer output errors are relatively large before final convergence. Thus, for higher-order QAMs, tentative decisions are liable to greater error probabilities and simplistic MSE estimates may suffer greater inaccuracy.

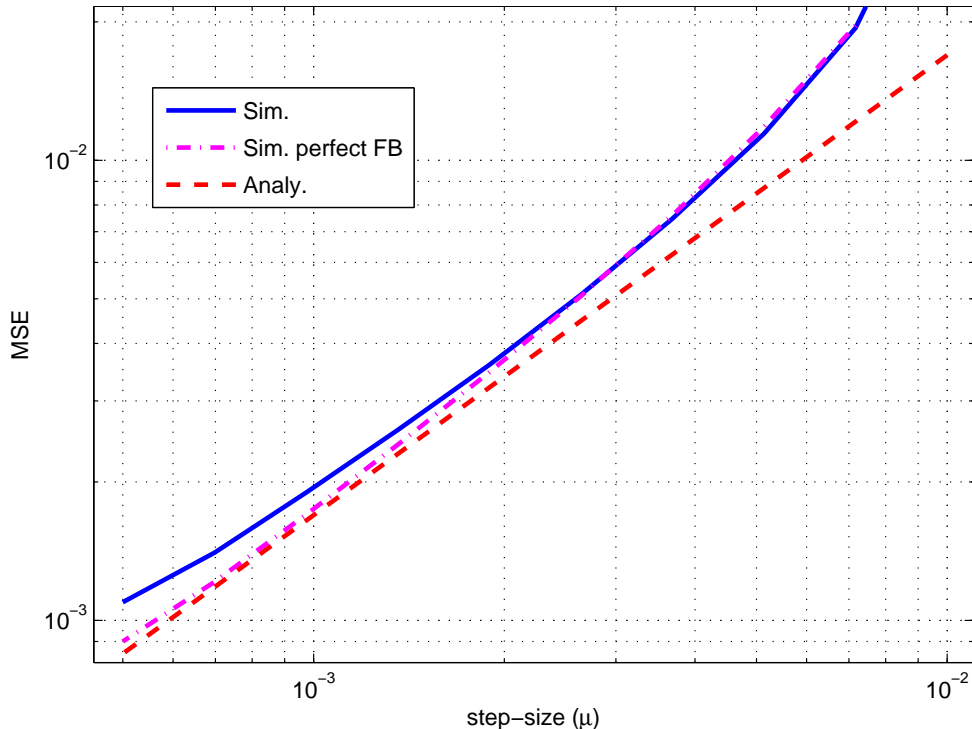


Figure 3.2: The simulated and analytical steady-state MSEs of the DFE with MMA versus different stepsize μ .

Another issue in the blind equalizer is the switching opportunity from the blind acquisition to DD-LMS tracking. Now blind equalization is usually employed only in the initial phase of receiver startup. After the equalizer coefficients are sufficiently converged, the receiver may cut over to decision-directed (DD) operation employing, e.g., the LMS-type algorithm for continued adaptation of the equalizer and tracking of channel variation. The selection of the cutover point presents another design issue, which has to be resolved balancing between convergence speed and algorithm stability. In fact, when the channel may vary greatly in time, such as the wireless channel, there may be a need to return to the blind mode from time to time. Hence it appears appropriate to consider a “soft combination” of blind and DD-LMS adaptations to sidestep the design issues associated with hard switching between blind and DD-LMS operations.

Some have proposed algorithms in this vein [65, 12, 30, 108]. The blended CMA [65] algorithm dynamically decides the use of DD-LMS or CMA based on whether the distance of the equalizer output and its hard decision is smaller than a certain threshold or not. The concurrent algorithm (CCA) [12] generates the equalizer output by combining the outputs of two filters; one adapted using CMA and the other using DD-LMS. If the decision output of the equalizer and the so-called “perturbed output” are the same, then the decision is declared reliable. When the MSE is sufficiently low, the adapter turn off the CMA and only keep the DD-LMS working. The complexity of CCA is approximately twice that of conventional SGA algorithms. In modified CMA (M-CMA) [30], a hybrid cost function called the “constellation matched error (CME)” is used in equalizer adaptation. To speed up the convergence, the authors of [30] further consider dynamic adjustment of the weighting factor in the hybrid cost function to result in the so-called “data-dependent cost function (DDCF)” [108]. However, the speed gain of DDCF M-CMA is obtained at the price of about five to six times the complexity of M-CMA.

In this section, we propose the blind VSS algorithm and the combination of blind VSS and DD-LMS, the hybrid VSS algorithm. The Key feature of the proposal is the convergence metric: the boundary MSE (BMSE), which is inspired from the observation of the PDF of the equalizer

output. Besides, we present two kinds of the stepsize function. The first kind stepsize control is the multistage gear-based function that a smaller stepsize is used if the BMSE reaches the predefined threshold. The other control considers the seamless design that the stepsize is a linear continuous function of the BMSE. On the combination of the blind algorithm and the DD-LMS, we also present two types based on the seamless design. The difference of the types is at the stepsize of the DD-LMS. We first use the complementary of the blind stepsize function as the stepsize control of the DD-LMS part; then, we import the reliability concept from the CCA [12] and adopt the “stop-and-go” function as the control.

3.3.1 MSE Measurement: Boundary Mean-Square Error

Key in this procedure is the estimation of actual SNR, or equivalently, the estimation of the actual MSE given by $E\{|y_k - a_k|^2\}$, the mean-square difference between equalizer filter output and the transmitted QAM symbol. To see how this can be accomplished, consider Fig. 3.3 which illustrates the situation of 4-PAM (applicable also to 16-QAM), where the signal points are at ± 1 and ± 3 . In the figure, the dashed lines illustrate the PDFs of the equalizer filter output y_k corresponding to different values of a_k and the solid line is their sum. An estimator of the MSE can be obtained from analyzing the PDF of y_k . However, when the SNR is not high, the center part of the PDF is relatively flat. The variation in this part with changes in MSE is relatively small. Thus this part does not contribute significantly to the ability of MSE estimation. Numerical results also verify this observation. PDF variation outside the boundary symbol values is greater. Thus we base our MSE estimation on analysis of values of y_k that fall outside the boundary symbol values. Accordingly, we call this approach boundary MSE estimation.

From Fig. 3.3, we also see that only about $1/M$ of the equalizer input samples will be used in performing the estimate, but not all samples. This is a price we pay to have good sensitivity in MSE estimation.

Treat a QAM symbol as the direct sum of two PAM symbols. Let \bar{y} denote the value of either dimension of the equalizer filter output y . The boundary MSE, for PAM, is defined as

$$B = E\{(\bar{y} - \bar{a}_{\max})^2 \mid |\bar{y}| > \bar{a}_{\max}\}, \quad (3.29)$$

where \bar{a}_{\max} is the largest symbol value in the PAM constellation.

For convenience, let the constellation points of M -PAM have values $\pm 1, \pm 3, \dots, \pm(M-1)$. Due to symmetry, in theoretical analysis we only need to consider the positive side. Let P_n be the probability that the transmitted symbol value is $(M-1-2n)$ but $\bar{y} > \bar{a}_{\max}$. Then

$$P_n = \int_0^\infty \frac{1}{\sqrt{2\pi\sigma^2}} \exp\left(-\frac{(x+2n)^2}{2\sigma^2}\right) dx = \Phi\left(\frac{2n}{\sigma}\right), \quad (3.30)$$

where we have assumed that the sum of the residual intersymbol interference (ISI) and additive noise is Gaussian and let σ^2 denote its variance. Note that σ^2 is the target of estimation. The corresponding mean-square boundary error is given by

$$\begin{aligned} V_n &= \int_0^\infty \frac{x^2}{\sqrt{2\pi\sigma^2}} \exp\left(-\frac{(x+2n)^2}{2\sigma^2}\right) dx \\ &= (4n^2 + \sigma^2)P_n - \sqrt{\frac{2}{\pi}} n\sigma \exp\left(-\frac{2n^2}{\sigma^2}\right). \end{aligned} \quad (3.31)$$

Assume all constellation points are transmitted with equal probability. Then the total boundary error probability and total mean-square boundary error, on the positive side, are given by

$$P = \frac{1}{M} \sum_{n=0}^{M-1} P_n \quad \text{and} \quad V = \frac{1}{M} \sum_{n=0}^{M-1} V_n, \quad (3.32)$$

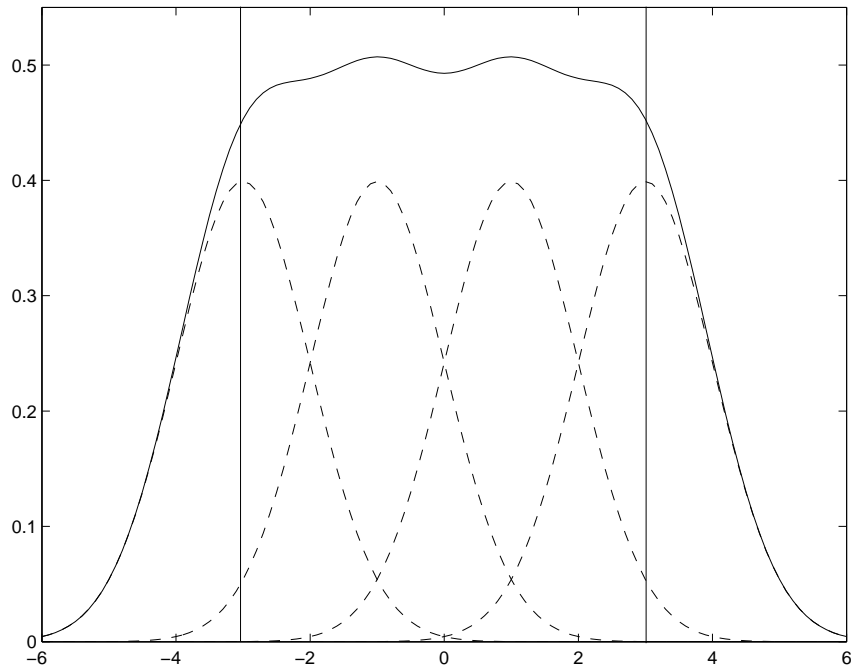


Figure 3.3: Motivation and principle of boundary MSE estimation, illustrated for the case of 4-PAM (applicable also to 16-QAM). The constellation points are at ± 1 and ± 3 . Dashed lines illustrate PDFs of equalizer filter output $y(n)$ corresponding to different values of a_k ; solid line their sum.

respectively. The BMSE is thus given by

$$B = \frac{V}{P} = \sigma^2 + \frac{4 \sum_n n^2 \Phi(2n/\sigma) - \sqrt{2/\pi} \sigma \sum_n n \exp(-2n^2/\sigma^2)}{\sum_n \Phi(2n/\sigma)}. \quad (3.33)$$

Fig. 3.4 plots the ratios of σ^2 to BMSE in log scale for QPSK, 16QAM, 64QAM, 256QAM and 1024QAM over a range of SNR values (where $\text{SNR} = E\{|a|^2\}/\sigma^2$). The length of the simulated symbols at each SNR points is 5×10^4 for all the QAMs. As shown, the simulation ratios satisfy the analytic ones with only small variations in log domain. Beside, the ratios are nearly unity in large SNR. This is because when the true MSE σ^2 is small, the last two terms in the RHS of (3.33) are close to zero. Even for an SNR as low as 0 dB, the difference is only about 1.65 dB for 1024QAM and smaller for other QAMs.

Practical estimation of the BMSE, for QAM, may be effected by time averaging, such as

$$B_k = \beta \cdot B_{k-1} + (1 - \beta) \cdot 2(|\bar{y}_k| - \bar{a}_{\max})^2, \quad (3.34)$$

where β is the forgetting factor, the factor 2 is to account for the difference between QAM and PAM, and the recursion is executed only when $|\bar{y}_k| > \bar{a}_{\max}$.

3.3.2 Variable Stepsize Algorithm

Besides the MSE measurement, the stepsize control is another design issue in the VSS approach. This subsection introduces two kinds of the stepsize control functions. Similar to the dynamic loop bandwidth control, first kind design is the gear-based design that adopts the multiple step function to implement the control function. The other considers the seamless design that employs a continuous function for the stepsize control. We first present the multistage VSS (MS-VSS) approach, and then the linear decayed VSS (LD-VSS) approach.

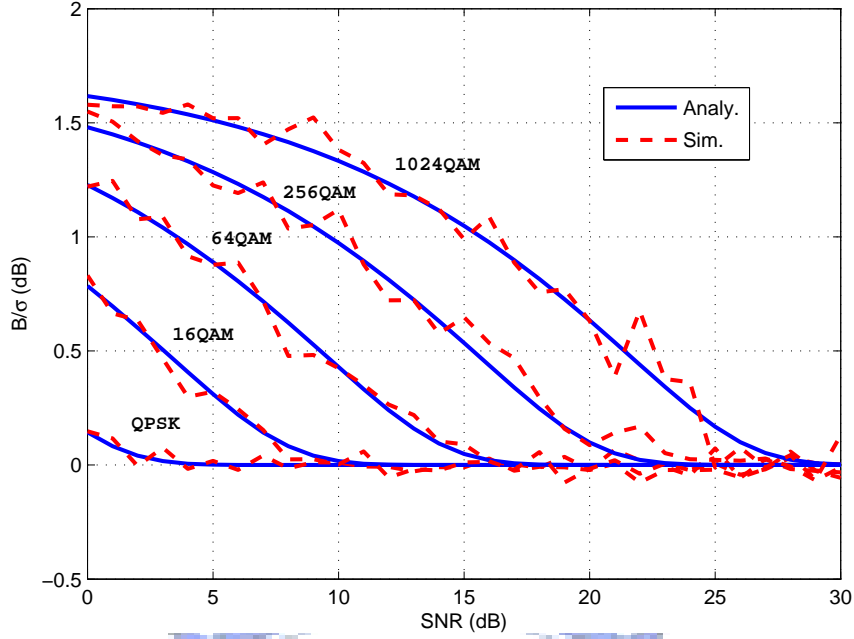


Figure 3.4: Simulated and analytic ratios of MSE to BMSE for QPSK, 16QAM, 64QAM, 256QAM, and 1024QAM.

Multistage Stepsize Function

The multistage VSS control function can be represented by

$$\mu_{ms}(B_k) = \sum_{s=1}^S \mu_s u(T_s - B_k) \quad (3.35)$$

where S is the number of total stages, μ_s is the stepsize at s th stage, T_s is its threshold value and $u(t)$ is the unit step function which satisfies $u(t) = 1$ if $t \geq 0$, else $u(t) = 0$. Conveniently, we set $T_S = 0$, and $\mu_s = \mu_{\max}$, the maximal acceptable stepsize.

The selections of the stepsizes and the corresponding thresholds should content with the conditions: the threshold at next stage must be a reachable value at the setting of the previous stepsize. Based on the analytical steady-state MSE formula in (3.26), we have that

$$T_{s+1} > K\mu_s + \sigma_n^2 \quad (3.36)$$

where σ_n^2 is the variance of the AWGN and

$$K = \left(\frac{1}{2} \frac{E\{|\psi(a)|^2\}}{E\{\Re[\psi'(a)]\}} \cdot \sigma_a^2 (\sigma_h^2 L_f + L_b) \right) \quad (3.37)$$

is a constant value, which depends on the DFE settings. However, when considering those effects: the noise due to AWGN and the decision error, the mismatch between BMSE and actual MSE, and the variation of the BMSE estimator, we should keep a achievable backup margin; for example, a possible selection of 50% backup margin yields that

$$T_{s+1} = 1.5K\mu_s + \sigma_n^2. \quad (3.38)$$

Proportional Stepsize Function

The proportional stepsize function is given by

$$\mu_l(B_k) = \mu_{\max} \min \{1, K_b B_k\} \quad (3.39)$$

where μ_{\max} is the maximal acceptable stepsize of the adaptive filter, K_b is a constant, which is the slope of the decayed stepsize function. To avoid the saturation effect, the suitable selection of the K_b should satisfy the condition that

$$\sigma_a^2(k) = \mu_l(B_k) \cdot K < \sigma_a^2(k-1). \quad (3.40)$$

Roughly replacing $\sigma_a^2(k)$ by B_k , we have that

$$K_b < \frac{1}{\mu_{\max} K}. \quad (3.41)$$

Actually, we can treat the proportional function as a special case of the multistage function with infinite stages.

3.3.3 Hybrid Algorithm: Combination of Blind and DD-LMS

To facilitate soft switching between blind equalization and DD-LMS operation, we consider the soft-combined error function

$$\psi(y_k) = \mu_b(k)\psi_b(y_k) + \mu_d(k)\psi_d(y_k), \quad (3.42)$$

where $\psi_b(y_k)$ is the error function associated with the blind algorithm, $\psi_d(y_k) = \hat{a}_k - y_k$ is the error function associated with the DD-LMS algorithm, \hat{a}_k is the decision of y_k , and $\mu_b(k)$ and $\mu_d(k)$ provide the relative weighting between the blind part and the DD-LMS part of the adaptation at time k . The step size μ in the stochastic gradient algorithm herein becomes a redundant since it can be represented in the hybrid error function.

Note that the above only modifies the error function without changing the fundamental adaptive filter structure. Hence it is of low complexity if the stepsize functions of $\mu_b(k)$ and $\mu_d(k)$ are also implemented in simple manner. On the selection of the blind part stepsize function, we adopt the linear decayed function since it is simpler than the multistage approach and easy to determine the single parameter K_b . Therefore, we have that $\mu_b(k) = \mu_l(B_k)$.

Anti-proportional Stepsize Function

Now, we present the selection of the blind part stepsize function. To provide a propoert of the similar fade-out of the blind part and fade-in of the DD-LMS part, we can straightforwardly adopt the ‘‘complementary’’ function of the linear decayed function in (3.39), which is a linearly increased function given by

$$\mu_d(k) = \mu_{d,\max} \max\{0, 1 - K_d B_k\}, \quad (3.43)$$

in which K_d is the control parameter similar to K_b and $\mu_{d,\max}$ is the maximal stepsize in the tracking mode. Herein, to prevent the ambiguity of the notation, we redefine μ_{\max} in μ_b as $\mu_{b,\max}$

‘‘Stop-And-Go’’ Stepsize Function

The ‘‘stop-and-go’’ (SAG) stepsize function comes from the CCA proposed in [12] that the DD-LMS is turned on if the current decision is reliable.

The CCA adopts two adaptive filters to maintain update of the filter coefficient in the blind acquisition and the DD-LMS tracking. At each iteration, the blind adaptation works before the DD-LMS part. After the adaptation in blind mode, the equalizer with the same input samples and newest updated coefficients derives the so-called perturbed output. The DD-LMS

adaptation is a conditional update that executes only if the decision values of the equalizer output and the perturbed equalizer output are the same.

The main drawback of the CCA is the price of the twice complexity in the adaptive filters. For CCA, the reason why the two adaptations can not execute in one-shot per iteration is because of the requirement of the perturbed output in DD-LMS adaptation. Actually, it is possible to use only one adaptive filter. With simple derivation, we have that

$$\begin{aligned}\tilde{y}_k &= \langle \underline{w}_k - \mu_b \psi_b(y_k) \underline{x}_k, \underline{x}_k \rangle \\ &= y_k - \mu_b \psi(y_k) \|\underline{x}_k\|^2;\end{aligned}\quad (3.44)$$

therefore, we can directly derive the perturbed output via the error function $\psi_b(y_k)$. Besides, a furthermore simplification can be achieved by replacing $\|\underline{x}_k\|^2$ with its expectation value $E\|x\|^2 = \sigma_a^2(\sigma_h^2 L_f + L_b)$.

From the description above, we use the same concept of the conditional update in the DD-LMS part and yields the SAG stepsize function as given by

$$\mu_d(k) = \mu_{d,\max} \delta(\hat{a}_k - \tilde{a}_k) \quad (3.45)$$

where \tilde{a}_k is the decision of $\tilde{y}_k = y_k - \mu_b C \psi_b(y_k)$ and $\delta(x)$ is the discrete delta function. The C here may not be restricted as $\sigma_a^2(\sigma_h^2 L_f + L_b)$, but can be a control parameter of the design.

3.3.4 Simulation Studies

Comparisons of Proposed Algorithms

We adopt the 256QAM system over the fixed two-paths channel with 33 dB input SNR, which path gains are 1 and $0.6i$ and path delays are 0 and 20 samples. There are 16 taps FFF and 32 taps FBF both operated at symbol spacing in the DFE design. We compare five kinds of the adaptive algorithm, which include the conventional MMA, the MMA based multistage VSS (MS-VSS), the MMA based continuous VSS (denoted as ‘‘VSS’’), the MMA based hybrid VSS with anti-proportional function of the DD part (denoted as ‘‘HVSS’’), and hybrid VSS with SAG function of the DD part (denoted as ‘‘HVSS-SAG’’).

The parameters of the algorithms are given as follows: $\mu = 2.5e^{-4}$ for the pure adaptive, $\beta = 0.025$ for the BMSE estimator, $\mu_{\max} = \mu_{b,\max} = \mu_{d,\max} = 2 \times 10^{-3}$ for the VSS, HVSS and HVSS-SAG, $K = K_b = K_d = 15$ for the VSS, HVSS and HVSS-SAG, $C = (L_f + L_b)$ for the HVSS-SAG. There are four stages used in the MS-VSS with stepsizes = $2e^{-3}$, $2e^{-4}$, $2e^{-5}$, and $2e^{-6}$ and the corresponding thresholds = 0.0181, 0.023, 0.007, 0 which are following the formula in (3.38).

Fig.3.5 illustrates the comparisons of simulation results in terms of the decision point SNR. The convergence of the pure MMA algorithm is extremely slower than other ones and even though the steady-state SNR is poor than others. The VSS based algorithms (including the VSS and MS-VSS) provide good convergence speed, but it is difficult to reach the good steady-state SNR. The HVSS and the HVSS-SAG both achieve the best steady-state SNR in a very fast convergence speed. The best convergence time is roughly 16000 iterations when the HVSS algorithm is used in this case.

Now we consider a realistic channel model, the ‘‘SPIB chan10,’’ an outdoor channel model whose parameters are available at <http://spib.rice.edu/spib/microwave.html>. We also consider 256-QAM signaling with normalized symbol energy. The input SNR to the equalizer is 36 dB. We employ a DFE with $T/2$ -spaced FFF of length $N_f = 5 \times 2$ and T -spaced FBF of length $N_b = 10$. The highest reachable equalizer output SNR is about 30 dB under MMSE DFE with these parameters.

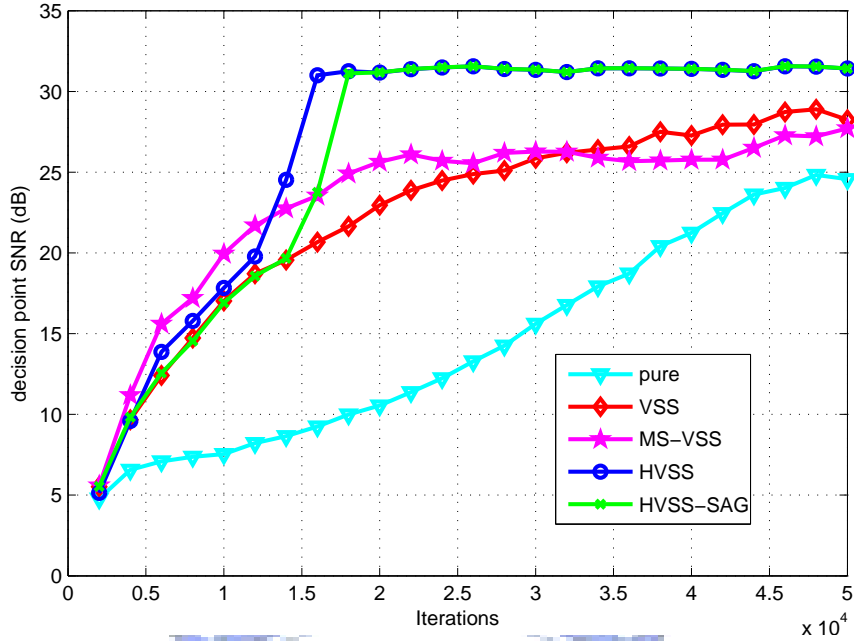


Figure 3.5: Comparisons of the proposed blind adaptive algorithms which include the pure blind, the VSS MMA, the MS-VSS MMA, the HVSS MMA and the HVSS-SGA MMA.

Comparisons with Other Algorithms

We consider both the CMA class and the MMA class of algorithms and their SNR convergence results are shown in Figs. 3.6 and 3.7, respectively. For CMA, the adaptation algorithms simulated are the hybrid VSS CMA (H-VSS CMA), the concurrent CMA (CC-CMA) [12], the M-CMA [30], and the DDCF M-CMA [30]. For MMA, we carry out a similar simulation with CC-CMA modified to use the MMA algorithm in place of CMA (thus named CC-MMA), M-CMA modified to M-MMA, and DDCF M-CMA modified to DDCF M-MMA, all compared with our hybrid VSS MMA (H-VSS MMA). Recall that the complexity of the M-CMA and M-MMA algorithms are similar to that of H-VSS CMA and H-VSS MMA, respectively. The concurrent algorithms have about twice the complexity, and the DDCF algorithms have about five to six times the complexity.

The cosine square function is used in the CME parts of the modified algorithms (DDCF M-CMA, DDCF M-MMA, M-CMA and M-MMA). The blind part of the concurrent algorithms and of the modified algorithms are turned off after the MSE reaches 0.0045 to reduce the adaptation noise, where the threshold is as suggested in [12]. Other parameters of these algorithms are determined by trial and error from simulations to provide the fastest convergence speed and yield a steady-state SNR of approximately 30 dB. The parameters for the CMA algorithms are as follows: for H-VSS CMA, $\mu_{bmax} = \mu_{dmax} = 10^{-2}$, $K_b = K_d = 5$, and $\beta = 0.975$; for CC-CMA, blind step size $\mu_b = 10^{-3}$ and DD step size $\mu_d = 10^{-2}$; for M-CMA, $\mu = 10^{-3}$ and $\beta = 2 \times 10^{-2}$; and for DDCF M-CMA, $\mu = 10^{-2}$, $\beta = 2 \times 10^{-3}$, and $\gamma = 10^{-3}$. The parameters for the MMA algorithms are as follows: for H-VSS MMA, $\mu_{bmax} = 2 \times 10^{-2}$, $\mu_{dmax} = 10^{-2}$, $K_b = K_d = 5$, and $\beta = 0.975$; for CC-MMA, $\mu_b = 1.5 \times 10^{-3}$ and $\mu_d = 10^{-2}$; for M-MMA, $\mu = 2 \times 10^{-3}$ and $\beta = 10^{-2}$; and for DDCF M-MMA, $\mu = 2 \times 10^{-2}$, $\beta = 10^{-3}$, and $\gamma = 10^{-3}$. (The parameters for the modified algorithms are quite different from those given in [30], because we have used QAM with $E_s = 1$.)

The figures show that the H-VSS CMA and the H-VSS MMA are the fastest algorithms in their respective classes. They converge about equally fast for this channel. As a group, the MMA class of algorithms converge faster than the CMA in this case.

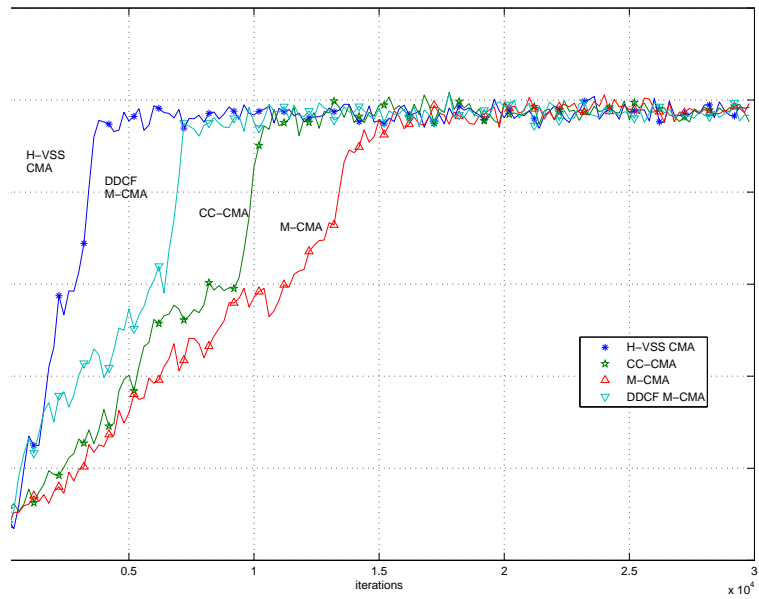


Figure 3.6: Output SNR of H-VSS CMA(*), CC-CMA(*), M-CMA(Δ) and DDCF M-CMA(∇) under 256-QAM in the SPIB chan10.

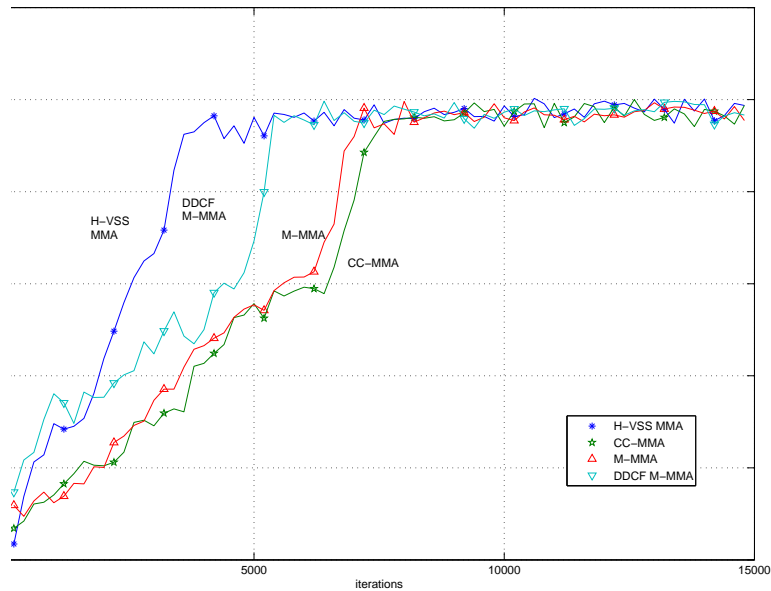
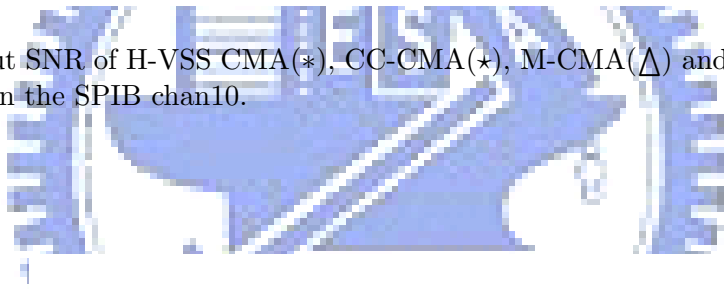
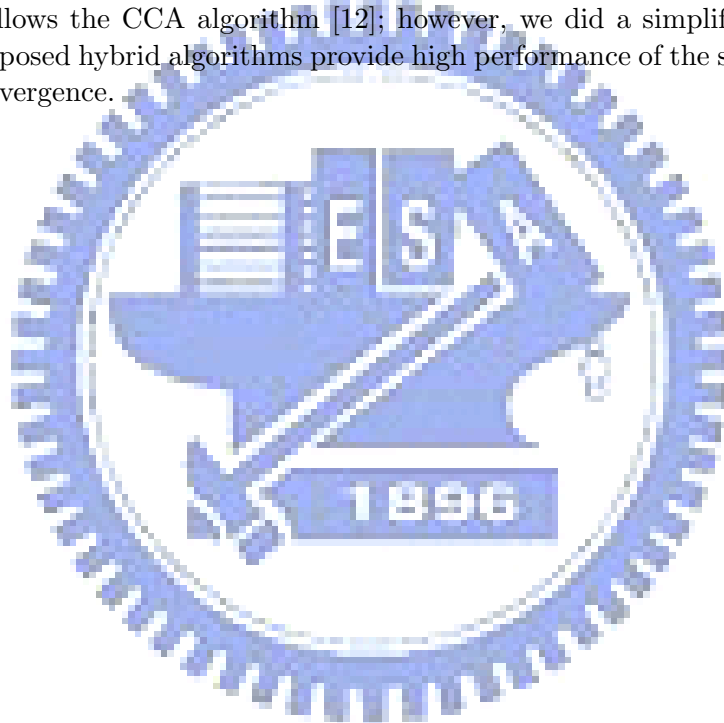


Figure 3.7: Output SNR of H-VSS MMA(*), CC-MMA(*), M-MMA(Δ) and DDCF M-MMA(∇) under 256-QAM in the SPIB chan10.

3.4 Conclusions

This chapter introduced the blind adaptive decision feedback equalizer for the cable application. The key factors in the design are the selection of the blind algorithm and the choice of the stepsize. We mainly focus on the choice of the stepsize that exists the compromise between the convergence speed and the steady-state MSE. To enhance the convergence speed without loss of the steady-state performance, we adopted the VSS approach and proposed a BMSE metric for the convergence measurement. We then proposed two kinds of the VSS algorithms.

Another issue of the DFE startup is the switching point from the blind adaptation to DD-LMS. Instead of the conventional hard switching, we considered the soft switching process, which smoothly translates the operation mode from blind startup to tracking. For this, we proposed the hybrid adaptive algorithm based on the VSS approach, which is the directly combination of the blind error function and DD error. We also present two kinds of the stepsize function in the DD part. One adopted the complementary behavior of the blind stepsize function; the other adopted the stop-and-go concept that the DD part works only if the current decision is reliable. The reliability follows the CCA algorithm [12]; however, we did a simplification. Simulations show that the proposed hybrid algorithms provide high performance of the steady-state behavior in a very fast convergence.



Chapter 4

Jointly Operation of Carrier Synchronization and Blind Adaptive DFE

So far, we introduce individually the CFO synchronization and the blind adaptive equalizer. However, it is necessary to consider the joint operation of the synchronization and the equalization. There are two types of the joint CRL and DFE design as illustrated in Fig. 4.1. It can be classified as the post-FFF CRL and the pre-FFF CRL designs according to the placement of the CRL. This chapter gives several procedures to deal with the joint operation. We first present two procedures existed in typical receiver design; then, we present a new approach adopting the phase irrelevant convergence property of the CMA.

4.1 Conventional Procedure

4.1.1 Multi-stage Procedure

The first startup procedure considers the individual training periods for each modules. The process is given as follows:

1. Start linear equalizer (LE) with CMA algorithm. The purpose of the blind LE startup is to equalize the channel and reduce the ISI effect of the received signals coarsely, since the

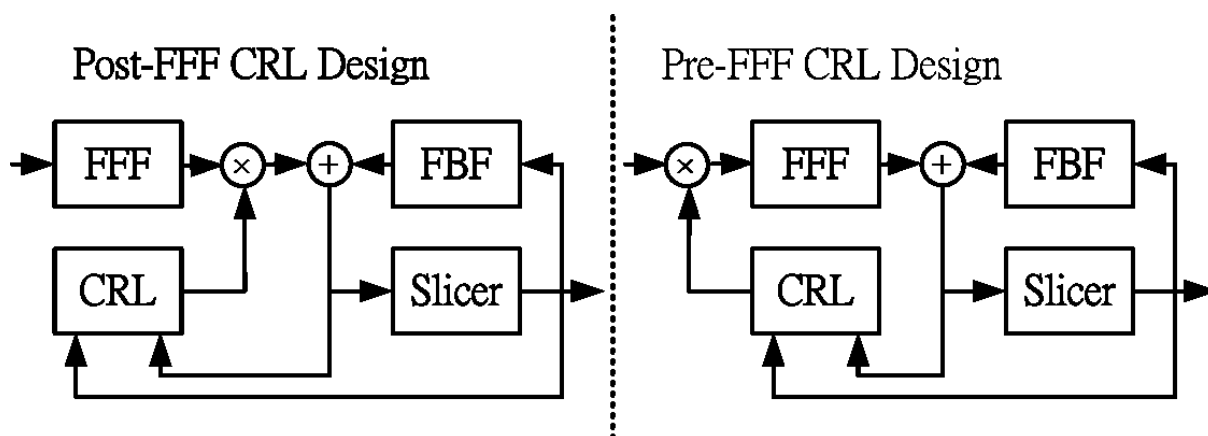


Figure 4.1: The structure of the joint CRL and DFE, which can be classified as left part: the post-FFF CRL design and right part: the pre-FFF CRL design

ISI would affect acutely the performance of the carrier frequency estimation and synchronization. The CMA is only the candidate of the blind algorithm since it has the property of the phase irrelevant convergence, which the phase rotation would interfere the convergence of the CMA. The MMA can not work in this scenario.

2. Start CFO synchronization after convergence of LE, and/or keep on the blind LE. After the coarse ISI reduction, the carrier synchronizer turns on to acquire the CFO and combat the CFO effect. Either the open loop SFE or the close loop CRL can be used to estimate the CFO. However, if the SFE is used in prior, we still need a close loop CRL to track the phase and its variation due to the residual CFO. The adaptive filter in this period can still keep on for the stabilization of the equalizer; however, it also can be turned off if the channel is quasi-static.
3. Keep on CFO synchronizer and start blind DFE after the lock of the CRL. When the CRL is locked, the CFO is tracked; thus, we train the DFE coefficient using the blind adaptive filter. Herein, the blind algorithm can be either the CMA or the MMA.
4. Switch to DD-LMS tracking when the equalizer is converged. Finally, to derive minimal steady-state MSE, the adaptive filter switches to the LMS operation.

To guarantee the convergence in each stage, we may set a long training period for each stage; however, this consumes the training time. If we want to shorten the training periods, we should involve the convergence indicators. For example, in the CRL training stage, we use the lock indication as mentioned in [58] or its modification. In the blind DFE training stage, the BMSE can be the convergence indication. However, for the convergence of LE with blind CMA, one way is to observe the convergence of the tap weights. However, it is just a conception.

The advantage of this approach is the independence of the convergence of each module, but it pays the price of the long training time, since the first LE stage is used only for the environment of the CRL convergence and we retrain the DFE when the CRL is stabilized.

4.1.2 Multi-module Co-training

One way to shorten the waiting time is directly to co-train the multiple modules. We can immediately turn on both the CRL and the adaptive DFE. In this case, the CRL first should adopt the PD that has the blind component, since the pure DDPD has poor convergence property in large ISI environments. Besides, to shorten the convergence time and to provide the stabilization, the concept of multiple stages with different parameters is applied that the coarse parameters are used in prior to fast converge and the fine parameters used later to reduce the excess MSE due to the adaptations. From our experience, it can be converged in the conventional cable environment. However, there are no strong supports to guarantee the convergences.

4.2 Approach based on Phase Irrelevant DFE

The conventional multistage procedure takes first LE stage for the purpose to create a roughly ISI-eliminated environment for CFO synchronization, which is just the intermediary stage. If we can directly train the DFE coefficient in the CFO environment, the intermediary stage can be omitted. That is we first startup the DFE training before the CFO synchronization, and then synchronizes the CFO after the DFE convergence, which can provide a better ISI-eliminated environment. What we need is the DFE training over the CFO environment. For this, we suggest the phase irrelevant DFE by modifying the tentative decision module in the DFE and using the CMA to train the DFE blindly.

4.2.1 Phase Irrelevant DFE (π DFE)

The phase rotation causes critical decision errors and makes the DFE unable to get convergence. To prevent this decision error, we may directly remove the decision circuit in the feedback loop, and this yields the infinite impulse response (IIR) equalizer. In addition to the stability issue of the IIR filter, the major drawback is the significant noise propagation in feedback loop. Therefore, removing the decision circuit is harmful in the DFE structure since it causes massive noise in feedback path.

On the other way, we may consider the functionality of the phase irrelevant decision (π D), which the decision is independent with the phase rotation. Equivalently, we consider jointly the phase estimation and the symbol decision for the equalizer output. Let $y = re^{j\theta} + n$ be the equalizer output with the phase rotation. When additive noise is complex Gaussian, the ML metric of the joint detection and estimation is given by

$$\{\hat{r}, \hat{\theta}\} = \arg \min_{\theta, r \in |a|} |y - re^{j\theta}|^2 \quad (4.1)$$

where a is the alphabet of the constellation. Algebraical derivation yields that

$$\hat{r} = \arg \min_{|a|} ||y| - |a||, \quad (4.2)$$

$$\hat{\theta} = \angle y, \quad (4.3)$$

and the π D

$$\hat{a} = \Pi(y) = \hat{r}e^{j\hat{\theta}}. \quad (4.4)$$

4.2.2 Startup Procedure Using π DFE

The startup procedure based on π DFE is given as follows.

1. Start π DFE training with CMA algorithm.
2. After the convergence of π DFE, start CFO estimation with SFE.
3. Translate the filter coefficients from frequency-offset version to normal version.
4. Start CRL to compensate phase offset and operate DFE in normal mode with the blind adaption.
5. Start DD-LMS/CRL tracking after stabilization of the CRL/DFE.

The procedure is similar to conventional one except for the stage 1 and stage 3. In stage 1, this is the particular feature of the proposed flow. The only one needed to be explained is the translation of the coefficients from the frequency-offset version to normal version.

Now we explain the translation with the example of the LE, which can be easily extended to the DFE case. Assume that the optimal LE output can be expressed as

$$y(n) = \sum_{k=0}^{K-1} w_k r(n-k), \quad (4.5)$$

where $\underline{w} = [w_0 w_1 \cdots w_{K-1}]$ is the optimal weight vector trained by the CMA algorithm.

If the received signal exists the CFO effect, we have that $r'(n) = e^{j\omega_o n} r(n)$ where ω_o is the residual CFO. The LE output in this condition is given by

$$y'(n) = \sum_{k=0}^{K-1} w'_k r'(n-k). \quad (4.6)$$

If the perfect equalization holds in this scenario, we have that $y'(n) = y(n)e^{j(\omega_0 n + \phi)}$. Therefore, we can obtain that

$$\sum_{k=0}^{K-1} w'_k r'(n-k) = e^{-j\phi} \sum_{k=0}^{K-1} (w_k e^{-j\omega_0 k}) r(n-k); \quad (4.7)$$

thus, to maintain the equivalence, we have that

$$w_k = w'_k e^{j\omega_0 k}, \quad (4.8)$$

which is the translation from the offset version into normal version. Besides, the additional constant rotation factor $e^{-j\phi}$ in the equation can be compensated by the CRL.

If the post-FFF CRL (as illustrated in left part of Fig. 4.1) is used, the FFF is always operated in offset version; therefore, we just need to translate the coefficients of the FBF after the normal operation of the DFE. However, if the pre-FFF CRL (as illustrated in right part of Fig. 4.1), we need to translate both the FFF and the FBF.

4.2.3 Radius BMSE for VSS Algorithm in π DFE

The (hybrid) VSS for the normal DFE shortens the startup time. We now adopt the same concept to speed up the convergence of the π DFE. To achieve this goal, we should redefine the convergence metric for the stepsize control, which is equivalent to the BMSE for the conventional DFE. Although BMSE can not work well when the constellation is rotated with time, its basic concept is still workable. It means that we can adopt the equalizer outputs that exceed the boundary of the radius of the constellation to estimate the instantaneous MSE.

The radius boundary MSE (RBMSE) is defined by

$$B_r = 2E \left[(|y| - r_{\max})^2 \mid |y| > r_{\max} \right] \quad (4.9)$$

where r_{\max} is the maximal radius of the constellation. When the noise variance is small and $|y| > r_{\max}$ happens iff $y = r_{\max} e^{j\theta}$, we have that

$$|y|_{|y| > r_{\max}} = r_{\max} + \Im \left\{ n e^{j\angle y} \right\}. \quad (4.10)$$

Therefore, we get

$$B_r \approx 2E \left[\left(\Im \left\{ n e^{j\angle y} \right\} \right)^2 \right] = \sigma_n^2 \quad (4.11)$$

where σ_n^2 is the variance of the noise.

To estimate the RBMSE, we still use the exponential average as in BMSE estimator. Although the RBMSE can represent the instantaneous MSE, its accuracy is still not good enough due to long updating period for the RBMSE.

4.2.4 Simulation Studies

We give an example of the proposed design. Consider a 64QAM over two-path static channel, which discrete response is given by $h(n) = \delta(n) + 0.7e^{-j\pi/4}\delta(n-10)$. The input SNR is 33 dB. The post-FFF structured joint CRL and DFE is adopted with 32-tap FFF and 32-tap FBF operated in symbol space. We adopt 3-stage approach. At first stage, the π DFE is trained with the HVSS CMA algorithm; then, when the B_r reaches the threshold, the SFE with multi-resolution algorithm works to estimate the CFO. In the CFO estimation stage, the adaptive keeps on training the DFE. Final, both the CRL and normal DFE work after the estimation of the CFO and the translation of the FBF coefficients.

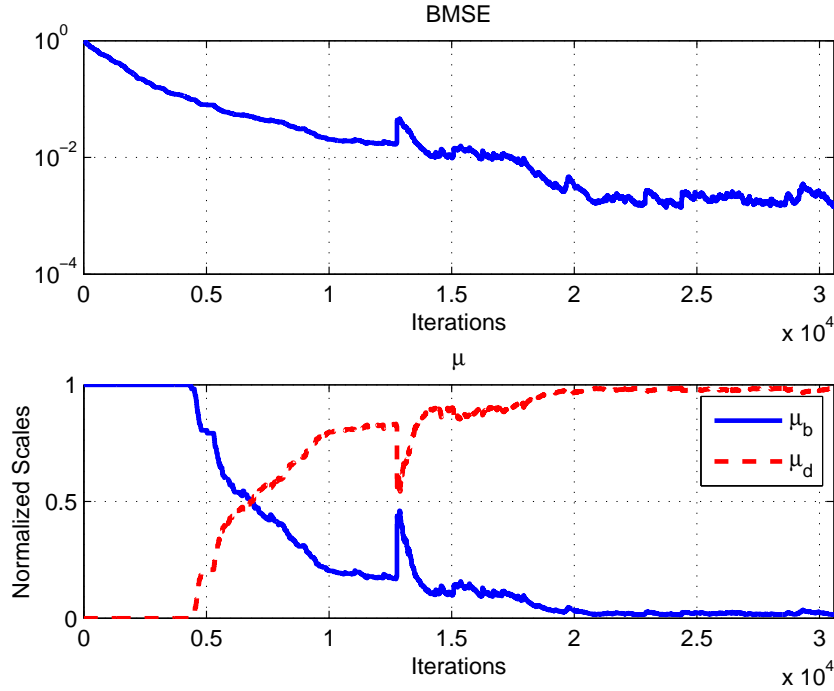


Figure 4.2: Top: (R)BMSE estimation trajectory; bottom: μ_b and μ_d normalized to $\mu_{b,\max}$ and $\mu_{d,\max}$ correspondingly

The detail parameters are given by $\mu_{b,\max} = \mu_{d,\max} = 2^{-9}$, $K_b = K_d = 10$ for HVSS DFE; $K_i = 2.5 \times 10^{-5}$, $K_p = 7.1 \times 10^{-3}$ for the loop filter of the CRL; $K = [1 \ 3 \ 9 \ 30]$ -th delay correlations, 4096 average samples for the multi-resolution algorithm; the switching threshold of the BMSE value (from stage 1 to stage 2) = 0.03. The conventional DDPD is used only in the CRL.

Figs. 4.2, 4.3 and 4.4 illustrate the convergence behaviors of the design example. Fig. 4.2 shows the estimation trajectory of the (R)BMSE and the dynamic variations of μ_b and μ_d . As shown, the (R)BMSE reaches the switching threshold roughly after 8500 iterations and approaches the steady state in additional 7800 iterations when the operation begins the 3rd stage. The BMSE happens the sudden jump from the operation switch of the π DFE to normal DFE. The μ_d variation is similar to the (R)BMSE trajectory, whereas the μ_b variation is complementary to the (R)BMSE trajectory. Fig. 4.3 demonstrates the estimation of the CFO. The actual CFO in this simulation is set to 0.11 baud rate. It shows that the estimation from CRL meets the actual CFO roughly at 12700 iterations which is the transition from stage 2 to stage 3. Fig. 4.4 shows the snapshots of the constellations of the DFE inputs (at left-top part), the DFE outputs in starting stage (at right-top), the DFE outputs in stage 2 (at left-bottom), and the DFE outputs in final stage (at right-bottom). The simulation shows the fast convergence of the proposed flow since it only takes overall 20500 iterations to achieve the steady-state tracking mode.

4.3 Conclusions

This section proposed the startup procedure of the joint CRL and DFE design. We first introduce two conventional approaches. Then, to improve the convergence speed, we suggest a new approach based on the proposed π DFE with HVSS CMA algorithm. In addition, to achieve the HVSS algorithm in phase rotated environment, we investigate the RBMSE metric to represent

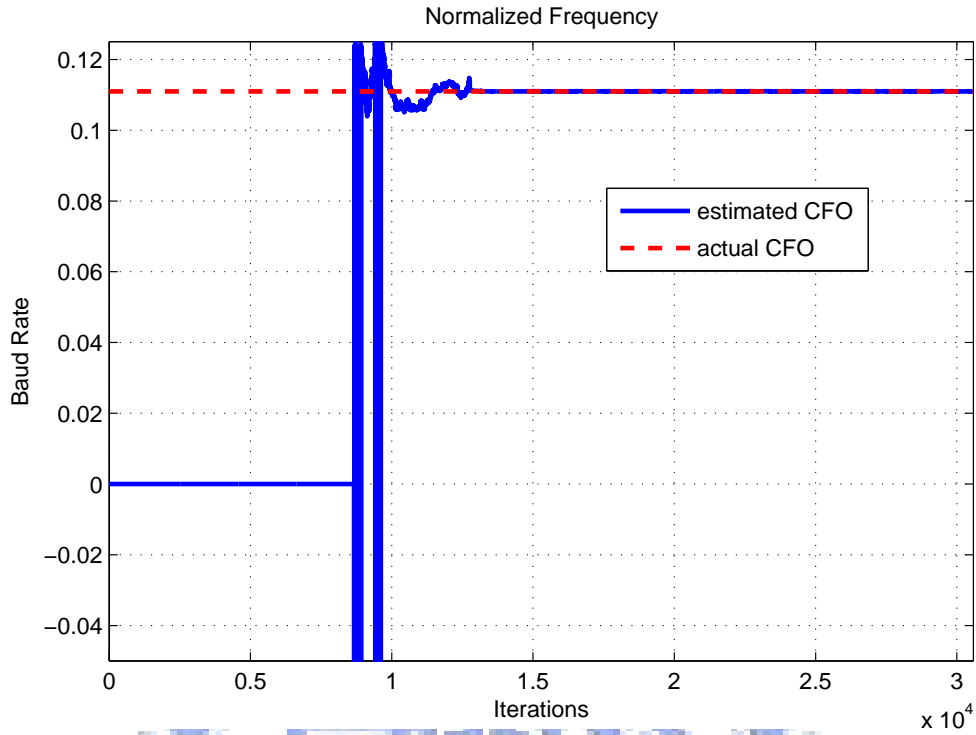


Figure 4.3: Estimation of the CFO.

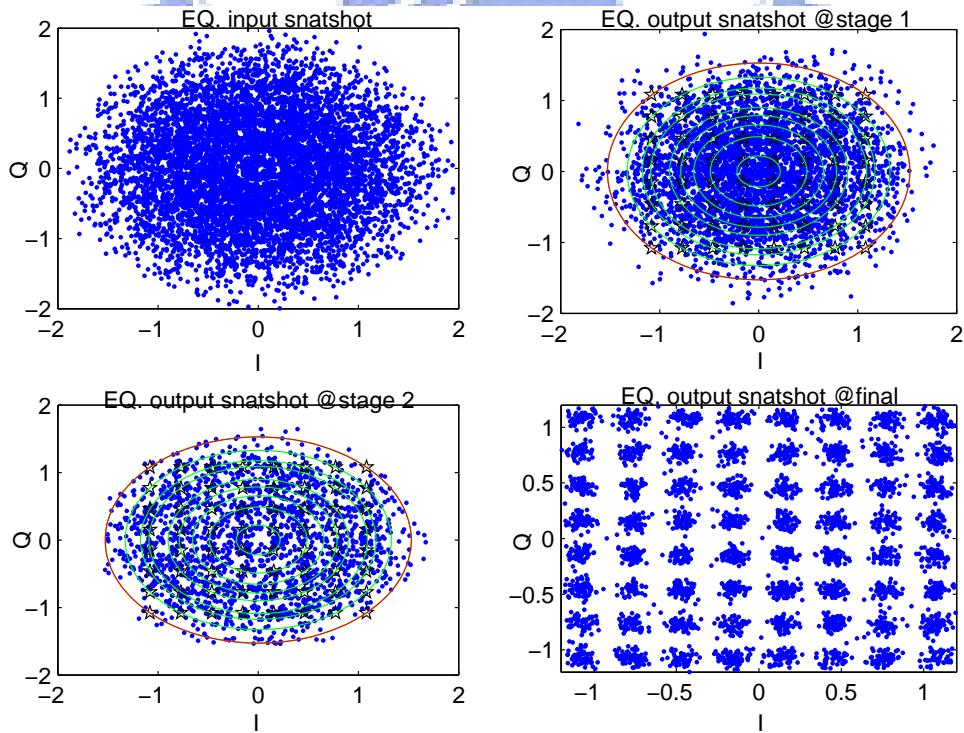


Figure 4.4: Snapshots of the constellations, left-top: DFE inputs; right-top: DFE outputs at first stage; left-bottom: DFE outputs at 2nd stage; right-bottom: DFE outputs at final stage.

the convergence of the DFE. The SFE with multi-resolution algorithm is used to directly estimate the CFO in an open-loop manner. The CRL with DDPD is finally used to lock the phase offset of the equalizer.



Part II

Receiver Design in OFDM/OMDMA System over Wireless Channels



Two major issues are considered in multi-carrier OFDM receiver. One is the synchronization and the other is the channel estimation. The synchronization issue includes the mismatch compensation and the unknown parameter estimation at the receiver. The mismatch compensation in OFDM system requires the synchronization of the carrier frequency offset and the sampling frequency offset, and the symbol time estimation. The unknown parameter estimation in OFDM includes the CP ratio detection, the bandwidth estimation and the cellular identification in cellular system. In recent OFDM system, the pilot-aided channel estimation is major considered. Two-step approach is common used in pilot-aided OFDM. First step estimates channel frequency response(CFR) at pilot subcarriers using least-square manner ; then, second step estimates CFR at data subcarriers using the interpolations with the estimated CFR at pilots.

In this part, we study the OFDM synchronization problems of WiMAX system [48, 98] in the estimation of the carrier frequency offset and the symbol time, and the identification of the Cell-ID. The CP-correlation based estimator [64] is used to jointly estimate fractional part CFO and the symbol time. The integral CFO estimation is required when the CP-correlation based estimator is used. For this, some integral CFO estimation schemes using one OFDM training symbol are proposed in [33, 53] according to coherence bandwidth concept. However, there are limited theoretical explanations. We consider the joint detection of the Cell-ID and integral CFO in WiMAX system. By treating the integral-offset preamble as another Cell-ID, the problem of joint detection is formulated as the matching of the candidate sequence with the received signal over multipath channel. We derive the maximal likelihood detection criterion. With furthermore simplification of the detection, we propose the general concept in the frequency domain filtering, which can explain the differential detection scheme presented in [53]. In addition, we also propose several furthermore simplified detectors based on the frequency domain filtering. The performance analyses of the proposed algorithms are also studied.

Pilot-aided channel estimation methods can be classified roughly into three types: channel model-based, channel statistics-dependent, and channel statistics-independent. The model-based methods try to identify the channel path delays, which define the so-called “delay subspace.” The channel can then be estimated (in a least-square manner) via projection onto the subspace, which also eliminates the noise outside the subspace. A main concern with this approach consists in the complexity and robustness of delay subspace estimation [103, 78, 91, 101], especially when the channel delays are not sample-spaced. For the channel statistics-dependent methods, the most common approach is Wiener or linear minimum mean-square (LMMSE) filtering [18, 61, 72, 19]. The filtering may be one-dimensional (along the frequency dimension only) [18] or two-dimensional (along both the frequency and the time dimensions) [61]. Approximations and computational techniques can be used to reduce the high computational complexity in some situations [72, 19]. However, Wiener filtering requires knowledge of channel correlation function and noise variance, which raises problems not only in the complexity of their estimation but also in the impact of the estimation accuracy on channel estimation performance. A suboptimal solution is to use a predefined shape of correlation function in place of real-time estimates. The predefined shape is usually that associated with a uniform or a negative exponential power-delay profile [18, 3]. The channel statistics-independent methods use interpolation to reconstruct the channel responses at the data subcarriers based on the initial channel estimates at pilot subcarriers. The simplest of these methods is low-order polynomial interpolation in the frequency domain [32]. The maximum-likelihood interpolator of [72], by its channel-independent nature, can also be categorized into this class, but it is substantially more complicated.

In this thesis, we study two channel estimation algorithms using the polynomial interpolation and the approximate LMMSE estimation for the comb-type pilot-aided OFDM and the WiMAX. For the polynomial interpolation, we study the performance in large delay spread environment and present a window shift concept to minimize the interpolation MSE in such environments. The key contributions are the derivation and the estimation of the optimal window shift. In the

approximate LMMSE CE, the mean delay and the root-mean-square delay spread are required. We propose simple estimators of the mean delay and RMS delay spread in frequency domain and study the performances of the estimators. The application of the delay estimators in approximate LMMSE CE and its performance analysis are also presented.



Chapter 5

Introduction to Receiver Design in WiMAX System

This part presents the receiver design in orthogonal frequency division multiplexing (OFDM) system. OFDM modulation scheme is widely adopted in current transmission system since its orthogonal property in frequency makes it easy to combat the multipath distortion with the single tap equalizer. To maintain the orthogonality after the multipath channel, the modulation scheme inserts a cyclic prefix (CP) in the front of the symbol as a guard interval, which is a copy of the symbol tail. The duration of the guard interval (as well as the CP length) should be larger than the expected maximal channel delay spread for the avoidance of the inter-block interference (IBI) that the prior OFDM symbol interferes with the current one.

Orthogonal frequency division multiple access (OFDMA) is a kind of the OFDM application, which supports multiuser communications within an OFDM symbol. Currently, a well-discussed example of the OFDMA system is the specification of IEEE 802.16e OFDMA [48], which is also called the Worldwide Interoperability for Microwave Access (WiMAX) system. In this part, we take the WiMAX OFDMA receiver as the examples, and introduce several synchronization and channel estimation algorithms in OFDM receiver and their applications in WiMAX. We first introduce the frame structure and the subchannel organization of the WiMAX OFDMA system and the signal processing functions in OFDMA receiver in this chapter. After the introduction, we present the issues in the synchronization and the channel estimation in the following chapters.

5.1 Frame Structure and Types of Subchannel Organization

The WiMAX OFDMA PHY defines four selectable FFT sizes: 2048, 1024, 512 and 128. The subcarriers are divided into three types: null (guard bands and DC), pilot, and data. The data subcarriers are organized into subchannels, which form the basic units of allocation for user data transmission. A data stream can be borne over one or more subchannels depending on its rate. The spec [48] defines three basic types of subchannel organization including partial usage of subchannels (PUSC), full usage of subchannels (FUSC), and adaptive modulation and coding (AMC); among them, the PUSC is mandatory and the other two are optional.

In PUSC DL, the entire channel bandwidth is divided into three segments, which are used separately for each directional sector. More details of the PUSC DL and UL are given in the next subsection. The FUSC is employed only in the DL and it uses the full set of available subcarriers to maximize the throughput. In both PUSC and FUSC, the subcarriers that constitute a subchannel are pseudo-randomly distributed to attain frequency diversity. In AMC, in contrast, the subchannels are formed using adjacent subcarriers. A key idea is that, if the transmitter does not know the channel response, then by distributing the transmitted data randomly over the subcarriers, it can maximize the frequency diversity. However, if the relative quality of

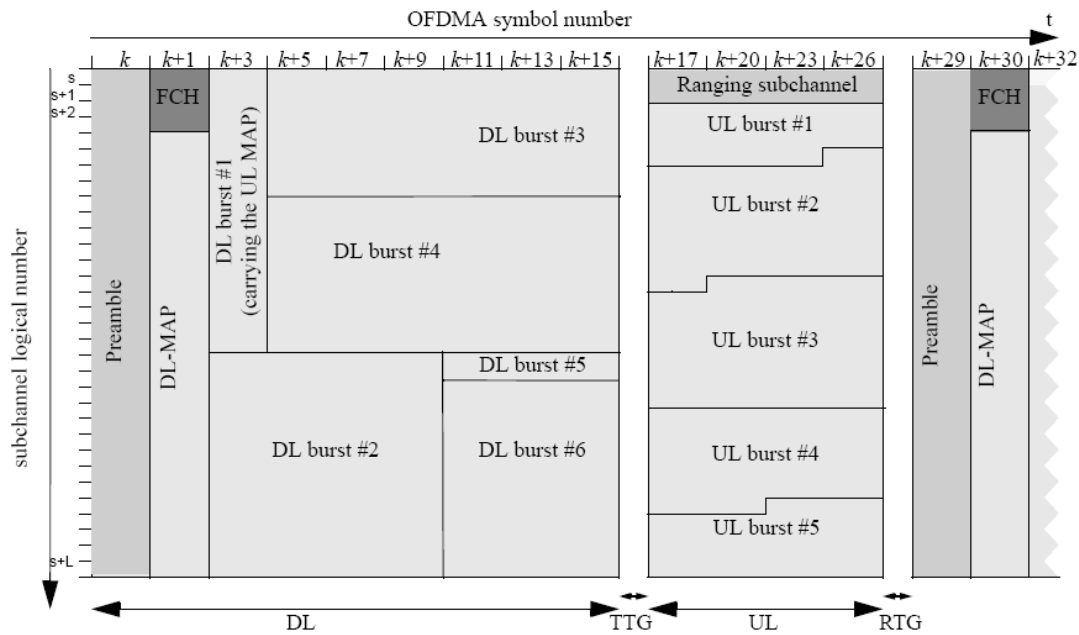


Figure 5.1: OFDMA TDD frame example, showing mandatory zone only [48, Fig. 218].

different subcarriers can be aware, then there lies the option of transmitting the data over the better subcarriers to maximize the efficiency. Now since the channel variation is typically smooth across subcarriers within the coherence bandwidth, it is natural to form subchannels using adjacent subcarriers.

In what follows, we concentrate on SISO transmission instead of MIMO transmission. In addition, we concentrate on the mandatory PUSC subchannel organization.

5.1.1 Subchannel Organization in PUSC

Fig. 5.1 illustrates the structure of a TDD frame containing only the mandatory PUSC zone. Excluding the preamble, the DL subframe consists of $2n$ OFDMA symbols and the UL subframe, $3m$, where n and m are some integers.

The DL subframe starts with a preamble, which is an OFDM symbol that can use one of three disjoint subcarrier sets. In each set, the indexes of the used subcarriers are given by $3k + n$ where $n \in \{0, 1, 2\}$ indicates the subcarrier set and k runs over a range of values excluding the guard bands and DC. The preamble subcarrier set is BPSK-modulated with one of a set of selectable PN (pseudo-noise) sequences. The number of selectable sequences is 114, which is used to indicate the local ID of the BS to the MSs. The power level of each modulated subcarrier is 9 dB above the normal average data

Following the preamble, the FCH, DL-MAP, and UL-MAP contain broadcast messages in PUSC mode that inform the MSs about how the subsequent DL and UL bursts are organized in time and in frequency, the associated coding and modulation schemes, and for which MS each burst is intended.

Except for the preamble, the subcarriers of both DL and UL are grouped into subchannels in a pseudo-random fashion. The brief permutation process is presented in our previous work [109, Chap. 3] and we omit it herein. However, need to be mentioned, the basic reception unit of the DL has a cluster structure as illustrated in Fig. 5.2, which carries 4 pilots and 24 data samples within a region of two successive OFDM symbols and 14 adjacent subcarriers; similarly, the unit of the UL is the tile shown in Fig. 5.3, which contains 4 pilots and 8 data samples in a region of three successive OFDM symbols and 4 adjacent subcarriers. In both DL and UL, the

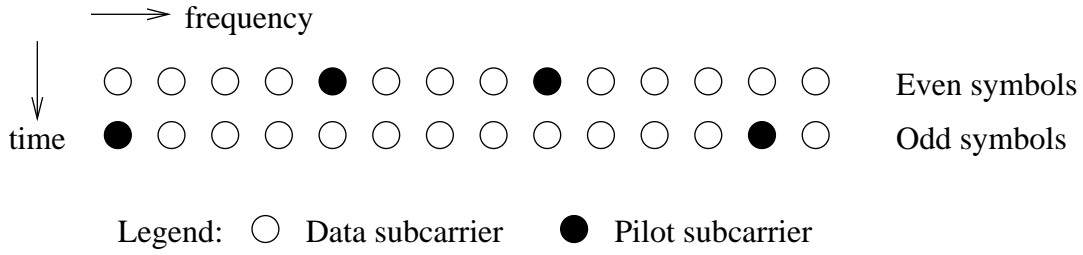


Figure 5.2: PUSC DL cluster structure.

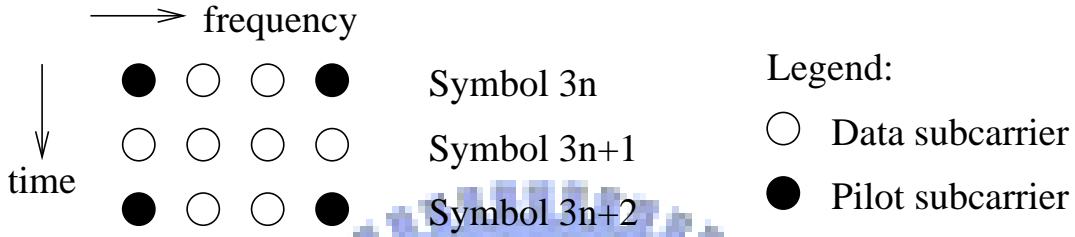


Figure 5.3: PUSC UL tile structure.

pilot subcarriers are BPSK-modulated with a pseudo-random binary sequence (PRBS). The DL pilot subcarrier power is 2.5 dB higher than the average data subcarrier power, whereas the UL pilot subcarrier power is the same as the average data subcarrier power.

5.2 Main Signal Processing Functions in OFDMA Receiver

Fig. 5.4 depicts a typical OFDMA baseband receiver structure. Among its functions, the synchronizer, the channel estimator, and the demodulator-decoder block are more complex in algorithm and play a major role in signal reception. The synchronizer estimates and compensates any offsets in carrier, sampling time, OFDMA symbol time, and frame time in the receiver in reference to the transmitter. The channel estimator acquires the channel response for use in data detection. And the demodulator-decoder block does the data detection.

In summary, the key tasks to be completed in the MS receiver in the DL subframe upon its initial entrance to the network are as follows:

1. Synchronization of the MS carrier and timing (including estimation and compensation of offsets), and identify the preamble index.
2. Channel estimation in the broadcast message part of the signal.
3. Decoding of the broadcast message to identify the locations of the allocated data bursts.
4. Channel estimation or tracking for the allocated DL burst locations.
5. Decoding of data received in the allocated DL burst locations.

The key tasks in UL data reception performed in the BS receiver during normal data transmission are:

1. Synchronization in carrier and timing for each MS.
2. Channel estimation for each MS, for the allocated UL burst locations only.
3. Decoding of data received from each MS in its allocated DL burst locations.

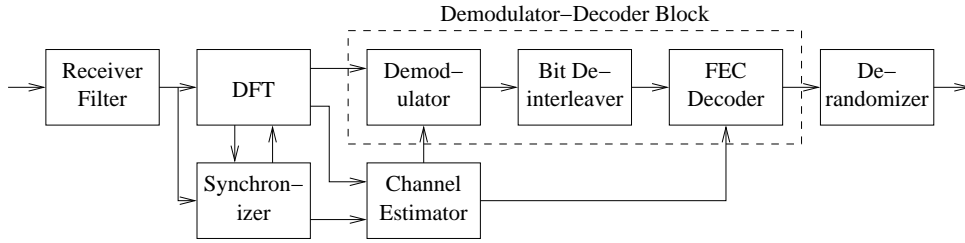


Figure 5.4: Typical OFDMA baseband receiver structure.

In the following sections, except for the demodulator-decoder block, which is briefly introduced in our previous work [109, Chap. 3], we discuss the initial synchronization and channel estimation respectively. For the synchronization, we mainly focus on the acquisition of the preamble ID and its joint operation with the integer CFO estimate. For the channel estimation, we propose two estimation schemes including the time shifted polynomial interpolator and the linear minimal mean-square error estimator with exponential delay profile approximation.



Chapter 6

Synchronization in WiMAX System

Synchronization in cellular system contains the cases in both DL and UL, which deals with the oscillator mismatch between the sender and the receiver, and acquires the parameters used in the communication. In DL, the oscillator mismatch results the carrier frequency offset (CFO) and the sampling frequency offset (SFO), which is the typical issue in the receiving process for all the system. In WiMAX OFDMA system, as conventional OFDM receiver, the synchronization needs to deal with CFO, SFO and the symbol time that points out the start position of the OFDM symbol. Additionally, the main parameter is the preamble index as well as the IDCell, which indicates the potential serving BS and the associated permutation scheme used in the downlink (DL) transmission burst.

The WiMAX is a point to multiple point (PMP) structure which one BS will serve several MSs. Thus, all MSs are forced to synchronize to the serving BS. Unlike synchronization in DL, the UL synchronization mainly concerns the transmission power, the propagation delay, and the residual CFO. The estimated parameters in BS side should be adjusted in MS side; therefore, the UL synchronization performs in a closed loop manner and the entire synchronization mechanism is called the ranging process. Besides the ranging process, the BS also need to estimate the symbol time of the received OFDM symbols in UL, which is the only parameter adjusted in BS.

In what follows, we only focus on the DL synchronization in the initial phase and mainly on the preamble search process. The normal phase of the DL synchronization is similar to the initial phase except that the preamble is available in normal phase. We first introduce the initial synchronization and present the commonly adopted scheme using the CP correlation for the estimation of the CFO and the symbol time. Then, we pay more attention to the preamble search techniques.

6.1 Initial Synchronization

As mentioned, in OFDMA DL, initial synchronization (at the MS) involves carrier recovery, timing recovery, and preamble index identification, where carrier recovery involves estimation and compensation of the carrier frequency offset (CFO) and timing recovery, in principle, should include estimation and compensation of the sampling frequency offset (SFO) and the OFDMA symbol time offset. The carrier phase offset may be considered part of the channel response and taken care of in channel estimation. The sampling time offset can also be absorbed into the channel response if the CP is long enough.

Now, note that the IEEE 802.16e OFDMA requires not only that the MS carrier frequency be synchronized to the BS to within 2% of subcarrier spacing, but also that the transmitted center frequency and the sampling frequency of the MS be derived from one reference oscillator. When these are true, the sampling phase difference from the beginning of an OFDMA symbol to the end of it will only differ by at most $2\% \times (1 + 1/4)$ of the true sample period, where the

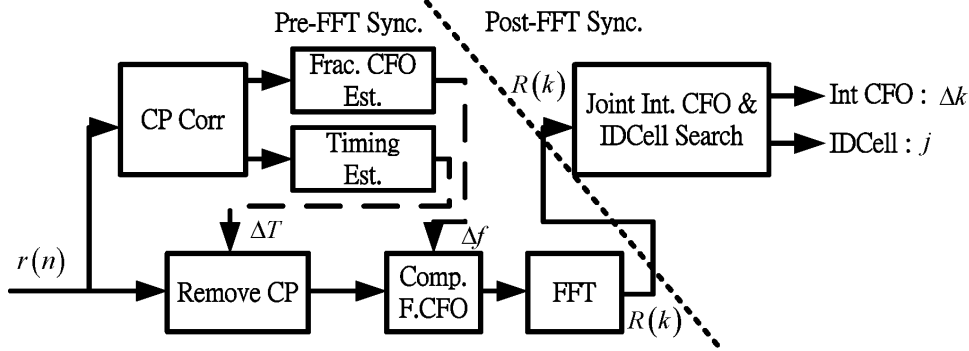


Figure 6.1: Two stage synchronization structure includes pre-FFT synchronization to acquire the fractional CFO and symbol time and post-FFT synchronization to estimate the integral CFO and the preamble index.

factor 1/4 accounts for the largest allowed CP time ratio. Therefore, it appears unnecessary to perform separate SFO recovery in either the MS or the BS if the CFO can be accurately recovered. In addition, this certainly would be the case after the startup period. What remain to be synchronized, besides preamble index identification in the DL, are therefore the CFO and the OFDMA symbol timing.

In abstraction, the initial synchronization scheme has a two-stage approach as illustrated in Fig.6.1. First stage performs in time domain before the discrete Fourier transform (DFT), which is called the pre-FFT synchronization. Then, the second works in frequency domain after the FFT; thus it is attributed as the post-FFT synchronization. The pre-FFT synchronization adopts the widely used cyclic prefixing correlation scheme [5, 64] to estimate the symbol timing and the CFO. However, the CP correlation can only appear the fractional subcarrier spacing of the CFO, so we need additional to deal with the integer part. Therefore, besides the preamble index search, the post-FFT synchronization also takes care with the integer CFO. In following subsection, we first introduce the blind CP correlation scheme in pre-FFT synchronization and then, present the post-FFT synchronization that is a joint operation of the preamble search and the integer CFO estimation in next section.

6.1.1 Pre-FFT Synchronization Using CP Correlation

There are several approaches for the CFO estimation in OFDM system. One is the data-aided approach [88, 73], applicable when the preamble consists of known signal (or when a reliable decision on the preamble contents can be made). In the case of IEEE 802.16e OFDMA, it is not suitable because in DL, the preamble can be one of 114 choices. The second approach is based on subspace analysis, e.g., via the ESPRIT algorithm. While the resolution in CFO estimation of these methods can be high, the computational complexity can also be high. The third approach is completely blind estimation relying solely on the repetitive signal structure of OFDMA symbols, e.g., the presence of CP [5, 64]. This appears simplest and suitable for use in IEEE 802.16e OFDMA.

Likewise, there are multiple approaches to symbol timing estimation. However, again, one simplest and appropriate for IEEE 802.16e OFDMA is blind estimation based on the CP structure. Indeed, the DL preamble in IEEE 802.16e OFDMA, by having its nonzero subcarriers spaced regularly in the frequency domain, gives rise to a quasi-periodic signal structure in the time domain. This quasi-periodicity may also be exploited for the benefit of CFO and symbol timing estimation. However, the following discussion considers use of CP only.

Fig. 6.2 illustrates the method. Let N be the FFT size and L be the CP length in number of samples. Under the assumption that the received samples are jointly Gaussian, quasi-maximum-

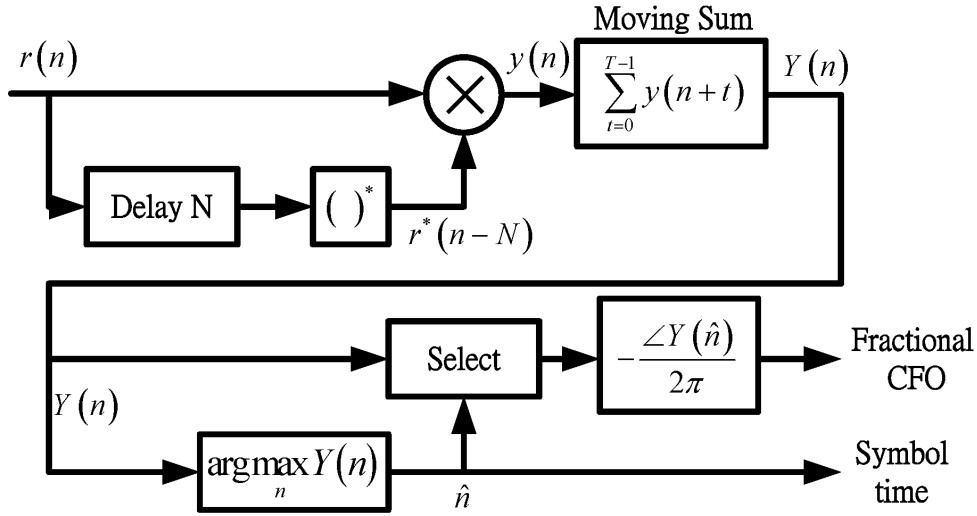


Figure 6.2: Pre-FFT synchronization use blind CP correlation to estimate CFO and symbol time.

likelihood (ML) estimators in Rayleigh fading for symbol timing and CFO have been derived as [64]

$$\hat{n} = \arg \max_n \{|Y(n)|\} \quad (6.1)$$

and

$$\hat{\varepsilon} = -\frac{\angle Y(\hat{n})}{2\pi}, \quad (6.2)$$

respectively, where

$$Y(n) = \sum_{t=n}^{n+L-1} r(t)r^*(t+N). \quad (6.3)$$

A similar structure has also been derived in [5]. We can employ average over the symbols to obtain a more accurate estimate of the CFO and the symbol timing.

In applying the above method to multipath channels, note that (6.1) tends to be determined by the strongest path rather than the first significant path. Therefore, starting at \hat{n} , one should search in the direction of smaller timing offsets to find the earliest significant path (e.g., by finding the smallest offset where $|Y(n)|$ is above a sizable fraction of $|Y(\hat{n})|$) in order to avoid lag-error.

Note that (6.2) can only obtain the fractional part (normalized by subcarrier spacing) of the CFO. The integer part of the CFO needs to be estimated by another means. Now, for simplicity, consider estimating the DL CFO separately from the preamble index. Without knowing the preamble index, no data-aided methods can be used. The natural resort is blind estimation by finding which integer CFO value results in the highest total power in any of the three preamble subcarrier sets. Since the three preamble subcarrier sets are (nearly) indistinguishable in power content, there is a three-value ambiguity in the estimated integer CFO. One will need to wait until after having found the preamble sequence to determine the precise integer CFO. In fact, it may be better off to consider a joint search of the integer CFO and the preamble index and we present this scheme in next section.

6.2 Joint Operation of Preamble Search and Integral CFO Estimate

This section discusses two major variables in the post-FFT process of the initial synchronization for WiMAX DL. One is the integer subcarrier-spacing shift of the carrier frequency and the other is the preamble index as well as the IDCell [48] in the WiMAX system. The residual integer CFO is the ambiguity part of the pre-FFT synchronization using the CP correlation, so the additional process is required to identify this integer offset. The preamble index points out the serving BS identification and the corresponding reception parameters; thus, in the post-FFT synchronization, we need to detect the most possible IDCell of the serving BS as well as the preamble indexing from the pools of the 114 possible candidates.

Several literatures [88, 33, 53] for the integer CFO estimation in data-aided manner typically adopt the concept of the coherence time/bandwidth of the channel that the channel responses in successive symbols or at the nearby subcarriers does not vary significantly. By adopting the coherence time concept, Schmidl and Cox [88] suggest using two successive training symbols to detect the integer CFO with a manner of the inter-symbol differential detection. However, their approach requires the knowledge of the inter-symbol cross correlation of the two symbols. Later, from the coherence bandwidth concept, Kim *et al.* propose the estimator adopting the inter-subcarrier differential detection to identify the integer CFO. Similarly, the inter-subcarrier cross correlation must be aware in their approach. Hsieh and Wei [33] also adopt the coherence bandwidth concept to estimate the integer CFO. Unlike the manner of the differential detection, they suggest the detection criteria via the difference of the channel responses at the adjacent subcarriers. With this difference metric, it is possible to realize the integer CFO estimation in a multiplier-free fashion. However, all of them are developed in a heuristic way by following the coherence time/bandwidth concepts.

Logically, in mathematical formulation, the problems of the integer CFO and the preamble-indexing search are equivalent to the problem that, either in time or in frequency, we want to detect the most possible symbol from the received signal, which is passed over the multipath channel. The preamble symbols are different with the IDCell [48]; thus, it is naturally presented in the problem formulation. When considering the problem of the integer CFO estimation, we can treat the symbols with different integer shifts as the different symbols; therefore, the same problem representation can also be applied in this issue. Moreover, the joint consideration of the integer CFO estimation and the preamble index search now is reasonable in the same problem formulation when we regard the combinations of the integer shifts and the preamble sequences as the candidates.

This section mainly derives the maximal likelihood (ML) criteria of the sequence detection over multipath Rayleigh fading channel and gives the furthermore simplifications in the application in the post-FFT synchronization. We first analyze the likelihood function of the sequence searching problem and give the ML criteria. Then, some complexity reduced manners and realizations in joint preamble search and integer CFO estimation are proposed and analyzed in the following discussions. Finally, we show some numerical analysis and simulative comparisons of the proposed algorithms as the performance study.

6.2.1 Maximum Likelihood Symbol Detection

The maximal likelihood criterion of the symbol detection problem is to select the symbol that has the highest probability from the observed samples, which are the channel outputs interfered by the AWGN.

Before the derivation of ML criterion, we first consider the multipath Rayleigh fading channel

in discrete equivalent low-pass model as given by

$$h(n) = \sum_{l=1}^L \alpha_l \delta(n - d_l) \quad (6.4)$$

where d_l is the l th path delay in units of $\frac{T_s}{N}$, T_s is the symbol period and N is the number of samples in a complete symbol herein. For simplification in the derivation, we assume d_l be integer number which means that the delay paths are located in the ‘‘sample spacing’’. However, the derived results should be still applicable in the practical condition. We furthermore assume that the path gains α_l has the complex Gaussian distribution. Based on the equivalent low-pass channel model, the received data in discrete can be formulated by

$$r(n) = \sum_{l=1}^L \alpha_l x(n - d_l) + w(n) \quad (6.5)$$

where $w(n)$ is additive white noise, which has the complex Gaussian distribution and $x(n)$ is a sequence of the candidates.

Assume that two candidate symbols $x_j(n)$ and $x_i(n)$ have the following properties

$$\frac{1}{N} \sum_{t=0}^{N-1} x_j(t) x_i^*((t-n)_N) = \begin{cases} R_x(n) \approx \delta(n) & \text{if } i = j \\ \eta & \text{otherwise} \end{cases}, \quad (6.6)$$

where $(\cdot)_N$ denotes the module operation corresponding to N and η is a complex Gaussian random variable based on law of large number (LLN) when N is large enough.

The problem of the symbol detection is to recognize the most possible symbol $x_j(n)$ from the observed samples $r(n)$. Additionally, we consider the detection problem on the condition that the channel state information is not available but just parts of its information are aware.

Maximal Likelihood Criteria

On the condition when the channel response $h(n)$ and the symbol $x_j(n)$ are given, we have the likelihood function

$$L(R|X_j, H) = \exp \left\{ -\frac{\sum_{n=0}^{N-1} \left| r(n) - \sum_{l=1}^L \alpha_l x_j(n - d_l) \right|^2}{2\sigma_a^2} \right\}, \quad (6.7)$$

since the noise have the Gaussian distribution. Moreover, if the symbol energies of the candidates are the same, we have the same $\sum_{n=0}^{N-1} \left| \sum_{l=1}^L \alpha_l x_j(n - d_l) \right|^2$ for all symbols. Thus, the likelihood function can be furthermore simplified as

$$L(R|X_j, H) = \exp \left\{ \frac{\sum_{l=1}^L \Re \{ \alpha_l^* y_{d_l, j} \}}{\sigma_a^2} \right\}, \quad (6.8)$$

where

$$y_{n, j} = \sum_{t=0}^{N-1} r(n+t) x_j^*(t). \quad (6.9)$$

If the system has cyclic prefix extension, we can rewrite $y_{k, j}$ as

$$y_{n, j} = \sum_{t=0}^{N-1} r((t+n)_N) x_j^*(t) \quad (6.10)$$

where $(\cdot)_N$ denotes the module operation with respect to N .

Case in Knowing Power-Delay Profile

In previous equations, we have assumed that the channel parameters are available; however, in the practical situations, this assumption is not valid. Once, if we have the probability model of the channel, for example the power-delay profile (PDP), we can eliminate the uncertainty of the channel. Now, assume the channel response has the model that

$$h(n) = \sum_{l=1}^L A_l \beta_l \delta(n - d_l), \quad (6.11)$$

where β_l has zero-mean complex Gaussian distribution with variance = 1, and A_l is the square root of the power of l th path. Based on this, the sufficient likelihood function now becomes

$$L(R|X_j, H) = \exp \left\{ \frac{\sum_{l=1}^L \Re \{ A_l \beta_l^* y_{d_l, j} \}}{\sigma_a^2} \right\}. \quad (6.12)$$

Averaging the unknown random parameter β_l yields the likelihood function

$$\begin{aligned} L(R|X_j) &= E_{\beta} \left[\exp \left\{ \frac{\sum_{l=1}^L \Re \{ A_l \beta_l^* y_{d_l, j} \}}{\sigma_a^2} \right\} \right] \\ &= \exp \left\{ \frac{\sum_{l=1}^L A_l^2 |y_{d_l, j}|^2}{\sigma_a^2} \right\}. \end{aligned} \quad (6.13)$$

Therefore, the detection rule is to find out the symbol that has the largest likelihood function or equivalently the one has the metric

$$M(X_j) = \sum_{l=1}^L A_l^2 |y_{d_l, j}|^2, \quad (6.14)$$

which is the weighted sum of $|y_{d_l, j}|^2$.

In actual condition, the PDP is not aware at receiver, but we can adopt the possible assumption of the PDP in the metric calculation. For example, we can assume that the PDP has uniform distribution within a spread duration T and it results in

$$M(X_j) = \sum_{n=0}^{T-1} |y_{n, j}|^2. \quad (6.15)$$

Besides, another alternative assumption is the exponential decayed PDP, which is given by

$$M(X_j) = \sum_{n=0}^{T-1} e^{-n/\tau} |y_{n, j}|^2 \quad (6.16)$$

where τ is the time constant of the exponential weighting function.

Case in Deterministic Channel Assumption

If we treat the channel responses as unknown but deterministic parameters, the ML detector now becomes a joint optimization problem. The ML criterion for the joint optimization problem is given by

$$\hat{j} = \arg \max_j \left\{ \max_H L(R|X_j, H) \middle| X_j \right\}. \quad (6.17)$$

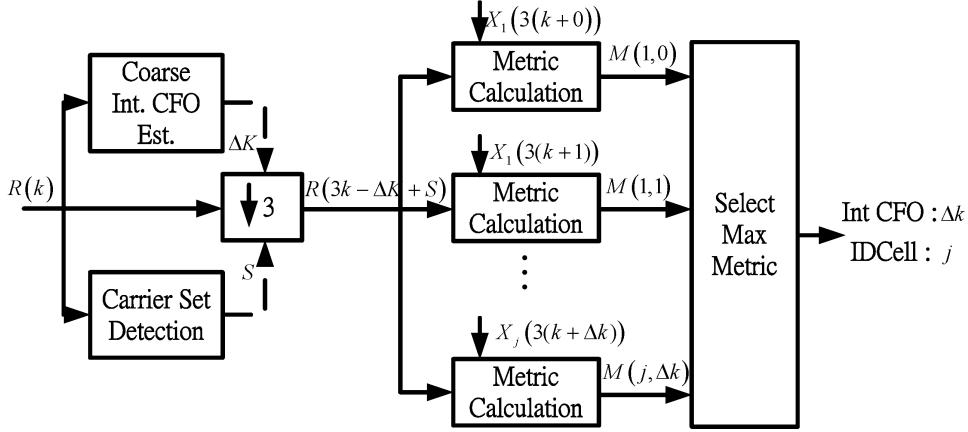


Figure 6.3: Two-stage Implementation of the post-FFT synchronization comprises the coarse integer CFO estimate and the fine joint detection.

It is a two-stage approach. First, we acquire the maximal likelihood estimation of the channel response corresponding to the given alternative symbol. Then, we pick up the symbol that has the largest likelihood when the associated optimal channel response is applied.

From derivation, the ML channel estimation for X_j is given by

$$H_{o|j} = \mathbf{R}_X^{-1} Y_j, \quad (6.18)$$

where

$$\mathbf{R}_X = \begin{bmatrix} R_x(0) & R_x(1) & \cdots & R_x(T-1) \\ R_x(1) & R_x(0) & \cdots & R_x(T-2) \\ \vdots & \vdots & \ddots & \vdots \\ R_x(T-1) & R_x(T-2) & \cdots & R_x(0) \end{bmatrix} \quad (6.19)$$

is the auto-correlation matrix of X_j and $Y_j = [y_{0,j} \ y_{1,j} \ \cdots \ y_{T-1,j}]^T$. Substituting $H_{o|j}$ into (6.8) we have the metric

$$M(X_j) = Y_j^H \mathbf{R}_X^{-1} Y_j. \quad (6.20)$$

Moreover, if the autocorrelation function of X_j is a delta function, it results in the same metric of the uniform PDP in (6.15).

6.2.2 Joint Preamble Search and Integer CFO Estimation

Now, we apply the ML symbol detection in the post-FFT synchronization. As mentioned, we treat the same preamble sequences with different integer CFOs as different symbols. We first review the preamble structure in WiMAX OFDMA. In frequency, the preambles are pseudo-random binary sequences modulated by the boosted BPSK. A preamble comprises several bits which are placed in the sectored carrier sets. The preamble carrier set is defined by $s + 3 \times n$ where $s \in [0, 1, 2]$ is the sector index and k is the running index; specially, the bit located in DC subcarrier must be discarded. For the case of 1024 point FFT system, the length of preamble sequence is 284 and placed in the subcarrier index $(86 : 3 : 935) + s$.

The proposed implementation of the joint detection algorithm comprises a two-stage process as shown in Fig.6.3. When we directly adopt the joint detection algorithm, the candidate pool from the combinations of the preamble sequences and the integer CFOs would be large. Therefore, to eliminate the realization cost, we can narrow down the search candidates via the coarse integer CFO estimation. Thus, the received signal is first down-sampled in the factor of

three via the coarse integer CFO estimation and the carrier set detection. Then, the fine joint detection algorithm is realized by the metric calculation and the maximal metric selection.

The carrier set detector is to recognize the most possible carrier set. Let $R(k)$ be the received symbol in frequency domain, N_p be the length of the preamble sequence. The straightforward approach is to select the set that has the largest received signal strength, which is given by

$$s = \arg \max_s \left\{ \sum_{n=0}^{N-1} |R(3k + s)|^2 \right\}. \quad (6.21)$$

For simplified realization, we can consider the one-norm detector by replacing $|R(k)|^2$ with

$$|R|_1 = |\Re \{R\}| + |\Im \{R\}|. \quad (6.22)$$

The coarse integer CFO estimate adopts the edge detection to find out the most interest of the region of the received symbol. The coarse integer CFO estimator is given by

$$\Delta K = \arg \max_k \left\{ \Delta |R(k)|^2 + \Delta |R(k + 3N_p)|^2 \right\} \quad (6.23)$$

where $\Delta |R(k)|^2 = |R(k)|^2 - |R(k-1)|^2$. Similarly, the one-norm edge detection also can be applied. We now present several approaches from the simplification of the ML symbol detection.

Time Domain Windowing After Frequency Domain Correlation

Based on the joint optimization in deterministic channel assumption, the first decision metric adopts the equation in (6.15) when we apply the assumption that $\mathbf{R}_X \approx \mathbf{I}$. Due to the CP insertion, the correlation values $y_{n,j}$ can be derived in (6.10). Naturally, we set the window width T to the maximal expected channel delay spread, for example, the CP duration.

However, for the direct implementation, it takes N multiplications for an observing point $y_{n,j}$ and $N \times T$ ones for a metric calculation. To simplify this, we can adopt the frequency domain approach to derive the correlations. After the coarse integer CFO estimation and compensation, the received symbol in frequency is point-wisely multiplied by the testing sequence to get the frequency domain correlations. Then, taking the inverse FFT, we can obtain the time domain correlations. Therefore, the main price in the metric calculation now is the inverse FFT operation per candidates.

Concept of Frequency Domain Filtering

In the given PDP approach, the metric is the weighted sum of $|y_{n,j}|^2$ as given in (6.14). If we assume that the PDP has the following formulation

$$A_n = \left| \sum_{k=0}^{N_{tap}-1} F(k) \exp\left(\frac{j2\pi nk}{N}\right) \right|^2 \quad (6.24)$$

where $F(k)$ is the square root of the power spectrum density (PSD) of the channel, we can directly calculate the metric in frequency domain. From the metric calculation in (6.14), we can obtain that

$$M(x_j) = \sum_{n=0}^{N-1} \left| \sum_{k=0}^{N_{tap}-1} F(k) \exp\left(\frac{j2\pi kn}{N}\right) y_{n,j} \right|^2. \quad (6.25)$$

Now, based on Parseval's theorem, the metric is equivalent to

$$M(x_j) = \sum_{k=0}^{N_p-1} |F(k) \otimes Y_j(k)|^2, \quad (6.26)$$

where \circledast denotes the circular convolution, $Y_j(k)$ is the adjusted frequency response of $y_{n,j}$ after the coarse integer CFO estimation, and N_p is the number of the preamble sequence. Moreover, it is equivalent to use the linear convolution for the circular convolution since the preamble symbol exists the guard band in both sides of the spectrum.

We can adopt a pre-defined low-pass filter for the reference PSD as well as the PDP since the channel has the decayed PDP in nature. For low cost implementation, we can consider the simplest moving-average filters (MAFs) as the pre-defined filter, which are multiplier-free filters. Let N_{tap} be the number of the filter taps, the metric with N_{tap} order MAF is given by

$$M(x_j) = \sum_{k=0}^{N_p - N_{tap} - 1} \left| \sum_{f=0}^{N_{tap} - 1} Y_j(k + f) \right|^2. \quad (6.27)$$

Furthermore reduction suggests that we can use parts of the filter outputs instead of all. For example, if we adopt the averages of the successive N_{tap} segmentations of the samples to replace the MAF outputs, we have the

$$M(x_j) = \sum_{k=0}^{\lfloor N_p / N_{tap} \rfloor - 1} \left| \sum_{f=0}^{N_{tap} - 1} Y_j(N_{tap}k + f) \right|^2. \quad (6.28)$$

Alternatively, the one-norm approximation of the $|\cdot|^2$ in the metric calculation can provide furthermore simplifications and results in the multiplier-free implementation.

Differential Detection

Now, we consider the simplest two-tap moving average (MA) filter with impulse response given by

$$F(k) = \frac{1}{2}\delta(k) + \frac{1}{2}\delta(k-1) \quad (6.29)$$

to implement the frequency domain filter based metric calculation. Employing this filter, we obtain the following metric:

$$M(x_j) = \frac{1}{2} \sum_{k=1}^{N_p-1} \Re \{ Y_j(k) Y_j^*(k-1) \} + \frac{1}{2} \sum_{k=0}^{N_p-1} |Y_j(k)|^2. \quad (6.30)$$

Since the preamble sequences have constant amplitude and the maximum possible integral CFO is relatively small compared to N_p , the second term in the right-hand-side (RHS) of (6.30) is nearly constant over all j . Thus, the detection metric can be further simplified to

$$\begin{aligned} M(x_j) &= \sum_{k=0}^{N_p-1} \Re \{ Y_j(k) Y_j^*(k-1) \} \\ &= \sum_{k=0}^{N_p-1} \Re \{ R(k) R^*(k-1) D_j(k) \} \end{aligned} \quad (6.31)$$

where $D_j(k) = X_j(k) X_j^*(k-1)$. Additionally, $D_j(k)$ is real and binary (± 1) since we have BPSK modulated preamble sequences in WiMAX OFDMA. Thus,

$$M(x_j) = \sum_{k=0}^{N_p-1} D_j(k) \Re \{ R(k) R^*(k-1) \}. \quad (6.32)$$

The detection metric $M(x_j)$ easily reminds one of the detection variable used in differential detection. Indeed, the final approach above can be interpreted as a kind of differential detection in the frequency domain, which concept has been proposed in [63, 37]. And this interpretation is complementary to the LPF view given previously.

If the spacing of the nonzero subcarriers in the preamble is much smaller than the coherence bandwidth of the channel, then the channel responses at neighboring preamble subcarriers are approximately equal, i.e., $H(k+1) = H(k) + \Delta H(k)$ where $|\Delta H(k)| \ll |H(k)|$ and k is index for nonzero preamble subcarriers. Hence, from definition of $R(k)$ with the noise term neglected,

$$\begin{aligned} & \Re \{R(k)R^*(k-1)\} \\ &= \Re \{H(k)X_j(k)H^*(k-1)X_j^*(k-1)\} \\ &\approx |H(k)|^2 D_j(k). \end{aligned} \tag{6.33}$$

Therefore,

$$M(x_j) \approx \sum_{k=0}^{N_p-1} |H(k)|^2 D_j(k) D_{j'}(k), \tag{6.34}$$

which certainly is maximized when $j' = j$.

Hardlimiting of the Differential Signal

Simplified to the extreme, we may consider hardlimiting the “differential signal” $\Re\{R(k)R^*(k-1)\}$. Then the computation of M_j becomes equivalent to computing the Hamming distance between the sequence $D_j(k)$ and the hardlimited $\Re\{R(k)R^*(k-1)\}$. The D_j with the smallest Hamming distance will be the winner. This method is particularly useful for reducing the complexity of hardware implementation.

Early Dropping of Bad Candidates by Dynamic Metric Thresholding

Another way to reduce the computational complexity is to drop the bad candidates early on. For example, we may consider dividing the summation over N_p subcarriers in the metric computation into a number of fixed-length sections (or windows). Rather than finish computing the metric for each X_j over the total number of N_p subcarriers and then compare for the best, we may set a threshold after each window. The x_j that perform below the threshold are dropped. This continues until only one x_j remains or until we come to the end of the last window when all the surviving x_j 's will be compared. The method resembles, to some extent, certain reduced-complexity breadth-first tree search methods.

Several detailed design issues exist in this method. First, comes the window size. We will give some examples in the section on simulation results. Second, there is the threshold for each window. We consider setting it to a fraction of the current best (largest) metric of all the retained x_j 's. Needless to say, the detection performance depends on the choice of the window size and the threshold, so is the computational complexity. And third, considering that the channel may be subject to multipath fading, it may not be good to let each window consist of contiguous preamble subcarriers. Rather, the windows should be interleaved, with the subcarriers in each window spaced, for example, beyond the coherence bandwidth.

6.3 Performance Studies of Joint Detection Schemes

This evaluates the performance of the proposed algorithms over single-path and multi-path channels from the mathematical analysis and the simulative studies and comparisons. We first present the mathematical analysis of the false detection probability; then, simulate and gather the statistics of the probability in the numerical experiments with the presented detectors.

6.3.1 Mathematical Analysis

We analyze the performance of the joint detection algorithms via the mathematical derivations and the simulation comparisons. We mainly discuss the false detection probability where a false detection happens if the transmitted symbol is different the detected one. Let P_e be the false error probability when j th symbol is sent and i th symbol is detected, and assume P_e be nearly the same for different pairs of $i \rightarrow j$. If there are total J candidates, the entire FDP can be expressed

$$P_f = 1 - (1 - P_e)^{J-1} \approx (J - 1)P_e \quad (6.35)$$

where the last approximation holds if the P_e is small enough.

Property of χ^2 distribution

Before the analysis of the FDE, we introduce some used properties and distribution in the probability. First, we consider the detection error probability in χ^2 distribution. If a random variable x has a χ^2 distribution with $2L$ degree of freedom (DOF), its probability density function (PDF) is respectively given by

$$f_{\chi^2}(x; 2L) = \frac{(1/2)^L}{\Gamma(L)} x^{L-1} e^{-x/2}, \quad (6.36)$$

and cumulative distribution function (CDF) is

$$F_{\chi^2}(x; 2L) = \frac{\gamma(L, x/2)}{\Gamma(L)}, \quad (6.37)$$

where $\gamma(L, x)$ is the lower incomplete Gamma function defined by

$$\gamma(L, x) = \int_0^x t^{L-1} e^{-t} dt, \quad (6.38)$$

and $\Gamma(L) = \gamma(L, \infty)$ is the Gamma function.

Now, we consider the general case of the error detection probability in χ^2 distribution. Let two random variable X_1 and X_2 have the χ_{2L}^2 distribution, M be known number and V_1 and V_2 are two positive value, the probability of " $M + V_1 X_1 \leq V_2 X_2$ " can be calculated via the integration :

$$\begin{aligned} & P(M + V_1 X_1 \leq V_2 X_2; 2L) \\ &= \int_0^\infty P\left(\frac{M + V_1 X_1}{V_2} \leq X_2 | X_1 = x\right) f_{\chi^2}(x; 2L) dx \\ &= \int_0^\infty \left(1 - F_{\chi^2}\left(\frac{M + V_1 x}{V_2}; 2L\right)\right) f_{\chi^2}(x; 2L) dx \\ &= 1 - \frac{1}{\Gamma(L)^2} \int_0^\infty \gamma\left(L, \frac{\frac{1}{2}M + V_1 x}{V_2}\right) x^{L-1} e^{-x} dx. \end{aligned} \quad (6.39)$$

However, this integration may not exist the closed-form; thus, to evaluate the probability, we may perform the integrations via the numerical programs; for examples, the C language, the MATLAB or the Mathematical.

Distribution of $|y_{k,j}|^2$

Next, we consider the statistic property and distribution of the cross correlation of r and x_j . Recall the definition of the correlation, we refine the correlation as

$$y_{n,j} = \frac{1}{N} \sum_{t=0}^{N-1} r(t)x_j^*(t+n). \quad (6.40)$$

For simplified derivation, we assume the candidate symbol is white where its autocorrelation is a delta function and the cross correlations between two symbols are uncorrelated zero-mean complex Gaussian random variable; thus, we have

$$R_{j,i}(n) = \frac{1}{N} \sum_{t=0}^{N-1} x_j(t)x_i^*(t-n) = \begin{cases} \delta(n) & \text{if } j = i \\ \eta & \text{otherwise} \end{cases}, \quad (6.41)$$

and η has zero-mean (complex) Gaussian distribution. Additionally, without lost of generality, we let that the averaged sample power of the candidates is normalized to 1, which yields the symbol energy being N . Based on this assumption, the variance of η is given by

$$\sigma_\eta^2 = \frac{\sum_{k=0}^{N-1} |X_j(k)X_i^*(k)|^2}{N^2} = \frac{1}{N}. \quad (6.42)$$

The statistic property of $y_{n,j}$ depends on the correctness of the testing symbols and the existence of the delay path. If the testing symbol is the correct one, we have

$$y_{n,c} = y_{n,j'=j} = h(n) + w_a(n), \quad (6.43)$$

and $w_a(n) = \frac{1}{N} \sum_{t=0}^{N-1} w(t)x_j^*(t+n)$ is a zero-mean complex Gaussian variable with $\frac{\sigma_w^2}{N}$ variance. If $h(n)$ is a non-zero path gain, $|y_{n,c}|^2$ has the non-central χ^2 distribution. Moreover, if $|h_k|^2$ is much larger than the $w_a(n)$, $|y_{n,c}|^2$ can be expressed as

$$|y_{n,c}|^2 \approx |h(n)|^2 + \frac{\sigma_w^2}{2N} X_a(n) \quad (6.44)$$

where $X_a(n)$ has a χ^2 distribution with 2 DOF. On contrast, if $h(n)$ is zero or not significant, we have

$$|y_{n,c}|^2 = \frac{\sigma_w^2}{2N} X_a(n). \quad (6.45)$$

If the testing symbol is incorrect, $y_{n,j}$ contains only the noise term as given by

$$y_{n,j' \neq j} = Y_{n,e} = \sum_{l=1}^L \alpha_l \eta(d_l - n) + w_a(n) = w_e(n) \quad (6.46)$$

where $w_e(n)$ is the zero-mean complex Gaussian variable with $\frac{\sigma_h^2 + \sigma_w^2}{N}$ variance and the $\sigma_h^2 = \sum_{l=1}^L |\alpha_l|^2$ herein is the channel energy. Similarly,

$$|y_{n,e}|^2 = \frac{\sigma_h^2 + \sigma_w^2}{2N} X_e(n) \quad (6.47)$$

where $X_e(n)$ also has the same distribution as $X_a(n)$.

Detector Using Uniform PDP Assumption

To evaluate the false detection probability, we need to analyze the error probability P_e . In the following, we first evaluate the P_e in given channel energy σ_h^2 and then extend to the fading channel by averaging all possible σ_h^2 . Let that the observation window T is larger than the multipath delay spread and the delays are located at the sample spacing. The decision metric of the correct and incorrect events are given by

$$M_c = \sum_{n=0}^{T-1} |y_{n,c}|^2 = \sigma_h^2 + \frac{\sigma_w^2}{2N} X_C \quad (6.48)$$

$$M_e = \sum_{n=0}^{T-1} |y_{n,e}|^2 = \frac{\sigma_h^2 + \sigma_w^2}{2N} X_E \quad (6.49)$$

where X_C and X_E both the random variables that have the χ^2 distribution with $2T$ degrees since they are both the summations of T χ^2 random variables with 2 DOF.

Now, if h is deterministic and given, by substituting $M = \sigma_h^2$, $V_1 = \frac{\sigma_w^2}{N}$ and $V_2 = \frac{\sigma_h^2 + \sigma_w^2}{N}$ into (6.39), we have the error probability that

$$P_e(\sigma_h^2) = 1 - \frac{1}{\Gamma(T)^2} \int_0^\infty \gamma \left(T, \frac{N\sigma_h^2 + \sigma_w^2 x}{\sigma_h^2 + \sigma_w^2} \right) x^{T-1} e^{-x} dx. \quad (6.50)$$

When $h(n)$ is a fading channel, we may average the previous given probability over all possible $h(n)$ to get the averaged error probability. Alternatively, if the PDF of σ_h^2 is given by $f_h(x)$, the averaged false detection probability is given by

$$P_f = 1 - \int_0^\infty (1 - P_e(x))^{J-1} f_h(x) dx. \quad (6.51)$$

Actually, both the integrations in $P_e(\sigma_h^2)$ and P_f may not exist the closed form solutions; therefore, to evaluate the theoretical performance, we should consider the numerical solution via the programs.

Detector Using Frequency Domain Filter

Now, we consider the performance of the detector using the frequency domain filter concept. Likewise, we first derive the error probability in the given channel condition; then, extend to the case of the fading channel.

If $Z_{k,j} = F(f) \otimes Y_j(f - k)$ is the filter output, we first evaluate the probability distribution of $|Z_{k,j}|^2$. Consider the cases of correctness and incorrectness of the testing symbols. If the symbol is correct, we have

$$Z_{k,j} = F(f) \otimes H(f - k) + W_a(k) \quad (6.52)$$

where $W_a(k) = \sum_{f=0}^{N_{tap}-1} F(f) w_a(f - k)$, which is a zero-mean complex Gaussian variable with variance $= (\sum F(f)^2) \sigma_a^2$. By summation over all k , we have the correct metric given by

$$M_c = \frac{1}{N_d} \sum_{k=0}^{N_d-1} |Z_{k,j}|^2 \approx \sigma_{h|F}^2 + \frac{C\sigma_w^2}{2} X_C \quad (6.53)$$

where $N_d = N_p - N_{tap}$ is the total sample used in metric calculation, $\sigma_{h|F}^2 = \frac{1}{N_d} \sum_{k=0}^{N_d-1} |F(f) \otimes H(f - k)|^2$ is the average power of the channel filtered by $F(k)$, $C = \sum F(f)^2$, and X_C here has

the χ^2 distribution with $2N_d$ degrees. Besides, from Parseval's theorem, we furthermore have that

$$\sigma_{h|F}^2 = \frac{1}{N_d} \sum_{k=0}^{N_d-1} |F(f) \otimes H(f-k)|^2 = \sum_{l=1}^L A_{d_l}^2 |\alpha_l|^2 \quad (6.54)$$

where A_n is the time domain weight of $F(k)$ as given in (6.24). Moreover, if we consider the partial usages of the filter outputs, we approximately have the same result whereas N_d meanwhile is the number of used samples.

On contrast, when the testing symbol is incorrect, we similarly have that

$$M_e = \frac{C(\sigma_h^2 + \sigma_w^2)}{2} X_E \quad (6.55)$$

where X_E is the random variable that has the same distribution as X_C .

Now, if $h(n)$ is given, the error probability is given by

$$P_e(\sigma_h^2, \sigma_{h|F}^2) = 1 - \frac{1}{\Gamma(N_d)^2} \int_0^\infty \gamma \left(N_d, \frac{\frac{1}{C}\sigma_{h|F}^2 + \sigma_w^2 x}{\sigma_h^2 + \sigma_w^2} \right) x^{N_d-1} e^{-x} dx. \quad (6.56)$$

In additional, when the N_{tap} moving average filter is adopted, we furthermore have that $\frac{1}{C} = N_{tap}$ and

$$P_e(\sigma_h^2, \sigma_{h|F}^2) = 1 - \frac{1}{\Gamma(N_d)^2} \int_0^\infty \gamma \left(N_d, \frac{N_{tap}\sigma_{h|F}^2 + \sigma_w^2 x}{\sigma_h^2 + \sigma_w^2} \right) x^{N_d-1} e^{-x} dx. \quad (6.57)$$

When $h(n)$ is a fading channel, to derive the average false detection probability, we furthermore require the PDF of σ_h^2 and the mapping function from σ_h^2 to $\sigma_{h|F}^2$. If $f_h(x)$ is the PDF of σ_h^2 and $\sigma_{h|F}^2 = g(\sigma_h^2)$, the average false detection probability is derived by

$$P_f = 1 - \int_0^\infty (1 - P_e(x, g(x)))^{J-1} f_h(x) dx. \quad (6.58)$$

Also, the integrations should not exist the closed form solution and we still run the numerical integration to derive the theoretical result.

Performance in Single Path Channel

We now consider the case over the simplest single path channel. We firstly evaluate the performance of the cases over AWGN channel; then, average the error probability with respect to the channel energy in χ^2 distribution with 2 DOF to derive the performance of the cases over Rayleigh channel.

Assume ideal synchronization in symbol time and fractional CFO. For the cases of the detectors adopting the uniform PDP assumption and adopting the frequency domain filter, the error probabilities are derived via the integrations in (6.50) and (6.56) correspondingly, and the false error probability is obtained via substituting the derived error probability into (6.35). Furthermore, the performances over the single-path Rayleigh channel are calculated via the integrations in (6.51) and (6.58) correspondingly with respect

$$f_h(x) = \frac{2}{E\sigma_h^2} f_{\chi^2} \left(\frac{2x}{E\sigma_h^2}, 2 \right) \quad (6.59)$$

and " $g(\sigma_h^2) = (\sum F(n)) \sigma_h^2$ " in (6.58), where $E\sigma_h^2 = E[\sigma_h^2]$ is the average channel energy.

Additionally, we consider the performance in the case when the PDP is aware. Straightforwardly, letting $T = 1$ in (6.50), we can obtain the error probability in this case. Performing the integration, it exists the closed-form solution as given by

$$P_e(\sigma_h^2) = \frac{\sigma_w^2 + \sigma_h^2}{2\sigma_w^2 + \sigma_h^2} e^{-\frac{N\sigma_h^2}{(\sigma_w^2 + \sigma_h^2)}}, \quad (6.60)$$

which can approximate to

$$P_e(\sigma_h^2) = \frac{1}{2} e^{-\frac{N\sigma_h^2}{\sigma_w^2}}, \quad (6.61)$$

if σ_w^2 is larger than σ_h^2 ; i.e., in the extreme low SNR condition. When the channel response is a single-path Rayleigh channel, by averaging the false detection probability with respect to $f_h(\sigma_h^2) = \frac{2}{E\sigma_h^2} f_{\chi^2}(\frac{2\sigma_h^2}{E\sigma_h^2}, 2)$, we have that

$$\begin{aligned} P_f &= 1 - \int_0^\infty \left(1 - P_e(E\sigma_h^2 \frac{x}{2})\right)^{J-1} f_{\chi^2}(x; 2) dx \\ &\approx 1 - {}_2F_1\left(\frac{1+\rho}{N}, 1-J, 1 + \frac{1+\rho}{N}, \frac{1+\rho}{2+\rho}\right), \end{aligned} \quad (6.62)$$

where ${}_2F_1(a, b, c, d)$ is the standard Hyper-geometric series(function) and $\rho = \frac{\sigma_w^2}{E\sigma_h^2}$ herein is the averaged SNR reciprocal. If σ_w^2 is much larger than $E\sigma_h^2$, we can obtain the approximated P_f given by

$$P_f \approx 1 - 2^{\frac{\rho}{N}} {}_2F_1\left(\frac{\rho}{N}, \frac{\rho}{N} + J, 1 + \frac{\rho}{N}, -1\right). \quad (6.63)$$

6.3.2 Numerical Studies and Comparisons

In this section, we present the simulative comparisons of the proposed algorithms and the verification with the analytical results. We consider the situation when the received signal only contains one significant preamble from the nearest BS. The detections of the multiple preamble sequences require a threshold mechanism; however, it is out of the scope in this discussion. Besides, one main purpose of the initial synchronization is to find the BS that has the best communication quality, which is somehow equivalent to have the best signal strength in preamble symbol. Thus, we just consider detecting the preamble symbol that has the largest signal strength.

In the simulation, consider an OFDMA WiMAX system with channel bandwidth = 10 MHz, FFT size = 1024, and CP length = 128. Recall that there are 114 selectable preamble sequences, which are divided into three segments, and the nonzero subcarriers in each sequence are spaced three subcarriers apart. Since we have no idea about integral carrier offset before estimation and so do the preamble code sequences with largest energy belong to which set, we need to test all the 114 candidates for each alternative integral CFO.

Study in Single Path Channels

We first adopt the single path channels, which includes the AWGN and the single path fading channel, to verify the simulated results with the analytical ones and to exam the correctness of the analysis. The adopted algorithms in this comparison is listed by: case 1, the optimal detection with awareness of the PDP; case 2, the detection with uniform PDP assumption, in which $T = 128$; case 3, the detection adopting the frequency domain filter, where the metric adopts the averages of the successive four samples as in (6.28); case 4, the detection adopting the differential detection.

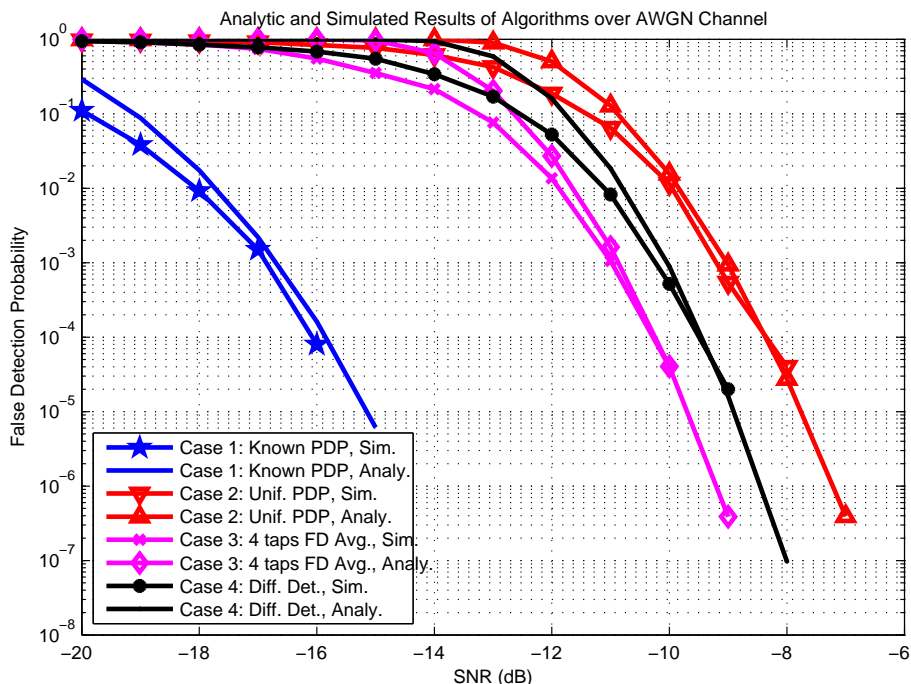


Figure 6.4: Performance comparison of proposed algorithms over AWGN channel.

Fig. 6.4 illustrates the performances over AWGN channel. As shown in the performance curves, the simulated and analytic results are quite matching for all algorithms when SNR is “high” (herein, high SNR is still really low enough). The SNR definition is the ration of the received preamble signal power relative to the noise power. The results show that, except case 1, case 3 using four taps average in frequency domain has the best performance; then, case 4 adopting differential detection performs better the detection with assumption of the uniform PDP.

Fig. 6.5 illustrates the results over single path Rayleigh channel. The simulated results also agree with the analytical ones in this channel conditions. However, in this channel condition, the detectors of case 3 and case 4 have no significant difference and they both perform roughly 2 dB better than detector of case 2.

Comparisons in Multipath Rayleigh Fading Channel

Now, we compare the algorithms over the multipath fading channel via the simulations. We consider jointly detecting the preamble sequence and the integer CFO in the second phase of the initially post-FFT synchronization. Assume that the true carrier set is detected, the true integer part of the CFO becomes zero after the coarse integer CFO estimation. The additional search range of the integer CFO is ± 3 subcarrier spacings. However, due to the preamble structure, we only need to perform three different candidates of the integer CFO in $[-3, 0, 3]$. Therefore, there are total $114 \times 3 = 342$ combinations of the integer CFOs and the preamble sequences to be tested in one reception.

The compared algorithms are listed as follows: case 1, the detector with uniform PDP assumption, in which $T = 128$; case 2, the detector adopting the four samples frequency domain average as in (6.28); case 3, 1-norm version of case 2 where the detector is the same as case 2 except for replacing $|\cdot|^2$ by $|\cdot|_1$ in (6.28); case 4, the detector adopting the differential detection; case 5, the detector adopting the hard-limited differential detection; case 6, the detector adopting

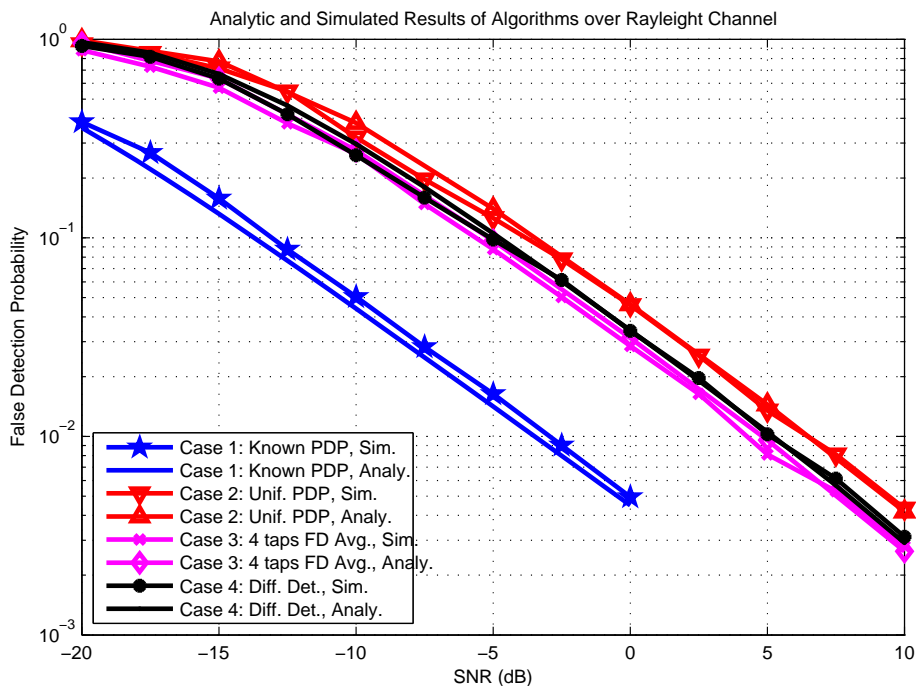


Figure 6.5: Performance comparison of proposed algorithms over Rayleigh fading channel.

the differential detection with early dropping scheme in 5 maximal iterations; case 7, the detector same as 6 except for 10 maximal iterations. We test these algorithms over the block static Rayleigh fading channel that has the Vehicular-A PDP [21]. Furthermore, in the early dropping scheme, we set the length of the comparative samples to $\lfloor N_p/K \rfloor$ where K is the number of the maximal iterations. For example, in case 6, the length is $\lfloor 284/5 \rfloor = 56$. Besides, the dropping threshold is arbitrarily set to 1/2 of the maximal metric in current iteration.

Fig. 6.6 depicts the simulation results. If the false detection probability in 10^{-3} is the comparative margin, the case 2 has the minimal requirement of the SNR. The sorting of the performances are given by: case 2 > case 3 = case 4 > case 1 > case 5 = case 6 > case 7. In the sort of the differential detection algorithms, the poor performances in case 5–7 are the penalties of the lower cost implementations. In the sort of the frequency domain filter, the $|\cdot|_1$ version has just little performance loss than $|\cdot|^2$ version, whereas it has fewer cost from the multiplier-free realization.

6.4 Conclusions

This chapter presented the initial synchronization of the 802.16e OFDMA DL. We proposed the two-stage process of the initial synchronization. First stage performs before the FFT to acquire the symbol time and fractional CFO using the CP correlation. The second stage works after the FFT, which jointly estimates the integer CFO and the preamble index.

We mainly discussed the post-FFT synchronization step and specially focused on the problem of the symbol identification over multipath channel. We formulated the joint detection problem as the symbol identification. For this, we proposed the ML criteria of the symbol detection, which is the weighted sum of the cross-correlations of the reception and the candidate symbols, as well as several implementations of the joint detections in low-cost manners. One major contribution in this place is the concept of the frequency domain filter, which gives direct detection in frequency domain instead of the detection after translating into time domain. Additionally,

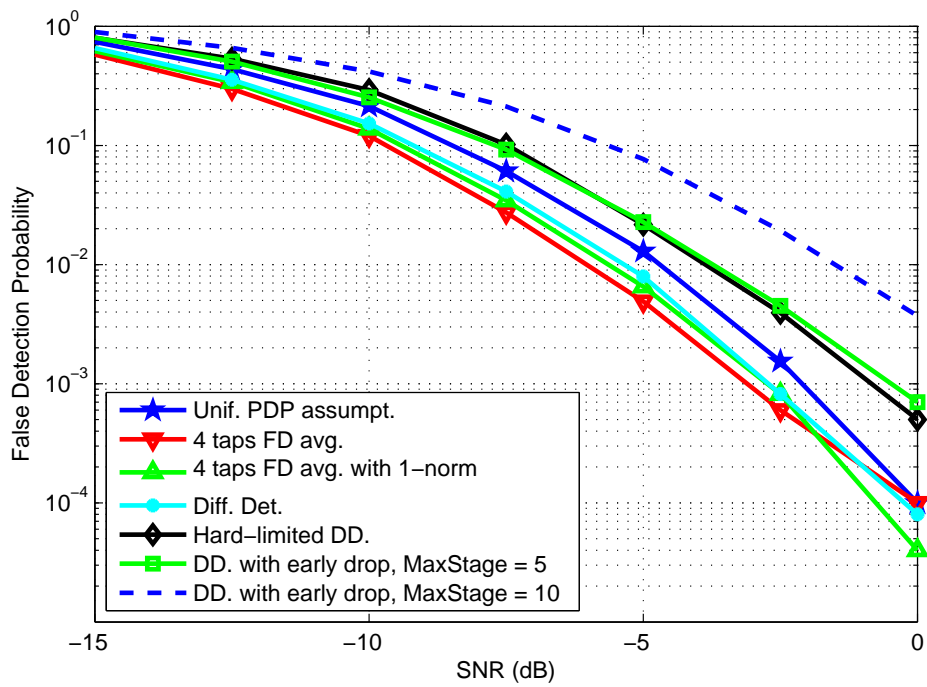


Figure 6.6: Simulation results over vehicular A channel.

the well-known differential detection scheme can be treated as a special case in this concept.



Chapter 7

Channel Estimations in Pilot-Aided Multi-Carrier System

Channel estimation in pilot-aided multi-carrier system is an important and well-discussed issue. The estimation algorithms mainly can be classified as the model-based, the statistical-dependent and the statistical-independent approaches. The subspace least-square method is one of the first class, which uses the projection onto the delay-subspace to eliminate the noise out-side the channel delay subspace. The major issue in this approach is the estimation of the channel delay subspace [103, 78, 91, 101], which takes great costs in realization, especially when the channel delays are not integer-spaced.

The Wiener MMSE estimator [18, 61, 72] is the most common statistical-dependent approach. The MMSE channel estimation may perform in 1-D [18] if the channel is estimated individual per symbol or 2-D [61] if joint frequency and temporal channel correlation are used. The Wiener filter requires additional computation cost in the estimation of the channel correlation and the noise variance. A sub-optimal approach is to use the pre-defined correlation matrix instead of the real-time estimation. The used assumption of the pre-defined power-delay profile is usually the uniform or the exponential decayed distribution [18, 3]. However, the root-mean-square (RMS) delay of the channel is additionally required when the exponential decayed power-delay profile is used [3, 99].

The third approach uses the interpolation concept to reconstruct the missing channel responses. One of this approach is the transform-based interpolation, such as the maximal likelihood interpolator [72]. To reduce the implementation cost, the discrete Fourier transform (DFT) based interpolator are typically used [19]. However, it is only applicable in equal-pilot-spacing multi-carrier system. Besides the transform-based interpolator, the frequency filtering interpolator is mostly popular scheme in low-cost consideration. The polynomial interpolation is the well-established approach in the frequency-domain interpolator [32].

This chapter presents two CE approaches. We first consider the interpolative channel estimation. Following the phase-shift concept in [32], we present the MMSE optimal window shift of the interpolation and its estimation. Then, we consider the approximate Wiener interpolation using predefined channel channel correlations. To generate the correlations, we investigate a simple estimation scheme of the mean delay and the root-mean-square delay spread. The proposed estimators are applied in the comb-type pilot-aided multi-carrier system and the 802.16e mobile WiMAX system.

7.1 MMSE Optimization of Polynomially Interpolative Channel Estimate

Pilot-aided channel estimation is widely adopted in orthogonal frequency division multiplexing (OFDM) and multiple access (OFDMA) systems. And frequency-domain polynomial interpolation is an often considered approach for such channel estimation. However, for channels that exhibit large delay spreads, the performance of polynomial interpolators suffers due to modeling error. Some have proposed to remedy the problem by increasing the interpolation order or by adding a linear phase shift to linear interpolation. The linear phase shift is equivalent to window shift in time domain. We thus derive a method to estimate the optimal window shift, in the minimum mean-square error (MMSE) sense, for polynomial-interpolative channel estimation of arbitrary order. As a practical application, we show how to apply phase-shifted interpolative channel estimation to Mobile WiMAX downlink transmission and propose a method to automatically select the interpolation order based on some MSE estimation.

7.1.1 Introduction

The polynomial interpolation is the well-established approach in the frequency-domain interpolator [32]. The most advantage of the polynomial interpolation is the low cost in hardware realization due to the properties. First, the coefficients are real that requires half complexity less than the same size filter with complex coefficients. Then, the coefficients are fixed and independent to channel state information. The fixed-coefficient multipliers can be used to reduced hardware complexity. In addition, unlike MMSE estimator, we do not need the coefficient generator in the realization.

No matter what kind of the channel estimation, the timing estimation is a critical factor that affects the performance of the estimation [2, 74]. In the MMSE channel estimation, the authors [2] takes notice of the timing estimation error and presents enhanced MMSE channel estimation according to timing statistic. In the FFT transform based estimation, some literatures [57, 97] consider to jointly estimate the symbol timing and the channel response in OFDM based wireless local area network (WLAN) system. Besides, Mostofi and Cox [74] analyze the impairment of timing error in the inter-block interference (IBI) and the inter-carrier interference (ICI) effects over large delay-spread channel and investigate the estimation of the robust symbol time with the OFDM system using pilot-aided channel estimation.

The interpolative channel estimation is also affected by the symbol timing. For instance, linear interpolation may suffer great performance loss in poor symbol synchronization [80] or under a large channel delay spread [41]. As a result, some have proposed to alleviate the problem by resorting to high-order interpolation [32]. The reason why different interpolation orders may give different performance can be interpreted via some well-known results in signal processing theory, which not only provide a useful perspective for understanding and analysis of the phenomenon but also hint at improved interpolator design. Specifically, polynomial interpolation is effectively a linear filtering operation [87]. Since convolution in the frequency domain corresponds to multiplication in the time domain [76], different orders of interpolation for the frequency response correspond to different kinds of windowing on the channel impulse response. Fig. 7.1 is a conceptional illustration of the situation. Linear interpolation (dashed line) has a smaller window size than quadratic interpolation (dash-dot line) and hence results in a greater distortion of the channel response. However, the figure also indicates that, if one can shift the window corresponding to linear interpolation by some amount to better capture the time range of the significant channel response samples (solid line), then one could expect an improved performance. The same also applies to higher-order interpolation.

In this section, we mainly consider the optimal (time-domain) window-shift of the polynomial interpolative channel estimation under given interpolation order, where the “window-shift” may

refer to the shifting of the zeroth index of the OFDM symbol or the frequency linear phase-rotation. As a linear phase shift amounts to modulating the time-domain signal with a single complex exponential, Hsieh and Wei [32] adopt the single frequency estimators proposed in [51] directly to find the desired offset. Unfortunately, for channel estimation this is not optimal in the mean-square error (MSE) sense, as later derivation will show. We will derive the optimal window shift that achieves minimum MSE (MMSE) in channel estimation for arbitrary polynomial order. Besides, the window-shifting operation can be performed in frequency domain as the phase-rotation or phase-compensated interpolation. The simplest phase-compensated/-rotated linear interpolation is presented in these papers [32, 41]. An alternative is to (circularly) shift the received signal before it is discrete-Fourier transformed (DFT) in the receiver.

Moreover, it is instinctively expected (and will be confirmed in later analysis) that the MMSE in channel estimation should depend on the amount of channel noise. In fact, analysis will show that, in high channel noise, higher-order interpolation may be affected so more adversely than lower-order interpolation as to yield worse channel estimates. Therefore, it would be desirable if the interpolation order can be selected adaptively according to the channel condition to attain best possible channel estimation performance. We will also address this issue.

The contribution of this section are given as follows. We consider the optimization of the polynomial interpolative channel estimation in multi-carrier system. We observe the symbol timing issue and analyze the MSE with the factor of timing offset. According to the analytical result, we derive the MMSE optimization criterion of the symbol timing and propose a suboptimal estimation of the optimal window shift. We further than analyze the performance in additive

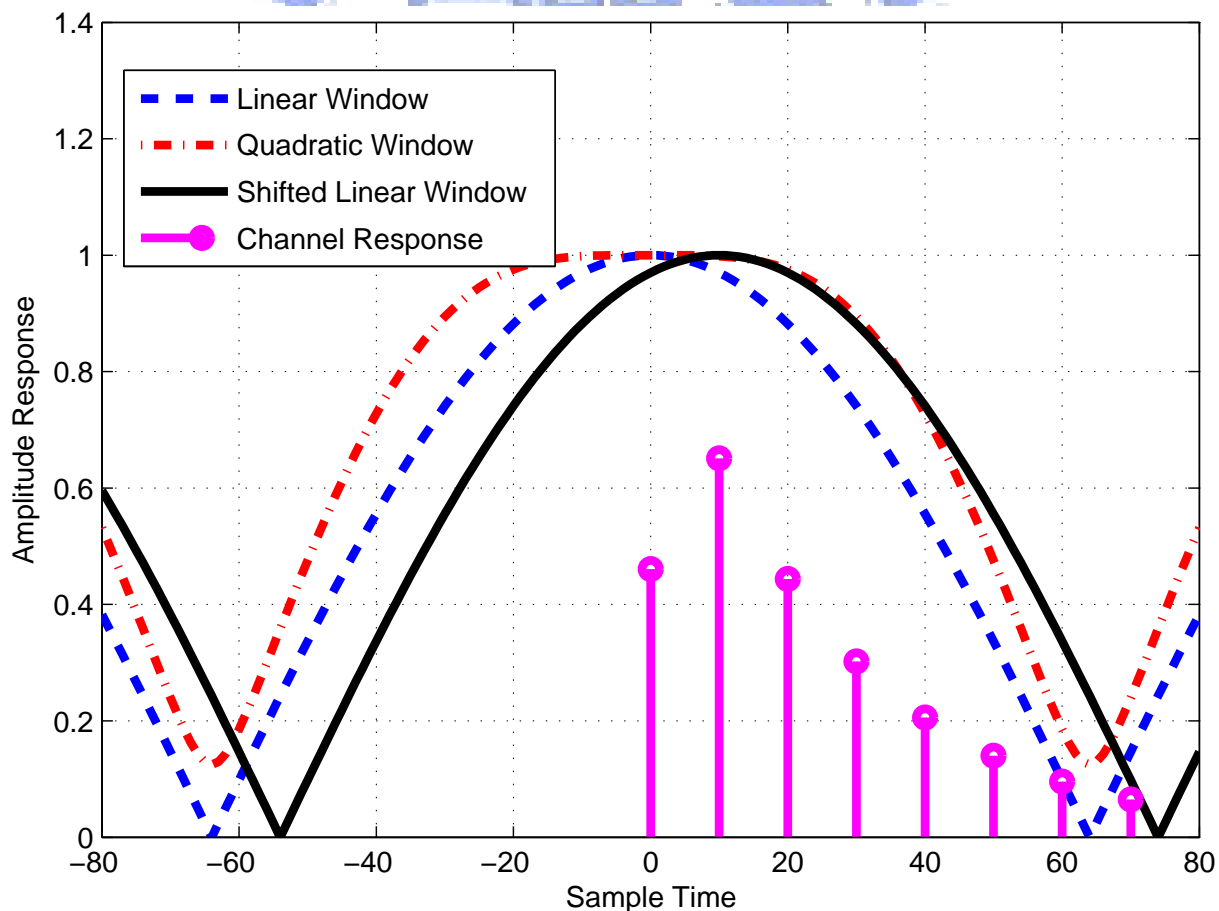


Figure 7.1: Comparison of different ways of interpolation in terms of the equivalent time-windowing effects.

noise environment. Then, the application of the proposed algorithm in mobile WiMAX system is also addressed and analyzed. According to the analytical result, we propose the adaptive selection of the interpolation order to minimize the MSE.

In what follows, we first consider the determination of MMSE window shift under given polynomial order in Section 7.1.2. We formulate the problem by expressing the MSE in polynomial channel interpolation in terms of the amount of window shift. Then we derive a way to estimate the optimal window shift approximately. Subsequently, we evaluate the performance of the resulting estimate in noisy channel, both by approximate theoretical analysis and via computer simulation, in Section 7.1.3. The Mobile WiMAX system [48, 98] provides an interesting and practically meaningful context to examine algorithm application. In Section 7.1.4, we adapt the proposed channel estimation technique to suit this context and examine the resulting performance. We also investigate the adaptive selection of interpolation order in this context, where the interpolation order is determined based on a predicted partial MSE of channel estimation. While adaptive order selection can be treated more broadly, the underlying principles are sufficiently borne out in the Mobile WiMAX context.

7.1.2 MMSE Window Shifting

Consider a generic discrete-time, equivalent lowpass multipath Rayleigh wireless channel impulse response

$$h(t) = \sum_{l=1}^L \alpha_l \delta(t - \tau_l), \quad (7.1)$$

where L is the number of paths, α_l is the complex Gaussian gain of the l th path, and τ_l is the associated path delay. Both t and τ_l are integers whose unit is the sampling period. The corresponding (normalized) frequency response is given by

$$H(f) = \sum_{l=1}^L \alpha_l W^{\tau_l f} \quad (7.2)$$

where $W = \exp(-j2\pi/N_s)$ and $H(f)$ has period N_s , with N_s being the DFT size used in multicarrier transformation.

Consider comb-type pilot allocation and let the m th pilot subcarrier be located at frequency $p_0 + mF$ where F is the spacing of pilot subcarriers. Let $\hat{H}(p_0 + mF)$ be some estimated channel responses at the pilot locations; how they are estimated is immaterial at this point. Then conventional polynomial interpolation between two pilot locations p and $p + F$ can be written as

$$\hat{H}(p + k) = \sum_{n=0}^N C_{n,k} \hat{H}(p + x_n) \quad (7.3)$$

where $0 < k < F$, N is the interpolation order, x_n defines the n th pilot location used in interpolation, and $C_{n,k}$ is the corresponding interpolation coefficient. While the pilots used in interpolation are usually chosen to be those nearest to $p+k$, their choice does not matter for now. The interpolation coefficients are real and are well-known [7] to be given in the Vandermonde form by

$$\begin{aligned} \underline{C}_k &\triangleq [C_{0,k} \ C_{1,k} \ \cdots \ C_{N,k}] \\ &= \underbrace{[1 \ k \ \cdots \ k^N]}_{\triangleq \underline{V}(k)} \underbrace{\begin{bmatrix} 1 & x_0 & \cdots & x_0^N \\ 1 & x_1 & \cdots & x_1^N \\ \vdots & \vdots & \ddots & \vdots \\ 1 & x_N & \cdots & x_N^N \end{bmatrix}}_{\triangleq \underline{X}}^{-1} \end{aligned} \quad (7.4)$$

or in the Lagrange form by

$$C_{n,k} = \prod_{m=0, m \neq n}^N \frac{k - x_m}{x_n - x_m}. \quad (7.5)$$

Now consider phase-rotated interpolation that corresponds to a window shift (i.e., time delay) of τ_c units of sample time, where τ_c is some value to be determined. The interpolator coefficients are given by $W^{\tau_c(k-x_n)}C_{n,k}$, yielding

$$\begin{aligned} \hat{H}(p+k) &= \sum_{n=0}^N \left[W^{\tau_c(k-x_n)} C_{n,k} \right] \hat{H}(p+x_n) \\ &= W^{\tau_c(p+k)} \sum_{n=0}^N C_{n,k} \left[W^{-\tau_c(p+x_n)} \hat{H}(p+x_n) \right]. \end{aligned} \quad (7.6)$$

The right-hand side (RHS) of the last equation adopts a useful intuitive interpretation as follows. If we advance the channel impulse response by τ_c , then we obtain an altered channel frequency response as

$$H_\tau(f) \triangleq W^{-\tau_c f} H(f) = \sum_{l=1}^L \alpha_l W^{\Delta \tau_l f} \quad (7.7)$$

where $\Delta \tau_l = \tau_l - \tau_c$ is the τ_c -early version of the l th path delay. Comparing with the last bracketed term in (7.6), we see that the latter represents a τ_c -advanced channel estimate, but only for the pilot subcarriers. This channel estimate is interpolated in the conventional way, as indicated by the last summation in (7.6). The result is then phase-rotated, through premultiplication with $W^{\tau_c(p+k)}$, by an amount corresponding to a time delay of τ_c to undo the earlier time advancement. With this we obtain the window-shifted channel estimate.

To recapitulate, we have arrived at the following procedure for channel estimation, assuming that a proper value for τ_c has been found: 1) obtain channel estimates at the pilot subcarriers using an appropriate method, 2) phase-rotate the above channel estimates by an amount corresponding to time advance by τ_c , 3) perform conventional polynomial interpolation to obtain channel estimates at the data subcarriers, and 4) phase-derotate the channel estimates to undo the effect of the earlier time advance. As indicated previously, when τ_c is an integer, a simple time-domain equivalent exists for steps 2) and 4) that can eliminate the need of phase rotation and derotation. But for theoretical derivation below we stay with the above formulation.

Note that, though we have limited the treatment to comb-type pilot allocation, the results can be readily extended to noncomb-type pilot allocation. But the equations become somewhat cumbersome, and thus we omit the discussion.

Now we turn to the key issue of determining τ_c . For this we first find how the channel estimation MSE depends on τ_c under arbitrary polynomial interpolation order. Then in the next subsection we derive a suboptimal solution for τ_c .

MSE As Function of Window Shift

For convenience, let

$$\hat{H}_\tau(f) = W^{-\tau_c f} \hat{H}(f). \quad (7.8)$$

Then by (7.6) we have

$$\hat{H}_\tau(p+k) = \sum_{n=0}^N C_{n,k} \hat{H}_\tau(p+x_n). \quad (7.9)$$

The MSE in $\hat{H}_\tau(p+k)$ (as an estimate of $H_\tau(p+k)$) is the same as that in $\hat{H}(p+k)$ (as an estimate of $H(p+k)$), for the two estimates are related by mere phase rotation. Hence

we derive the former. To concentrate on the modeling error due to τ_c -advanced N th-order polynomial interpolation, we ignore the effect of channel noise for the moment. That is, we assume temporarily that the channel estimates at the pilot subcarriers are perfect, so that $\hat{H}_\tau(p + x_n) = H_\tau(p + x_n)$.

The N th-order Taylor series expansion of $H_\tau(p + k)$ about a subcarrier p is given by

$$H_\tau(p + k) = \sum_{n=0}^N \frac{H_\tau^{(n)}(p)k^n}{n!} + R_N(p + k) \quad (7.10)$$

where $H_\tau^{(n)}(p)$ is the n th derivative of $H_\tau(p)$ and $R_N(p + k)$ is the remainder term. By the integral form of the remainder term,

$$\begin{aligned} R_N(p + k) &= \int_0^k \frac{H_\tau^{(N+1)}(p + u)}{N!} (k - u)^N du \\ &= \sum_{l=1}^L \alpha_l (-j2\pi\Delta\tau_l/N_s)^{N+1} W^{\Delta\tau_l p} \\ &\quad \cdot \int_0^k \frac{W^{\Delta\tau_l u}}{N!} (k - u)^N du. \end{aligned} \quad (7.11)$$

From (7.9) and (7.4), the estimation error for $H_\tau(p + k)$ is given by

$$\begin{aligned} \bar{e}(p + k) &\triangleq H_\tau(p + k) - \hat{H}_\tau(p + k) \\ &= H_\tau(p + k) - \underline{C}_k \hat{\underline{H}}(p) \\ &= H_\tau(p + k) - \underline{V}(k) X^{-1} \hat{\underline{H}}(p) \end{aligned} \quad (7.12)$$

where

$$\hat{\underline{H}}(p) = \left[\hat{H}_\tau(p + x_0), \hat{H}_\tau(p + x_1), \dots, \hat{H}_\tau(p + x_N) \right]^T. \quad (7.13)$$

Since no error arises in interpolating a polynomial function of order N or below, all errors in (7.12) are from the remainder terms $R_N(p + k)$ and $R_N(p + x_n)$, $n = 0, 1, \dots, N$. Hence

$$\bar{e}(p + k) = R_N(p + k) - \underline{V}(k) X^{-1} \underline{R}_N(p) \quad (7.14)$$

where

$$\underline{R}_N(p) = [R_N(p + x_0), R_N(p + x_1), \dots, R_N(p + x_N)]^T. \quad (7.15)$$

From (7.11), if subcarriers p and $p + k$ are spaced closely compared to the coherence bandwidth such that $W^{\Delta\tau_l u} \approx 1$ for $0 \leq u \leq k$, then

$$\int_0^k \frac{W^{\Delta\tau_l u}}{N!} (k - u)^N du \approx \frac{k^{N+1}}{(N + 1)!} \quad (7.16)$$

and thence

$$\begin{aligned} R_N(p + k) &\approx \frac{k^{N+1}}{(N + 1)!} \sum_{l=1}^L \alpha_l \left(\frac{-j2\pi\Delta\tau_l}{N_s} \right)^{N+1} W^{\Delta\tau_l p} \\ &\triangleq \frac{k^{N+1}}{(N + 1)!} \xi_N(p). \end{aligned} \quad (7.17)$$

Assume that the approximation (7.17) also holds for $k = x_n$ and substitute it into (7.14). We get

$$\bar{e}(p + k) \approx \frac{1}{(N + 1)!} [k^{N+1} - \underline{V}(k) X^{-1} \underline{x}] \xi_N(p) \quad (7.18)$$

where

$$\underline{x} = [x_0^{N+1}, x_1^{N+1}, \dots, x_N^{N+1}]^T. \quad (7.19)$$

In the Appendix, we show that

$$G(k) \triangleq [k^{N+1} - \underline{V}(k)X^{-1}\underline{x}] = \prod_{n=0}^N (k - x_n). \quad (7.20)$$

As a result, the MSE is given by

$$\begin{aligned} \sigma_e^2(k) &= \frac{1}{[(N+1)!]^2} G^2(k) \langle\langle |\xi_N(p)|^2 \rangle\rangle \\ &= \frac{1}{[(N+1)!]^2} G^2(k) \frac{(2\pi)^{2N+2}}{N_s^{2N+2}} \sum_{l=1}^L |\alpha_l|^2 \Delta\tau_l^{2N+2} \\ &\triangleq \frac{1}{[(N+1)!]^2} G^2(k) \sigma_\xi^2(N, \tau_c) \end{aligned} \quad (7.21)$$

where $\langle\langle \cdot \rangle\rangle$ denotes averaging over all pilot subcarriers, that is, $\langle\langle v(p) \rangle\rangle = \sum_{p=p_0+mF, \forall m} v(p)/M$ with M being the number of pilot subcarriers. The second equality in the last equation indicates that the MSE is dominated by the channel paths with larger values of $|\alpha_l|^2 \Delta\tau_l^{2N+2}$, each of which in turn is proportional to the $2N+2$ nd power of the associated differential delay $\Delta\tau_l$.

Estimation of Optimal Window Shift

From previous results, we see that the channel estimation MSE is minimized by minimizing $\sigma_\xi^2(N, \tau_c)$. Hence by elementary calculus, the optimal window shift can be obtained by solving the equation

$$\frac{d\sigma_\xi^2(N, \tau_c)}{d\tau_c} = \frac{(2\pi)^{2N+2}(2N+2)}{N_s^{2N+2}} \sum_{l=1}^L |\alpha_l|^2 (\tau_l - \tau_c)^{2N+1} = 0 \quad (7.22)$$

However, this requires knowing the multipath gains and delays, which are usually unknown until after channel estimation. Below we present a technique that sidesteps this dilemma.

A key to solving the problem is to note that since

$$H_\tau^{(N+1)}(f) = \sum_{l=1}^L \alpha_l (-j2\pi\Delta\tau_l/N_s)^{N+1} W^{\Delta\tau_l f}, \quad (7.23)$$

by Parseval's theorem we get

$$\sigma_\xi^2(N, \tau_c) = \langle |H_\tau^{(N+1)}(f)|^2 \rangle \quad (7.24)$$

where $\langle \cdot \rangle$ denotes averaging over all frequencies. Thus minimizing $\sigma_\xi^2(N, \tau_c)$ is equivalent to minimizing $\langle |H_\tau^{(N+1)}(f)|^2 \rangle$. While $H_\tau^{(N+1)}(f)$ is usually not available, either, it can be approximated by the $N+1$ st order difference.

For example, consider approximating it by the $N+1$ st forward difference given by

$$\begin{aligned} &D_{N+1}H_\tau(p) \\ &= \frac{1}{F^{N+1}} \sum_{n=0}^{N+1} (-1)^n \binom{N+1}{n} H_\tau(p + (N+1-n)F). \end{aligned} \quad (7.25)$$

The approximate cost function is then given by

$$\begin{aligned} \sigma_{\xi}^2(N, \tau_c) &\approx J \\ &\triangleq \frac{1}{F^{2N+2}} \cdot \left\langle \left\langle \left| \sum_{n=0}^{N+1} (-1)^n \binom{N+1}{n} \hat{H}_{\tau}(p + (N+1-n)F) \right|^2 \right\rangle \right\rangle. \end{aligned} \quad (7.26)$$

Some algebraic manipulations result in

$$J = \frac{1}{F^{2N+2}} [P_N R_0 + 2J_N(\theta)] \quad (7.27)$$

where $P_N = 2^{N+1}(2N+1)!!/(N+1)!$, $\theta = 2\pi F\tau_c/N_s$, $R_n = \langle \langle \hat{H}(p+nF)\hat{H}^*(p) \rangle \rangle$, and

$$J_N(\theta) = \Re \left\{ \sum_{m=1}^{N+1} (-1)^m A_{N,m} e^{-jm\theta} R_m \right\} \quad (7.28)$$

with $m!! = m(m-2)(m-4)\cdots x$ where $x = 2$ for even m and $x = 1$ for odd m , and

$$\begin{aligned} A_{N,m} &= \sum_{n=m}^{N+1} \binom{N+1}{n} \binom{N+1}{n-m} \\ &= \frac{2^{N+1}(2N+1)!!(N+1)!}{(N+1-m)!(N+1+m)!}. \end{aligned} \quad (7.29)$$

Noting that only $J_N(\theta)$ depends on τ_c , we may obtain an estimate of the optimal window shift as

$$\hat{\tau}_c = \frac{N_s}{2\pi F} \arg \min_{\theta} J_N(\theta). \quad (7.30)$$

For linear, quadratic and cubic interpolators, we have

$$\begin{aligned} J_1(\theta) &= \Re \left\{ e^{-j2\theta} R_2 - 4e^{-j\theta} R_1 \right\}, \\ J_2(\theta) &= \Re \left\{ -e^{-j3\theta} R_3 + 6e^{-j2\theta} R_2 - 15e^{-j\theta} R_1 \right\}, \\ J_3(\theta) &= \Re \left\{ e^{-j4\theta} R_4 - 8e^{-j3\theta} R_3 + 28e^{-j2\theta} R_2 \right. \\ &\quad \left. - 56e^{-j\theta} R_1 \right\}. \end{aligned} \quad (7.31)$$

To actually compute (7.30), one way is to solve the equation $dJ_N(\theta)/d\theta = 0$ and find the solution that minimizes $J_N(\theta)$. Note that the desired θ must lie in the interval $[0, 2\pi F\tau_{\max}/N_s]$ where τ_{\max} is the maximum path delay. Unfortunately, algebraic solution exists only in the case of linear interpolation, for it is the only case where the equation to be solved has order less than 5 [41]. Numerical solutions have to be resorted to in other cases. This being so, one might as well search over $[0, 2\pi F\tau_{\max}/N_s]$ directly for value of θ that minimizes $J_N(\theta)$ rather than find it indirectly through solving $dJ_N(\theta)/d\theta = 0$. The density of searched points can be chosen according to the desired accuracy. Indeed, direct search may even require less computation than equation solving when the searched points are not excessively many. By experience, we find that a suitable search granularity is roughly 2 to 6 times $2\pi F/N_s$, or equivalently, 2 to 6 sample periods.

Moreover, in current systems the channel path delays usually do not vary significantly over several multicarrier symbols. Nor do the path gains vary violently over consecutive multicarrier symbols. These have several implications. First, after proper initialization, it is reasonable to perform incremental search for optimal θ within a small range around the previous solution, instead of conducting a full search over the entire interval. And secondly, if the optimal window shift should not vary significantly over multiple multicarrier symbols, then we may update the shift only once every few symbols. Thus the computational complexity can be further reduced.

7.1.3 Performance With Comb-Type Pilots

Now consider the overall MSE in channel estimation by the proposed method. The estimation error arises from three sources, namely, 1) error from interpolation (i.e., the modeling error analyzed in Section 7.1.2), 2) use of the suboptimal window shift given by (7.30), and 3) the channel noise (which has been ignored thus far). The effect of source 2 (suboptimal estimation of window shift) defies an easy and general characterization as, from (7.21), it not only enters the modeling error in a complicated way but also depends on the channel property. Fortunately, in the simulated conditions presented later where the pilots are relatively densely spaced, it turns out that this error source contributes a minor amount in the total MSE. So we omit its effect and assume perfect estimation of the (approximately) optimal window shift defined by (7.22). In the following analysis, assume that the channel noise is additive white Gaussian, i.e., AWGN, and that it is independent of the modeling error.

For simplicity, let the pilot spacing F be an integer fraction of N_s . Then from (7.21), the average MSE due to modeling error is given by

$$\begin{aligned}\sigma_e^2 &\triangleq \frac{1}{F-1} \sum_{k=1}^{F-1} \sigma_e^2(k) \\ &= \underbrace{\frac{1}{(F-1)[(N+1)!]^2}}_{\triangleq Q(N,F)} \sum_{k=1}^{F-1} G^2(k) \sigma_\xi^2(N, \tau_c^o)\end{aligned}\quad (7.32)$$

where τ_c^o is the (approximately) optimal delay defined by (7.22). To calculate specific values for $Q(N, F)$, we need to define x_n specifically. For this, consider letting x_n lie in the range $-\lfloor N/2 \rfloor F$ to $\lfloor (N+1)/2 \rfloor F$ so that it is as small in magnitude as possible. And discard the nonpilot subcarriers that are too near a bandedge that there do not exist $N+1$ pilots in the above range for interpolation use. Then for linear, quadratic, and cubic interpolation we get, respectively,

$$\begin{aligned}Q(1, F) &= \frac{1}{120} F(F+1)(F^2+1), \\ Q(2, F) &= \frac{1}{7560} F(F+1)(2F-1)(2F+1)(4F^2+5), \\ Q(3, F) &= \frac{1}{362880} F(F+1) \\ &\quad \cdot (103F^6 + 103F^4 + 61F^2 + 21).\end{aligned}\quad (7.33)$$

The value of $\sigma_\xi^2(N, \tau_c^o)$ is channel-dependent and no general formulas can be given.

For the contribution of the AWGN, consider (7.3). Let the pilots have unity magnitude and let the frequency response $H(p+x_n)$ be estimated by the least-squares (LS) method, that is, by simply dividing the received signal value at subcarrier $p+x_n$ by the transmitted pilot value there. Then the MSE in $\hat{H}(p+x_n)$ is equal to the AWGN variance, which we denote by σ_n^2 . Hence, the AWGN contribution in the channel estimation MSE at subcarrier $p+k$ is given by

$$\sigma_w^2(k) \triangleq \sigma_n^2 \|\underline{C}_k\|^2 = \sigma_n^2 \underline{V}(k) (\underline{X}\underline{X}^T)^{-1} \underline{V}(k)^T. \quad (7.34)$$

and the average over all data subcarriers is given by $\sigma_w^2 = \sum_{k=1}^{N-1} \sigma_w^2(k)/(F-1)$. In particular,

we have

$$\begin{aligned}
\sigma_w^2 &= \left(0.667 - \frac{0.333}{F} \right) \sigma_n^2, \\
\sigma_w^2 &= \left(0.8 - \frac{0.2}{F} + \frac{0.05}{F^2} + \frac{0.05}{F^3} \right) \sigma_n^2, \\
\sigma_w^2 &= \left(0.776 - \frac{0.224}{F} - \frac{0.058}{F^2} - \frac{0.058}{F^3} - \frac{0.013}{F^4} + \frac{0.013}{F^5} \right) \cdot \sigma_n^2,
\end{aligned} \tag{7.35}$$

for linear, quadratic, and cubic interpolations, respectively.

The overall approximate channel estimation MSE is given by $\sigma_e^2 + \sigma_w^2$.

Numerical Examples

As an example, consider an OFDM system with comb-type pilot arrangement. Let bandwidth = 10 MHz, DFT size $N_s = 1024$, CP length = $N_s/8 = 128$, and pilot spacing $F = 4$ subcarriers. We compare phase-shifted linear, quadratic, and cubic interpolation with conventional interpolation. In phase-shifted interpolation, the amount of shift is obtained by search over the interval $[0, \pi]$ for the best θ value at 32 uniformly spaced points. That is, the search granularity is 2 sample periods. The SUI-4 and SUI-5 power-delay profiles (PDPs) are simulated [20], whose power profiles are $[0, -4, -8]$ and $[0, -5, -10]$ (in dB) and delay profiles are $[0, 14, 36]$ and $[0, 45, 112]$ (in sample periods), respectively. In our simulation, we let the path coefficients be Rayleigh distributed and change from symbol to symbol (i.e., subject to block-static fading). A total of 2000 simulation runs are used to obtain the MSE statistics for each signal-to-noise (SNR) value.

Figs. 7.2 and 7.3 show histograms of the estimated window shifts for different interpolation orders over SUI-4 and SUI-5, respectively. Figs. 7.4 and 7.5 illustrate the corresponding channel estimation performance, where the normalization of MSE is relative to channel power gain. In the case of SUI-4 (Fig. 7.4), the approximate analysis for phase-shifted interpolation and the corresponding simulation results are almost indistinguishable. The figure also shows that conventional interpolation suffers significant loss at high SNR values from the MSE floor caused by higher modeling error compared to phase-shifted interpolation, which can maintain a -1 slope in the performance curves to much higher SNR values. In the case of cubic interpolation, the range of -1 slope goes up to as high as approximately 50 dB in SNR.

For SUI-5, which has a greater delay spread than SUI-4, the approximate analysis for phase-shifted interpolation overestimates the MSE by some amount. And the slopes of the MSE curves level off at lower SNR values in comparison to SUI-4. Conventional interpolation again performs significantly worse than phase-shifted interpolation, by roughly 5, 9, and 13 dB in MSE floor for linear, quadratic, and cubic interpolations, respectively.

For comparison, Figs. 7.4 and 7.5 also show the performance of four-tap linear MMSE channel estimation under two conditions. One of them has the filter coefficients calculated using the exact channel correlation function (the “exact MMSE” curves) and the other has them calculated using the channel correlation function corresponding to a uniform PDP of length equal to the CP (the “approximate MMSE” curves). Not surprisingly, the “exact MMSE” case has the best performance among all, but it is not practical. Moreover, in a channel with reasonably short delay spread, such as SUI-4, phase-shifted cubic interpolation can provide comparable performance. Regarding the approximate MMSE solution, it is quite poor in SUI-4 compared to phase-shifted polynomial interpolation, but is comparable to phase-shifted cubic interpolation in SUI-5 that has a longer delay spread.

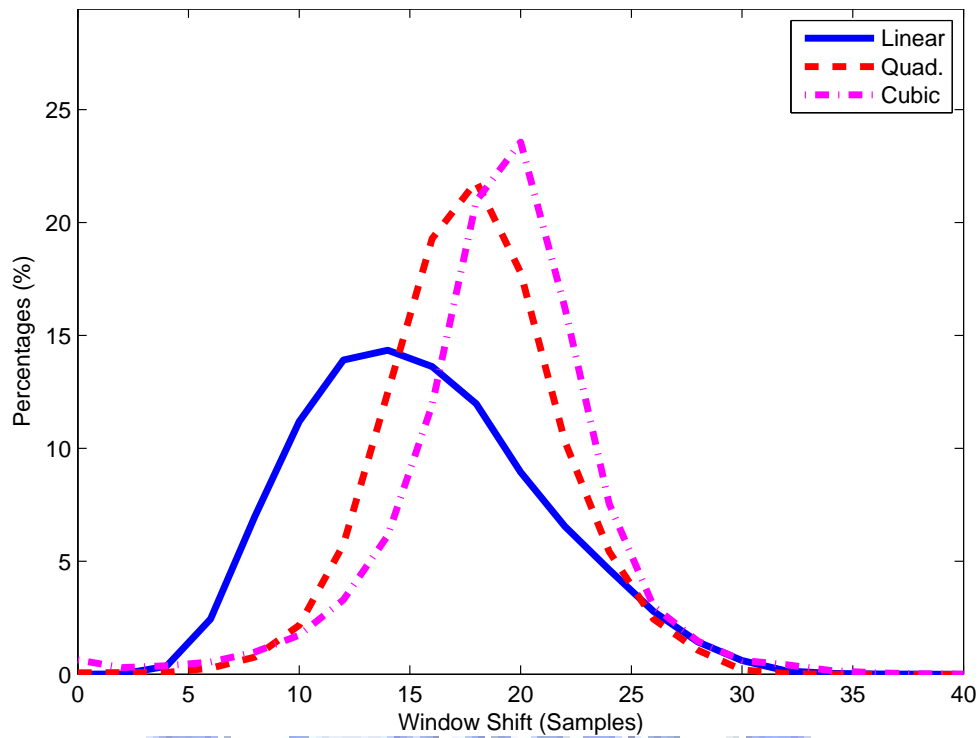


Figure 7.2: Histogram of estimated window shifts for different orders of polynomial interpolations over SUI-4 at 30 dB SNR.

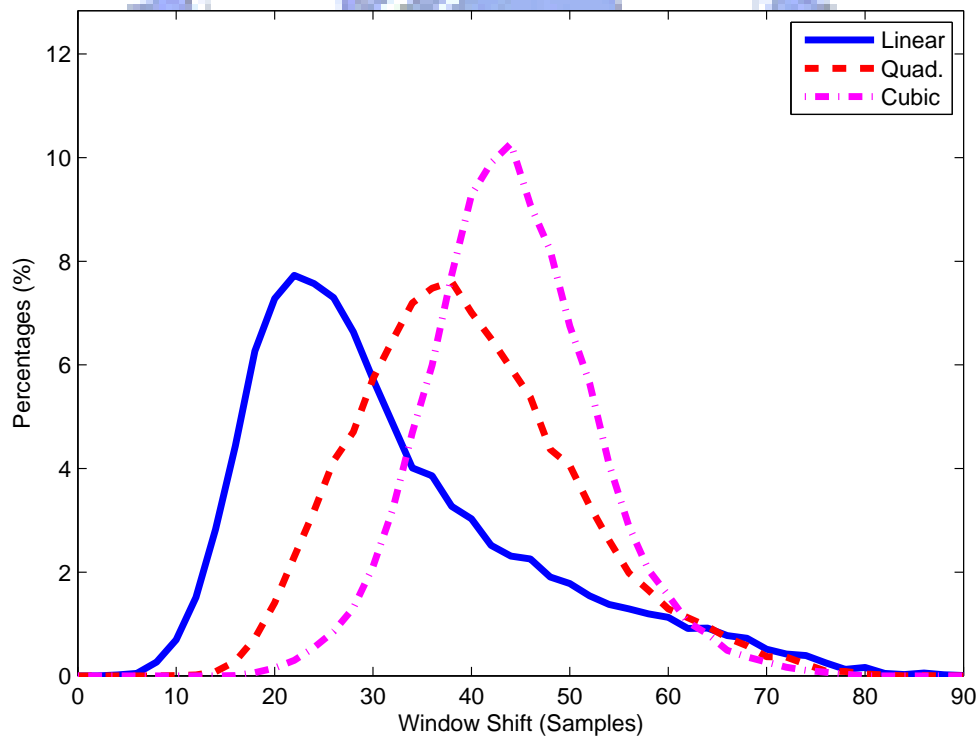


Figure 7.3: Histogram of estimated window shifts for different orders of polynomial interpolations over SUI-5 at 30 dB SNR.

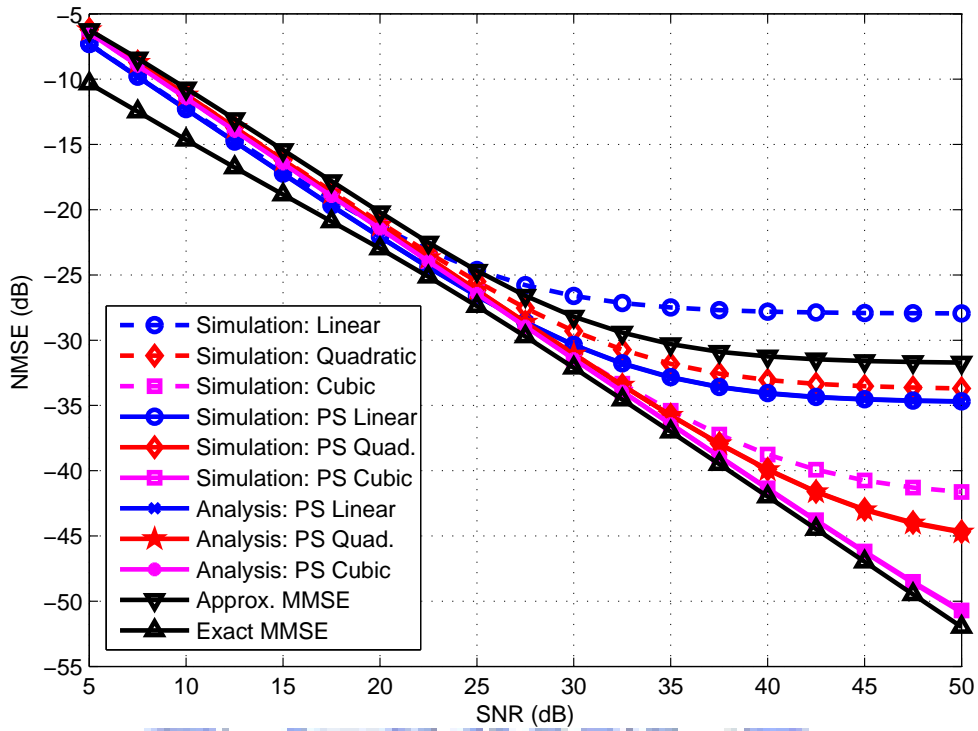


Figure 7.4: Normalized MSE (NMSE) of different channel estimation methods under the SUI-4 PDP, where “PS” stands for “phase-shifted.”

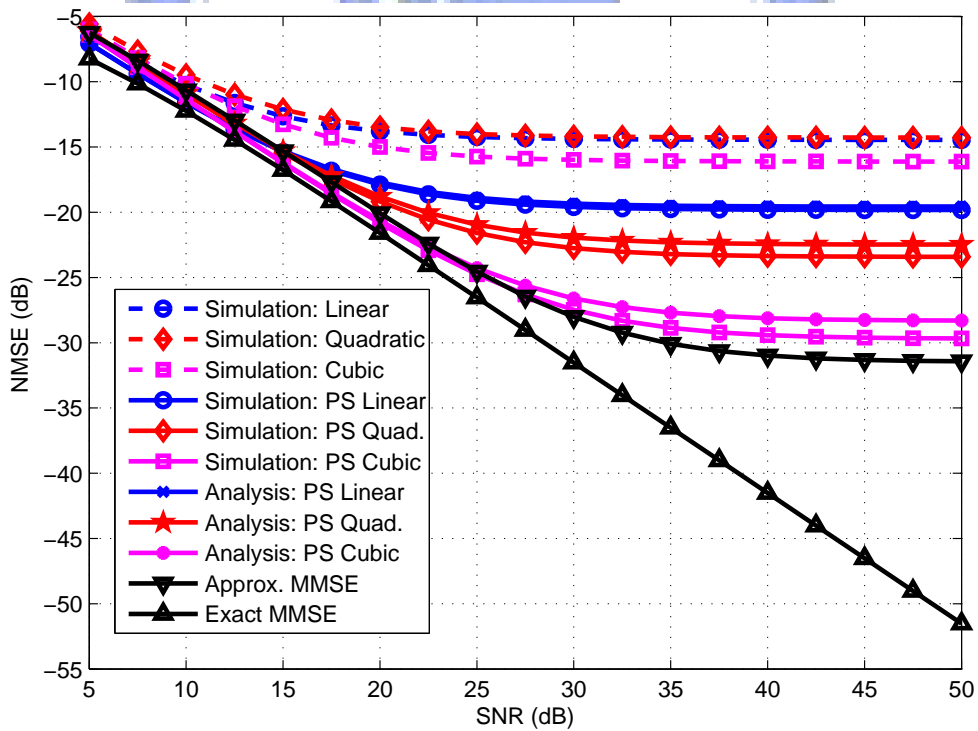


Figure 7.5: NMSE of different channel estimation methods under the SUI-5 PDP, where “PS” stands for “phase-shifted.”

Periodic Update of Window Shift

Near the end of Section 7.1.2, we indicated the possibility of updating the window shift at a longer period than one multicarrier symbol for reduced computational complexity. Its impact is increased suboptimality in the estimated window shift $\hat{\tau}_c$. However, as pointed out towards the beginning of this section, we are unable to obtain a simple and more general characterization of the effect on channel estimation MSE of such suboptimality beyond that already characterized, e.g., in (7.21). Hence we resort to simulation to investigate the effect.

For this, consider the SUI-5 PDP again. Let the carrier frequency be 2.5 GHz. Other system parameters are the same as before. We consider three update periods (T): 1, 10, and 20 OFDM symbol times. Figs. 7.6(a)–7.6(c) depict the simulation results with the channel subject to block-static fading at rates corresponding to mobile speeds of 30, 100, and 200 km/h, respectively. (The corresponding peak Doppler shifts are 0.008, 0.0267, and 0.0533 per OFDM symbol, respectively.) At 30 km/h, the update period of 10 symbols degrades the performance by only very little compared to updating every symbol. Even a period of 20 symbols causes only a small loss. The degradations due to longer update periods are more pronounced at the higher speeds of 100 and 200 km/h. At 100 km/h, about 1 dB loss in the MSE floor is incurred with a 10-symbol update period and about 2 dB loss with a 20-symbol period, for all interpolation orders. At 200 km/h, the loss increases to roughly 1.5 and 2 dB, respectively, for update periods of 10 and 20 symbols for all interpolation orders.

Fig. 7.6(d) shows the results under the SUI-4 PDP at 200 km/h of mobile speed. With the smaller delay spread of this channel compared to SUI-5, the loss due to increased update period becomes significantly smaller. In particular, no perceivable degradation occurs in the case of cubic interpolation.

In summary, the limited simulation results demonstrate that the performance loss due to an increased update period of the window shift is dependent on the mobile speed and the channel delay spread. It also depends on the interpolation order, but maybe to a lesser degree. A more exact characterization of these dependencies is outside the scope of the present work and is left to potential future work.

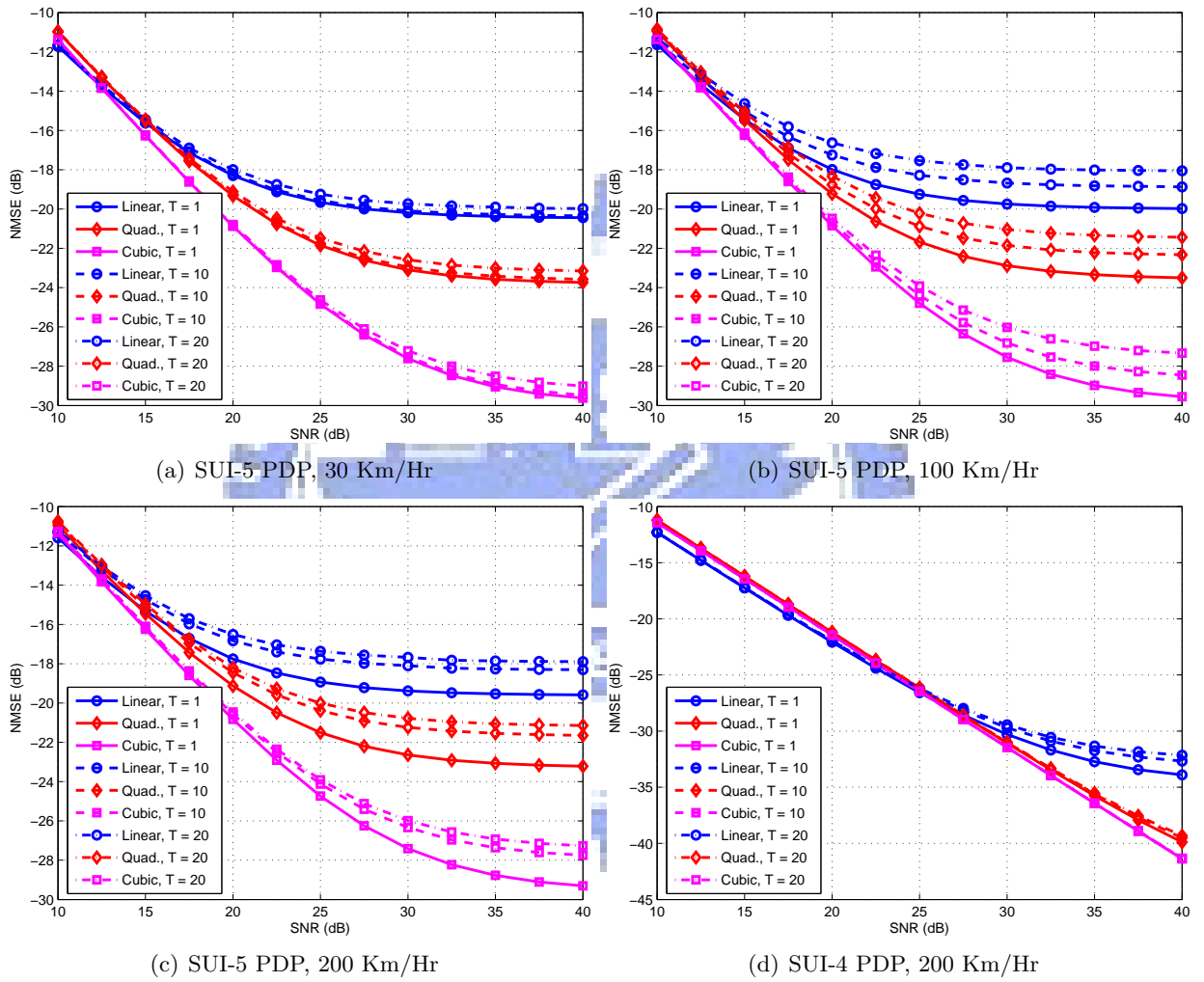


Figure 7.6: MSE performance in different update periods of window shift under different channel models and motion speed.

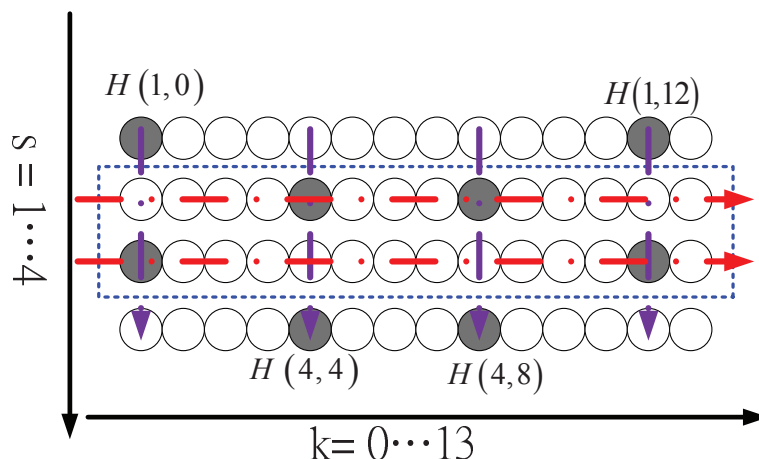


Figure 7.7: Cluster structure in Mobile WiMAX downlink and corresponding channel estimation method.

7.1.4 Application to WiMAX Downlink

The Mobile WiMAX specifications furnish an interesting example to test the performance of the proposed technique. In the WiMAX downlink (DL), the subcarriers in an orthogonal frequency-division multiple access (OFDMA) symbol are divided into “clusters” that contain 14 consecutive subcarriers each. Alternating patterns of pilot subcarriers are placed in temporally successive symbols. Fig. 7.7 illustrates how pilots are placed in a cluster, where each circle indicates a subcarrier and the 14 subcarriers in the cluster are ordered from left to right. The dark circles indicate pilot subcarriers. For convenience, in this section let $H(s, k)$ denote the channel response at the k th subcarrier of some cluster in symbol s . In the following, we tailor the proposed channel estimation technique to suit the WiMAX downlink signal structure and investigate the resulting channel estimation performance, assuming perfect carrier frequency and symbol timing synchronization. We also propose a method to adaptively select the interpolation order for minimizing the channel estimation MSE.

Channel Estimator Design

Since the assignment of clusters to users is pseudo-random, two nearest clusters of a user may not be adjacent in frequency. Thus it is simplest to let the channel estimator handle the clusters at different frequency positions separately. In each cluster, there are only two pilot subcarriers whose distance varies with symbol index. In a typical system with 10 MHz bandwidth and $N_s = 1024$, two adjacent subcarriers are approximately 10 kHz apart [48, 98]. Hence in odd-numbered symbols the pilots are spaced by over 100 kHz, which is about the same order of magnitude as the coherence bandwidth of a typical urban outdoor channel [84]. Linear interpolation, even with optimal window shift, is not expected to yield good performance over this distance. But with only two pilots, we cannot perform higher-order interpolation. In even-numbered symbols, extrapolation is needed to estimate the channel at the data subcarriers on the outsides of the pilots. Such extrapolation amplifies the noise because at least one extrapolation coefficient is greater than 1. Therefore, for better performance, a channel estimator should not limit itself to using the two only pilots in the current cluster, but should avail itself of the channel information at the two other pilot frequencies in temporally close clusters. This prompts the following basic design. For convenience, we describe it for symbols 2 and 3 (enclosed in the dashed box in Fig. 7.7) together.

1. Do LS channel estimation for all pilot subcarriers in symbols 1 to 4.
2. Linearly interpolate in time to obtain $\hat{H}(2, 0)$, $\hat{H}(2, 12)$, $\hat{H}(3, 4)$ and $\hat{H}(3, 8)$ (indicated by vertical arrows in Fig. 7.7).
3. Do phase-shifted polynomial interpolation in frequency to obtain channel estimates for the remaining subcarriers in symbols 2 and 3 (indicated by horizontal arrows in Fig. 7.7).

Now, we mentioned previously that the phase-shifting effect in step 3 can be achieved in several ways. In particular, if the corresponding amount of window shift $\hat{\tau}_c$ is a known integer, then the effect can be achieved by circular shifting of the received signal by $-\hat{\tau}_c$ before DFT. In this regard, earlier discussion indicates that we need not go to a fractional-sample accuracy in the value of $\hat{\tau}_c$; rather, a granularity of 2 to 6 samples can be enough. Therefore, we may let $\hat{\tau}_c$ be an integer. In addition, to save computation, we estimate $\hat{\tau}_c$ only once per DL subframe, employing the preamble symbol that begins the subframe. Thus $\hat{\tau}_c$ is known for all later OFDMA symbols in the subframe. The final channel estimation method (for symbols 2 and 3) is as follows.

1. Recall the value of $\hat{\tau}_c$ that has been estimated using the preamble symbol by the method of Section 7.1.2.
2. Circularly shift the signal samples in symbols 1 to 4 by $-\hat{\tau}_c$ before taking their DFT. This is equivalent to having a channel with phase-rotated frequency response $H_\tau(s, k) = W^{-\hat{\tau}_c f(k)} H(s, k)$ where $f(k)$ denotes the normalized frequency of subcarrier k . (We have used an adapted version of the notations in (7.7) here.)
3. Do LS channel estimation for pilot subcarriers in symbols 1 to 4. This yields, for each pilot with time-frequency index (s, k) , a phase-rotated channel estimate $\hat{H}_\tau(s, k) = W^{-\hat{\tau}_c f(k)} \hat{H}(s, k)$. (We have used an adapted version of the notations in (7.8) here.)
4. Linearly interpolate in time to obtain $\hat{H}_\tau(2, 0)$, $\hat{H}_\tau(2, 12)$, $\hat{H}_\tau(3, 4)$ and $\hat{H}_\tau(3, 8)$.
5. Perform conventional interpolation (and extrapolation) in frequency to obtain channel estimates for the remaining subcarriers in symbols 2 and 3. This corresponds to the operation described in (7.9), or equivalently, that in the last summation in (7.6).

Note that we do not have to carry out the phase-derotation indicated by the premultiplication with $W^{\tau_c(p+k)}$ in the RHS of (7.6), for by the circular signal shifting in step 2, the phase-rotated channel becomes what is needed for signal detection, not the phase-derotated one. Note also that step 4 (temporal interpolation) results in four reference data points per cluster. Hence in step 5 we may employ an interpolation order up to three. For N th-order interpolation, to minimize the modeling error in step 5, we use the $N + 1$ nearest pilots of each data subcarrier to interpolate for its channel response.

Performance Analysis

Four factors contribute to the channel estimation error. They are, in order of their appearance in the channel estimation steps, 1) suboptimality in the estimated window shift (introduced in step 1), 2) the AWGN (introduced in step 3), 3) modeling error due to time-domain interpolation (introduced in step 4), and 4) modeling error due to frequency-domain interpolation (introduced in step 5). Compared to the earlier analysis done in Section 7.1.3, the only additional item is item 3. However, due to this item, the AWGN propagates among the subcarriers in a different way than in the previous analysis. The time-domain interpolation error itself propagates through algorithm step 5, too. Moreover, the pilots used for interpolation at a data subcarrier are chosen

somewhat differently than in Section 7.1.3 and the bandedge subcarriers are not discarded as before. Therefore, we will need to redo some analysis.

Again, item 1 is difficult to analyze but, fortunately, constitutes a minor contribution in the total MSE. Thus only the other three factors need to be analyzed. Assume that these three kinds of error are uncorrelated.

First, consider the AWGN. It enters the channel estimator computation through the LS channel estimation conducted at the pilot subcarriers. Since the pilots are BPSK-modulated, let the estimation noise variance at a pilot be denoted σ_n^2 as in the previous analysis. This estimation noise propagates to other subcarriers in the temporal interpolation of step 4 and the frequency interpolation of step 5. Via the temporal interpolation, it contaminates $\hat{H}_\tau(s, k)$ where $(s, k) \in \{(2, 4), (2, 8), (3, 0), (3, 12)\}$. Since $\hat{H}_\tau(s, k) = [\hat{H}_\tau(s-1, k) + \hat{H}_\tau(s+1, k)]/2$ where $\hat{H}_\tau(s-1, k)$ and $\hat{H}_\tau(s+1, k)$ contain independent additive noise, the noise variance in $\hat{H}_\tau(s, k)$ is given by

$$\sigma_w^2(s, k) = \left(\frac{1}{2}\right)^2 \sigma_n^2 + \left(\frac{1}{2}\right)^2 \sigma_n^2 = \frac{1}{2}\sigma_n^2. \quad (7.36)$$

Via the frequency interpolation, it results in an estimation noise variance

$$\sigma_w^2(s, k) = \sum_{n=0}^N C_{n,k}^2 \sigma_w^2(s, x_n) \quad (7.37)$$

where $s \in \{2, 3\}$, $k \in \{1, 2, 3, 5, 6, 7, 9, 10, 11, 13\}$, and $x_n \in \{0, 4, 8, 12\}$, with $C_{n,k}$ indexed similarly to (7.3). Averaging all data subcarriers, we obtain the average noise variance as

$$\sigma_{w,1}^2 = 0.5130\sigma_n^2, \quad \sigma_{w,2}^2 = 0.6699\sigma_n^2, \quad \sigma_{w,3}^2 = 0.8121\sigma_n^2, \quad (7.38)$$

where the second subscript to σ denotes interpolation order.

Secondly, consider the modeling error in temporal interpolation. Its mean-square value is defined by

$$\sigma_D^2(s, k) = E \left| H_\tau(s, k) - \frac{1}{2} [H_\tau(s-1, k) + H_\tau(s+1, k)] \right|^2 \quad (7.39)$$

for $(s, k) \in \{(2, 0), (2, 12), (3, 4), (3, 8)\}$. Assume Rayleigh faded paths. Then [84, 41]

$$\begin{aligned} \sigma_D^2(s, k) &= \sum_{l=1}^L A_l^2 \left[\frac{3}{2} - 2J_0(2\pi f_l) + \frac{1}{2}J_0(4\pi f_l) \right] \\ &\approx \frac{3\pi^4}{2} \sum_{l=1}^L f_l^4 A_l^2 \triangleq \sigma_D^2 \end{aligned} \quad (7.40)$$

where $A_l^2 = E|\alpha_l|^2$, f_l is the peak Doppler shift of path l times the OFDMA symbol period, $J_0(\cdot)$ is the Bessel function of the first kind of order 0, and the approximation is obtained by expanding the Bessel function into a second-order Taylor series. Assume that the channel responses at different subcarriers are uncorrelated. Then a relation similar to (7.37) exists concerning the propagation of the temporal modeling error in the frequency domain via channel estimation step 5. Noting that the temporal interpolation error is zero at the pilot locations, we get the average MSE of temporal interpolation over all data subcarriers as

$$\sigma_{d,1}^2 = 0.4531\sigma_D^2, \quad \sigma_{d,2}^2 = 0.5577\sigma_D^2, \quad \sigma_{d,3}^2 = 0.6525\sigma_D^2, \quad (7.41)$$

where the second subscript to σ again indicates the interpolation order.

Finally, consider the modeling error in frequency interpolation. The MSE at any data subcarrier is as given in (7.21), except that the averages are different from that given in (7.32) and

(7.33) due to the difference in choice of interpolating pilots as well as the presence of extrapolation for subcarrier 13. Straightforward numerical calculation yields the following average MSE of frequency interpolation over all data subcarriers:

$$\begin{aligned}\sigma_{i,1}^2 &= 2.6458 \sigma_\xi^2(1, \tau_c^o), \\ \sigma_{i,2}^2 &= 12.8125 \sigma_\xi^2(2, \tau_c^o), \\ \sigma_{i,3}^2 &= 93.0820 \sigma_\xi^2(3, \tau_c^o),\end{aligned}\tag{7.42}$$

where the second subscript to σ once again indicates the interpolation order.

Putting all together, we obtain the overall average channel estimation MSE as

$$\begin{aligned}\sigma_{H,1}^2 &= 0.5130\sigma_n^2 + 0.4531\sigma_D^2 + 2.6458 \sigma_\xi^2(1, \tau_c^o), \\ \sigma_{H,2}^2 &= 0.6699\sigma_n^2 + 0.5577\sigma_D^2 + 12.8125 \sigma_\xi^2(2, \tau_c^o), \\ \sigma_{H,3}^2 &= 0.8121\sigma_n^2 + 0.6525\sigma_D^2 + 93.0820 \sigma_\xi^2(3, \tau_c^o),\end{aligned}\tag{7.43}$$

respectively, for linear, quadratic, and cubic interpolations.

Simulation Examples

We simulate a system with carrier frequency = 2.5 GHz, bandwidth = 10 MHz, DFT size = 1024, and cyclic prefix length = 128. We let a DL subframe contain 24 OFDMA symbols following the preamble. Again, we simulate the SUI-4 and SUI-5 PDPs with block-static fading at a rate corresponding to 100 km/h of mobile speed.

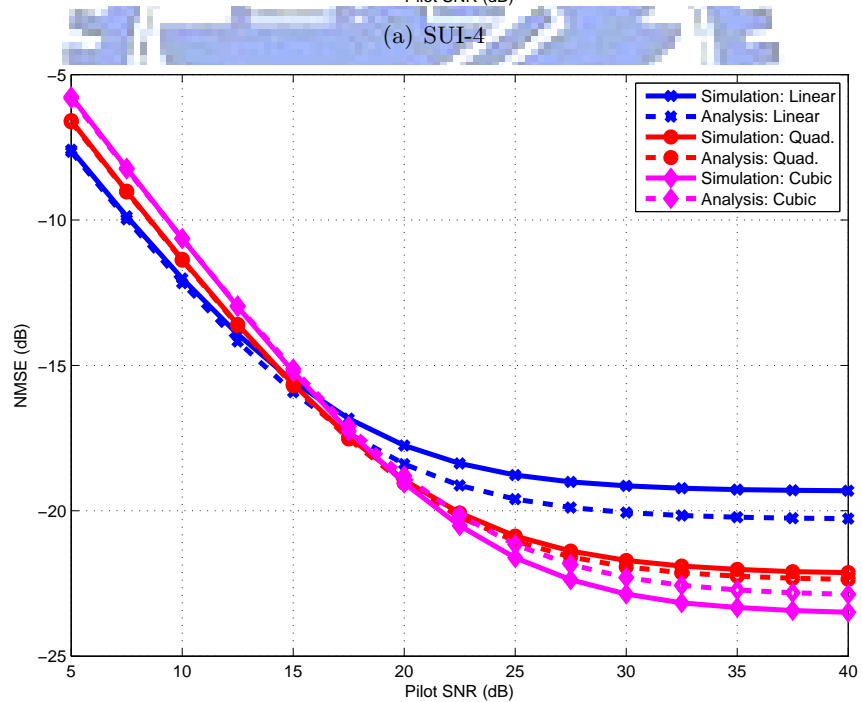
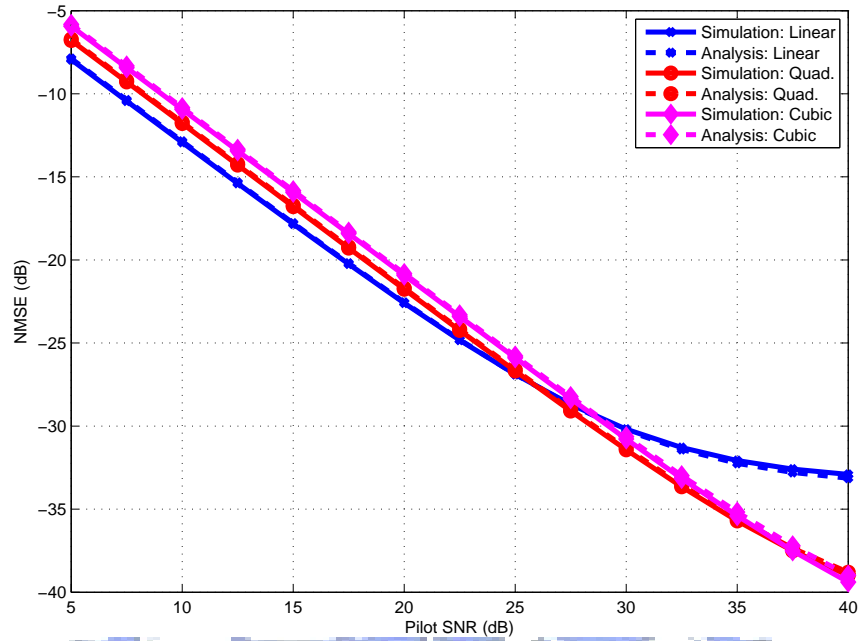
The histograms of estimated window shifts for different interpolation orders are similar to that in Fig. 7.2 and 7.3, and are thus omitted. Figs. 7.8(a) and 7.8(b) show some channel estimation performance results. In the case of SUI-4, the approximate analysis matches the simulation results almost exactly. For linear interpolation, the MSE floor due to frequency interpolation starts to manifest at about 30 dB of pilot SNR, which is lower than either quadratic or cubic interpolation. But it performs somewhat better in lower SNR values where the AWGN effect is more prominent. For SUI-5, which has a larger delay spread than SUI-4, the approximate analysis is less accurate, but still follows the general behavior of the simulation results. The MSE performance of the three different interpolation orders, though poorer than under SUI-4, shows characteristically similar relation. In particular, higher-order interpolations perform better at higher pilot SNR values by having lower frequency interpolation errors, but lower-order interpolations are somewhat better at lower pilot SNR values due to smaller AWGN contributions there.

Adaptive Selection of Interpolation Order

That lower-order interpolators are less prone to AWGN whereas higher-order ones have smaller modeling errors suggests adaptive selection of the interpolator order. This can be accomplished if we can estimate σ_n^2 , $\sigma_\xi^2(N, \tau_c^o)$, and σ_D^2 and use the results to predict the MSE via (7.43). The interpolation order that yields the least MSE can then be chosen.

It is relatively easy to estimate σ_n^2 using the null subcarriers in the preamble symbol. But it is hard to estimate σ_D^2 using only the preamble symbol, because it is a function of the channel variation over time. Fortunately, σ_D^2 is the least dominating term of three and its coefficient varies the least with interpolator order. Thus we disregard it in the selection of interpolation order. What remains is the estimation of $\sigma_\xi^2(N, \tau_c^o)$. From (7.26) and (7.27), we can estimate it from the preamble symbol as

$$\hat{\sigma}_\xi^2(N, \tau_c^o) = \frac{1}{F^{2N+2}} \left[P_N \hat{R}_0 + 2 \min_\theta \{ J_N(\theta) \} \right]\tag{7.44}$$



(b) SUI-5

Figure 7.8: CE performance in WiMAX DL transmission at 100 km/h mobile speed with different orders of interpolation.

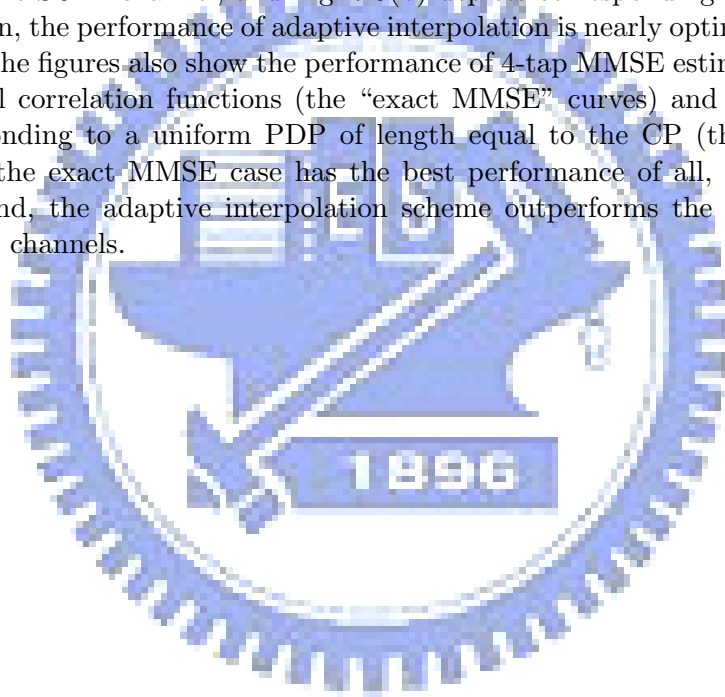
where $\hat{R}_0 = \langle\langle |\hat{H}(f)|^2 \rangle\rangle - \hat{\sigma}_n^2$ with $\hat{\sigma}_n^2$ being estimate of σ_n^2 . Note that $P_1 = 6$, $P_2 = 20$, and $P_3 = 70$.

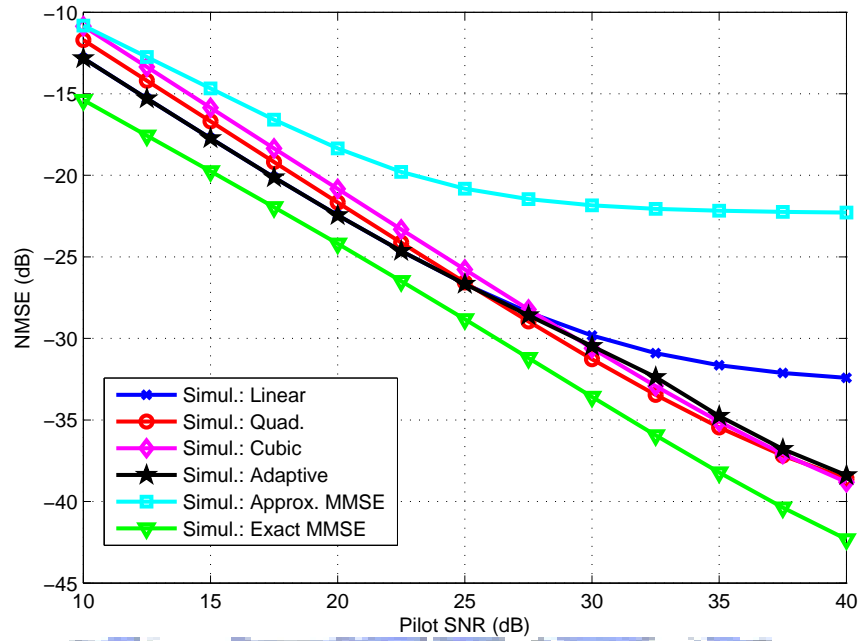
In summary, for each DL subframe, we determine the interpolation order by comparing the following predicted partial MSEs for linear, quadratic, and cubic interpolations, respectively:

$$\begin{aligned}\hat{\sigma}_{H,1}^2 &\triangleq 0.5130\hat{\sigma}_n^2 + 0.01034 \left[6\hat{R}_0 + 2 \min_{\theta} \{J_1(\theta)\} \right], \\ \hat{\sigma}_{H,2}^2 &\triangleq 0.6699\hat{\sigma}_n^2 + 0.003128 \left[20\hat{R}_0 + 2 \min_{\theta} \{J_2(\theta)\} \right], \\ \hat{\sigma}_{H,3}^2 &\triangleq 0.8121\hat{\sigma}_n^2 + 0.001420 \left[70\hat{R}_0 + 2 \min_{\theta} \{J_3(\theta)\} \right],\end{aligned}\tag{7.45}$$

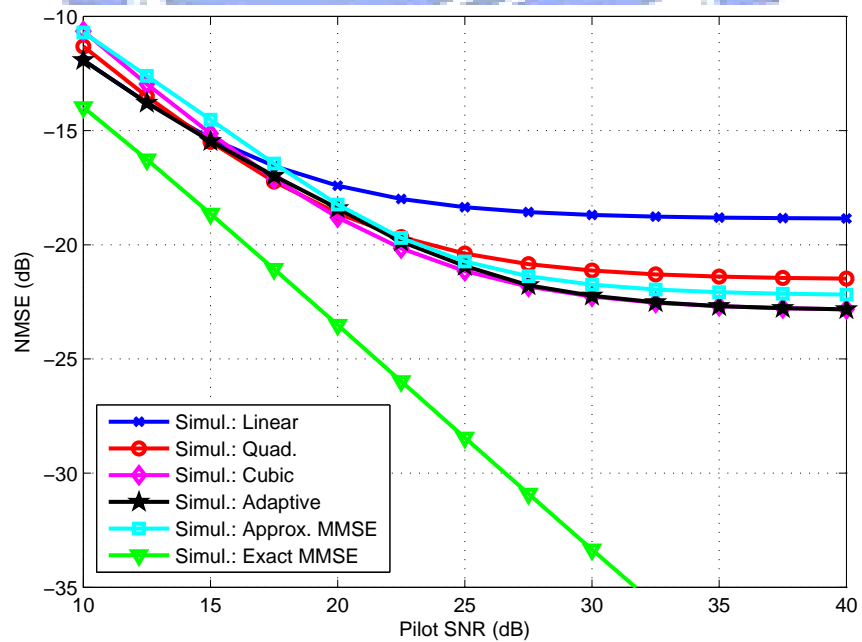
where the estimates are calculated using the received preamble of the DL subframe. The interpolation order with the smallest predicted partial MSE is selected.

Fig. 7.9(a) compares the MSE performance of adaptive interpolation with that of fixed interpolation in the SUI-4 channel, and Fig. 7.9(b) depicts corresponding results for the SUI-5 channel. As shown, the performance of adaptive interpolation is nearly optimal in both channels. For comparison, the figures also show the performance of 4-tap MMSE estimators obtained with the exact channel correlation functions (the ‘‘exact MMSE’’ curves) and with the correlation function corresponding to a uniform PDP of length equal to the CP (the ‘‘approx. MMSE’’ curves). Again, the exact MMSE case has the best performance of all, but is not practical. On the other hand, the adaptive interpolation scheme outperforms the approximate MMSE estimator in both channels.





(a) SUI-4 Channel Model



(b) SUI-5 Channel Model

Figure 7.9: Comparison of adaptive interpolation with fixed interpolation at 100 km/hr mobile speed.

7.2 Approximate LMMSE CE with Estimations of Mean Delay and RMS Delay Spread

This section considers the mean delay and the root-mean-square delay spread estimation problem in multi-carrier system for the purpose of the channel estimation. Wiener channel estimation yields good performance, but requires the knowledge of the channel correlation. An alternative suboptimal approach uses the pre-defined correlation model, such as the correlation shape according to exponential decayed power-delay profile (PDP) [75, 18] or the uniform distributed PDP. However, this approach requires the delay-spread and the mean delay parameters to generate the correlation function. In this section, we present a simple estimation scheme for the delay parameters and apply this scheme to the channel estimations for the multi-carrier system with typical comb-type pilot assignment and the WiMAX systems.

7.2.1 Introduction

Wiener filtering or linear minimum mean-square error (LMMSE) estimation can yield good performance in multicarrier channel estimation [18, 61, 72]. Given estimated frequency responses of the channel at some pilot subcarriers, standard LMMSE optimization leads to the LMMSE channel estimate at any subcarrier d as [18]

$$\hat{H}_d = \underline{w}^H \hat{\underline{H}}_p \quad (7.46)$$

with

$$\underline{w} = (\mathbf{R}_p + \sigma_n^2 \mathbf{I})^{-1} \underline{r}_{dp}, \quad (7.47)$$

where \hat{H}_d is the desired LMMSE channel estimate, \underline{w} is the Wiener filter, superscript H denotes Hermitian transpose, $\hat{\underline{H}}_p$ is the vector of given channel estimates at pilot subcarriers, $\mathbf{R}_p = E(\underline{H}_p \underline{H}_p^H)$ is the autocorrelation matrix of channel responses at the pilot subcarriers, $\underline{r}_{dp} = E(\underline{H}_p \hat{H}_d^*)$ is the vector of crosscorrelations between the channel responses at the pilot subcarriers and that to be estimated, σ_n^2 is the variance of the additive channel noise (assumed to be white Gaussian, i.e., AWGN), and \mathbf{I} denotes an identity matrix.

To generate the LMMSE coefficients, we need the knowledge of the autocorrelation function of the channel frequency response. In convention, we may either use the all pilot-aided or the decision-aided estimation of the correlation function. This constrain may not be available or may take great computation in estimation of the correlation function. Alternative to measuring the correlation, A way using a predefined shape for the correlation has been proposed in [75, 18]. Typically, the shape using exponential decayed power-delay profile (PDP) and the uniform distributed PDP are widely considered. For the exponential PDP, the correlation $R_f(k)$ is given by [75]

$$R_f(k) = \frac{1}{1 + j2\pi\tau_{\text{rms}}k/N} \quad (7.48)$$

where N is the discrete Fourier transform (DFT) size used in the OFDM or the OFDMA system, and we have assumed that the first path has zero delay. If the first path has delay τ_o (which may arise, for example, from OFDM symbol synchronization error or variation in the uplink transmission timing of different users in OFDMA), then the correlation function is

$$R_f(k) = \frac{e^{-j2\pi\tau_o k/N}}{1 + j2\pi\tau_{\text{rms}}k/N}. \quad (7.49)$$

In addition, we have the mean-delay of the channel profile

$$\tau_c = \tau_o + \tau_{\text{rms}}. \quad (7.50)$$

Alternatively, in the case of a uniform PDP of width T , we have

$$R_f(k) = \frac{e^{-j2\pi\tau_c k/N} \sin(\pi T k/N)}{\pi T k/N}, \quad (7.51)$$

with $\tau_c = \tau_o + T/2$ and $T = \sqrt{12} \tau_{\text{rms}}$. In these approaches, the factors: root-mean-square (RMS) delay spread and the mean delay are necessary. To perform better correlation model, we need to estimate the RMS delay spread as well as the mean delay for the channel estimation using the approximate LMMSE.

Before the estimation issue, we formulate the definition of the RMS delay and the mean delay. Consider a discrete-time multipath channel impulse response

$$h(n, t) = \sum_{l=1}^L \alpha_l(t) \delta(n - \tau_l) \quad (7.52)$$

where τ_l is the l th path delay in units of the sampling period T_s and α_l is its complex path gain. When only one OFDM symbol is available, we may consider the “instantaneous” RMS delay, which is defined by

$$\tau_{\text{rms}}(t) = \sqrt{\frac{\sum_{l=1}^L |\alpha_l(t)|^2 (\tau_l - \bar{\tau})^2}{\sum_{l=1}^L |\alpha_l(t)|^2}} \quad (7.53)$$

with “instantaneous” mean delay

$$\tau_c(t) = \frac{\sum_{l=1}^L |\alpha_l(t)|^2 \tau_l}{\sum_{l=1}^L |\alpha_l(t)|^2}. \quad (7.54)$$

However, if there exists multiple samples of the OFDM symbols, the (“averaged”) RMS delay spread is given by

$$\bar{\tau}_{\text{rms}} = \sqrt{\frac{\sum_{l=1}^L E\{|\alpha_l|^2\} (\tau_l - \bar{\tau})^2}{\sum_{l=1}^L E\{|\alpha_l|^2\}}} \quad (7.55)$$

in which

$$\bar{\tau}_c = \frac{\sum_{l=1}^L E\{|\alpha_l|^2\} \tau_l}{\sum_{l=1}^L E\{|\alpha_l|^2\}} \quad (7.56)$$

is the (“averaged”) mean delay.

Several RMS delay spread estimation methods have been proposed in the literature [99, 100, 3, 107]. Witrisal [99] proves that the RMS delay spread is proportional to the level crossing rate of the channel frequency response. However, accurate estimation of the level crossing rate requires dense frequency sampling of the channel response, which is not provided by typical OFDM and OFDMA systems that employ widely spaced pilots. Athaudage and Jayalath [3] elaborate on the relation between the cyclic prefix (CP) correlation and the power-delay profile and apply this relation to RMS delay spread estimation. But to calculate the CP correlation may take many OFDM symbols and the search procedure used to solve for the RMS delay spread may cost much computation. Moreover, the algorithm is derived for a single-transmitter scenario and is not suitable for the uplink of an OFDMA system where different users may have different RMS delay spreads. The paper [107] suggests using multiple cross-correlations of the channel frequency responses to estimate the RMS delay. However, there are several constrains in their algorithms. First, multiple correlations are required; Second, the inverse Fourier transform is used to derive the time domain correlations, both of which take great computations in practice.

In follows, we first review the LMMSE channel estimation and derive the performance loss due to in-accurate auto-correlation. Then, as the key contribution in this section, we present

a extreme low complexity estimation of the RMS delay spread and the mean delay, and the estimation accuracy analyses. We also present the application of the delay spread estimations in the OFDM channel estimation with the approximate LMMSE estimator. Finally, we adopt this estimator in WiMAX system.

7.2.2 LMMSE Channel Estimation with Approximate Channel Correlation

Let $R_f(k)$ be the autocorrelation function of the discrete channel frequency response as would be encountered in an orthogonal frequency-division multiplexing (OFDM) or an orthogonal frequency-division multiple access (OFDMA) system. Typical LMMSE channel estimation may be decomposed into a two-step process where one first obtains the least-square (LS) channel estimate at some pilot subcarriers and then interpolates for the channel response at each desired subcarrier using a Wiener filter with coefficients [18]

$$\underline{w} = (\mathbf{R}_p + \sigma_n^2 \mathbf{I})^{-1} \underline{r}_{dp} \quad (7.57)$$

where $\mathbf{R}_p = E[\underline{H}_p \underline{H}_p^H]$ is the autocovariance matrix of channel frequency responses at the pilot positions, $\underline{r}_{dp} = E[H_d^* \underline{H}_p]$ is the cross-correlation vector between the channel frequency responses at the pilots and the data subcarrier to be estimated, and σ_n^2 is the variance of the additive white Gaussian noise. The estimation formula is given by

$$\hat{H}_d = \underline{w}^H \hat{\underline{H}}_p \quad (7.58)$$

where $\hat{\underline{H}}_p$ is the channel responses at pilots using LS estimator. The entries of \mathbf{R}_p and \underline{r}_{dp} are defined by $R_f(k)$. However, the real correlation function is not available. One way to approximate the MMSE Wiener coefficients is adopting the per-defined correlation matrix, for example, the exponential power-delay profile as given in (7.48).

Performance Evaluation in Approximate LMMSE CE

We evaluate the theoretical estimate MSE of the LMMSE CE adopting the approximate power-delay profile. At least two factors cause the estimate MSE, which are the minimal MSE with the true correlations and the additional perturbation due to approximate correlations.

Assume $\mathbf{R}_{p,o}$ and $\underline{r}_{d,o}$ be the true correlation matrices of pilots and data, whereas \mathbf{R}_p and \underline{r}_{dp} be the approximations. First, when the true correlations are known, the minimal MSE of the LMMSE CE is given by

$$\sigma_{H,o}^2 = E \left| H_d - \hat{H}_{d,o} \right|^2 = P_H - \underline{r}_{d,o}^H (\mathbf{R}_{p,o} + \sigma_n^2 \mathbf{I})^{-1} \underline{r}_{d,o} \quad (7.59)$$

where $\hat{H}_{d,o}$ is the estimated response, $P_H = E|H_d|^2$, $\mathbf{R}_{p,o}$ is the true correlation matrix of the pilot responses, and $\underline{r}_{d,o}$ is the cross-correlation vector of the pilot responses and the desired data response. Now, the estimate MSE of the approximate LMMSE CE is given by

$$\sigma_H^2 = E \left| H_d - \hat{H}_d \right|^2 = P_H - 2\Re \{ \underline{w}^H \underline{r}_{d,o} \} + \underline{w}^H (\mathbf{R}_{p,o} + \sigma_n^2 \mathbf{I}) \underline{w}. \quad (7.60)$$

Let $\underline{w}_o = (\mathbf{R}_{p,o} + \sigma_n^2 \mathbf{I})^{-1} \underline{r}_{d,o}$ be the optimal coefficient vector of the true LMMSE CE, and

$$\Delta \underline{w} \triangleq \underline{w} - \underline{w}_o = (\mathbf{R}_p + \sigma_n^2 \mathbf{I})^{-1} \underline{r}_d - (\mathbf{R}_{p,o} + \sigma_n^2 \mathbf{I})^{-1} \underline{r}_{d,o}. \quad (7.61)$$

Since

$$\begin{aligned} \underline{w}^H (\mathbf{R}_{p,o} + \sigma_n^2 \mathbf{I}) \underline{w} &= \underline{w}_o^H (\mathbf{R}_{p,o} + \sigma_n^2 \mathbf{I}) \underline{w}_o + \Delta \underline{w}^H (\mathbf{R}_{p,o} + \sigma_n^2 \mathbf{I}) \Delta \underline{w} \\ &\quad + 2\Re \{ \Delta \underline{w}^H \underline{r}_{d,o} \}; \end{aligned} \quad (7.62)$$

$$\begin{aligned} &= \Delta \underline{w}^H (\mathbf{R}_{p,o} + \sigma_n^2 \mathbf{I}) \Delta \underline{w} + 2\Re \{ \underline{w}_o^H \underline{r}_{d,o} \} \\ &\quad - \underline{r}_{d,o}^H (\mathbf{R}_{p,o} + \sigma_n^2 \mathbf{I})^{-1} \underline{r}_{d,o}, \end{aligned} \quad (7.63)$$

we have that

$$\sigma_H^2 = \sigma_{H,o}^2 + \Delta\sigma_H^2 \quad (7.64)$$

where

$$\Delta\sigma_H^2 = \Delta\underline{w}^H (\mathbf{R}_{p,o} + \sigma_n^2 \mathbf{I}) \Delta\underline{w} = \left\| R_o^{1/2} \Delta\underline{w} \right\|^2 \quad (7.65)$$

is the perturbation and $R_o^{1/2}$ is the square-root matrix of the positive definite matrix $\mathbf{R}_{p,o} + \sigma_n^2 \mathbf{I}$. The derivation in [62] yields the same result in the perturbation.

7.2.3 Simple Estimation Scheme of RMS Delay Spread and Mean Delay

Estimation Schemes

The (normalized) frequency response of the channel in (7.52) is given by

$$H(f, t) = \sum_{l=1}^L \alpha_l(t) e^{-j2\pi\tau_l f/N}. \quad (7.66)$$

Consider advancing the channel response by τ time units. The corresponding frequency response is given by

$$\bar{H}_\tau(f, t) = e^{j2\pi\tau f/N} H(f, t) = \sum_{l=1}^L \alpha_l(t) e^{-j2\pi(\tau_l - \tau) f/N}. \quad (7.67)$$

Differentiating $\bar{H}_\tau(f, t)$ with respect to f , we get

$$\frac{d\bar{H}_\tau(f, t)}{df} = \frac{-j2\pi}{N} \sum_{l=1}^L \alpha_l(t) \cdot (\tau_l - \tau) e^{-j2\pi(\tau_l - \tau) f/N}. \quad (7.68)$$

(The above is a manifestation of the well-known Fourier transform property $-j2\pi\mathcal{F}\{n h(n)\} = dH(f)/df$.) From Parseval's theorem, we have

$$J(\tau, t) \triangleq \left\langle \left| \frac{d\bar{H}_\tau(f)}{df} \right|^2 \right\rangle = \frac{4\pi^2}{N^2} \sum_{l=1}^L |\alpha_l(t)|^2 (\tau_l - \tau)^2 \quad (7.69)$$

and thence

$$\bar{J}(\tau) = E \left\langle \left| \frac{d\bar{H}_\tau(f)}{df} \right|^2 \right\rangle = \frac{4\pi^2}{N^2} \sum_{l=1}^L \overline{|\alpha_l|^2} (\tau_l - \tau)^2, \quad (7.70)$$

where $\langle \cdot \rangle$ denotes frequency averaging, and $\overline{\{\cdot\}}$ and $E\{\cdot\}$ denote expectation by ideal time-averaging.

The above provides an alternative characterization of the mean delay and the RMS delay spread. First, $\bar{J}(\tau)$ is a quadratic function in τ . It is minimized when $\tau = \bar{\tau}_c$. And secondly, the minimum value of $\bar{J}(\tau)$ is proportional to the mean-square delay spread $\bar{\tau}_{\text{rms}}^2$. Therefore, we have that

$$\bar{\tau}_c = \arg \min_{\tau} \bar{J}(\tau), \quad (7.71)$$

and

$$\bar{\tau}_{\text{rms}}^2 = \frac{N^2 \min_{\tau} \bar{J}(\tau)}{4\pi^2 \sum_{l=0}^L \overline{|\alpha_l|^2}}. \quad (7.72)$$

Similarly, when only one OFDM symbol is used, we also have the instantaneous delays

$$\tau_c(t) = \arg \min_{\tau} J(\tau, t) \quad (7.73)$$

and

$$\tau_{\text{rms}}^2(t) = \frac{N^2 \min J(\tau, t)}{4\pi^2 \sum_{l=0}^L |\alpha_l(t)|^2}. \quad (7.74)$$

The novelty of the present proposal consists in the solution for $\bar{\tau}/\tau(t)$ and $\bar{\tau}_{\text{rms}}/\tau_{\text{rms}}(t)$ via a frequency-domain formulation.

Specifically, let f and $f + F_s$ be two adjacent pilot subcarriers and let $H_\tau(f)$ and $H_\tau(f + F_s)$ be the LS channel estimates at these positions. Ignore the effect of the AWGN for the moment. Using first-order difference to approximate $dH_\tau(f)/df$ in (7.70), we get

$$\begin{aligned} \bar{J}(\tau) &\approx \bar{J}'(\tau) \triangleq E \left\langle \left| \frac{e^{j\phi} \hat{H}(f + F_s, t) - \hat{H}(f, t)}{F_s} \right|^2 \right\rangle \\ &= \frac{2(\bar{R}_0 - \Re\{e^{j\phi} \bar{R}_1\})}{F_s^2} \end{aligned} \quad (7.75)$$

where $\phi = 2\pi\tau F_s/N$, $R_0 = \frac{1}{2} \langle |\hat{H}(f, t)|^2 + |\hat{H}(f + F_s, t)|^2 \rangle \approx \langle |\hat{H}(f, t)|^2 \rangle \approx \sum_{l=1}^L |\alpha_l(t)|^2$, $R_1 = \langle \hat{H}(f + F_s, t) \hat{H}^*(f, t) \rangle$, and the $\langle \cdot \rangle$ operation here averages over all available pilot subcarriers only. In writing the above, we have assumed equally spaced pilots for simplicity. The formulation can be easily extended to deal with unequally spaced pilots. Space does not allow additional details.

Straightforward algebraic manipulation yields

$$\hat{\tau}_c \triangleq \arg \min_{\tau} \bar{J}'(\tau) = \frac{N \angle \bar{R}_1}{2\pi F_s}, \quad (7.76)$$

$$\min \bar{J}(\tau) \triangleq \min \bar{J}'(\tau) = \frac{2(\bar{R}_0 - |\bar{R}_1|)}{F_s^2}. \quad (7.77)$$

Substituting into (7.72), we get an estimation of the RMS delay spread as

$$\hat{\tau}_{\text{rms}} = \frac{N}{2\pi F_s} \sqrt{2 \left(1 - \frac{|\bar{R}_1|}{\bar{R}_0} \right)}. \quad (7.78)$$

Similarly, the estimation of the instantaneous delays are given by

$$\hat{\tau}_c(t) = \frac{N \angle R_1}{2\pi F_s}, \quad (7.79)$$

$$\hat{\tau}_{\text{rms}}(t) = \frac{N}{2\pi F_s} \sqrt{2 \left(1 - \frac{|R_1|}{R_0} \right)} \quad (7.80)$$

From (7.50), we also obtain an estimation of the initial delays:

$$\hat{\tau}_o = \hat{\tau}_c - \hat{\tau}_{\text{rms}}, \text{ and } \hat{\tau}_o(t) = \hat{\tau}_c(t) - \hat{\tau}_{\text{rms}}(t) \quad (7.81)$$

Now consider the effect of the AWGN. All we need to do is to modify R_0 to

$$R_0 = \langle |\hat{H}(f)|^2 \rangle - \hat{N}_o \quad (7.82)$$

where \hat{N}_o is the estimated noise variance. The estimation of \hat{N}_o can be achieved by estimating the power of the subcarriers in the guard band and those that have a null value.

Estimate Accuracy of the RMS Delay

The accuracy depends on two factors: the approximation of the differential equation and the estimation of R_0 and R_1 in (7.75). Assume estimation parameters are derived over T OFDM symbols and \bar{x} denotes the expectation of x . Let $\overline{R_0} - \hat{N}_0 = \overline{A_0} + \Delta R_0$ and $\overline{R_1} = \overline{A_1} + \Delta R_1$, where now $\overline{A_k} = \sum_{l=1}^L |\alpha_l|^2 e^{-j2\pi\tau_l k F_s}$ are the actual values of R_k 's respectively, and ΔR_0 and ΔR_1 are the estimate errors of A_0 and A_1 correspondingly. Substituting the assumptions into (7.78), we have that

$$\hat{\tau}_{\text{rms}}^2 = \frac{2N^2}{4\pi^2 F_s^2} \left(1 - \frac{|\overline{A_1}|}{\overline{A_0}} + \Delta J_e \right) \quad (7.83)$$

with

$$\Delta J_e = \left(\frac{|\overline{A_1}|}{\overline{A_0}} - \frac{E\{|R_1|\}}{E\{|R_0|\}} \right). \quad (7.84)$$

Now, we consider the expansion of $|\overline{R_1}|$. Since we have $|\overline{A_1}| = \max_{\phi} \Re \{ e^{-j\phi} \overline{A_1} \}$ and

$$\phi^o \triangleq \angle \overline{A_1} = -\frac{2\pi F_s \bar{\tau}_c}{N} \quad (7.85)$$

maximizes $\Re \{ e^{-j\phi} \overline{A_1} \}$, we get $|\overline{A_1}| = \Re \{ e^{-j\phi^o} \overline{A_1} \}$. Furthermore, fourth order Taylor expansion of $e^{-j\phi^o} \overline{A_1}$ gives that

$$|\overline{A_1}| \approx \overline{A_0} - \frac{(2\pi F_s/N)^2}{2} \sum |\alpha_l|^2 (\tau_l - \bar{\tau})^2 + \overline{A_0} \Delta J_a \quad (7.86)$$

where $\Delta J_a = \frac{(2\pi F_s/N)^4}{24\overline{A_0}} \sum |\alpha_l|^2 (\tau_l - \bar{\tau})^4$. Applying the expansion into (7.83), we have that

$$\hat{\tau}_{\text{rms}}^2 - \bar{\tau}_{\text{rms}}^2 \triangleq \Delta \tau_{\text{rms}}^2 = -\frac{2N^2}{4\pi^2 F_s^2} (\Delta J_a + \Delta J_e), \quad (7.87)$$

where ΔJ_a is the error term due to the difference approximation and ΔJ_e is the term due to estimation errors of R_0 and R_1 .

Next, we analyze the property of ΔJ_e . From derivation, we have the approximation

$$\Delta J_e \approx \frac{|\overline{A_1}| \Delta R_0}{\overline{A_0}^2} - \frac{\Re \{ \Delta R_1 e^{-j\phi^o} \}}{\overline{A_0}}, \quad (7.88)$$

which is corresponding to the properties of ΔR_0 and ΔR_1 . We assume that the pilots have the comb-type assignment that the samples for estimation are located at $f \triangleq f_0 + kF_s$ for integer k . In addition, we assume perfect estimated noise variance that $\hat{N}_0 = \sigma_w^2$. Then,

$$\Delta R_0 = \overline{R_0} - \sigma_w^2 - \overline{A_0} = \delta_0 + \eta_0 + \varepsilon_0 \quad (7.89)$$

with

$$\begin{aligned} \delta_0 &= \overline{\langle |H(f)|^2 \rangle} - \overline{A_0}, \\ \eta_0 &= 2\Re \left\{ \overline{\langle H(f) w^*(f) \rangle} \right\}, \\ \varepsilon_0 &= \overline{\langle |w(f)|^2 \rangle} - \sigma_w^2; \end{aligned} \quad (7.90)$$

$$\Delta R_1 = \overline{R_1} - \overline{A_1} = \delta_1 + \eta_1 + \varepsilon_1 \quad (7.91)$$

with

$$\begin{aligned}
\delta_1 &= \overline{\langle H(f + F_s)H^*(f) \rangle} - \overline{A_1}, \\
\eta_1 &= \overline{\langle H(f + F_s)w^*(f) + H^*(f)w(f + F_s) \rangle}, \\
\varepsilon_1 &= \overline{\langle w(f + F_s)w^*(f) \rangle}.
\end{aligned} \tag{7.92}$$

Since η_n and ε_n for $n \in \{0, 1\}$ are composed by AWGN and Rayleigh channel assumption yields that $\overline{\delta_0} = \overline{\delta_1}$, we have that $\overline{\Delta J_e} = 0$ and

$$\begin{aligned}
\overline{\Delta J_e^2} &= \frac{|A_1|^2}{A_0^4} \left(\overline{\delta_0^2} + \overline{\varepsilon_0^2} + \overline{\eta_0^2} \right) \\
&+ \frac{1}{2A_0^2} \left[\Re \left\{ \left(\overline{\delta_1^2} + \overline{\eta_1^2} \right) e^{-j2\phi^o} \right\} + \overline{|\delta_1|^2} + \overline{|\varepsilon_1|^2} + \overline{|\eta_1|^2} \right] \\
&- 2 \frac{|A_1|}{A_0^3} \cdot \Re \left\{ \left(\overline{\delta_0 \delta_1} + \overline{\eta_0 \eta_1} \right) e^{-j\phi^o} \right\}
\end{aligned} \tag{7.93}$$

where $\overline{\delta_0^2} = \overline{|\delta_1|^2} = \sum_l (\overline{|\alpha_l|^2})^2$, $\overline{\delta_1^2} = \sum_l (\overline{|\alpha_l|^2})^2 e^{-j4\pi\tau_l F_s/N}$, $\overline{\delta_0 \delta_1} = \sum_l (\overline{|\alpha_l|^2})^2 e^{-j2\pi\tau_l F_s/N}$, $\varepsilon_0 \cdot 2N/(F_s\sigma_w^2)$ is χ^2 of degree $2N/F_s$, $\overline{\varepsilon_0^2} = \overline{|\varepsilon_1|^2} = F_s\sigma_w^4/(NT)$, $\overline{\eta_0^2} = \overline{|\eta_1|^2} = 2F_s\overline{A_0}\sigma_w^2/(NT)$, $\overline{\eta_1^2} = (\overline{A_2}/\overline{A_0})\overline{\eta_0^2}$, and $\overline{\eta_0 \eta_1} = (\overline{A_1}/\overline{A_0})\overline{|\eta_1|^2}$. Hence the mean and the variance of $\Delta\bar{\tau}_{\text{rms}}^2$ are given by, respectively,

$$\overline{\Delta\bar{\tau}_{\text{rms}}^2} = \frac{N^2}{2\pi^2 F_s^2} \Delta J_a = -\frac{\pi^2 F_s^2}{3N^2 A_0} \sum_l \overline{|\alpha_l|^2} (\tau_l - \bar{\tau})^4, \tag{7.94}$$

$$\sigma_{\Delta\bar{\tau}_{\text{rms}}^2}^2 = \frac{N^4}{4\pi^4 F_s^4} \overline{\Delta J_e^2}. \tag{7.95}$$

The results simplify considerably if we only estimate the instantaneous parameters from one OFDM(A) symbol: the terms involving δ_0 or δ_1 disappear. We get

$$\Delta\bar{\tau}_{\text{rms}}^2(t) = -\frac{\pi^2 F_s^2}{3N^2 A_0} \sum_l |\alpha_l(t)|^2 (\tau_l - \tau_c)^4 \tag{7.96}$$

and

$$\begin{aligned}
\sigma_{\Delta\bar{\tau}_{\text{rms}}^2}^2 &= \frac{N^3 \sigma_w^2}{8\pi^4 F_s^3 T A_0^4} \left[(A_0^2 + 2|A_1|^2) \sigma_w^2 \right. \\
&\left. + A_0 \left(A_0^2 - 2|A_1|^2 + A_0 \Re \{ A_2 e^{-j2\phi^o} \} \right) \right],
\end{aligned} \tag{7.97}$$

where $A_k = \sum_{l=1}^L |\alpha_l(t)|^2 e^{-j2\pi\tau_l k F_s}$

Estimate Accuracy of the Mean Delay

According to estimation of $\bar{\tau}_c$ in (7.76), the accuracy of mean delay relies on the estimation of $E\{R_1\}$. Following the suggestion in [93], we have that

$$\hat{\bar{\tau}}_c \approx -\frac{N}{2\pi F_s} \left(\phi^o + \Im \left\{ \frac{\Delta R_1}{A_1} \right\} \right) \tag{7.98}$$

when $\Delta R_1 \ll \overline{A_1}$.

According to third order Taylor expansion of $\overline{A_1}$, we have that

$$\overline{A_1} \approx e^{-j2\pi F_s \bar{\tau}_c / N} \left(\overline{A_0} - 2 \frac{\pi^2 F_s^2 \overline{A_0}}{N^2} \bar{\tau}_{\text{rms}}^2 - j \frac{4\pi^3 F_s^3}{3N^3} \sum_{l=1}^L \overline{|\alpha_l|^2} (\tau_l - \bar{\tau})^3 \right) \quad (7.99)$$

and

$$\phi^o \approx -2\pi F_s \bar{\tau} / N - \Delta J_{a1} \quad (7.100)$$

with $\Delta J_{a1} = \frac{4\pi^3 F_s^3}{3N^3 A_0} \sum_{l=1}^L \overline{|\alpha_l|^2} (\tau_l - \bar{\tau})^3$.

Next, consider the perturbation due to noise and fading as given

$$\Delta J_{e1} = \frac{1}{|\overline{A_1}|} \left(\Im \left\{ \frac{\overline{A_1^*}}{|\overline{A_1}|} \delta_1 \right\} + \Im \left\{ e^{-j\phi^o} \eta_1 \right\} + \Im \left\{ e^{-j\phi^o} \varepsilon_1 \right\} \right), \quad (7.101)$$

in which $\Im \{ e^{-j\phi^o} \eta_1 \}$ and $\Im \{ e^{-j\phi^o} \varepsilon_1 \}$ are zero-mean real Gaussian and

$$\begin{aligned} \Im \left\{ \frac{\overline{A_1^*}}{|\overline{A_1}|} \delta_1 \right\} &= \frac{1}{|\overline{A_1}|} \Im \left\{ \overline{A_1^*} \sum_l \langle |\alpha_l(t)|^2 \rangle e^{-j2\pi \tau_l F_s} \right\} \\ &= \frac{1}{|\overline{A_1}|} \sum_m \sum_l \overline{|\alpha_m|^2} \langle |\alpha_l(t)|^2 \rangle \Im \{ e^{j2\pi(\tau_m - \tau_l)} \} \\ &= \frac{1}{|\overline{A_1}|} \sum_l C_l \langle |\alpha_l(t)|^2 \rangle \end{aligned} \quad (7.102)$$

where $C_l = \sum_{m \neq l} \overline{|\alpha_m|^2} \sin(2\pi F_s(\tau_m - \tau_l))$ and $\langle \cdot \rangle$ here is the symbol average.

We have that

$$\overline{\Delta J_{e1}^2} = \frac{1}{|\overline{A_1}|^2} \left(\overline{\left\{ \frac{\overline{A_1^*}}{|\overline{A_1}|} \delta_1 \right\}^2} + \overline{\left\{ e^{-j\phi^o} \eta_1 \right\}^2} + \overline{\left\{ e^{-j\phi^o} \varepsilon_1 \right\}^2} \right) \quad (7.103)$$

with

$$\overline{\left\{ \frac{\overline{A_1^*}}{|\overline{A_1}|} \delta_1 \right\}^2} = \frac{1}{|\overline{A_1}|^2} \sum_l C_l^2 \overline{|\alpha_l|^2}, \quad (7.104)$$

$$\overline{\left\{ e^{-j\phi^o} \eta_1 \right\}^2} = \frac{\sigma_n^2 F_s}{NT} \left(\overline{A_0} - \Re \{ \overline{A_2} e^{-2j\phi^o} \} \right), \quad (7.105)$$

$$\overline{\left\{ e^{-j\phi^o} \varepsilon_1 \right\}^2} = \frac{\sigma_n^4 F_s}{2NT}. \quad (7.106)$$

Hence, the mean and variance of $\Delta \tau_c$ are given by, respectively,

$$\overline{\Delta \tau_c} = \frac{N \Delta J_{a1}}{2\pi F_s} = \frac{8\pi^3 F_s^2}{3N^2 A_0} \sum_{l=1}^L \overline{|\alpha_l|^2} (\tau_l - \bar{\tau})^3 \quad (7.107)$$

and

$$\overline{\Delta \tau_c^2} = \frac{N^2 \overline{\Delta J_{e1}^2}}{4\pi^2 F_s^2}. \quad (7.108)$$

Moreover, when instantaneous mean-delay is considered, we have that

$$\Delta \bar{\tau}_c = \frac{8\pi^3 F_s^2}{3N^2 A_0} \sum_{l=1}^L |\alpha_l(t)|^2 (\tau_l - \bar{\tau})^3 \quad (7.109)$$

and

$$\overline{\Delta \bar{\tau}_c^2} = \frac{N \sigma_n^2}{8\pi^2 F_s |\overline{A_1}|^2} \left(\sigma_n^2 + 2A_0 - 2\Re \{ \overline{A_2} e^{-j\phi^o} \} \right) \quad (7.110)$$

where $A_k = \sum_{l=1}^L |\alpha_l(t)|^2 e^{-j2\pi \tau_l k F_s}$.

7.2.4 Numerical Evaluation and Simulation Study

We first evaluate the analytical result of the delay estimator accuracy, and then apply the proposed delay estimator in the channel estimation for the OFDM system with comb-type pilot assignment.

Evaluation of Delay Estimation Accuracy

We simulate OFDM transmission with the following parameters: bandwidth = 10 MHz, DFT size = 1024, CP length = 128, pilot spacing = 8, and carrier frequency = 2.5 GHz. The channel has 6 Rayleigh paths with power profile [0, -1, -9, -10, -15, -20] (in dB) and delay profile [10, 13, 17, 21, 27, 35] (in samples), which follow ETSI's Vehicular A channel model except that the path delays are rounded to integer sample numbers and that an initial delay of 10 samples (approximately 0.9 μ s) is added.

We consider estimating the instantaneous delay parameters based on one OFDM symbol only, i.e., $K = 1$. This is useful, for example, in channel estimation based on only one received OFDM symbol. By using the least amount of data possible, the estimation should be most prone to noise effects, as is also confirmed by (7.110) for the mean delay and by (7.97) for the RMS delay spread where the leading factors are both inverse proportional to K .

We consider SNR values between 10 and 40 dB, total 100 Rayleigh distributed channels and perform 100 simulation runs per channel for each SNR value simulated. Fig. 7.10 shows the probabilities of the analytical mean estimation errors of $\Delta\tau_\mu$ and $\Delta\tau_{\text{RMS}}^2$, and the simulated means of 100 channels at 20 dB SNR. It shows perfect matches between the analytical and the simulated mean errors. In addition, we get that the mean estimation errors are not significant in all the channels. Fig. 7.11 shows results for the averaged standard deviations of $\Delta\tau_\mu$ and $\Delta\tau_{\text{RMS}}^2$ of total 100 channels. The theory and the simulation results agree well over the large range of SNR values tested, where the estimator performance also varies over a large range. Note that, in both plots, the curves roughly show a -1 slope at lower SNR values and a -0.5 slope at higher SNR. This agrees with the presence of a σ_n^2 term in the brackets in both (7.110) and (7.97), whose effect is more prominent in lower SNR but negligible in higher SNR. Together with the σ_n^2 term outside the brackets in either equation, it yields a -1 slope in lower SNR and a -0.5 slope in higher SNR after taking the square root.

Apply to Channel Estimation

We simulate OFDM transmission with comb type pilot assignment. The system parameters are as follows: carrier frequency = 2.5 GHz, bandwidth = 10 MHz, DFT size = 1024, length of CP = 128, pilot spacing = 4 subcarriers. The ETSI Vehicular A and SUI-4 channel models are used in the simulation. The channel estimator uses four-tap Wiener filter. Both the exponential PDP and the uniform distributed PDP are used as the correlation models. In addition, the optimal Wiener filter with true correlation model is also studied as the optimal reference. In this simulations, the mean delay and delay spread is estimated once per OFDM symbol and all samples at pilot subcarriers are used to estimate the delays.

Fig. 7.12(a) shows the simulation result over ETSI Vehicular-A channel; whereas, Fig. 7.12(b) shows the result over SUI-4. Both the simulation and analysis results are illustrated, and we can see the perfect matches of the simulation and analysis results in both channel. In ETSI Vehicular-A channel, the performances of the approximate filters are near the optimal one. In SUI-4 channel, they are a little far away from the optimal one at high SNR region. When compare to the adopted correlation model, the exponential PDP assumption is more suitable than uniform distributed assumption in these two cases.

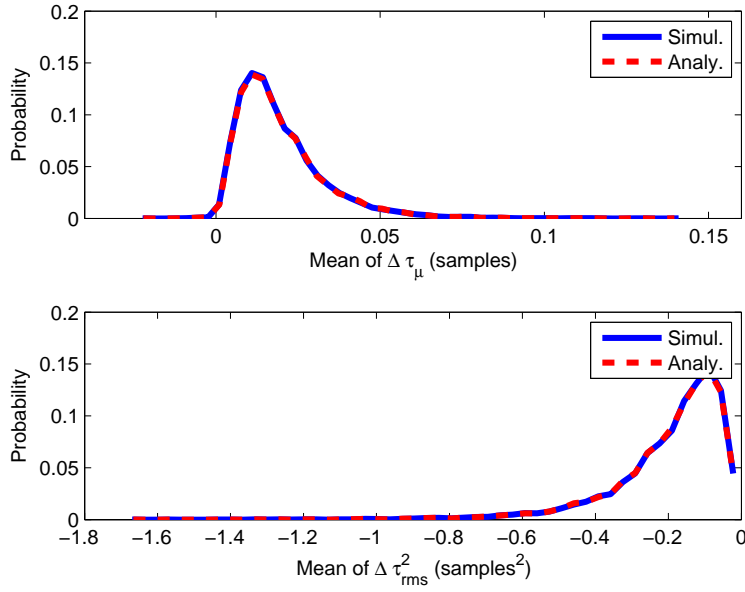


Figure 7.10: Mean of estimation errors in delay estimation. Top: Probability of mean in $\Delta\tau_\mu$; bottom: probability of mean in $\Delta\tau_{\text{rms}}^2$.

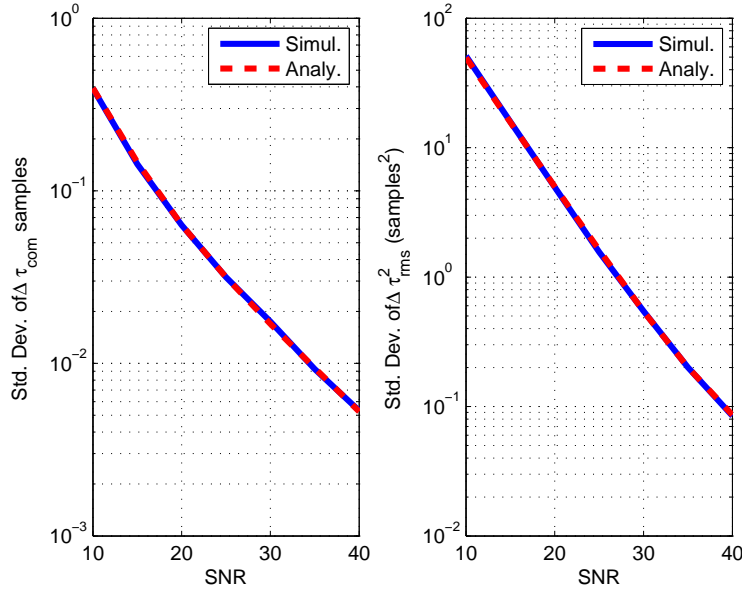
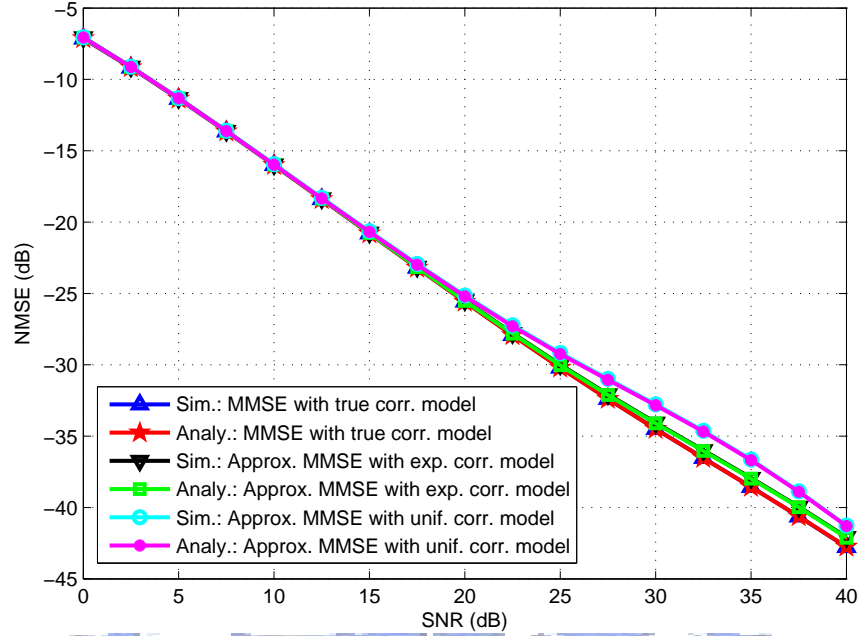


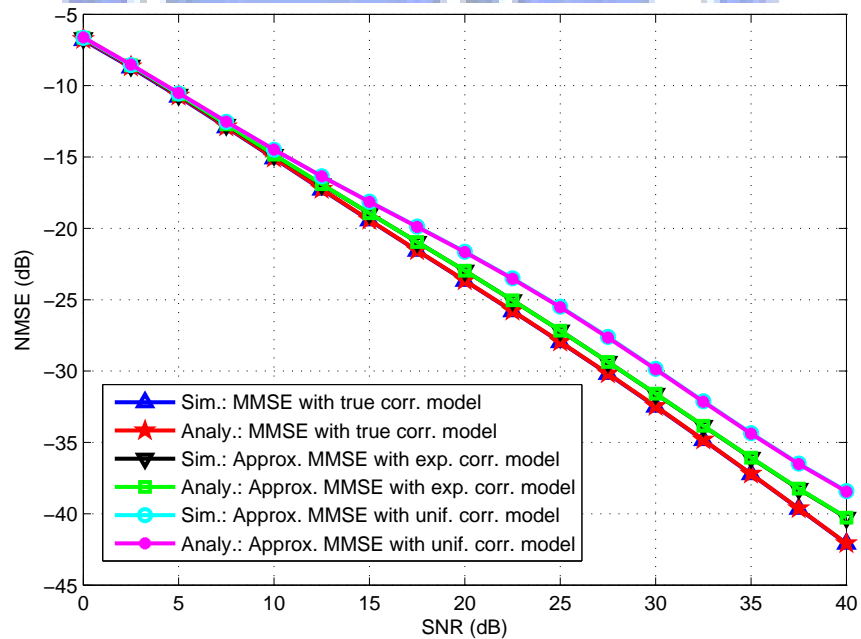
Figure 7.11: Precision of theory in predicting noise effects in delay estimation. Left: standard deviation in $\Delta\tau_\mu$; right: standard deviation in $\Delta\tau_{\text{rms}}^2$.

Periodic Update of Wiener Coefficients

In actual system realization, the delays can be updated in a period to reduce the implementation complexity. Consider the system described previous as an example. We give a design example to realize the proposed estimator. Recall the required parameters of the channel estimator. We divide the process into three steps. First, we need to estimate the noise variance and the correlations R_0 and R_1 . Second, the Wiener coefficients are updated according to the noise



(a) Vehicular-A Channel Model



(b) SUI-4 Channel Model

Figure 7.12: Normalized MSE in channel estimation for multi-carrier system with comb-type pilot assignment.

variance and estimated delay parameter, which is generated by estimated R_0 and R_1 . Finally, the channel response is estimated via the approximate Wiener filtering. At first step, in frequency dimension, we use 16 interleaved sample pairs to estimate instantaneous R_0 and R_1 ; then, in temporal dimension, we adopt the exponential average to smooth the correlations with forgetting factor $\beta = 1 - 2^{-8}$. In addition, the noise variance is estimated via the null subcarrier of the OFDM symbols and also smoothed by the exponential average filter. At second step, the Wiener coefficients are updated per 64 symbols. With the proposed design, the cost in generating the coefficients is extremely lower than the channel estimation.

The Vehicular-A and SUI-4 channel models are also used in the following simulations. In addition, the channel responses are generated symbol-by-symbol according to Jakes model and the mobility speeds of each paths are all set to 100 KM/Hr. Figs. 7.13(a) and 7.13(b) illustrate the simulated NMSEs of the estimators over the Vehicular-A and SUI-4 correspondingly. The optimal Wiener estimator is also given as the benchmark. As shown, in Vehicular-A channel, the NMSEs of both approximate estimators are closed to the optimal one. In SUI-4 model, the NMSE of the approximate estimator according exponential model is also quite close to the benchmark. But, the estimator using uniform model is a little bit poor.

7.2.5 Application in WiMAX Channel Estimation

We apply the approximate LMMSE channel estimation in the WiMAX UL and DL. Unlike the classic comb-type based pilot structure in OFDM system, the WiMAX adopts the cluster structure in downlink and the tile structure in uplink. These discrete pieced structure makes the common transform based estimation not feasible in WiMAX. Thus, the per piece estimation is considered. The approximate LMMSE is one suitable approach.

WiMAX DL Channel Estimations

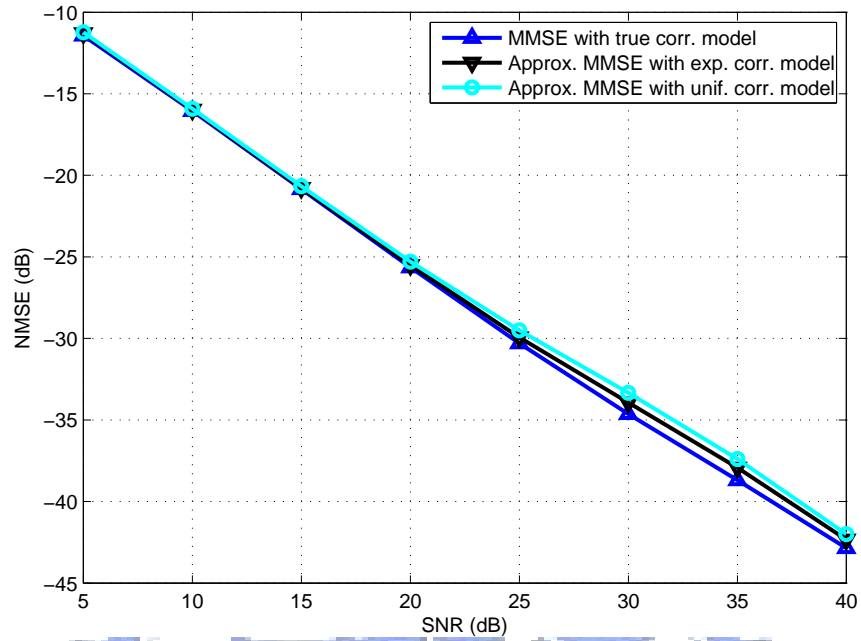
We consider two approaches using four taps LMMSE CE in DL channel estimation. At first approach, the delay parameters are updated in every time slots of the receptions using the pilot responses of the associated cluster for the user. The second approach estimates the parameters once per subframe adopting the preamble symbol. In complexity issue, the first approach is more complicate than the second due to the updating of the delay parameters and Wiener coefficients; whereas, in performance issue, the second approach has poor performance than the first one due to time-varying parameters.

In the first approach, referring to Fig.7.7, we have the following process:

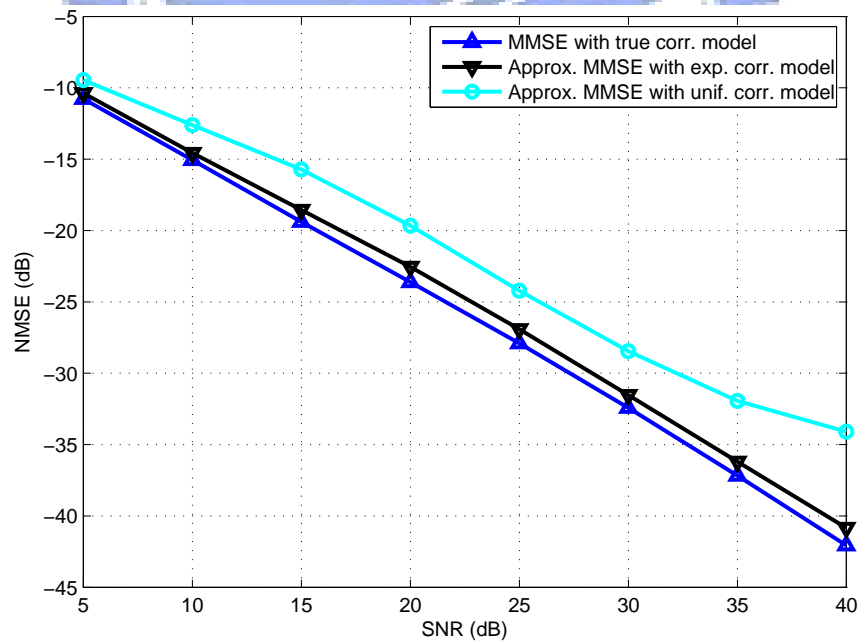
1. estimate noise variance using the null subcarrier in the preamble symbol;
2. do least-square channel estimation at existing pilots of the clusters;
3. do time domain average to acquire the responses of $H(2, 0)$, $H(2, 12)$, $H(3, 4)$ and $H(3, 8)$;
4. estimate RMS delay and mean delay, and generate the associated coefficients for the interpolator; and
5. perform the interpolation to obtain the residual responses.

For the second approach, it is similar to the first, except for skipping the step 4 and using preamble to generate the delay parameters and coefficients in step 1.

We study the proposed estimators and compare to the optimal MMSE estimator with true correlation. Four-tap estimators are used in the simulation. Besides, we also compare to phase-shifted polynomially interpolator with the adaptive selection scheme proposed in section 7.1.4. The simulated system parameters are given as follows: FFT size = 1024, bandwidth = 10 MHz,



(a) Vehicular-A Channel Model



(b) SUI-4 Channel Model

Figure 7.13: Simulation studies of the periodic update scheme for multi-carrier with comb-type pilots at 100 KM/Hr mobility speed.

center frequency = 2.5 GHz and 6 subchannels for a specified burst. The ETSI Vehicular-A [21], SUI-4 and SUI-5 channel are used in the comparisons, and the mobility is set to 100 Km/Hr.

Figs. 7.14(a), 7.14(b) and 7.14(c) show the comparisons of the approaches over ETSI Vehicular-A, SUI-4 and SUI-5 channel profile correspondingly. As shown in Figs. 7.14(a), the proposed estimators are closed to the optimal benchmark, except for the adaptive selection in low SNR region. In SUI-4 channel, the approximate MMSE approaches have good performance near the optimal at low SNR condition; however, the performances are far away from the optimal one at high SNR due to the correlation model error. At high SNR, the adaptive selection scheme is better than the approximate MMSE approaches, but poorer at low SNR. In SUI-5 channel, the proposed algorithms perform significantly poorer than the optimal estimator. The SUI-5 has much larger delay spread than SUI-4 and ETSI Vehicular-A. As shown, the proposed estimators have bad estimation quality in the large delay spread, especially when the SNR is high. However, the performances of the approach 1 using exponential correlation model and the adaptive selection scheme are similar and better than others.

WiMAX UL Channel Estimations

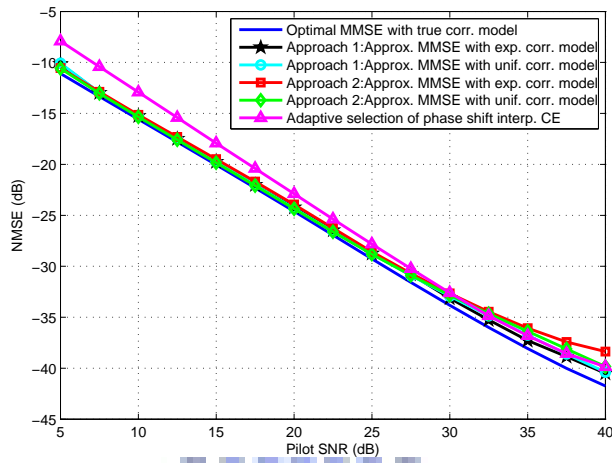
According to the pilot assignment in the tile structure, the two-tap Wiener filter is used to estimate the channel response. We assume that carrier and symbol timing synchronization are done in UL subframe during the ranging process. The proposed channel estimation works in the unit of the tile. First, the channel responses at pilot subcarrier is estimated via the least square estimator. Then, the delay parameters are estimated by the estimated channel responses associated to the user and the corresponding Wiener coefficients are generated. At third step, the LMMSE channel estimation is performed in frequency dimension to generate the responses at the first and third symbols. Finally, the time domain interpolation is performed to estimate the responses at the second symbol.

We compare the proposed estimators to others methods. The conventional linear interpolator and the phase-compensated linear interpolator [32] are studied in the comparisons. Both the exponential and the uniform distributed PDPs are used for generating the approximate correlation models. Besides, the optimal MMSE estimator with true correlation model is also performed as the optimal benchmark. The system profile and channel condition is similar to previous. Besides, we consider that an additional 0.8 μ seconds propagation delay occurs in the propagation, which roughly yields 9 samples in a OFDM symbol.

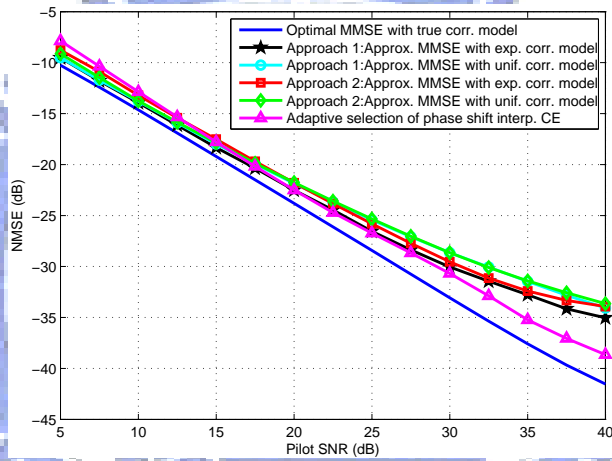
The simulation results according to the channel models: ETSI, Vehicular-A, SUI-4, and SUI-5 are illustrated in Figs. 7.15(a), 7.15(b) and 7.15(c) correspondingly. For all channel models, the approximate MMSE with exponential correlation model has best performance, which is nearest one to the optimal benchmark. The secondary one is the approximate approach with uniform distributed correlation model, but it does not have significant difference to the phase-compensated linear interpolator [32]. As we expect, the poorest one is the conventional linear interpolation. When compare to different channel models, the SUI-5 have poorest simulation results for all estimators. This is because the delay spread of SUI-5 is much larger than others.

7.3 Conclusions

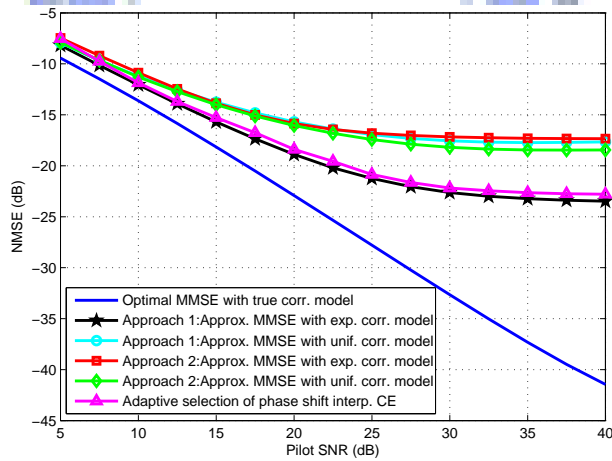
This chapter considered the factors of the symbol timing and the channel delay parameters in the channel estimation issue. We studied two commonly used channel estimation schemes: the polynomial interpolation and the LMMSE estimation. For polynomial interpolation, we presented the time-shifted interpolation scheme and the estimate of the associated optimal shift. Several cost-reduced implementations were proposed to realize the WiMAX DL CE. Besides, we also proposed the scheme of adaptive selection of the interpolation order in the DL subframe to



(a) Vehicular-A Model

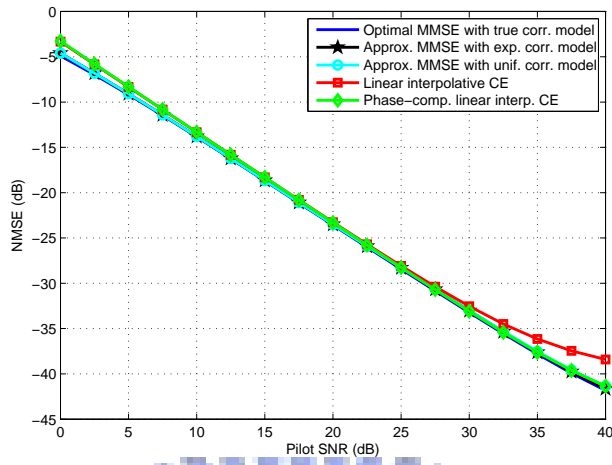


(b) SUI-4 Model

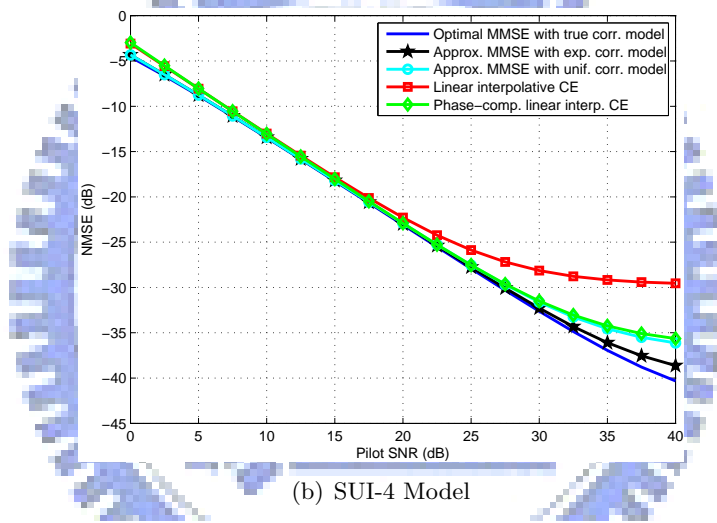


(c) SUI-5 Model

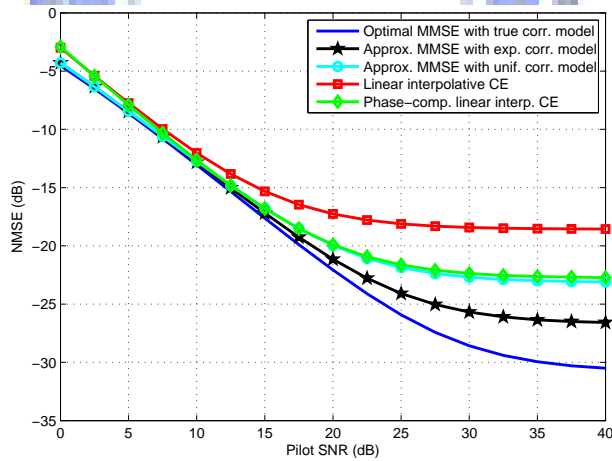
Figure 7.14: Simulation studies of the CE schemes for WiMAX DL path at 100 Km/Hr mobility speed.



(a) Vehicular-A Model



(b) SUI-4 Model



(c) SUI-5 Model

Figure 7.15: Simulation studies of the CE schemes for WiMAX UL in 100 Km/Hr mobility speed.

minimize the estimate MSE. In LMMSE channel estimation, we proposed a simple estimation scheme of the mean delay and RMS delay spread. And, we apply this estimator to the suboptimal LMMSE channel estimator by generating the correlation function according to the predefined channel model and the estimated delay parameters. The realizations of the channel estimators for the comb-type multi-carrier system and the WiMAX are also innovated.

Appendix: Derivation of $G(k)$

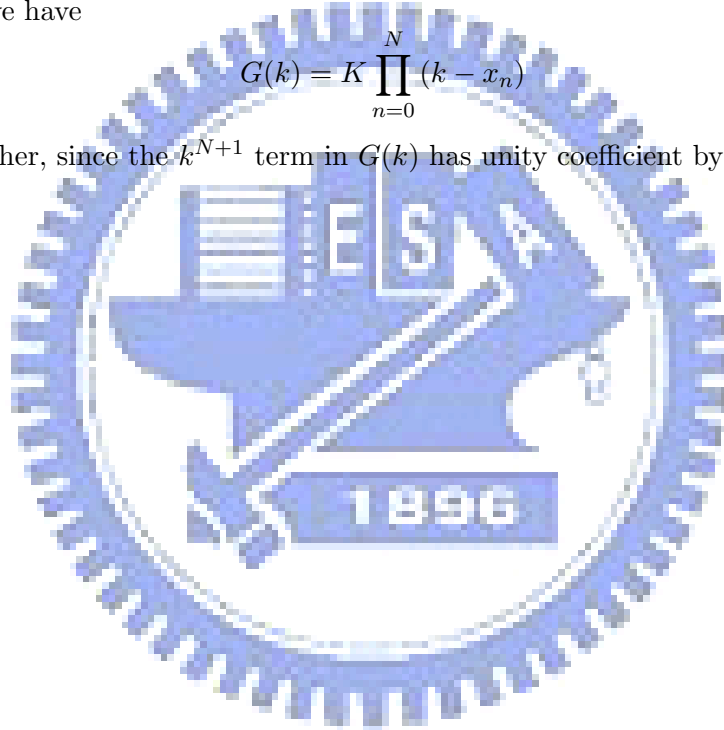
Let $\underline{G} = [G(x_0), G(x_1), \dots, G(x_N)]^T$. Then

$$\begin{aligned} \underline{G} &= \underline{x} - [\underline{V}(x_0)^T, \underline{V}(x_1)^T, \dots, \underline{V}(x_N)^T]^T X^{-1} \underline{x} \\ &= \underline{x} - X X^{-1} \underline{x} = \underline{0}. \end{aligned} \quad (7.111)$$

Thus x_n is a root of $G(k) \forall n \in \{0, \dots, N\}$. Now that $G(k)$ is an $N + 1$ st-order polynomial in k by definition, we have

$$G(k) = K \prod_{n=0}^N (k - x_n) \quad (7.112)$$

for some K . Further, since the k^{N+1} term in $G(k)$ has unity coefficient by definition, $K = 1$.



Part III

**Transmitter Design over Wide-band
MIMO and Its Block Iterative
Receiver**



Orthogonal frequency-division multiplexing (OFDM) with multiple transmit and receive antennas has drawn much recent attention in research on high-speed transmission over multipath fading channels. To exploit more fully the inherent diversity under multi-input multi-output (MIMO) OFDM in fading channels, one usually needs to employ space-time and/or space-frequency coding [92, 1]. There is now abundant literature on space-time/frequency coding. Taking space-time coding as an example, the approaches can be divided into two broad categories: the coding approach (as represented by space-time trellis coding and space-time block coding) and the linear preprocessing approach (as represented by linear constellation precoding for signal space diversity [102, 8]).

It has been shown that a key factor influencing the performance of space-time/frequency coded transmission is the determinant of the correlation matrix of pairwise codeword differences [105, 31]. In this part, we show that the determinant is maximized when the correlation matrix is a multiple of the identity matrix; or in other words, when the codeword differences are “white.” In attempting to use this result in system design, however, we find that, when the block size of the system is large (the meaning of “block size” will become clear later), there is difficulty in achieving such whiteness. As a result, we resort to an approximately white design.

For signal reception, we consider block-based turbo decision-feedback equalization (TDFE) [56, 13, 47] to exploit the available diversity while keeping the complexity under guard. Moreover, we propose a multi-stage technique for turbo DFE to further reduce the complexity. In association with the reduced-complexity turbo DFE, we propose a particular space-frequency transform (SFT) technique for quasi-whitening of the transmitted signal. The SFT combines an orthogonal transform (for which fast computational algorithms exist) and a certain way of space-frequency interleaving (SFI) whose details will be given later.

For channel estimation, we give a pilot-data separated frame structure for the proposed scheme and present a joint channel estimation (CE) and data detection (DD) scheme to iteratively estimate channel and detect data. With the cooperation of the channel prediction scheme, we greatly reduce the pilot utilization in the frame structure. For jointly iterative CE and DD, we formulate the data reception as the constrained least square problem and adopt the jointly block gradient descent algorithm to solve the problem, which is a TDFE-like iterative solution.

Chapter 8

Space Frequency Transformed MIMO OFDM System

8.1 System Model

8.1.1 Transmission System Structure

Fig. 8.1 illustrates the structure of the considered transmission system. There are N transmit and $M (\geq N)$ receive antennas. The binary source data S are grouped into blocks containing $rKN \log_2(Q)$ bits each, where r is the channel code rate, K is the IDFT size, and Q is the modulation order. After channel coding and modulation mapping, therefore, each block contains KN signal samples. In principle, the channel coding is not restricted to any particular type. For example, it could be bit-interleaved coded modulation (BICM) employing convolutional coding, trellis coded modulation, or turbo coding. The coded signal samples then pass through the transform block whose design lies at the heart of the present study. After the transform, the signal samples are divided into N streams of K samples each, with each stream undergone a K -point IDFT and cyclic prefixing prior to being transmitted through one of the N antennas. In the receiver, the K received samples at each of the M antennas for each signal block are subject to de-cyclic prefixing and DFT before entering the signal detector. Several approaches to signal detection are maximum-likelihood (ML) detection and turbo equalization (including turbo DFE) [56, 13, 47].

8.1.2 Channel Model

Assuming perfect synchronization and disregarding the cyclic prefix, the signal samples in each block can be organized several ways for mathematical manipulation. For example, we may arrange the concurrently transmitted or received samples into a column vector, or we may arrange the K -sample sequence transmitted or received by one antenna into a column vector. Each of the two representations has its advantage, and we consider both of them below.

First, consider representing the sample sequence at each antenna by a column vector. Let

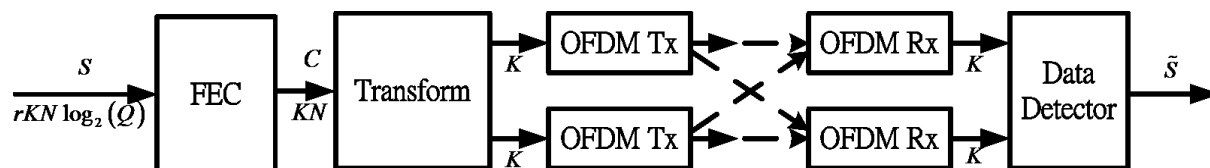


Figure 8.1: Structure of the MIMO OFDM system considered.

\underline{x}_n be the vector transmitted by antenna n and \underline{r}_m that received by antenna m . Then

$$\begin{aligned}\underline{r}_m &= \sum_{n=1}^N H_{mn}\underline{x}_n + \underline{n}_m \\ &= H_m \underline{x} + \underline{n}_m\end{aligned}\quad (8.1)$$

where, assuming that the channel stays unchanged over one signal block period and that the cyclic prefix is long enough to cover the delay spread, H_{mn} is a circulant matrix whose first column gives the channel impulse response from transmit antenna n to receive antenna m , \underline{n}_m is the vector of additive noise, $H_m = [H_{m1}, H_{m2}, \dots, H_{mN}]$, and $\underline{x} = [\underline{x}_1^T, \underline{x}_2^T, \dots, \underline{x}_N^T]^T$, with superscript T denoting matrix transpose. We assume that the noise is white Gaussian. Alternatively, since $H_{mn}\underline{x}_n = X_n \underline{h}_{mn}$ where X_n is the circulant matrix whose first column is given by \underline{x}_n and \underline{h}_{mn} is the first column of H_{mn} (i.e., the channel impulse response from transmit antenna n to receive antenna m), we have

$$\begin{aligned}\underline{r}_m &= \sum_{n=1}^N X_n \underline{h}_{mn} + \underline{n}_m \\ &= \mathbf{X} \underline{\mathbf{h}}_m + \underline{n}_m\end{aligned}\quad (8.2)$$

where $\mathbf{X} = [X_1, X_2, \dots, X_N]$ and $\underline{\mathbf{h}}_m = [\underline{h}_{m1}^T, \underline{h}_{m2}^T, \dots, \underline{h}_{mN}^T]^T$.

Assume that the length of the channel response is L samples where $L < K$. Then the last $K - L$ elements of each of \underline{h}_{mi} , $i = 1, 2, \dots, N$, are zero. These zeros can be excised from $\underline{\mathbf{h}}_m$ to result in a vector, denoted \underline{h}_m , of smaller dimension, yielding

$$\underline{r}_m = \mathbf{X} \mathbf{D} \underline{h}_m + \underline{n}_m \quad (8.3)$$

where $\mathbf{D} = I_{K \times L} \otimes I_N$ with I_N being the $N \times N$ identity matrix, $I_{K \times L}$ the $K \times L$ matrix composed of the first L columns of I_K , and \otimes the Kronecker product. Stacking up \underline{r}_m , \underline{h}_m , and \underline{n}_m into higher-dimensional vectors as $\underline{r} = [\underline{r}_1^T, \underline{r}_2^T, \dots, \underline{r}_M^T]^T$, $\underline{h} = [\underline{h}_1^T, \underline{h}_2^T, \dots, \underline{h}_M^T]^T$, and $\underline{n} = [\underline{n}_1^T, \underline{n}_2^T, \dots, \underline{n}_M^T]^T$, we obtain

$$\underline{r} = (\mathbf{X} \mathbf{D} \otimes I_M) \underline{h} + \underline{n}. \quad (8.4)$$

Now consider representing the concurrently transmitted or received samples by a column vector. Then the input-output relation of the MIMO channel can be written as

$$\mathbf{r}(k) = \sum_{l=0}^{L-1} \mathbf{H}_l \mathbf{x}(k-l) + \mathbf{n}(k) \quad (8.5)$$

where $\mathbf{r}(k)$ is the received M -vector sequence, $\mathbf{x}(k)$ is the transmitted N -vector sequence, \mathbf{H}_l is the $M \times N$ matrix channel impulse response (whose (m, n) th element is the $l + 1$ st element in \underline{h}_{mn}), and $\mathbf{n}(k)$ is the M -vector sequence of noise. For quasi-static correlated multipath Rayleigh fading channels, \mathbf{H}_l can be modeled as [77, 86]

$$\mathbf{H}_l = \mathbf{R}_l^{1/2} \mathbf{A}_l \mathbf{T}_l^{1/2}, \quad l = 0, 1, \dots, L-1, \quad (8.6)$$

where \mathbf{A}_l is an $M \times N$ matrix with zero-mean complex Gaussian entries, \mathbf{T}_l is the $N \times N$ matrix summarizing the pairwise correlations between the channel responses associated with different transmit antennas at delay l , and \mathbf{R}_l is the $M \times M$ matrix summarizing the pairwise correlations between the channel responses associated with different receive antennas at delay l .

8.2 Condition for Maximum Diversity Gain

In this section, we look into the condition on transmitted signals which would yield the maximum diversity gain under multipath MIMO Rayleigh fading. We approach this by minimizing the pairwise codeword error probability (PEP). The result will be used to guide the system design in later sections.

8.2.1 PEP of Coded and Transformed MIMO OFDM under Multipath Rayleigh Fading

In designing coded transmission systems, one often seeks to minimize the worst PEP rather than the average error probability because the latter is often difficult to compute and because the transmission performance is often dominated by the worst PEP.

Consider two codewords \mathbf{c} and $\hat{\mathbf{c}}$. With slight abuse of the notation \mathbf{X} defined in the last section, let $\mathbf{X}(\mathbf{c})$ and $\mathbf{X}(\hat{\mathbf{c}})$ denote the transmitted signal blocks associated with these codewords, respectively. After channel transmission, the PEP between these codewords under ML detection is given by [92]

$$P(\mathbf{c} \rightarrow \hat{\mathbf{c}}) = Q \left(\sqrt{\frac{E_s}{2N_0}} \| (\mathbf{E}\mathbf{D} \otimes I_M) \underline{h} \| \right) \quad (8.7)$$

where E_s is the average symbol energy, N_0 is the power spectral density (PSD) of the additive white Gaussian noise (AWGN), and $\mathbf{E} = \mathbf{X}(\mathbf{c}) - \mathbf{X}(\hat{\mathbf{c}})$. The matrix \mathbf{E} has been termed the error matrix of the codeword pair. Therefore, maximizing the Euclidean distance

$$d(\mathbf{c}, \hat{\mathbf{c}}) \triangleq \| (\mathbf{E}\mathbf{D} \otimes I_M) \underline{h} \| \quad (8.8)$$

will minimize the worst PEP.

To continue, let $\underline{h}(l) = \text{vec}\{\mathbf{H}_l\}$ and $\underline{\alpha}(l) = \text{vec}\{\mathbf{A}_l\}$ (where $\text{vec}\{\cdot\}$ means stacking up of the columns of its matrix argument into a vector). Then from (8.6) we have

$$\underline{h}(l) = \left(\mathbf{T}_l^{\frac{1}{2}} \otimes \mathbf{R}_l^{\frac{1}{2}} \right) \underline{\alpha}(l). \quad (8.9)$$

Now let

$$\begin{aligned} \underline{h}' &= [\underline{h}^T(0), \underline{h}^T(1), \dots, \underline{h}^T(L-1)]^T \\ &= \bigoplus_{l=0}^{L-1} G_l^{\frac{1}{2}} \cdot [\underline{\alpha}^T(0), \underline{\alpha}^T(1), \dots, \underline{\alpha}^T(L-1)]^T \\ &\triangleq \mathbf{G}^{\frac{1}{2}} \underline{\alpha} \end{aligned} \quad (8.10)$$

where $G_l^{\frac{1}{2}} = \mathbf{T}_l^{\frac{1}{2}} \otimes \mathbf{R}_l^{\frac{1}{2}}$ and $\bigoplus_{l=0}^{L-1} G_l^{\frac{1}{2}}$ stands for a block-diagonal matrix with diagonal entries $G_0^{\frac{1}{2}}, G_1^{\frac{1}{2}}, \dots, G_{L-1}^{\frac{1}{2}}$. It is easy to see that \underline{h}' and \underline{h} are related by permutation. Therefore,

$$\underline{h} = \mathbf{Z} \mathbf{G}^{\frac{1}{2}} \underline{\alpha} \quad (8.11)$$

where \mathbf{Z} is an $MNL \times MNL$ permutation matrix. We remark that the above way of decomposing a correlated channel response \underline{h} into the product of a vector of i.i.d. (independent and identically distributed) random elements and a matrix that characterizes the correlation has been adopted in some researches addressing channel conditions closely related to that considered in the present work.

Putting the above results together, we have

$$\begin{aligned}
d^2(\mathbf{c}, \hat{\mathbf{c}}) &= \|(\mathbf{E}\mathbf{D} \otimes I_M) \underline{h}\|^2 \\
&= \underline{h}^H (\mathbf{D}^H \mathbf{E}^H \mathbf{E} \mathbf{D} \otimes I_M) \underline{h} \\
&= \underline{\alpha}^H \mathbf{C}_e \underline{\alpha}
\end{aligned} \tag{8.12}$$

where superscript H denotes Hermitian transpose and

$$\mathbf{C}_e \triangleq \mathbf{G}^{\frac{1}{2}H} \mathbf{Z}^H (\mathbf{D}^H \mathbf{E}^H \mathbf{E} \mathbf{D} \otimes I_M) \mathbf{Z} \mathbf{G}^{\frac{1}{2}}. \tag{8.13}$$

Taking average over all channel realizations and applying known results about the Chernoff bound of the PEP under Rayleigh fading, we have [92]

$$\begin{aligned}
\bar{P}(\mathbf{c} \rightarrow \hat{\mathbf{c}}) &= E_{\underline{\alpha}} \{P(\mathbf{c} \rightarrow \hat{\mathbf{c}})\} \\
&\leq \prod_{i=1}^{r(\mathbf{C}_e)} \left(1 + \frac{E_s}{4N_0} \lambda_i(\mathbf{C}_e)\right)^{-1} \\
&= \left| \mathbf{I} + \frac{E_s}{4N_0} \mathbf{C}_e \right|^{-1},
\end{aligned} \tag{8.14}$$

where $r(\mathbf{C}_e)$ denotes the rank of \mathbf{C}_e , $\lambda_i(\mathbf{C}_e)$ denotes the i th eigenvalue of \mathbf{C}_e , and the last equality holds if \mathbf{C}_e has full rank. Moreover, when \mathbf{C}_e has full rank and the signal-to-noise ratio (SNR) is high, we have the approximate Chernoff bound

$$\bar{P}(\mathbf{c} \rightarrow \hat{\mathbf{c}}) \leq \left(\frac{E_s}{4N_0}\right)^{-MNL} |\mathbf{C}_e|^{-1}. \tag{8.15}$$

8.2.2 Principle of Design for Maximum Diversity Gain

Now consider how to design the system to minimize the average PEP under a given channel coding scheme. From the above results, we see that it is appropriate to consider maximizing $|\mathbf{C}_e|$. Now, given any unitary linear transform, if $d(\mathbf{c}, \hat{\mathbf{c}}) = \|\mathbf{c} - \hat{\mathbf{c}}\| = d_0$, then it can be easily shown that $\text{tr}(\mathbf{D}^H \mathbf{E}^H \mathbf{E} \mathbf{D}) = Ld_0^2$ where $\text{tr}(\cdot)$ takes the trace of its argument. Therefore, the optimization problem can be stated as

$$\max |\mathbf{C}_e| \quad \text{s.t.} \quad \text{tr}(\mathbf{D}^H \mathbf{E}^H \mathbf{E} \mathbf{D}) = Ld_0^2. \tag{8.16}$$

Towards a solution, note first that

$$\begin{aligned}
|\mathbf{C}_e| &= \left| \mathbf{G}^{\frac{1}{2}H} \mathbf{Z}^H \mathbf{Z} \mathbf{G}^{\frac{1}{2}} \right| |\mathbf{D}^H \mathbf{E}^H \mathbf{E} \mathbf{D} \otimes I_M| \\
&= |\mathbf{G}| |\mathbf{D}^H \mathbf{E}^H \mathbf{E} \mathbf{D}|^M.
\end{aligned} \tag{8.17}$$

Hence maximization of $|\mathbf{D}^H \mathbf{E}^H \mathbf{E} \mathbf{D}|$ maximizes $|\mathbf{C}_e|$. Now, the Hadamard inequality gives

$$|\mathbf{D}^H \mathbf{E}^H \mathbf{E} \mathbf{D}| \leq \prod_{j=1}^{NL} \epsilon_j \tag{8.18}$$

where ϵ_j is the j th diagonal term of $\mathbf{D}^H \mathbf{E}^H \mathbf{E} \mathbf{D}$ and the equality holds if and only if $\mathbf{D}^H \mathbf{E}^H \mathbf{E} \mathbf{D}$ is diagonal. By the arithmetic-geometric inequality, we have

$$\begin{aligned}
\prod_{j=1}^{NL} \epsilon_j &\leq \left(\frac{1}{NL} \sum_{j=1}^{NL} \epsilon_j \right)^{NL} \\
&= \left(\frac{\text{tr}(\mathbf{D}^H \mathbf{E}^H \mathbf{E} \mathbf{D})}{NL} \right)^{NL} = \left(\frac{d_0^2}{N} \right)^{NL},
\end{aligned} \tag{8.19}$$

where the first equality holds if and only if ϵ_j is the same for all j . In summary, therefore,

$$|\mathbf{C}_\epsilon| \leq \left(\frac{d_0^2}{N}\right)^{NL} |\mathbf{G}| = \left(\frac{d_0^2}{N}\right)^{NL} \prod_{l=0}^{L-1} |\mathbf{R}_l|^N |\mathbf{T}_l|^M, \quad (8.20)$$

where the first equality holds iff $\mathbf{D}^H \mathbf{E}^H \mathbf{E} \mathbf{D}$ is a constant times the identity matrix or equivalently iff $\mathbf{E}^H \mathbf{E}$ is a constant times the identity matrix.

In conclusion, to attain the maximum diversity and coding gain, the system should be designed such that $\mathbf{E}^H \mathbf{E}$ is a constant times the identity matrix.

8.2.3 Performance of Coded MIMO OFDM Without Transform

In light of the above results, we comment on the performance of coded MIMO OFDM that does not have a transform between channel coding and the IDFT units in the transmitter. Alternatively, such a system can be interpreted as employing an identity transform. This design can be shown to yield relatively poor performance.

First, when there is no transform, the highest rank of $\mathbf{E}^H \mathbf{E}$ is given by the minimum Hamming distance of the channel code. If this distance is smaller than NL , then \mathbf{C}_ϵ does not have full rank and the system cannot achieve maximum diversity gain. Second, if the IDFT size is large and the Hamming distance between codewords is small, then the nonzero elements of the corresponding error matrix are located sparsely in the space-frequency domain. This makes the eigenvalues of $\mathbf{D}^H \mathbf{E}^H \mathbf{E} \mathbf{D}$ highly uneven in magnitude, which deviates significantly from the optimal condition that the eigenvalues be identical. Therefore, the performance of coded MIMO OFDM without transform can be highly suboptimal.

8.3 Principles of Practical Transform Design

We have shown that the optimal transform is a “white” one in the sense that $\mathbf{E}^H \mathbf{E} = d_0^2 \mathbf{I}$. When the transform order is large, however, one may not be able to find a transform that satisfies the equality exactly. Hence we seek for an “approximately white” design that gives $\mathbf{E}^H \mathbf{E} - d_0^2 \mathbf{I} \ll d_0^2 \mathbf{I}$.

In fact, several transformed transmission methods have been proposed in different contexts to achieve different objectives, for example, the energy-spreading transform (EST) for MIMO transmission [47, 46] and the linear constellation precoding (LCP) for MIMO or multi-carrier CDMA transmission [102]. In our context, cyclic-prefixed block single-carrier transmission can also be treated as a transformed OFDM system. Here we present a transform design that has relatively low complexity and can help lower the complexity of the receiver.

The upper part of Fig. 8.2 illustrates the proposed transmitter structure, where the transform has a two-stage architecture. The first stage involves N orthogonal transforms and the second stage involves a space-frequency interleaving (SFI) operation. For ease of implementation, the first stage may employ a simple orthogonal transform (such as the Hadamard transform) or one for which fast computation methods exist (such as the FFT). Ideally, the orthogonal transforms should spread the coded symbols over all the subcarriers so that any differential codeword $\mathbf{c} - \hat{\mathbf{c}}$ is not contained in a few subcarriers but is spread over the entire transmission band. Then, the SFI randomizes the distribution of the codeword energy (already spread across the frequencies by the orthogonal transform) in the spatial dimension to further exploit the spatial as well as the multipath diversity. Through this two-stage transform we attain the approximate whitening effect on the transmitted signal.

Mathematically, the transmitted signal “super-vector” \underline{x} (see Section II for its definition) with the proposed SFT is given by

$$\underline{x} = (\mathbf{W}^H \otimes \mathbf{I}_N) \mathbf{P} (\mathbf{T} \otimes \mathbf{I}_N) \underline{X} \triangleq (\mathbf{W}^H \otimes \mathbf{I}_N) \mathbf{S} \underline{X} \quad (8.21)$$

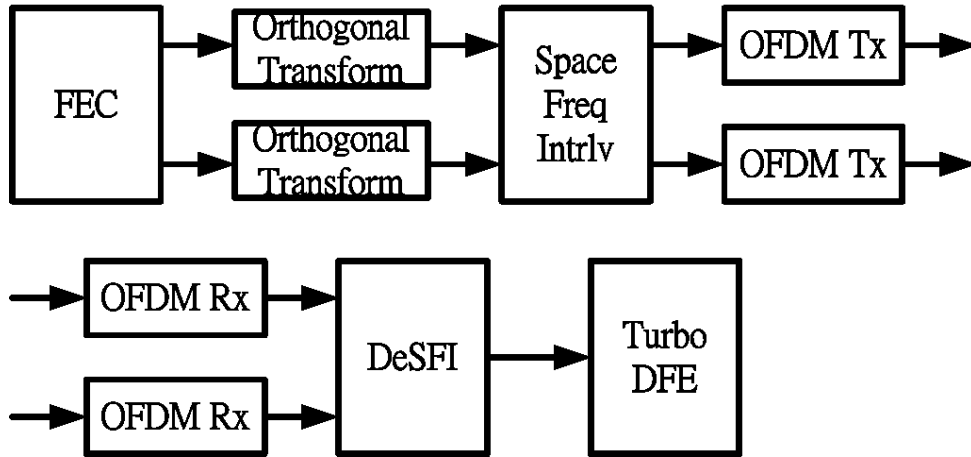
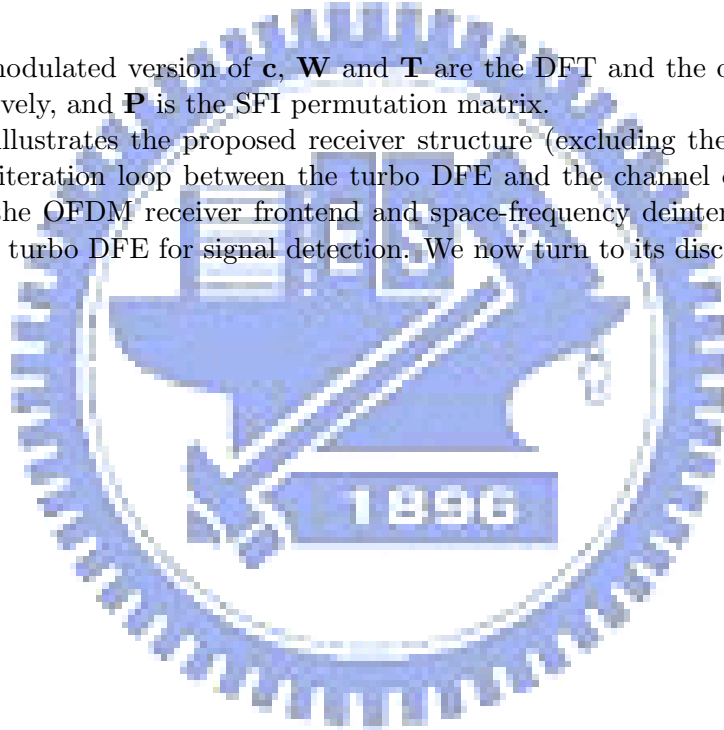


Figure 8.2: Proposed transform design and associated receiver structure.

where \underline{X} is the modulated version of \underline{c} , \mathbf{W} and \mathbf{T} are the DFT and the orthogonal transform matrices, respectively, and \mathbf{P} is the SFI permutation matrix.

Fig. 8.2 also illustrates the proposed receiver structure (excluding the subsequent channel decoder and the iteration loop between the turbo DFE and the channel decoder) in its lower part. Following the OFDM receiver frontend and space-frequency deinterleaving (DeSFI), we can employ block turbo DFE for signal detection. We now turn to its discussion.



Chapter 9

Receiver Design In Transformed MIMO OFDM System

9.1 Block Turbo DFE

In this section, we first consider how block turbo DFE operates under MIMO OFDM in general. Then in the next section, we consider how it works together with SFI. It will become clear that, unlike the conventional turbo equalizer that operates in the time domain, the proposed block turbo DFE operates in the frequency domain.

9.1.1 Block Turbo DFE as Iterative Solution to Constrained Least-Square Problem

Employing earlier notations, the signal propagation behavior of a coded MIMO OFDM system can be described as

$$r = \mathbf{H}x + n \quad (9.1)$$

where (with slight abuse of the notation) $\underline{x} = \underline{x}(\mathbf{c})$ for some codeword \mathbf{c} and

$$\mathbf{H} = \begin{bmatrix} H_{11} & H_{12} & \dots & H_{1N} \\ H_{21} & H_{22} & \dots & H_{2N} \\ \vdots & \vdots & \ddots & \vdots \\ H_{M1} & H_{M2} & \dots & H_{MN} \end{bmatrix} \quad (9.2)$$

with the entries H_{ij} being circulant matrices. When n is white Gaussian and \mathbf{H} is known, the ML detection can be formulated as a constrained least-square (CLS) problem which seeks to minimize the cost function

$$J(\mathbf{c}) = \|\underline{r} - \mathbf{H}\underline{x}(\mathbf{c})\|^2 \quad (9.3)$$

subject to the constraint that \mathbf{c} is a valid codeword.

A block turbo DFE estimates the transmitted signal in the following way:

$$\hat{\underline{x}}^k = \mathbf{F}\underline{r} + \mathbf{B}\bar{\underline{x}}^{k-1} \quad (9.4)$$

where k is the iteration count, $\bar{\underline{x}}^{k-1}$ is the decision output of the $k - 1$ st iteration (which could be the soft output from the channel decoder), $\hat{\underline{x}}^k$ is the signal estimate of the k th iteration, and \mathbf{F} and \mathbf{B} are the feedforward filter (FFF) matrix and the feedback filter (FBF) matrix, respectively. Taking the gradient descent approach [26, 24], we obtain the DFE coefficients as

$$\mathbf{F} = \mu\mathbf{H}^H, \quad \mathbf{B} = I - \mu\mathbf{H}^H\mathbf{H}, \quad (9.5)$$

where I is an identity matrix and $\mu = KN/\|H\|_F^2$ with $\|H\|_F^2 = \text{tr}\{\mathbf{H}^H\mathbf{H}\}$, i.e., the Frobenius norm of \mathbf{H} . With this set of DFE coefficients, the k th iteration equalizer output can also be written as

$$\hat{\underline{x}}^k = \bar{\underline{x}}^{k-1} + \mu\mathbf{H}^H \left(r - \mathbf{H}\bar{\underline{x}}^{k-1} \right). \quad (9.6)$$

If the decision output of the $k - 1$ st iteration is error-free, i.e., if $\bar{\underline{x}}^{k-1} = \underline{x}(\mathbf{c})$, then the block DFE cancels the intersymbol interference (ISI) completely.

In beginning iterations, however, $\bar{\underline{x}}^{k-1}$ may contain many or large decision errors. Such errors would affect adversely the signal estimate $\hat{\underline{x}}^k$ in the k th iteration, especially if $\|\mathbf{B}\|_F^2$ is large. To alleviate such effects, therefore, we consider the generalized gradient descent approach which improves the convergence property by “conditioning” the iterative updates with a shaping filter or precondition filter as [82]

$$\hat{\underline{x}}^k = \bar{\underline{x}}^{k-1} + \mathbf{C}\mathbf{H}^H \left(r - \mathbf{H}\bar{\underline{x}}^{k-1} \right). \quad (9.7)$$

In other words, we modify the DFE filters to

$$\mathbf{F} = \mathbf{C}\mathbf{H}^H, \quad \mathbf{B} = I - \mathbf{C}\mathbf{H}^H\mathbf{H}, \quad (9.8)$$

According to [82], \mathbf{C} should be Hermitian symmetric, positive semi-definite, and commute with $\mathbf{H}^H\mathbf{H}$. An example is given by the quasi-Newton method [50] where

$$\mathbf{C} = \mu \left(\mathbf{H}^H\mathbf{H} + \alpha I \right)^{-1}, \quad (9.9)$$

with α being some constant.

9.1.2 MMSE Shaping Filtering

We consider using a shaping filter that minimizes the mean-square error. Let $\underline{e}^{k-1} = \bar{\underline{x}}^{k-1} - \underline{x}(\mathbf{c})$. Then the error in equalizer output is given by

$$\underline{w}^k \triangleq \hat{\underline{x}}^k - \underline{x}(\mathbf{c}) = \mathbf{C}\mathbf{H}^H \underline{n} + (I - \mathbf{C}\mathbf{H}^H\mathbf{H}) \underline{e}^{k-1}. \quad (9.10)$$

In minimum mean-square error (MMSE) shaping filtering, we seek to minimize $E\{\|\underline{w}^k\|^2\}$. In addition, in order to avoid direct error feedback, we should constrain the average of the diagonal elements of \mathbf{B} to zero.

To proceed, let $\alpha = \sigma_n^2/\sigma_e^2$, i.e., the ratio of noise variance to the variance of the decision error \underline{e}^{k-1} . Note that both σ_e^2 and α are functions of k . But for notational convenience we have omitted explicit indication of this dependence. In the Appendix, we show that the MMSE shaping filter is given by

$$\mathbf{C} = \mu \left(\mathbf{H}^H\mathbf{H} + \alpha I \right)^{-1} \quad (9.11)$$

where

$$\mu = \frac{KN}{\text{tr} \left\{ (\alpha I + \mathbf{H}^H\mathbf{H})^{-1} \mathbf{H}^H\mathbf{H} \right\}}. \quad (9.12)$$

We see that the MMSE shaping filter has the same form as the quasi-Newton shaping filter.

In the case of single-input single-output systems, the above result is the same as that in [13]. But our result is more general in that it applies to MIMO systems. Note, in addition, that when the various quantities converge with iterations, σ_e^2 reduces to zero and α approaches infinity. Then the shaped DFE coefficients also approach that without shaping.

A major drawback of MMSE shaped turbo DFE is, of course, the heavy complexity burden associated with changing the filter coefficients with each iteration. We consider reducing the computational complexity in the next subsection.

9.1.3 Employing Fixed Shaping Filter for Reduced Complexity

To reduce the computational complexity, we consider fixing the shaping filter during the iterations. This results in a three-stage algorithm: 1) Initialization: Perform MMSE block linear equalization (i.e., let $\mathbf{B} = 0$), because no decision output is available at this time. 2) Middle stage: Use a fixed shaping filter that can tolerate a large range of decision error power. 3) Final stage: Use the unshaped DFE filters.

Based on the foregoing results, the determination of the shaping filter for the second stage reduces to the choice of a suitable operating value for α . For this, we do not have a theoretically optimal formula, but only some rules of thumb. Experience shows that underestimation of α would not cause significant enhancement of total MSE when the true α is large enough. In contrast, if the true α is small, then overestimation of it would cause great increase of the MSE. This phenomenon is heuristically reasonable, because (true) α is defined to be equal to σ_n^2/σ_e^2 . Assuming a smaller value for α than its true value is tantamount to assuming a less converged state, which may result in some slowdown in the convergence speed but would not likely cause stability problems. On the other hand, assuming a larger value for α than its true value means being over-optimistic on the convergence status, which would more likely cause performance degradation. Therefore, we choose to use a reasonably small value in the place of α . By experiment, we find that a suitable range of its values is 0.5–2, with the unity value being a good choice.

To decide whether to switch from the second stage to the final stage, we observe the variance of the likelihood ratio (LLR) of the decoded codeword. When the variation in the variance over two successive iterations is small, we assume that the equalizer has converged sufficiently and make the switch. Note that the LLR variance indicates the reliability of the decoded bits [59]. When its value over a number of iterations in stage 2 (shaped block turbo DFE) is even smaller than that in stage 1 (block linear equalization), we may safely conclude that the channel condition is very bad and the turbo DFE may not provide any advantage. In this case, we may simply use the linear equalizer output for decoding.

9.1.4 Benefit of Whitening Transform to Turbo DFE Performance

Similar to the EST (energy-spreading transform) [47], the proposed MIMO OFDM with transform can benefit the noise performance of block turbo DFE by reducing error propagation. This is due to its ability to spread the symbol energy over the whole block. As a result, any symbol decision error is also so spread. This reduces the interference contribution of each symbol decision error to all other symbols, thereby lowering the probability of error propagation and benefiting the convergence of turbo DFE. Note that the benefit applies not only to uncoded systems, but also to coded systems, because in typical channel codes the difference between two nearby codewords (in Hamming distance or Euclidean distance) is concentrated in only a few locations rather than having its energy spread over a large signal block. The mechanism can be compared to how coded MIMO OFDM with transform excels over coded MIMO OFDM without transform as discussed in an earlier section.

9.2 Design for Receiver Complexity Reduction

Thus far, we have described the operating principles of the transform (a transmitter component) and the block turbo DFE (a receiver component). We now present a particular design that enables receiver implementation at a reduced complexity. We first consider how the turbo DFE can operate in the frequency domain. Then we present a particular design of the SFI suited to the proposed way of receiver operation. And lastly, we discuss the computational complexity.

9.2.1 Turbo DFE in Frequency Domain

By the circulant nature of the channel matrix in (9.2), we may decompose it as

$$\begin{aligned} \mathbf{H} &= (\mathbf{W} \otimes I)^H \cdot \begin{bmatrix} \Lambda_{11} & \Lambda_{12} & \dots & \Lambda_{1N} \\ \Lambda_{21} & \Lambda_{22} & \dots & \Lambda_{2N} \\ \vdots & \vdots & \ddots & \vdots \\ \Lambda_{M1} & \Lambda_{M2} & \dots & \Lambda_{MN} \end{bmatrix} \cdot (\mathbf{W} \otimes I) \\ &= (\mathbf{W} \otimes I)^H \cdot \mathbf{\Lambda} \cdot (\mathbf{W} \otimes I) \end{aligned} \quad (9.13)$$

where \mathbf{W} is the DFT matrix and each Λ_{ij} is a $K \times K$ diagonal matrix of the frequency response of the channel from transmit antenna j to receive antenna i . By permutation, the “super-matrix” $\mathbf{\Lambda}$ can be reorganized into

$$\mathbf{\Lambda} = \mathbf{Q}^T \left(\bigoplus_{k=1}^K \Lambda(k) \right) \mathbf{Q} \quad (9.14)$$

where \mathbf{Q} is a permutation matrix, $\Lambda(k)$ is the MIMO channel response at subcarrier k , and recall that $\bigoplus_{k=1}^K \Lambda(k)$ denotes the block diagonal matrix with diagonal entries $\Lambda(1), \Lambda(2), \dots, \Lambda(K)$.

The FFF and FBF can be likewise decomposed as

$$\mathbf{F} = (\mathbf{W} \otimes I)^H \cdot \mathbf{Q}^T \left(\bigoplus_{k=1}^K F(k) \right) \mathbf{Q} \cdot (\mathbf{W} \otimes I), \quad (9.15)$$

$$\mathbf{B} = (\mathbf{W} \otimes I)^H \cdot \mathbf{Q}^T \left(\bigoplus_{k=1}^K B(k) \right) \mathbf{Q} \cdot (\mathbf{W} \otimes I), \quad (9.16)$$

where for unshaped turbo DFE we have, for the k subcarrier,

$$F(k) = \mu \Lambda^H(k), \quad B(k) = I - \mu \Lambda^H(k) \Lambda(k). \quad (9.17)$$

Similarly, for the shaping filter we have

$$C(k) = \mu (\Lambda^H(k) \Lambda(k) + \alpha I)^{-1} \quad (9.18)$$

for the k th subcarrier. These equations show that both the shaped and the unshaped DFE can be performed in the frequency domain, independently over the subcarriers. The complexity can be lower than performing equalization in the time domain.

9.2.2 The Equalizer-Decoder Loop

Thus far, we have omitted the details of the equalizer-decoder loop. To this subject we now turn. Let $\underline{\mathbf{x}} = (\mathbf{W} \otimes I) \cdot \underline{\mathbf{x}}$ be the frequency spectrum of $\underline{\mathbf{x}}$, and let $\hat{\underline{\mathbf{x}}}$ and $\bar{\underline{\mathbf{x}}}$ be the DFE output and the FBF input in the frequency domain, respectively. Since the transmitted signal is spread by the space-frequency transform \mathbf{S} , we must apply the inverse transform \mathbf{S}^{-1} to the DFE output before feeding it to the channel decoder. In addition, we also need to apply the transform \mathbf{S} to the decoder output to obtain the FBF input for the next iteration. The structure of the equalizer-decoder loop is illustrated in Fig. 9.1, where we have assumed the use of a soft-output decoder.

Mathematically, the decoder input is given by

$$\hat{\underline{\mathbf{X}}} = (\mathbf{T}^H \otimes I) \cdot \mathbf{P}^T \hat{\underline{\mathbf{x}}} \quad (9.19)$$

and the FBF input is obtained from the decoder output $\bar{\underline{\mathbf{X}}}$ by

$$\bar{\underline{\mathbf{x}}} = \mathbf{P} (\mathbf{T} \otimes I) \bar{\underline{\mathbf{X}}} \quad (9.20)$$

where \mathbf{P}^T corresponds to deinterleaving, $\mathbf{T}^H \otimes I$ to inverse orthogonal transform, $\mathbf{T} \otimes I$ to orthogonal transform, and \mathbf{P} to interleaving.

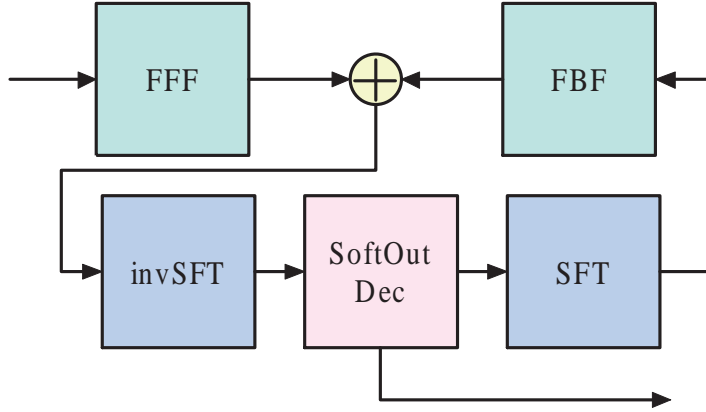


Figure 9.1: The equalizer-decoder loop.

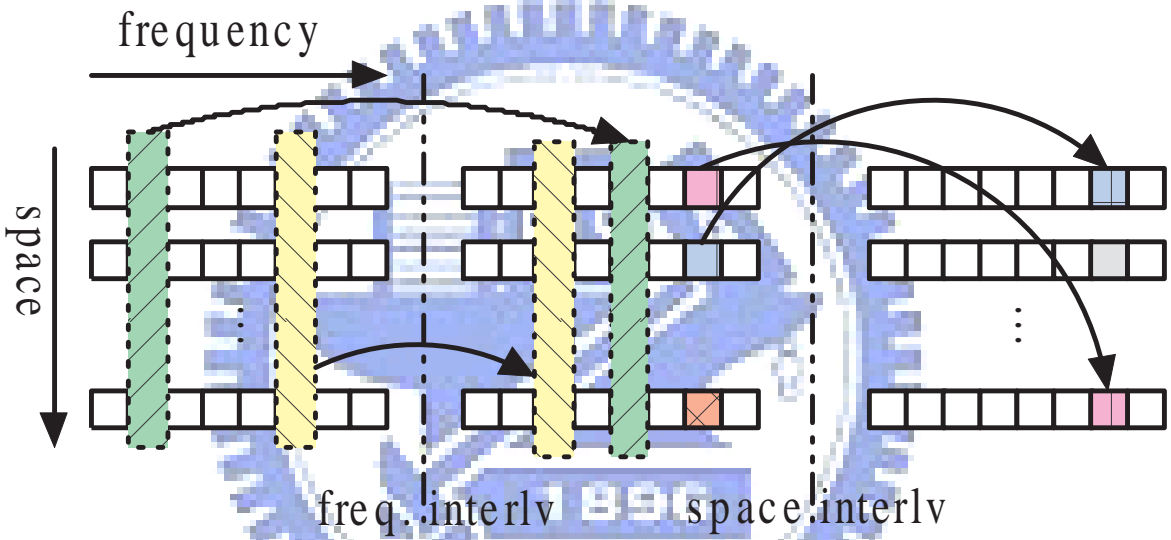


Figure 9.2: The illustration of separable space-frequency interleaving.

9.2.3 Design of Space-Frequency Interleaving

We note that the complexity of the equalizer-decoder loop can be reduced by moving the interleaving and deinterleaving functions outside the loop. This can be achieved by a proper design of the SFI method. Specifically, we employ a “separable SFI” in which the permutations in the spatial and the frequency domains are separable. Then in the receiver, the SFI and the inverse SFI can be replaced by equivalent operations on the received signal and the estimated channel response outside the equalizer-decoder loop.

The SFI is separable in the spatial and the frequency dimensions if the permutation matrix \mathbf{P} can be decomposed into the product of a spatial permutation matrix Θ and a frequency permutation matrix Φ , such as $\mathbf{P} = \Theta\Phi$. As illustrated in Fig. 9.2, in frequency interleaving, signal samples at the same subcarrier are moved to another subcarrier as a group, and in spatial interleaving, signal samples at the same subcarrier are permuted in a pseudo-random manner to different antennas.

Disregard the additive noise. Then the received signal after DFT and inverse SFI is given by

$$\mathbf{P}^T \underline{\mathbf{r}} = \mathbf{P}^T \Lambda \mathbf{P} (\mathbf{T} \otimes I) \underline{\mathbf{X}} \quad (9.21)$$

where $\mathbf{P}^T \mathbf{\Lambda} \mathbf{P}$ is the space-frequency interleaved channel frequency response. With $\mathbf{P} = \mathbf{\Theta} \mathbf{\Phi}$, we have

$$\mathbf{P}^T \mathbf{\Lambda} \mathbf{P} = \mathbf{\Phi}^T \mathbf{\Theta}^T \mathbf{\Lambda} \mathbf{\Theta} \mathbf{\Phi} \triangleq \mathbf{\Phi}^T \mathbf{\Lambda}^\dagger \mathbf{\Phi} \triangleq \mathbf{\Lambda}^\ddagger. \quad (9.22)$$

Note that $\mathbf{\Lambda}^\dagger$ and $\mathbf{\Lambda}^\ddagger$ have a similar structure as $\mathbf{\Lambda}$, because the two pairs of interleaving and deinterleaving operations amount to mere re-ordering of the spatial and the frequency indexes. Therefore, the frequency domain turbo DFE can be made to operate on $\mathbf{\Lambda}^\ddagger$ in exactly the same way as on $\mathbf{\Lambda}$ without any modification. In other words, the inverse SFI and SFI functions can be omitted in the equalizer-decoder loop.

9.2.4 Computational Complexity

We now consider the computational complexity of the proposed system. We only consider the receiver for it is much more complicated than the transmitter.

To start, we examine the complexity of equalization. Recall that the equalization process is divided into three stages: MMSE block linear equalization, shaped DFE, and basic DFE. Assume that the channel response is known. Assume also that, in each stage, we calculate the filter coefficients first (the setup phase) and then use the results in equalization (the processing phase). We use the number of complex multiplications to measure the complexity. In MMSE block linear equalization, the setup phase needs approximately $(2MN^2 + N^3)K$ computations and the processing phase M^2NK computations. In the shaped DFE stage, the setup phase requires a similar amount of computation for the FFF coefficients and MN^2K computations for the FBF coefficients. In the processing phase, the FFF output only needs to be calculated once per signal block, which costs M^2NK computations. Each iteration then needs N^3K computations for FBF filtering. In the basic DFE stage, the FFF needs no computation for setup, and the setup of FBF takes MN^2K computations. Again, the FFF output only needs to be calculated once per signal block, and it takes MN^2K computations. The complexity per iteration in the processing phase is the same as the shaped DFE stage.

Next, we examine the complexity associated with the transform. In the receiver, an inverse orthogonal transform and an orthogonal transform are needed for each turbo DFE iteration. Different transforms have different computational complexities. If the Hadamard or fast Hadamard transform (FHT) is employed, then there is no complex multiplication but only some complex additions ($2NK \log_2(K)$ for FHT). If the DFT is used (which applies to MIMO block single-carrier transmission with cyclic prefixing, or CPBSC), then the amount is $2NK \log_2(K)$ computations for IDFT and DFT.

9.3 Simulation Results

In this section, we present some simulation results to illustrate the performance of the proposed system and compare it with the performance of the coded MIMO OFDM and the coded MIMO block single-carrier transmission with cyclic prefixing (CPBSC). All simulations are run with the following conditions: 1) the channel code is the rate-1/2 recursive systematic convolutional code (RSC) with generator vectors (23,35); 2) the coded bits are randomly interleaved before being subjected to QPSK modulation; 3) two transmit antennas ($N = 2$) and two receive antennas ($M = 2$) are used; 4) the DFT size (K) is 1024; 5) the MIMO channel response and the noise variance are known exactly; 6) $\alpha = 1$ in the second equalization stage (shaped block turbo DFE); and 7) the channel decoder is of the soft-in soft-out type, employing the soft-output Viterbi algorithm (SOVA) [28], and the QPSK symbols are regenerated based on the ML criterion.

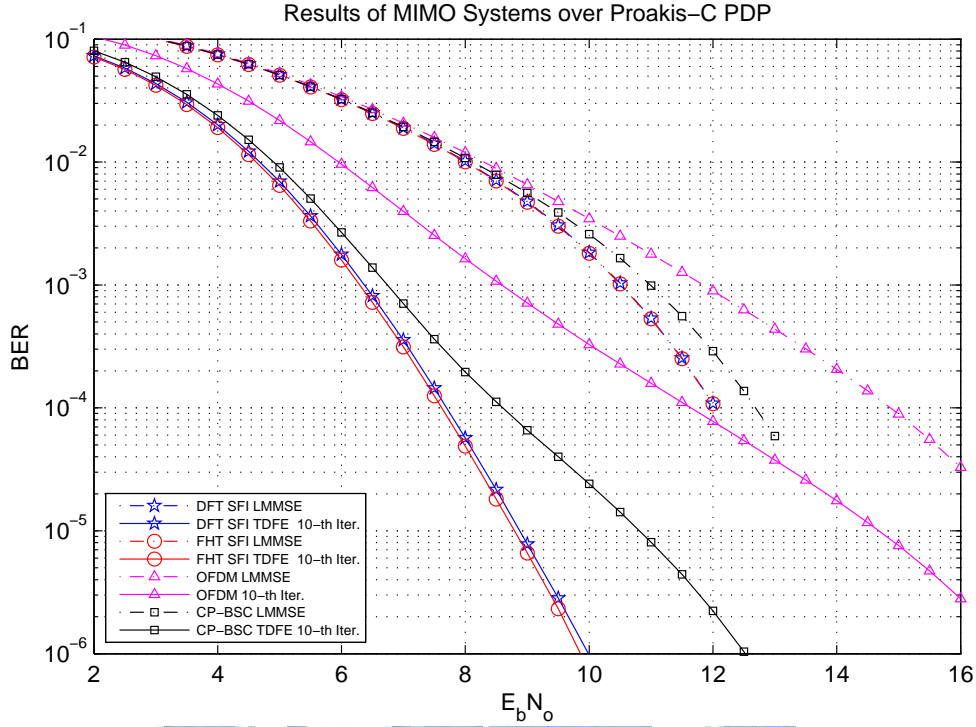


Figure 9.3: Simulation case 1: BER performance of different systems under a difficult channel.

9.3.1 Simulation Case 1: A Difficult Channel

In this set of simulations, we use the power-delay profile of the Proakis-C channel given by

$$[0.227 \ 0.460 \ 0.688 \ 0.460 \ 0.227]. \quad (9.23)$$

MIMO channels are generated based on the correlation matrices

$$\mathbf{R}_l = \mathbf{T}_l = \begin{bmatrix} 1 & 0.5 \\ 0.5 & 1 \end{bmatrix}, \quad l = 0, 1, 2, 3, 4. \quad (9.24)$$

This channel may not be realistic but is a difficult one to deal with.

Figs. 9.3 and 9.4 depict the simulated bit error rate (BER) and block error rate (BLER) performance of the different systems under several different conditions. The results show that the DFT and the FHT variants of the proposed system (both labeled SFI TDFE in the figures) perform close to each other and both exhibit superior performance compared to MIMO OFDM and MIMO CPBSC. At BLER = 10^{-2} and with a maximum of 10 equalizer iterations, the proposed system outperforms MIMO CPBSC by more than 2 dB and it outperforms MIMO OFDM by more than 6 dB.

9.3.2 Simulation Case 2: The ETSI Vehicular A Channel

Next, consider the power-delay profile of the ETSI Vehicular A channel. The channel has 6 paths. Let the channel bandwidth be 10 MHz. Then the path delays are equal to 0, 3.03, 6.93, 10.64, 16.89, and 24.51 sample spacings, respectively. The average power levels are 0, -1, -9, -10, -15, and -20 dB, respectively. The spatial correlation is the same as in the last case.

Fig. 9.5 and 9.6 depict the simulated BER and BLER performance. Very similar observations as for the last case can be made of this set of results.

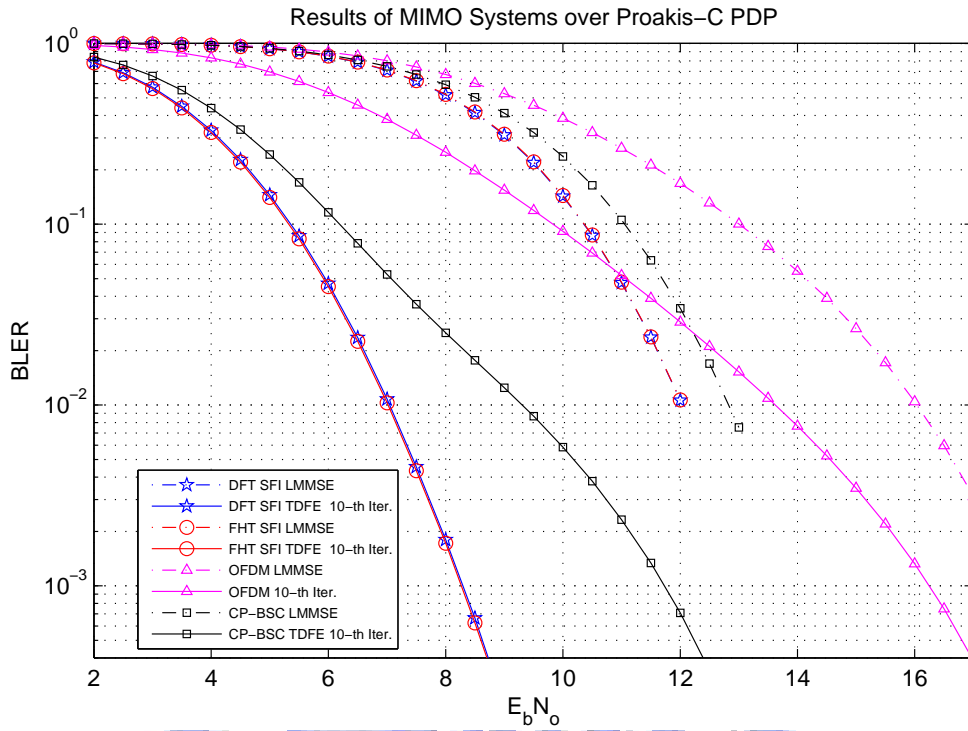


Figure 9.4: Simulation case 1: BLER performance of different systems under a difficult channel.

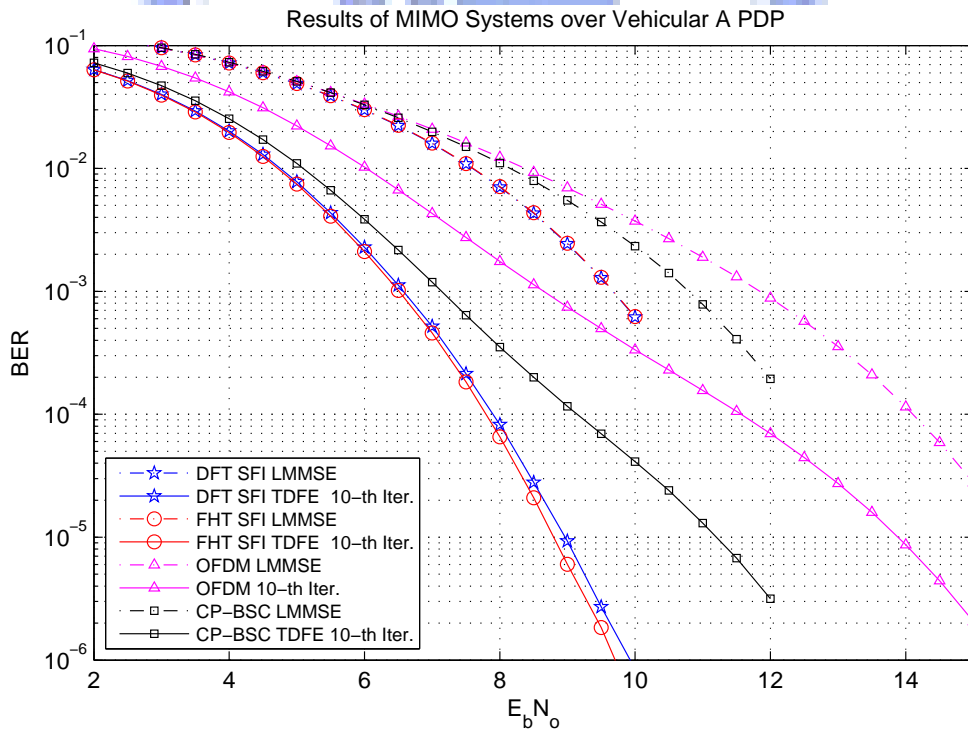


Figure 9.5: Simulation case 2: BER performance of different systems under an ETSI Vehicular A-based channel condition.

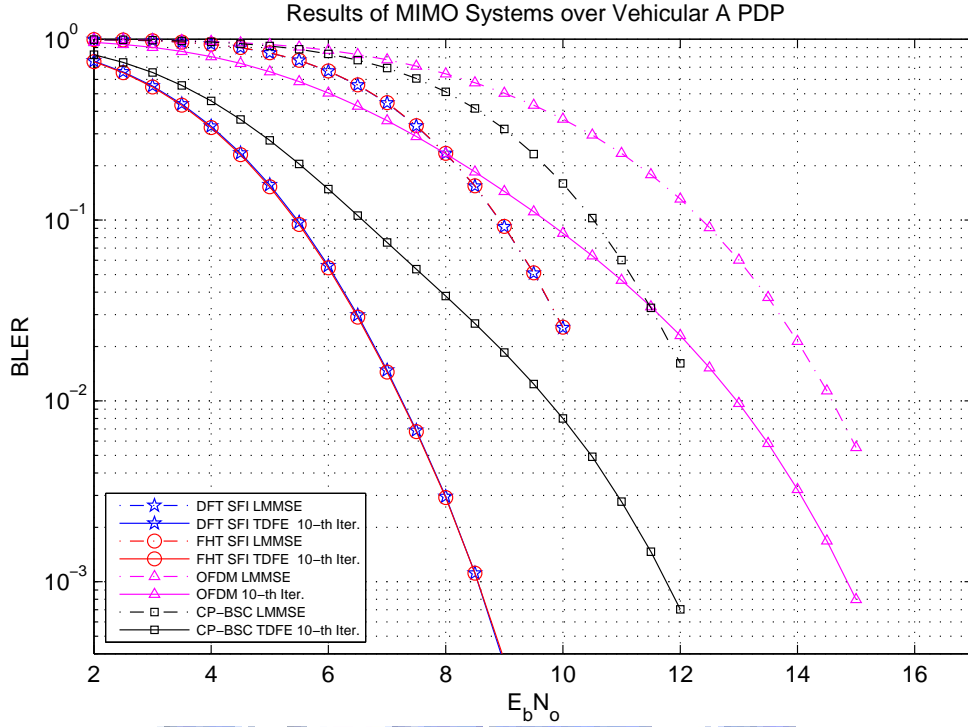


Figure 9.6: Simulation case 2: BLER performance of different systems under an ETSI Vehicular A-based channel condition.

9.4 Joint Channel Estimation and Data Detection

9.4.1 Frame Structure and Initial Channel Estimation

Note that in performing TDFE, the channel responses need be estimated first. For this, consider the frame structure illustrated in Fig. 9.7 which we call a pilot-data separated frame structure. A frame consists of a number of bursts where each burst starts with an all-pilot symbol as the preamble. It is then followed by a number of OFDM symbols. The pilot symbol is used to obtain an initial estimate of the channel response. During subsequent data symbols, adaptive channel prediction is used to track channel variation. For each symbol, iterative joint CE-DD is carried out, as described in more detail below.

For the pilot symbol, an LS channel estimation (LSCE) can be obtained by minimizing the cost function

$$J(\underline{h}_i) = \|\underline{r}_i - \mathbf{X}\underline{h}_i\|^2. \quad (9.25)$$

The solution is

$$\underline{h}_i^* = (\mathbf{Z}^H \mathbf{Z})^{-1} \mathbf{Z}^H \underline{r}_i \quad (9.26)$$

where $\mathbf{Z} = \mathbf{X}\mathbf{G}$. To achieve the minimum mean-square error in the estimate, the pilot symbol should be such that [4]

$$\mathbf{X}^H \mathbf{X} = \sigma_x^2 \mathbf{I}. \quad (9.27)$$

For channel prediction in subsequent symbols (which yields the initial channel estimate for each data symbol), we can employ block-based linear filtering whose basic form is

$$\hat{\alpha}(t) = \sum_{k=1}^{N_{tap}} w_k \alpha(t-k) \triangleq \mathbf{w} \underline{\alpha}(t) \quad (9.28)$$

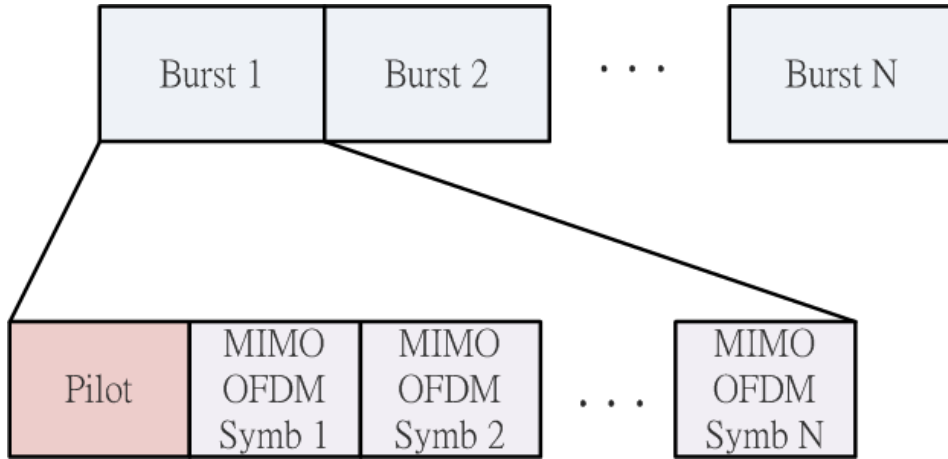


Figure 9.7: The pilot-data separated frame structure considered.

where $\alpha(t)$ represents one tap of the estimated channel response at time t and $\hat{\alpha}(t)$ is one tap of the predicted channel response. If the mobile speed is known and the fading follows Jakes' model, then the optimal prediction coefficient can be shown to be

$$\mathbf{w} = (\mathbf{R}_\alpha + \sigma_n^2 \mathbf{I})^{-1} \underline{R}_{\alpha,1} \quad (9.29)$$

where \mathbf{R}_α is the autocorrelation matrix of the channel response and $\underline{R}_{\alpha,1}$ is the crosscorrelation of the channel response and its delayed version. Under Jakes' model, the m th element in \mathbf{R}_α is given by $\mathbf{R}_\alpha(m, n) = J_0(2\pi f_m(m-n))$ and the n th element in $\underline{R}_{\alpha,1}$ by $\underline{R}_{\alpha,1}(n) = J_0(2\pi f_m(n+1))$, where $J_0(x)$ is zeroth-order modified Bessel function and f_m is the maximum Doppler shift normalized to sample spacing.

In practice, the mobile speed may not be known and the fading may not follow Jake's model. In this case, we may use an adaptive prediction filter in place of the filter above. By minimizing the cost function $E\{|\hat{\alpha}(k) - \alpha(k)|^2\}$, the simplest LMS adaptive algorithm yields the following adaptive prediction filter for \mathbf{w} :

$$\mathbf{w}(t+1) = \mathbf{w}(t) + \mu \alpha(t)^H (\alpha(t) - \hat{\alpha}(t)). \quad (9.30)$$

9.4.2 Jointly Iterative Channel Estimation and Data Detection

For each data symbol, following the initial channel estimation, we perform jointly iterative CE-DD. In each iteration, the TDFE output can be used to re-estimate the channel responses in the LS manner as in (9.26). However, the pseudo-inverse operation costs a very large computational effort. Hence, herein we propose performing the channel re-estimation using the projected gradient descent algorithm and combining it with the TDFE to yield the desired jointly iterative CE-DD.

For this, note first that the projected gradient descent algorithm is an iterative approach to solving the convex CLS problem such as that given in (9.25). Let $\bar{\mathbf{h}}_i^{k-1}$ be the estimate of \mathbf{h}_i in iteration $k-1$. By applying a similar recursion as in TDFE, we can obtain an iteration for channel estimation as

$$\hat{\mathbf{h}}_i^k = \bar{\mathbf{h}}_i^{k-1} - \mu \mathbf{X}^H (r_i - \mathbf{X} \bar{\mathbf{h}}_i^{k-1}) \quad (9.31)$$

and

$$\bar{\mathbf{h}}_i^k = \mathbf{G}^\dagger \hat{\mathbf{h}}_i^k = \mathbf{G} \hat{\mathbf{h}}_i^k. \quad (9.32)$$

Combining the above with the TDFE, we obtain the jointly iterative CE-DD procedure as

$$\underline{e}_i^k = r_i - \overline{\mathbf{X}}^{k-1} \overline{\underline{h}}_i^{k-1}, \quad (9.33)$$

$$\hat{\underline{h}}_i^k = \overline{\underline{h}}_i^{k-1} + \mu_h \left(\overline{\mathbf{X}}^{k-1} \right)^H \underline{e}_i^k, \quad (9.34)$$

$$\hat{\underline{x}}^k = \overline{\underline{x}}^{k-1} + \mu \left(\overline{\mathbf{H}}^{k-1} \right)^H \underline{e}^k, \quad (9.35)$$

where $\underline{e}^k = [\underline{e}_1^k, \underline{e}_2^k, \dots, \underline{e}_N^k]^T$, $\overline{\underline{h}}_i^k = \mathbf{G} \hat{\underline{h}}_i^k$, and $\overline{\underline{x}}^k = \mathbf{\Pi}(\hat{\underline{x}}^k)$ with $\mathbf{\Pi}(\cdot)$ denoting the combined actions of the inverse SFT, the soft-output FEC decoding, and the SFT. In the initial pass through the iterative loop, the channel estimate used is the output of the channel predictor and the TDFE output is that from linear MMSE equalization.

If shaping filtering is considered in the earlier iterations as discussed previously, (9.35) is replaced by

$$\hat{\underline{x}}^k = \overline{\underline{x}}^{k-1} + \mathbf{C} \left(\overline{\mathbf{H}}^{k-1} \right)^H \underline{e}^k. \quad (9.36)$$

To reduce the complexity, one may use a constant shaping filter \mathbf{C} calculated using the predicted channel responses.

Note also that, since the super-matrices \mathbf{X} and \mathbf{H} are composed of circulant matrices whose FFTs are diagonal matrices, many computations can be simplified by using this property as mentioned previous chapter.

9.4.3 Simulation Study

We illustrate the performance of the proposed SFT MIMO OFDM and compare it with that of the conventional MIMO OFDM [17] and the MIMO CP BSC [17, 90], all with FEC coding, by way of simulation. In fact, the MIMO CPBSC can be considered a particular kind of SFT MIMO OFDM. For the SFT, we use FFT for the orthogonal transform.

The profile of the simulated system is the same as described one in above simulations. In addition, a frame contains 5 bursts, with each burst made of 5 MIMO OFDM symbols following 1 short pilot symbol. The FFT size of the pilot symbol is 256 only. Therefore, the pilot-data ratio is 1/20 in terms of bandwidth consumption. The pilot symbol contains BPSK-modulated sequences that are mapped to the subcarriers of each antenna in an interleaved manner [4].

In the receiver, the adaptive channel predictor has five predictor taps. The maximum number of iterations of the joint CE-DD is 10 and the iteration may stop early if the decoder output contains no error. Shaping filtering is used in the earlier iterations of the TDFE and the switching from shaped to unshaped operation depends upon the convergence of the output log-likelihood ratio (LLR) of the FEC decoder.

Consider a 2×2 MIMO block time-varying channel with the same profile in section 9.3.2. Let the carrier frequency be 2.5 GHz and the channel bandwidth be 10 MHz. Consider three mobile speeds: 50, 100, and 200 km/h, which correspond roughly to maximum normalized Doppler shifts of 0.0125, 0.025, and 0.05, respectively.

Figs. 9.8 and 9.9 illustrate the block error rate (BLER) and the bit error rate (BER) performance of the three transmission schemes, where a block means the period of one OFDM symbol. At the two slower mobile speeds, the channel estimation mechanism proposed in this work can track the channel variation well. Its tracking ability is reduced at the highest mobile speed, as indicated by the error floors in the plots. In all cases, the SFT MIMO OFDM performs better than the conventional MIMO OFDM and the MIMO CPBSC. The performance gain is roughly 4 dB over conventional MIMO OFDM and 2 dB over MIMO CPBSC at the lower mobile speeds.

The error floor happens when mobile velocity is 400 Km/Hr, since the prediction error floor introduces large error of the initial channel estimation and the outage occurs frequently in high

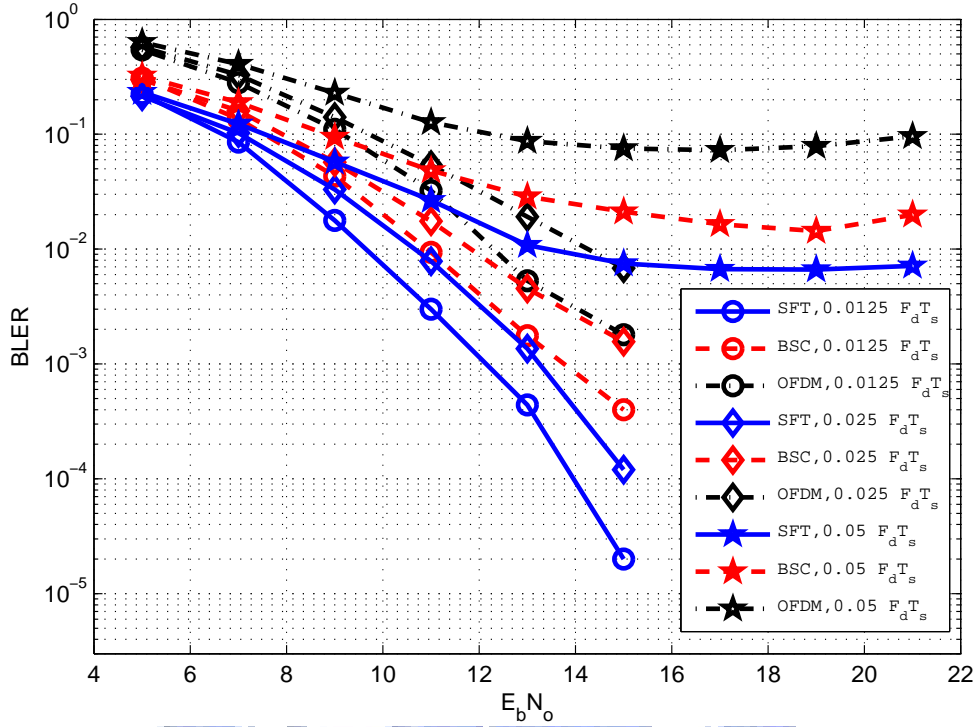


Figure 9.8: Block (symbol) error rates of different transmission schemes over block time-varying channel.

velocity, which yields poor tracking ability for the receiver. To eliminate this floor, one way is to insert pilot symbol frequently; however, this reduce the bandwidth efficiency. Another way may consider temporal domain interpolative channel estimation instead of the channel forecasting; which can be treated as a extrapolation and yields more error due to AWGN. Besides, the more accurate estimation of the delay subspace will provide larger noise reduction factor and give more clear channel estimation results to avoid the floor due to estimation error.

9.5 Conclusions

In this part, we showed the optimal design criteria of the coded MIMO OFDM transmission and proposed the design of the MIMO OFDM system, which involves the space-frequency transform, the frame structure and the receiver design. We suggested the SFT design to achieve the optimal design criteria, which is a two-step transform. The first step performs the orthogonal transform to spread the coded symbols and the second step interleaves the spread samples over frequent and spatial dimensions. For the frame design, we presented a simple pilot-data separated design to improve the spectrum efficiency by eliminating the pilot utilities. The receiver employs the IS process to jointly estimate the channel and detect the data. The prior channel references are required in the IS process. Thus, the LSCE from the pilot symbol and the channel prediction scheme are used to obtain these references. Simulations shown that the proposed SFT is superior to the conventional MIMO OFDM and the MIMO SC with CP in terms of the BER and the BLER.

For future researches, it is interest in the design to support multiuser based on the proposed SFT MIMO OFDM system. It could be a CDMA-like or a OFDMA-like schemes in either the uplink or the downlink, which depends on the position of the SFT in the transmission structure. Besides, another design issue is the receiver structure of the multiple access system. The performance, the complexity and the spectrum efficiency all are the design constrains in

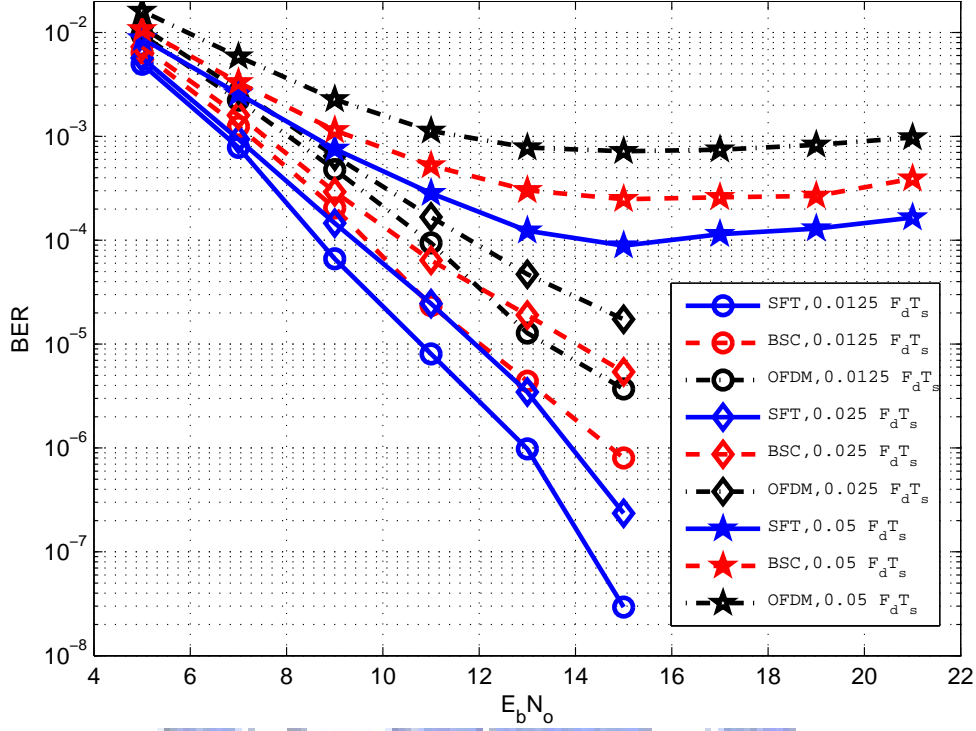


Figure 9.9: Bit error rates of different transmission schemes over block time-varying channel.

the realization.

Appendix Derivation of the MMSE Shaping Filter

First, let the singular value decomposition (SVD) of the channel matrix be given by

$$\mathbf{H} = \mathbf{U}\mathbf{\Lambda}\mathbf{V}. \quad (9.37)$$

Since the desired \mathbf{C} commutes with \mathbf{H} , we may let $\mathbf{C} = \mathbf{V}^H \mathbf{\Lambda}_c \mathbf{V}$. As in typical adaptive filter analysis, assume that \underline{e}^{k-1} is white and uncorrelated with \underline{n} . Then

$$\begin{aligned} J &\triangleq E\{\|\underline{w}^k\|^2\} \\ &= \sigma_e^2 \left(\alpha \|\mathbf{C}\mathbf{H}^H\|_F^2 + \|\mathbf{C}\mathbf{H}^H\mathbf{H} - \mathbf{I}\|_F^2 \right) \\ &= \sigma_e^2 \sum_{k=1}^{KN} \left(\alpha |\lambda_c(k)\lambda(k)|^2 + \left| \lambda_c(k)|\lambda(k)|^2 - 1 \right|^2 \right) \end{aligned} \quad (9.38)$$

where $\lambda(k)$ and $\lambda_c(k)$ are the k th singular values of \mathbf{H} and \mathbf{C} , respectively.

Now, constraining the average of the diagonal elements of \mathbf{B} to zero amounts to requiring

$$\text{tr}\{\mathbf{C}\mathbf{H}^H\mathbf{H}\} = KN, \quad (9.39)$$

or

$$\frac{1}{KN} \sum_{k=1}^{KN} \lambda_c(k) |\lambda(k)|^2 = 1. \quad (9.40)$$

Employing the Lagrange multiplier method, we consider the modified cost function

$$J_m \triangleq J + \mu \left(1 - \frac{1}{KN} \sum_{k=1}^{KN} \lambda_c(k) |\lambda(k)|^2 \right) \quad (9.41)$$

and set $\partial J_m / \partial \lambda_c(k) = 0$, which leads to the solution

$$\lambda_c^*(k) = \frac{\mu}{|\lambda(k)|^2 + \alpha} \quad (9.42)$$

and

$$\mathbf{C}^* = \mu (\mathbf{H}^H \mathbf{H} + \alpha \mathbf{I})^{-1}. \quad (9.43)$$

Substituting \mathbf{C}^* into the constraint on \mathbf{B} , we obtain

$$\mu = \frac{KN}{\text{tr} \{ (\mathbf{H}^H \mathbf{H} + \alpha \mathbf{I})^{-1} \mathbf{H}^H \mathbf{H} \}}. \quad (9.44)$$



Chapter 10

Thesis Conclusions and Future Topics

Several algorithms are proposed for the design of the communication receivers in SC QAM, OFDM, and MIMO-OFDM systems. A communication receiver contains two major processing modules. The synchronization calibrates the mismatches between the transmitter and the receiver, and estimates the unknown parameters. The channel distortion compensator is used to remove the channel effects. It can be divided into two parts: the equalization and the channel estimation. In SC QAM systems, we consider the issues in the carrier frequency recovery, the channel equalization, and the joint operation. Both the open-loop frequency estimation and closed-loop carrier recovery loop are studied in the carrier recovery problem. The blind adaptive DFE is used and studied in the channel equalization. In OFDM system, we consider the synchronization issues in the estimation of the carrier frequency offset and the symbol time, and the cell search of the mobile-WiMAX system. The issue in OFDM channel estimation is studied in the work. We propose two estimation schemes and apply these algorithms in mobile-WiMAX system. In wide-band MIMO system, we study the transform design at the transmitter, propose a space-frequency transform, and use the turbo-DFE as the data detector at the receiver. In summary, the designed algorithms for the corresponding receiver issues are given in Table 10.1.

10.1 Future Research Topics

Some potential research topics are given as follows. First, the adaptive system parameters of the OFDM system can be realized with the knowledge of the channel parameters. Specifically, the CP is used to prevent the IBI effect. If the system has the delay spread of the channel profile, the CP length can be optimized. Besides, the utilization of the pilots also can be optimized if the performance of the channel estimator can be predicted. For example, consider channel estimation with polynomial interpolation in the comb-type OFDM system. If $\sigma_{\xi}^2(N, \tau_c^o)$ and the noise variance can be estimated in advance, the estimate MSE is a function of the pilot subcarrier spacing F . Thus, the optimization of the pilot subcarrier spacing can optimize the pilot utilization.

Secondly, what is a good interpolator of the channel estimation according to the pilot structure? Specifically, consider the approximate LMMSE CE approach. The pre-defined PDP shape is constructed according the estimated delay spread and the mean delay of the channel, but it may not be the optimal approximation of the PDP event if the same profile model is used. It is interesting to estimate the optimal parameters of the profile model to match the true channel PDP or to optimize the channel estimate MSE. Besides, according to the window shift concept, what is a suitable interpolator for the given pilot assignment and what is the optimal window shift corresponding to the suitable interpolator?

Finally, the relay extension system in MIMO communication currently is a popular research topic. We may apply the transform MIMO-OFDM in such scenarios. The design of the transform, the receiving process, and the practical realization are potential topics.



Table 10.1: Proposed algorithms for the corresponding issues

Algorithm	System	Issue	Properties/Functionalities
Multi-resolution algorithm	SC QAM	carrier frequency estimation	high accuracy and low complexity frequency estimator
Reduced-constellation phase detector	SC QAM	carrier recovery loop	large frequency acquisition range
Hybrid phase detector	SC QAM	carrier recovery loop	large frequency acquisition range and small steady-state phase noise
Dynamic loop bandwidth control	SC QAM	carrier recovery loop	good tracking stability
Boundary mean-square error	SC QAM	channel equalization	high accuracy MSE estimator at low decision-point SNR
Blind variable step-size algorithm	SC QAM	channel equalization	fast convergence
Hybrid VSS algorithm	SC QAM	channel equalization	fast convergence and soft switching of operation mode
Phase-irrelevant decision feedback equalizer	SC QAM	channel equalization	convergence of blind DFF in CFO environment
Frequency domain filtering	OFDM, WiMAX	cell search	low complexity estimators in frequency domain
Phase-shift polynomial interpolation	OFDM, WiMAX	channel estimation	MMSE optimization of the polynomial interpolation
Adaptive selection of interpolator	OFDM, WiMAX	channel estimation	optimal interpolation-order estimation
Mean delay and RMS delay spread estimator	OFDM, WiMAX	channel estimation	low complexity frequency-domain estimation
Approximate LMMSE channel estimator	OFDM, WiMAX	channel estimation	low complexity and high performance channel estimator
Space-frequency transform	MIMO-OFDM	transmitter design	maximal coding and diversity gain
Separable space-frequency interleaver	MIMO-OFDM	receiver design	separation of de-interleaver outside turbo-DFE loop
MMSE Shaped turbo-DFE	MIMO-OFDM	channel equalizer	better convergence property of iterations in turbo-DFE
Joint channel estimation and equalization	MIMO-OFDM	channel estimation and equalization	low pilot utilization and joint estimation of channel and data

Bibliography

- [1] S. M. Alamouti, "A simple transmit diversity technique for wireless communications," *IEEE J. Sel. Area Commun.*, vol. 16, no. 8, pp. 1451–1458, Nov. 1998.
- [2] C. R. N. Athaudage and A. D. S. Jayalath, "Enhanced MMSE channel estimation using timing error statistics for wireless OFDM systems" *IEEE Trans. Broadcast.*, vol. 50, no. 4, pp. 369–376, Dec. 2004.
- [3] C. N. R. Athaudage and A. D. S. Jayalath, "Delay-spread estimation using cyclic-prefix in wireless OFDM systems," *IEE Proc.-Commun.*, vol. 151, no. 6, pp. 559–566, Dec. 2004.
- [4] I. Barhumi, G. Leus, and M. Moonen, "Optimal training design for MIMO OFDM systems in mobile wireless channels," *IEEE Trans Signal Process.*, vol. 51, no. 6, pp. 1615–1624, Jun. 2003.
- [5] J.-J. van de Beek, M. Sandell, and P. O. Börjesson, "ML estimation of time and frequency offset in OFDM systems," *IEEE Trans. Signal Processing*, vol. 45, pp. 1800–1805, Jul. 1997.
- [6] Roland E. Best, *Phase-locked Loops*, McGraw-Hill International, 1997.
- [7] E. K. Blum, *Numerical Analysis and Computation: Theory and Practice*. Reading, Mass.: Addison-Wesley, 1972.
- [8] J. Boutros and E. Viterbo, "Signal space diversity: power- and bandwidth-efficient diversity technique for the Rayleigh fading channel," *IEEE Trans. Inform. Theory*, vol. 44, no. 4, pp. 1453–1467, Jul. 1998.
- [9] T. Brown and M. M. Wang, "An iterative algorithm for single-frequency estimation," *IEEE Trans. Signal Process.*, vol. 50, no. 11, pp. 2671–2682, Nov. 2002.
- [10] K. V. Cartwright, "Blind phase recovery in general QAM communication systems using alternative higher order statistics," *IEEE Signal Processing Lett.*, vol. 6, no. 12, pp. 327–329, Dec. 1999.
- [11] K. V. Cartwright, "Blind phase recovery in cross QAM communication systems with eighth-order statistics," *IEEE Signal Processing Lett.*, vol. 8, no. 12, pp. 304–306, Dec. 2001.
- [12] F. C. C. De Castro, M. C. F. De Castro, and D. S. Arantes, "Concurrent blind deconvolution for channel equalizations," in *Conf. Rec., IEEE Int. Conf. Commun.*, Jun. 2001, pp. 366–371.
- [13] A. M. Chan and G. W. Wornell, "A class of block-iterative equalizers for intersymbol interference channels: Fixed channel results," *IEEE Trans. Commun.*, vol. 49, no. 11, pp. 1966–1976, Nov. 2001.

- [14] C.-C. Chang *et al.*, “A wide pull-in range fast acquisition hardware-sharing two-fold carrier recovery loop,” in *Proc. Int. Symp. Circuits Syst.*, vol. IV, pp. 358–361, May 2001.
- [15] P. Ciblat *et al.*, “Performance analysis of blind carrier frequency offset estimators for Non-circular transmissions through frequency-selective channels,” *IEEE Trans. Signal Process.*, vol. 50, no. 1, pp. 130–140, Jan. 2002.
- [16] P. Ciblat and M. Ghogho, “Blind NLLS carrier frequency-offset estimation for QAM, PSK, and PAM modulations: performance at low SNR,” *IEEE Trans. Commun.*, vol. 54, no. 10, Oct. 2006.
- [17] J. Coon *et al.*, “A comparison study of MIMO-OFDM and MIMO-SCFDE in WLAN environments,” in *Proc. GLOBECOM 2003*, vol. 6, Dec. 2003, pp. 3296–3301.
- [18] O. Edfors, *et al.* “OFDM channel estimation by singular value decomposition,” *IEEE Trans. Commun.*, vol. 46, no. 4, pp. 931–939, Jul. 1998.
- [19] O. Edfors, *et al.* “Analysis of DFT-based channel estimation for OFDM,” *Wireless Personal Commun.*, vol. 12, no. 1, pp. 55–70, Jan. 1998.
- [20] V. Erceg *et al.*, “Channel models for fixed wireless applications,” standards contribution IEEE 802.16.3c-01/29r1, Feb. 23, 2001.
- [21] ETSI TR 101 112, “Selection procedures for the choice of radio transmission technologies of the UMTS,” *ETSI Tech. Rep.*, V3.0.2, pp. 38–43, Apr. 1994.
- [22] X. Fang, X. P. Xu and H. Li “A new phase-unwrapping method used in the single frequency estimation,” *Proceedings of ICSP*, 2004.
- [23] M. P. Fitz, “Further results in the fast estimation of a single frequency,” *IEEE Trans. Commun.*, vol. 42, No. 2/3/4, pp. 862–864, Feb. 1994.
- [24] R. Freund, G. Golub, and N. Nachtigal, “Iterative solution of linear systems,” *Acta Numer.*, vol. 1, pp. 57–100, 1992.
- [25] H. Fu and P. Y. Kam “MAP/ML estimation of the frequency and phase of a single sinusoid in Noise,” *IEEE Trans. Signal Process.* vol. 55, no. 3, march 2007.
- [26] W. H. Gerstaecker, R. R. Muller, and J. B. Huber, “Iterative equalization with adaptive soft feedback,” *IEEE Trans. Commun.*, vol. 48, no. 9, pp. 1462–1466, 2000.
- [27] G. H. Golub and C. F. Van Loan *Matrix Computations*, Johns Hopkins Press Ltd., London, 3rd Edition, 1996.
- [28] J. Hagenauer and P. Hoehner, “A Viterbi algorithm with soft-decision outputs and its applications,” in *Conf. Rec., IEEE Global Telecommun. Conf.*, Nov. 1989.
- [29] S. Haykin, *Adaptive Filter Theory*, Prentice-Hall, Inc., New Jersey, 2002.
- [30] L. He, M. G. Amin, C. Reed, Jr., and R. C. Malmkemes, “A hybrid adaptive blind equalization algorithm for QAM signals in wireless communications,” *IEEE Trans. Signal Processing*, vol. 45, no. 7, pp. 2058–2069, Jul. 2004.
- [31] R. A. Horn and C. R. Johnson, *Matrix Analysis*. Cambridge, U.K.: Cambridge Univ. Press, 1999.

- [32] M.-H. Hsieh and C.-H. Wei, "Channel estimation for OFDM systems based on comb-type pilot arrangement in frequency selective fading channels," *IEEE Trans. Consumer Electron.*, vol. 44, no. 1, pp. 217–225, Feb. 1998.
- [33] M.-H. Hsieh and C.-H. Wei, "A Low-Complexity frame synchronization and frequency offset compensation scheme for OFDM systems over fading channels," *IEEE Trans. Vehicular Tech.* vol. 48, no. 5, pp. 1596–1609, Sep. 1999.
- [34] K.-C. Hung, D. W. Lin, and C.-N. Ke, "Variable-step-size multimodulus blind decision-feedback equalization for high-order QAM based on boundary MSE estimation," in *Proc. IEEE int. Conf. Acoust. Speech Signal Process.*, vol. 4, May 2004, pp. 881–884.
- [35] K.-C. Hung and D. W. Lin, "Joint carrier recovery and multimodulus blind decision-feedback equalization under high-order QAM," in *Conf. Rec., IEEE Globe Telecommun. Conf.*, Nov.–Dec. 2004.
- [36] K.-C. Hung and D. W. Lin, "A Hybrid Variable Step-Size Adaptive Blind Equalization Algorithm for QAM Signals," in *Conf. Rec., IEEE Globe Telecommun. Conf.*, Nov.–Dec. 2005.
- [37] K.-C. Hung and D. W. Lin, "Joint detection of integral carrier frequency offset and preamble index in OFDMA WiMAX downlink synchronization," in *IEEE Wireless Commun. and Networking Conf. (WCNC)*, Mar. 2007.
- [38] K.-C. Hung and D. W. Lin, "Theory and design of nearoptimal MIMO OFDM transmission system for correlated multipath Rayleigh fading channels," *J. Commun. Networks*, vol. 9, no. 2, Jun. 2007.
- [39] K.-C. Hung and D. W. Lin, "Joint channel estimation and data detection for space-frequency transformed MIMO OFDM system," in *Taiwan-Japan Joint Conference on Communications Technology*, Hsinchu, Taiwan, ROC, pp. 36–40, Nov. 2007.
- [40] K.-C. Hung and D. W. Lin, "Jointly iterative channel estimation and data detection for cyclic-prefixed block transmission over time-varying channels," in *International Conference on Information, Communications & Signal Processing*, Dec. 2007.
- [41] K.-C. Hung and D. W. Lin, "Optimal delay estimation for phase-rotated linear interpolative channel estimation in OFDM and OFDMA systems," *IEEE Signal Processing Lett.*, vol. 15, pp. 349–352, 2008.
- [42] K.-C. Hung and D. W. Lin, "Pilot-aided multicarrier wireless channel estimation via MMSE polynomial interpolation," in *Conf. Rec., IEEE Globe Telecommun. Conf.*, Nov.–Dec. 2008.
- [43] K.-C. Hung and D. W. Lin, "Pilot-aided multicarrier channel estimation via MMSE linear phase-shifted polynomial interpolation," submit to *IEEE Trans. Wireless Commun.*
- [44] K.-C. Hung and D. W. Lin, "Pilot-based LMMSE channel estimation for OFDM systems with power-delay profile approximation," submit to *IEEE Trans. Vehicular Tech.*
- [45] K.-C. Hung and D. W. Lin, "LMMSE channel estimation based on approximated power-delay profile for OFDM systems with distributed pilots," submit to *Proc. IEEE int. Conf. Acoust. Speech Signal Process.* 2009.

- [46] T. Hwang and Y. Li, "Space-time energy spreading transform based MIMO technique with iterative signal detection," in *Conf. Rec., IEEE Global Telecommun. Conf.*, Nov. 2004, pp. 2470–2474.
- [47] T. Hwang and Y. Li "Novel iterative equalization based on energy-spreading transform," *IEEE Trans. Signal Processing*, vol. 54, no. 1, pp. 190–203, 2006.
- [48] IEEE Std 802.16e-2005 and IEEE Std 802.16-2004/Cor1-2005, *IEEE Standard for Local and Metropolitan Area Networks — Part 16: Air Interface for Fixed and Mobile Broadband Wireless Access Systems — Amendment 2: Physical and Medium Access Control Layers for Combined Fixed and Mobile Operation in Licensed Bands*. New York: IEEE, Feb. 2006.
- [49] C. R. Johnson, Jr. *et al.*, "Blind equalization using the constant modulus criterion: a review," *Proc. IEEE*, vol. 86, no. 10, pp. 1927–1950, Oct. 1998.
- [50] B. Kaltenbacher, "Some Newton-type methods for the regularization of nonlinear ill-posed problems," *Inverse Problems*, vol. 13, no. 3, pp. 729–753, 1997.
- [51] S. Kay, "A fast and accurate single frequency estimator," *IEEE Trans. Acoust., Speech, Signal Process.*, vol. 39, no. 12, pp. 1987–1990, May 1989.
- [52] C.-N. Ke, C.-Y. Huang, and C.-P. Fan "An adaptive carrier synchronizer for M-QAM cable receiver," *IEEE Trans. Consum. Elect.*, vol. 49, no. 4, pp. 983-988, Nov. 2003.
- [53] Y. H. Kim, I. Song, S. Yoon, and S. R. Park, "An efficient frequency offset estimator for OFDM Systems and its performance characteristics," *IEEE Trans. Vehicular Tech.*, vol. 50, no. 5, pp. 1307–1312, Sep. 2001.
- [54] K.-Y. Kim and H.-J. Choi, "Design of carrier recovery algorithm for high-order QAM with large frequency acquisition range," in *Conf. Rec., IEEE Int Conf. Commun.*, vol. 4, pp. 1016–1020, Jun. 2001.
- [55] R. H. Kwong and E. W. Johnson, "A variable step size LMS algorithm," *IEEE Trans. Signal Processing*, vol. 40, no. 7, pp. 1633–1642, Jul. 1992.
- [56] C. Laot, A. Glavieux, and J. Labat, "Turbo equalization: adaptive equalization and channel decoding jointly optimized," *IEEE J. Sel. Areas Commun.*, vol. 19, pp. 1744–1752, Sep. 2001.
- [57] E. G. Larsson *et al.*, "Joint symbol timing and channel estimation for OFDM based WLANs" *IEEE Commun. Lett.*, vol. 5, no. 8, pp. 325–327, Aug. 2001.
- [58] K. H. Lee, S. C. Jung, and H. J. Choi, "A Novel digital lock detector for QPSK receiver," *IEEE Commun. Letter*, vol. 46, no. 6, pp. 750-753 Jun. 1998.
- [59] S. Lee, A. Singer, and N. Shanbhag, "Linear turbo equalization analysis via BER transfer and EXIT charts," *IEEE Trans. Signal Processing*, vol. 53, no. 8, pp. 2883–2897, 2005.
- [60] Y. Li and K. J. R. Liu, "Static and dynamic convergence behavior of adaptive blind equalizers," *IEEE Trans. Signal Processing*, vol. 44, no. 11, pp. 2736–2745, Nov. 1996.
- [61] Y. Li, "Pilot-symbol-aided channel estimation for OFDM in wireless systems," *IEEE Trans. Vehic. Tech.*, vol. 49, no. 4, pp. 1207–1215, Jul. 2000.
- [62] A. P. Liavas and D. Tsipouridou "On the performance of the mismatched MMSE and the LS linear equalizers", *IEEE Trans. Signal Process.*, vol. 55, no. 7, pp. 3302–3311, Jul. 2007.

- [63] H. Lim and D. S. Kwon, "Initial synchronization for WiBro," in *Asic-Pacific Conf. Commun.*, 2005, pp. 284–288.
- [64] J.-C. Lin, "Maximum-likelihood frame timing instant and frequency offset estimation for OFDM communication over a fast Rayleigh fading channel," *IEEE Trans. Vehic. Tech.*, vol. 52, no. 4, pp. 1049–1062, Jul. 2003.
- [65] L. R. Litwin, M. D. Zoltowski, T. J. Endres, and S. N. Hulyalkar, "Blended CMA: smooth, adaptive transfer from CMA to DD-LMS," in *Proc. IEEE Wireless Commun. Networking Conf.*, 1999, pp. 797–800.
- [66] X. Ma, *et al* "Non-data-aided carrier offset estimators for OFDM with nullsubcarriers: identifiability, algorithms, and performance," *IEEE J. Select. Areas Commun.*, vol. 19, pp. 2504–2515, Dec. 2001.
- [67] J. Mai and A. H. Sayed, "A feedback approach to the steady-state performance of fractionally spaced blind adaptive equalizers," *IEEE Trans. Signal Processing*, vol. 48, no. 1, pp. 80–91, Jan. 2000.
- [68] H. Meyr, M. Moeneclaey, and S. A. Fechtel, *Digital communication receivers: synchronization, channel estimation and signal processing*. John Wiley & Sons, inc. New York, 1997.
- [69] A. Mileant and S. Hinedi, "On the effect of phase jitter on QPSK lock detection," *IEEE Trans. Commun.*, vol. 41, no. 7, pp. 1043–1046, Jul. 1993.
- [70] T. Miyajima and Z. Ding "Second-order statistical approaches to channel shortening in multicarrier systems," *IEEE Trans. Signal Process.*, vol. 53, no. 11, pp. 3253–3264, Nov. 2004.
- [71] M. Moeneclaey and G. de Jonghe, "ML-oriented NDA carrier synchronization for general rotationally symmetric signal constellations," *IEEE Trans. Commun.*, vol. 42, no. 8, pp. 2531–2533, Aug. 1994.
- [72] M. Morelli and U. Mengali "A comparison of pilot-aided channel estimation methods for OFDM systems," *IEEE Trans. Signal Process.*, vol. 49, no. 12, pp. 3065–3073, Jan. 1998.
- [73] M. Morelli and U. Mengali, "An improved frequency offset estimator for OFDM applications," *IEEE Commun. Lett.*, vol. 3, no. 3, pp. 75–77, Mar. 1999.
- [74] Y. Mostofi and D. C. Cox "A robust timing synchronization design in OFDM system– part I: low-mobility case," *IEEE Trans. Wireless. Commun.*, vol. 6, no. 12, pp. 4329–4339, Dec. 2007.
- [75] R. Nee and R. Prasad, *OFDM for Wireless Multimedia Communications*. Norwell, Mass.: Artech House, 2000.
- [76] A. V. Oppenheim and A. S. Willsky with S. H. Nawab, *Signals and Systems, 2nd ed.* Upper Saddle River, New Jersey: Prentice-Hall, 1997.
- [77] O. Oyman, R. U. Nabar, H. Bolcskei, and A. J. Paulraj, "Characterizing the statistical properties of mutual information in MIMO channels," *IEEE Trans. Signal Processing*, vol. 51, no. 11, Nov. 2003.
- [78] M. Oziewicz, "On application of MUSIC algorithm to time delay estimation in OFDM channels," *IEEE Trans. Broadcasting*, vol. 51, no. 2, pp. 249–255, Jun. 2005.

- [79] L. C. Palmer, "Coarse frequency estimation using the discrete Fourier transform," *IEEE Trans. Inf. Theory*, vol. IT-20, pp. 104–109, Jan. 1974
- [80] J. Park *et al.*, "Performance analysis of channel estimation for OFDM systems with residual timing offset," *IEEE Trans. Wireless Commun.*, vol. 5, no. 7, pp. 1622–1625, Jul. 2006.
- [81] S. Y. Park and C. G. Kang "Complexity-reduced iterative MAP receiver for interference suppression in OFDM-based spatial multiplexing systems," *IEEE Trans. Vehic. Tech.*, vol. 53, no. 5, pp. 1316–1326, Sep. 2004.
- [82] M. Piana and M. Berterp, "Projected Landweber method and preconditioning," *Inverse Problems*, vol. 13, no. 2, pp. 441–463, 1997.
- [83] C. Pirak *et al.*, "Adaptive channel estimation using pilot-embedded data-bearing approach for MIMO-OFDM systems," *IEEE Trans. Signal Process.*, vol. 54, no. 12, pp. 4707–4716, Dec. 2006.
- [84] T. S. Rappaport, *Wireless Communications Principles and Practice, 2nd ed.* Upper Saddle River, New Jersey: Prentice Hall, 2002.
- [85] D. C. Rife and R. R. Boorstyn, "Single-tone parameter estimation from discrete-time observations," *IEEE Trans. Inf. Theory*, vol. IT-20, No. 5, pp. 591–598, Sep. 1974.
- [86] A. K. Sadek, W. Su, and K. J. R. Liu, "Diversity analysis for frequency-selective MIMO-OFDM system with general spatial and temporal correlated model," *IEEE Trans. Commun.*, vol. 54, no. 5, May 2006.
- [87] R. W. Schafer and L. R. Rabiner, "A digital signal processing approach to interpolation," *Proc. IEEE*, vol. 61, No. 6, pp. 692–702, Jun. 1973.
- [88] T. M. Schmidl and D. C. Cox, "Robust frequency and timing synchronization for OFDM," *IEEE Trans. Commun.*, vol. 45, no. 12, pp. 1613–1621, Dec. 1997.
- [89] O. Shalvi and E. Weinstein, "New criteria for blind deconvolution of nonminimum phase systems (channels)," *IEEE Trans. Inform. Theory*, vol. 36, no. 2, pp. 313–320, Mar. 1990.
- [90] J. Siew, *et al.*, "A channel estimation algorithm for MIMO-SCFDE," *IEEE Commun. Letter*, vol. 8, no. 9, pp. 555–557, Sep. 2004.
- [91] O. Simeone, Y. Bar-Ness, and U. Spagnolini "Pilot-based channel estimation for OFDM systems by tracking the delay-subspace," *IEEE Trans. Wireless Commun.*, vol. 3, no. 1, pp. 315–325, Jan. 2004.
- [92] V. Tarokh, N. Seshadri, and A. R. Calderbank, "Space-time codes for high data rate wireless communication: Performance criterion and code construction," *IEEE Trans. Inform. Theory*, vol. 44, no. 2, pp. 744–765, Mar. 1998.
- [93] S. A. Treutter, "Estimating the frequency of a noisy sinusoid by linear regression," *IEEE Trans. Inf. Theory*, vol. IT-31, no. 6, pp. 832–835, Nov. 1985.
- [94] U. Tureli, H. Liu, and M. D. Zoltowski, "OFDM blind carrier offset estimation: ESPRIT," *IEEE Trans. Commun.*, vol. 48, no. 9, pp. 1459–1461, Sep. 2000.
- [95] F.-B. Ueng and Y. T. Su, "Adaptive VSS blind equalizers," *IEEE Signal Processing Lett.*, vol. 4, no. 4, pp. 100–102, Apr. 1997.

- [96] Y. Wang, E. Serpedin, and P. Ciblat, "Optimal blind nonlinear least-squares carrier phase and frequency offset estimation for general QAM modulations," *IEEE Trans. Wireless Commun.*, vol. 2, no. 5, pp. 1040–1054, Sep. 2003.
- [97] C. L. Wei, B. Kannan, and T. T. Tjhung, "Joint channel estimation and OFDM synchronization in multipath fading" in *Proc. IEEE Int. Conf. Commun.*, vol. 2, pp. 20–24, Jun. 2004.
- [98] WiMAX Forum, *Mobile WiMAX — Part I: A Technical Overview and Performance Evaluation*. WiMAX Forum White Paper, Aug. 2006.
- [99] K. Witrisal, "On estimating the RMS delay spread from the frequency-domain level crossing rate," *IEEE Commun. Lett.*, vol. 5, no. 7, pp. 287–289, Jul. 2001.
- [100] K. Witrisal, Y.-H. Kim, and R. Prasad, "A new method to measure parameters of frequency-selective radio channels using power measurements," *IEEE Trans. Commun.*, vol. 49, no. 10, pp. 1788–1800, Oct. 2001.
- [101] C.-J. Wu and D. W. Lin, "Sparse channel estimation for OFDM transmission based on representative subspace fitting," in *IEEE 61st Vehic. Tech. Conf.*, 2005, vol. 1, pp. 495–499.
- [102] Y. Xin, Z. Wang, and G. B. Giannakis, "Space-time diversity system based on linear constellation precoding," *IEEE Trans. Wireless Commun.*, vol. 2, no. 2, Mar. 2003.
- [103] B. Yang, *et al.* "Channel estimation for OFDM transmission in multipath fading channels based on parametric channel modeling," *IEEE Trans. Commun.*, vol. 49, no. 3, pp. 467–478, Mar. 2001.
- [104] J. Yang, J.-J. Werner and G. A. Dumont, "The multimodulus blind equalization and its generalized algorithms," *IEEE J. Select. Areas Commun.*, vol. 20, no. 5, pp. 997–1015, Jun. 2002.
- [105] S. Yiu, R. Schober, and L. Lampe, "Distributed space-time block coding," *IEEE Trans. Commun.*, vol. 54, no. 7, Jul. 2006.
- [106] J.-T. Yuan, and K.-D. Tsai, "Analysis of the multimodulus blind equalization algorithm in QAM communication systems," *IEEE Trans. Commun.*, vol. 53, no. 9, Sep. 2005.
- [107] T. Yucek and H. Arslan, "Time dispersion and delay spread estimation for adaptive OFDM systems," *IEEE Trans. Vehic. Tech.*, vol. 57, no. 3, pp. 1715–1722, May 2008.
- [108] P. Yuvapoositanon and J. a. Chambers, "A mixed-cost blind adaptive receiver for DS-CDMA," in *Proc. IEEE Workshop Statis. Signal Processing*, Aug. 2001, pp. 94–97.
- [109] Y. Zen *et al.*, *Mobile WiMAX: Toward Broadband Wireless Metropolitan Area Networks*. New York: Auerbach, Dec. 2007.

簡歷

中文姓名	洪崑健
英文姓名	Hung, Kun-Chien
性別	男
出生日期	67 年 12 月 12 日
戶籍住址	屏東縣崁頂鄉園寮村田寮路 1-2 號
聯絡方式	humboldt2004@gmail.com

學歷資訊

高中	高雄中學(1994/9-1997/6)
大學	交通大學電子系(1997-2001/6)
研究所/博士班	交通大學電子所系統組(直升博士班)(2001/9-2008/10)

著作、論文

JNL Paper under Review	<u>K.-C. Hung</u> and D. W. Lin, "Pilot-Aided Multicarrier Channel Estimation via MMSE Linear Phase-Shifted Polynomial Interpolation," submit to <i>IEEE Trans. Wireless Commun.</i>
JNL Paper under Review	<u>K.-C. Hung</u> and D. W. Lin, "Pilot-Based LMMSE Channel Estimation for OFDM Systems with Power-Delay Profile Approximation," submit to <i>IEEE Trans. Vehicul. Tech.</i>
Conf. Paper under Review	<u>K.-C. Hung</u> and D. W. Lin, "LMMSE Channel Estimation Based on Approximated Power-Delay Profile for OFDM Systems with Distributed Pilots," submit to <i>ICASSP2009</i>
Letter	<u>K.-C. Hung</u> and D. W. Lin, "Optimal delay estimation for phaserotated linearly interpolative channel estimation in OFDM and OFDMA systems," <i>IEEE Signal Processing Lett.</i> , vol. 15, pp. 349-352, 2008.
Journal	<u>K.-C. Hung</u> and D. W. Lin, "Theory and design of nearoptimal MIMO OFDM transmission system for correlated multipath Rayleigh fading channels," <i>J. Commun. Networks</i> , vol. 9, no. 2, June 2007.
Book Chapter	<u>K.-C. Hung</u> , D. W. Lin, Y.-T Lee, K Loa WirelessMAN Physical Layer Specifications: Signal Processing Perspective. Mobile WiMAX: Toward Broadband Wireless Metropolitan Area, Chapter 3, ISBN: 78-0849326240
International Conference	<u>K.-C. Hung</u> and D. W. Lin, "Pilot-aided multicarrier wireless channel estimation via MMSE polynomial interpolation," in <i>Conf. Rec., IEEE Globe Telecommun. Conf.</i> , Nov.-Dec. 2008.

International Conference	<u>K.-C. Hung</u> and D. W. Lin, "Jointly iterative channel estimation and data detection for cyclic-prefixed block transmission over time-varying channels," in <i>International Conference on Information, Communications & Signal Processing</i> , Dec 2007.
International Conference	<u>K.-C. Hung</u> and D. W. Lin, "Joint channel estimation and data detection for space-frequency transformed MIMO OFDM system," in <i>Taiwan-Japan Joint Conference on Communications Technology</i> , Hsinchu, Taiwan, ROC, pp. 36-40, Nov, 2007.
International Conference	<u>K.-C. Hung</u> and D. W. Lin, "Joint detection of integral carrier frequency offset and preamble index in OFDMA WiMAX downlink synchronization," in <i>IEEE Wireless Commun. and Networking Conf. (WCNC)</i> , Mar. 2007.
International Conference	<u>K.-C. Hung</u> and D. W. Lin, "A Hybrid Variable Step-Size Adaptive Blind Equalization Algorithm for QAM Signals," in <i>Conf. Rec., IEEE Globe Telecommun. Conf.</i> , Nov.–Dec. 2005.
International Conference	<u>K.-C. Hung</u> and D. W. Lin, "Joint carrier recovery and multimodulus blind decision-feedback equalization under high-order QAM," in <i>Conf. Rec., IEEE Globe Telecommun. Conf.</i> , Nov.–Dec. 2004.
International Conference	<u>K.-C. Hung</u> , D. W. Lin, and C.-N. Ke, "Variable-step-size multimodulus blind decision-feedback equalization for high-order QAM based on boundary MSE estimation," in <i>Proc. IEEE int. Conf. Acoust. Speech Signal Processing</i> , vol. 4, May 2004, pp. 881–884.

